On the Application of Mathematical Methods in Hill–Type Muscle Modeling: Stability, Sensitivity and Optimal Control

by

Robert Rockenfeller
from Neuwied

Accepted Dissertation thesis
for the partial fulfilment of the requirements for a
Doctor of Natural Sciences
Fachbereich 3: Mathematik/Naturwissenschaften
Universität Koblenz–Landau

Reviewer:
Prof. Dr. Thomas Götz
Jun.-Prof. Dr.-Ing. Jörg Fehr

Examiner:
Prof. Dr. Stefan Ruzika
Prof. Dr. Thomas Götz
Prof. Dr. Karin Gruber

Date of the oral examination:
February 17$^{\text{th}}$ 2016

For Kim

Yer Jalan Atthirari Anni
(Moon of My Life)

For Ronja and Erik

Lame ma Vezh fin Saja Rhaesheseres
(The Mare and Stallion that Mount the World)

– Khal Drogo –

Abstract

While reading this sentence, you probably gave (more or less deliberately) instructions to approximately 100 to 200 muscles of your body. A sceptical face or a smile, your fingers scrolling through the text or holding a printed version of this work, holding your head, sitting, and much more. All these processes take place almost automatically, so they seem to be no real achievement. In the age of digitalization it is a defined goal to transfer human (psychological and physiological) behavior to machines (robots). However, it turns out that it is indeed laborious to obtain human facial expression or walking from robots. To optimize this transfer, a deeper understanding of a muscle's operating principle is needed (and of course an understanding of the human brain, which will, however, not be part of this thesis).

A human skeletal muscle can be shortened willingly, but not lengthened, thereto it takes an antagonist. The muscle's change in length is dependent on the incoming stimulus from the central nervous system, the current length of the muscle itself, and certain muscle–specific quantities (parameters) such as the maximum force. Hence, a muscle can be mathematically described by a differential equation (or more exactly a coupled differential–algebraic system, DAE), whose structure will be revealed in the following chapters. The theory of differential equations is well–elaborated. A multitude of applicable methods exist that may not be known by muscle modelers. The purpose of this work is to link the methods from applied mathematics to the actual application in biomechanics.

The first part of this thesis addresses *stability theory*. Let us remember the prominent example from middle school physics, in which the resting position of a ball was obviously less susceptible towards shoves when lying in a bowl rather than balancing at the tip of a hill. Similarly, a dynamical (musculo–skeletal) system can attain equilibrium states that react differently towards perturbations. We are going to compute and classify these equilibria.

In the second part, we investigate the influence of individual parameters on model equations or more exactly their solutions. This method is known as *sensitivity analysis*. Take for example the system "car" containing a value for the quantity "pressure on the break pedal while approaching a traffic light". A minor deviation of this quantity upward or downward may lead to an uncomfortable, abrupt stop or even to a collision, instead of a smooth stop with a sufficient gap. The considered muscle model contains over 20 parameters that, if changed slightly, have varying effects on the model equation solutions at different instants of time. We will investigate the sensitivity of those parameters regarding different sub–models, as well as the whole model among different dynamical boundary conditions.

The third and final part addresses the *optimal control* problem (OCP). The muscle turns a nerve impulse (input or control) into a length change and therefore a force response (output). This forward process is computable by solving the respective DAE. The reverse direction is more difficult to manage. As an everyday example, the OCP is present regarding self–parking cars, where a given path is targeted and the controls are the position of the steering wheel as well as the gas pedal. We present two methods of solving OCPs in muscle modeling: the first is a conjunction of variational calculus and optimization in function spaces, the second is a surrogate–based optimization.

Zusammenfassung

Während Sie diesen Satz lesen, werden Sie mit Sicherheit mindestens 100 bis 200 Muskeln Ihres Körpers (mehr oder weniger bewusst) einen Arbeitsauftrag erteilt haben. Ein ungläubiges Gesicht machen oder Lächeln, mit Hilfe der Finger die Maus veranlassen durch den Text zu scrollen oder eine ausgedruckte Version dieser Arbeit halten, sitzen, den Kopf heben und vieles mehr. All diese Prozesse laufen meist so automatisiert ab, dass es keine große Leistung scheint sie auszuführen. Im Zeitalter der Digitalisierung ist es ein erklärtes Ziel, menschliches (physisches und psychisches) Verhalten auf Maschinen (Roboter) zu übertragen. Es stellt sich heraus, dass es jedoch sehr wohl schwierig ist, etwa menschliche(n) Mimik oder Gang von Robotern ausführen zu lassen. Um diese Übertragung zu optimieren benötigt man ein vertieftes Verständnis der Arbeitsweise von Muskulatur (und natürlich auch des Gehirns, welches aber nicht Bestandteil dieser Arbeit sein wird).

Ein menschlicher Skelettmuskel kann willentlich kontrahiert werden, jedoch nicht verlängert. Hierzu bedarf es eines kontrahierenden Gegenspielers (Antagonist). Die Längenänderung ist dabei abhängig vom eingehenden Reiz des Zentralen Nervensystems, der momentanen Länge des Muskels selbst, sowie einigen muskelspezifischen Kenngrößen (Parametern) wie etwa der Maximalkraft. Folglich lässt sich ein Muskel mathematisch durch eine Differentialgleichung (genauer gesagt durch ein gekoppeltes differential–algebraisches System) beschreiben, deren Struktur wir in den folgenden Kapiteln aufzeigen werden. Die Theorie der Differentialgleichungen ist weit ausgearbeitet und beinhaltet eine Vielzahl von Verfahren, die Muskelmodellierern nicht im Detail bekannt sein dürften. Zu diesem Zweck möchten wir in der vorliegenden Arbeit eine Brücke schlagen zwischen der angewandten Mathematik und der Anwendung selbst; der Biomechanik.

Der erste Teil dieser Arbeit beschäftigt sich mit der *Stabilitätstheorie*. Erinnern wir uns an das bekannte Beispiel aus der Schulphysik, in dem die Ruheposition einer Kugel offenbar weniger anfällig gegenüber kleinen Schubsern ist, wenn sie in einer Schüssel liegt als auf der Spitze eines Hügels. Ähnlich nimmt ein dynamisches (muskulo–skelettales) System Gleichgewichtszustände ein, die auf Störungen unterschiedlich reagieren können. Diese Zustände werden wir für unser behandeltes Muskelmodell berechnen und klassifizieren.

Im zweiten Teil untersuchen wir den Einfluss einzelner Parameter auf die Modellgleichung beziehungsweise deren Lösung mit Hilfe der *Sensitivitätsanalyse*. Nimmt man etwa in dem dynamischen System ,,Auto" einen Wert für die Größe ,,Druck auf das Bremspedal an der Ampel", dann kann eine kleine Abweichung nach oben oder unten dazu führen, dass man entweder durchgeschüttelt wird oder sogar auffährt, anstatt sanft und mit ausreichend Abstand zum Stehen zu kommen. Das betrachtete Muskelmodell enthält über 20 Parameter, bei denen kleine Änderungen zu unterschiedlichen Zeiten unterschiedlich viel Einfluss auf die Lösung der Modellgleichungen haben. Wir werden verschiedene Teilsysteme sowie das gesamte System unter verschiedenen dynamischen Randbedingungen auf Sensitivität bezüglich der einzelnen Parameter untersuchen.

Der dritte und abschließende Teil beschäftigt sich mit dem Problem der *optimalen Steuerung*. Wenn der Nervenreiz (Input) bekannt ist, kann mit Hilfe des Modells eine Kraftantwort (Output) des Systems ,,Muskel" berechnet werden. Umgekehrt jedoch ist es ungleich schwerer. Im Alltag beobachtet man das Problem der optimalen Steuerung etwa bei selbsteinparkenden Autos, bei denen ein vorgegebener Einparkweg nur unter Steuerung der Lenkradposition und des Gaspedals erreicht werden soll. Wir werden zwei Verfahren optimaler Steuerung vorstellen. Das erste Verfahren stellt eine Verzahnung von Optimierung in Funktionenräumen und Variationsrechnung dar. Das zweite eine Stellvertreter–basierende Optimierungsmethode.

Acknowledgements

Mathematics has beauty and romance.
It's not a boring place to be, the mathematical world.
It's an extraordinary place; it's worth spending time there.

– Marcus du Sautoy –

It is worth spending time in the mathematical world. I could not agree more with that. On the other hand, it is also worth spending time in the real world. In this way, I want to thank everyone, who helps me linking both worlds together and not getting lost in either one.

The first person in doing so is my wife Kim. Thank you for so much love, beautiful days and experiences (and tiny fishes). You perceive my connection to the mathematical world, let me roam it, and reel me back into the real world if needed. Furthermore, you gave me (so far) two compelling reasons to pull me back from theory: Ronja and Erik, I am so proud of you! Keep your open mind and hopefully you someday find a passion that fulfills you.

But could I have come to this point without a supporting family? Hard to say, but I would tend to say no. Therefore, I thank my father (who is probably not reading this, because it is not German, hence: "Danke Vadder!") and my mother (who, I know, will work through this heap of words) for their unconditional support. You taught me so much, trusted me, and allowed me to follow my passion by stating "Do whatever you like, but do it good". I hope (no, I *know*) that you are proud of the outcome of your dedication. Concerning family: Thank you Richie (the best man) for all the fighting, laughing, marrying, arguing, drinking, travelling, camping and much more.

You cannot choose your family, but you can choose your friends. Although I consider myself lucky with the former, I appreciate the latter as much. Thank you Näls and Tom (and in one breath Kathrin) for being my children's heavy–metal godfathers. Watch over them! Additionally (even if by far not completely), thanks go out to Markus (for proof–reading), Seizi, Säppel, Domi, Moe, Daniel, and Paddy not only for being a proud (bachelor–)party crew, but also for not giving a rat's ass about algebraic geometry or differential equations. You are there, when I need you and vice versa. Without a detailed enumeration, thanks go also out to the Judo–Club Neuwied for providing the physical balance to the mental challenges.

Concerning the link to the mathematical world, I thank everyone who cared about satisfying my demands for a deeper mathematical understanding. Beginning with Toni Schade (R.I.P.), who taught me how to calculate the volume of a barrel and the square–root of large numbers with pen and paper at the age of 10, all this while standing by my side at the asparagus conveying band. My teachers, in particular Fingerloos, Stützel, and Bohl, who were willing to invest additional labor to supply me with a suitable mathematical workload. My diploma advisor Prof. Dempwolff, who showed me the world of pure mathematics. And of course my doctoral advisor Prof. Thomas Götz, who opened me the world of applied mathematics and with whom it is a great pleasure and fun to work.

Finally, I want to thank Michael Günther. Without you, this thesis would not be half as good. Thanks for the endless nocturnal discussions, your consulting, your friendship, and especially for your ruthless candor. If more people had your view on the world, we would have a good chance to overcome global sheepishness (I searched a long time for that last word, but I know that you will appreciate that it fits on multiple levels).

Contents

Abbreviations & List of Symbols 1

1. General Introduction 5

I. Stability Theory 11

2. Stability Investigations of Dynamic Muscle Properties 13
2.1. Introduction to Stability Theory . . . 13
2.2. Stability of Activation Dynamics . . . 15
2.2.1. Zajac's Activation Dynamics . . . 15
2.2.2. Hatze's Activation Dynamics . . . 16
2.3. Contraction Dynamics . . . 19
2.3.1. Simplified Contraction Dynamics . . . 19
2.3.2. Complete Contraction Dynamics . . . 22

II. Sensitivity Analysis 27

3. Research Paper I: Comparative Sensitivity Analysis of Muscle Activation Dynamics 29
3.1. Introduction . . . 31
3.2. Two Models for Muscle Activation Dynamics . . . 32
3.3. Local First and Second Order Sensitivity of ODE Systems Regarding Their Parameters . . . 33
3.4. Variance–Based Global Sensitivity Analysis . . . 35
3.5. An Analytical Example for Local Sensitivity Analysis . . . 36
3.6. The Numerical Approach and Results . . . 37
3.6.1. Results for Zajac's Activation Dynamics: Sensitivity Functions . . . 39
3.6.2. Results for Hatze's Activation Dynamics: Sensitivity Functions . . . 42
3.6.3. Variance–Based Sensitivity (VBS) and Total Sensitivity Indices (TSI) for Zajac's and Hatze's Activation Dynamics . . . 45
3.7. Consequences, Discussion, Conclusions . . . 46
3.7.1. A Bottom Line for Comparing Zajac's and Hatze's Activation Dynamics: Second Order Sensitivities . . . 46
3.7.2. A Plus for Hatze's Approach: Length Dependency . . . 47
3.7.3. An Optimal Parameter Set for Hatze's Activation Dynamics Plus CE Force–Length Relation . . . 48
3.7.4. A Generalized Method for Calculating Parameter Sensitivities . . . 49
3.7.5. Insights Through Global Methods . . . 50

4. Research Paper II: Extracting Concentric and Eccentric Dynamic Muscle Properties from Isometric Contraction Experiments 55
4.1. Introduction . . . 56
4.2. Model and Methods . . . 58
4.2.1. Model Description . . . 58
4.2.2. Determining Exact Switching Times in Experiments . . . 59
4.2.3. Sensitivity Analysis of Model Dynamics . . . 60
4.2.4. Estimation of Model Parameters by a Least–Square Fit . . . 61
4.3. Results and Discussion . . . 62
4.3.1. Switching Time Results and EMD . . . 62
4.3.2. Sensitivity Analysis Results . . . 65
4.3.3. Results From Evaluating Models 1–5 . . . 67
4.3.4. ICE Design for Determining S_e . . . 70
4.4. Conclusions and Outlook . . . 72

5. Sensitivity Analysis of Different Contraction Modes 79
5.1. Simulated Experiments . . . 79
5.1.1. Isometric Contractions . . . 79
5.1.2. Isotonic Contractions . . . 80
5.1.3. Quick–Release Contractions . . . 81
5.1.4. Concentric Contractions Against an Inertial Mass . . . 81
5.2. Phase Portrait Analysis . . . 83
5.2.1. Force–Length Characteristics . . . 83
5.2.2. Force–Velocity Characteristics . . . 85
5.2.3. SEE Characteristics . . . 86
5.2.4. SDE Characteristics . . . 87
5.3. Sensitivity Analysis . . . 89
5.3.1. Isometric Contractions . . . 89
5.3.2. Isotonic Contractions . . . 90
5.3.3. Quick–Release Contractions . . . 90
5.3.4. Concentric Contractions . . . 90
5.3.5. Comparison of the Contraction Modes . . . 95

III. Optimal Control Theory 97

6. Introduction to Optimal Control Theory 99
6.1. Fundamentals from Functional Analysis . . . 99
6.2. Formulation and Examples for Optimal Control Problems . . . 102

7. Research Paper III: Optimal Control of Isometric Muscle Dynamics 113
7.1. Introduction . . . 113
7.2. Model Description and Problem Formulation . . . 115
7.2.1. Model Description . . . 115
7.2.2. Problem Formulation . . . 118
7.3. Solution and Results . . . 119
7.4. Discussion . . . 120
7.4.1. Results for Muscle Length $\ell_{MTC} = \ell_{MTC,ref}$ . . . 120
7.4.2. Results for Muscle Lengths $0.85 \leq \ell_{MTC}/\ell_{MTC,ref} \leq 1.1$ . . . 122
7.5. Comparison with Commercial Software . . . 124

7.6. Conclusion and Outlook . . . 126

8. Research Paper IV: Optimization Problems in Epidemiology, Biomechanics & Medicine 135
8.1. Introduction . . . 135
8.2. General Outline of Optimal Control Problems . . . 136
8.3. Application in Epidemiology . . . 137
8.3.1. A Dengue Transmission Model . . . 137
8.3.2. Numerical Results . . . 139
8.4. Application in Biomechanics . . . 141
8.4.1. Motivation, Model and Method . . . 141
8.4.2. Results and Discussion . . . 142
8.5. Conclusion and Outlook . . . 145

9. Space–Mapping: An Alternative Optimal Control Approach 149
9.1. Mathematical Description . . . 149
9.2. Recovering Optimal Neural Stimulation Using ASM . . . 153
9.2.1. Isometric Contractions . . . 154
9.2.2. Concentric Contractions Against an Inertial Mass . . . 157

IV. Closing 161

10. Conclusion 163
10.1. Summary . . . 163
10.2. Outlook and Future Work . . . 163

Bibliography for Chapters 1, 2, 6, 9, 5 & 10 165

Abbreviations & List of Symbols

The first table contains abbreviations that were used throughout this thesis. Although we define them on demand within the respective section, this table may serve as a fallback.

The second table contains a list of consistently used symbols, such as special functions, parameters, and miscellaneous nomenclature. Note that some sections contain additional, individual denotations that are not given here, but will be defined and explained if needed.

List of Abbreviations:

ASM	aggressive space mapping
BVP	boundary value problem
CC	concentric contraction
CE	contractile element
DAE	differential algebraic equation (system)
EC	eccentric contraction
EMD	electro–mechanical delay
ICE	isometric contraction experiment
IVP	initial value problem
LES	linear equation system
MBS	multi–body system
MTC	muscle tendon complex
OCP	optimal control problem
ODE	ordinary differential equation
PDE	partial differential equation
PE	parameter estimation
PEE	parallel elastic element
PI	partial integration
PROPT	Per Rutquist OPTimizer
SDE	serial damping element
SEE	serial elastic element
TSI	total sensitivity index
VBS	variance–based sensitivity

cf.	confer (compare)
e.g.	exempli gratia (for example)
i.e.	id est (that is)
w.r.t.	with respect to

List of Symbols:

$\mathbf{1}_A$	indicator function of a set A
$\mathrm{d}/\mathrm{d}tF = \dot{F}$	derivative of X w.r.t. time t
$\partial_x F$	partial derivative of F w.r.t. x
$DF(x_0)$	Fréchet (total) derivative of F in x_0
$D_{v_0}F(x_0)$	Gâteaux (directional) derivative of F in x_0 in direction v_0
$\mathrm{Im}(f)$	image of (the mapping) f
$\Im(z)$	imaginary part of the complex number z
$\Re(z)$	real part of the complex number z

$a_{rel,0}$	Hill constant, representing the shortening heat of a muscle
$b_{rel,0}$	Hill constant, representing the velocity/length ratio
c	maximum calcium ion concentration
Ca^{2+}	calcium ion
D_{SE}	damping parameter at $F_{MTC} = F_{max}$
F_e	limit factor of the eccentric force–velocity relation
F_{isom}	isometric force
F_{max}	a muscle's maximum isometric force
F_X	force of element $X \in \{\text{CE, MTC, PEE, SDE, SEE}\}$
$\mathcal{F}_{PEE}$	scaling parameter for the PEE
g	gravitational constant
$\ell_{CE,opt}$	optimal length of CE
ℓ_X	(physiological) length of element X
$\ell_{X,0}$	slack (or initial) length of element X
$\ell_{X,ref}$	reference length of element X
$\ell_{X,rel}$ or ℓ_{Xrel}	relative length of element X
ℓ_ρ	pole in Hatze's length–dependency function $\rho(\ell_{CE})$
$\mathcal{L}_{PEE}$	PEE parameter, inducing the PEE slack length
m	activation time constant from Hatze
$mass$	the mass of an object
q	activity of a muscle
$\dot{q}$	activation
q_0	rest activity for zero stimulation
q_H or q_Z	activity according to Hatze (H) or Zajac (Z)
R_{SE}	damping parameter at $F_{MTC} = 0$
S_e	slope ratio between concentric and eccentric force–velocity branches
S_{y_k,λ_i}	sensitivity of state y_k w.r.t. parameter λ_i
$\tilde{S}_{y_k,\lambda_i}$	normalized sensitivity of y_k w.r.t. λ_i
x^* / X^*	in most cases the optimal value of x or the dual space of X
$\overline{X}$	in most cases the reference value of X

β	activation–deactivation time ratio from Zajac
γ	normalized calcium ion concentration
δ	Dirac delta (distribution)
ΔW_{asc}	width of ascending F_{isom} branch
ΔW_{des}	width of descending F_{isom} branch
$\Delta F_{SEE,0}$	force at non–linear/linear transition of the SEE
$\Delta U_{SEE,nll}$	relative stretch at non–linear/linear transition of the SEE
$\Delta U_{SEE,l}$	relative stretch in the linear part of the SEE
$\Theta(x)$	Heaviside function of x
λ	in most cases denotes a parameter
Λ	in most cases denotes a parameter set
ν	exponent in Hatze's activation dynamics
ν_{asc}	exponent of ascending F_{isom} branch
ν_{des}	exponent of descending F_{isom} branch
ν_X	exponent of the non–linear part of element X
$\rho(\ell_{CE})$	length–dependency function in Hatze's activation dynamics
ρ_0	scaling factor in $\rho(\ell_{CE})$
ρ_c	merging of ρ_0 and c
σ	stimulation / neural impulse (constant or function of time)
τ	time constant from Zajac
τ_{act}	activation time constant from Zajac
τ_{deact}	deactivation time constant from Zajac

1. General Introduction

At the beginning, we will pose and answer a few questions, providing an insight on the motivation, background, structure and aims of this thesis.

Why do we consider muscle models and their application?

As stated in the Abstract (Zusammenfassung), it is nowadays desired to transfer human motor skills to mechanical devices. There exist a variety of research areas dealing with this request: biomechanics, bioengineering, biomathematics and much more. Among the manifold applications of theoretical and artificial muscle models, we will list a few, divided into three categories: First, and maybe most important, are the medical applications. Creating artificial muscles from electro–active polymer (EAP) [3] or myoelectric prostheses [19] to restore or replace endogenous body material can increase the livability of affected people. A second field is robot technology [6, 72]. Besides from robots being able to play football [44], possible applications of humanoid robots can be easily thought of: More accurate manufacturer of components, replaceable disaster relief force or assistant for elderly people. As a third application, there is the facilitation of daily routines. A sought market for muscle models is the automobile industry; the application ranges from the design of car seats [37] to autonomous driving [57].

How is a muscle structured? How does it work?

We will shortly outline the structure and functional principles of a skeletal muscle. For an advanced insight to the topic, introductory literature about physiology is recommended, e.g. [46]. Note that there exist two other types of muscles such as smooth (found in the wall of organs) or cardiac muscles (found only in the heart). In contrast to skeletal muscles, these two muscle types are *involuntary*, i.e. can not be contracted at will, but rather work automatically. Therefore they possess no neuromuscular junction, but are controllable by a pacemaker.

Figure 1.1 shows the composition of a (human) skeletal muscle. Both ends of a muscle are attached to the bones via a *tendon*, which is a very stiff, visco–elastic, fibrous connective tissue consisting of collagen. The purpose of the tendon is to store mechanical energy or redirect forces around joints. The tendon material then continuously merges into the *muscle belly* that consists of muscle fiber bundles (fascicles), nerve fibers and blood vessels. The muscle belly and fascicles are encapsulated by the epi– and perimysium, respectively, a sheath of elastic connective tissue that protects the muscle from friction and rupture. It is still unclear, if this sheath plays a role in the active muscle contraction, i.e. if and how it is connected to the neural system [51]. Each muscle fiber consists of a variety of myofibrils that comprise the muscular motor units: the *sarcomeres*. With a rest length of around $3\,\mu$m, a sarcomere consists of an alternating assembly of the proteins actin and myosin. The previous is directly attached to the so–called Z-disc, whereas the latter is linked to the disc via another protein, namely titin. The exact role of titin is also not yet fully understood [69], but it seemingly acts like an adjustable spring.

Although everyone is used to the handling of (his own) muscles as a force producing actuator, the detailed molecular processes of this force production are not yet entirely

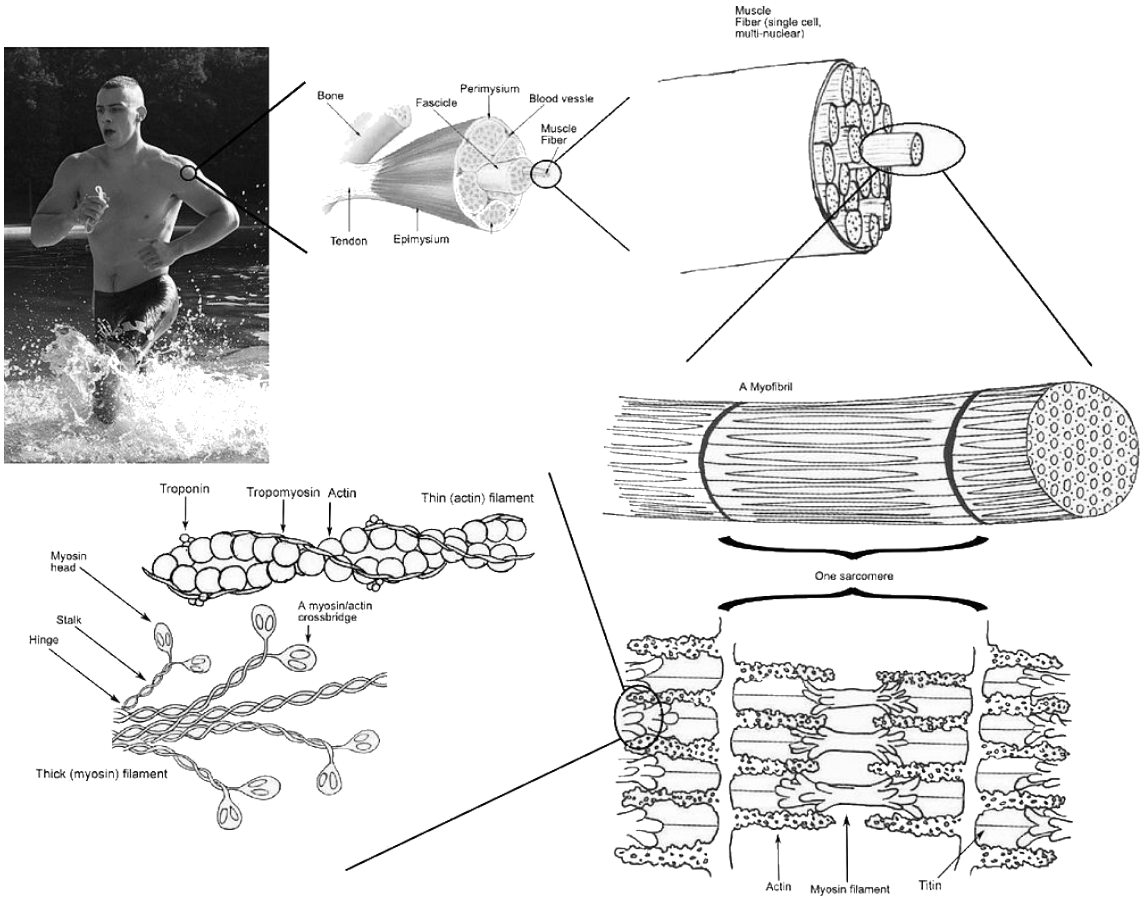

Figure 1.1.: "Skeletal muscle". Licensed under CC BY-SA 3.0 via Commons https://commons.wikimedia.org/wiki/File:Skeletal_muscle.jpg

revealed, see for example [39, pp. 169, C. 2.7] and [51]. However, a coarse sequence plan (which is sufficient for this work) from the thought "I should raise my arm" to the final execution covers the following steps:

Step 1: The brain gives a signal to raise the arm in form of an electrical, neural impulse via the nerve system.

Step 2: The neural impulse reaches the neuromuscular junction as an action potential and causes the release of calcium ions (Ca^{2+}).

Step 3: The calcium ions allow the myosin heads to tie to the actin filament. In the following we refer to this process as *activation* and the relative number of tied heads as *activity*.

Step 4: Further biochemical processes allow the myosin head to fold up along the actin filament and change the length of the sarcomere.

Step 5: The length change of multiple sarcomeres causes the muscle belly to change its length. We call this process a *contraction*, regardless of whether the muscle shortens (concentric contraction) or elongates (eccentric contraction) due to external load.

Step 6: The length change of the muscle induces a force change in the connective tissue and therefore perturb the mechanical equilibrium of the musculo–skeletal system.

Step 7: The muscle transmits the force to the bone via the tendon and literally *forces* the musculo–skeletal system into a new equilibrium, hopefully a raised arm.

Note that the presented sequence plan takes *macroscopic* effects into account rather than *microscopic*, molecular processes. An insight into the molecular processes, the so–called *cross–bridge theory*, can be found in [31, 33, 38, 39, 40], but will not be part of this thesis.

How is a skeletal muscle mathematically modeled?

Mathematically modeling a real world system requires to simplify as much as necessary to describe the system's processes with (more or less simple) mathematical language, but only as little as possible to preserve the system's characteristics. Walking through our sequence plan from Step 1 to Step 7, we comment our simplifications and notations of our underlying mathematical muscle model. A detailed, formal description can be found in Section 7.2 ([66]) or in [30].

The neural impulses from the nerve system reach the neuromuscular junction as discrete action potentials with a duration of 1–2 ms and thus a maximal frequency of approximately 500 Hz. Since we aim at modeling whole muscle contractions that take seconds rather than milliseconds, we average the incoming action potentials into a piecewise continuous function over time: the neural stimulation denoted by $\sigma(t)$.

For Steps 2 and 3 there are different approaches existing, of which we address two in this work. The first approach according to H. Hatze [35] takes physiological observations into account. The concentration of free Ca^{2+} ions, denoted by $\gamma(t)$, is modeled by an ordinary differential equation (ODE), where the right hand side linearly depends on $\gamma(t)$ and $\sigma(t)$. Subsequently, the solution of this ODE is inserted in a non–linear equation for the activity, denoted $q(t)$. This differential–algebraic system can be transformed to a single non–linear ODE, see [26, 68]. The second approach according to F. Zajac [84] is more phenomenological. It describes the activation as directly, linearly dependent from $q(t)$ and $\sigma(t)$. The advantages and disadvantages of both models are discussed in Section 3 ([68]).

The contraction dynamics in Steps 4 to 6 were modeled by A. V. Hill in [41]. Therefore, muscle models containing this contraction dynamics are classified as "Hill–type". Hill proposed a hyperbolic relation between the velocity of the muscle belly and its exerted force, and formulated the respective ODE. Note that the differential equation itself is not called hyperbolic, which is a term in the field of partial differential equations (PDEs).

To macroscopically describe a muscle, we use the abbreviation CE, for *contractile element*, to describe the entirety of sarcomeres in one muscle. In parallel to the CE, the encapsulating connective tissue is modeled as a non–linear spring and denoted as PEE for *parallel elastic element*. A possible pennation of the muscle [39, 46, 51] is not explicitly taken into account, but covered by the choice of model parameters. To model the visco–elastic tendon, which is placed in series to the CE/PEE component, we use so–called *Kelvin–Voigt material* (cf. [16]). The tendon is modeled as a non–linear spring denoted by SEE (*serial elastic element*) in parallel to a force–dependent damping element SDE (*serial damping element*). The whole muscle is further referred to as *muscle–tendon complex* (MTC). In the course of this thesis, the length of an element $X \in \{\text{CE, PEE, SEE, SDE, MTC}\}$ is denoted with ℓ_X and the respective force with F_X. Figure 1.2 shows the described model according to the work of [27, 30].

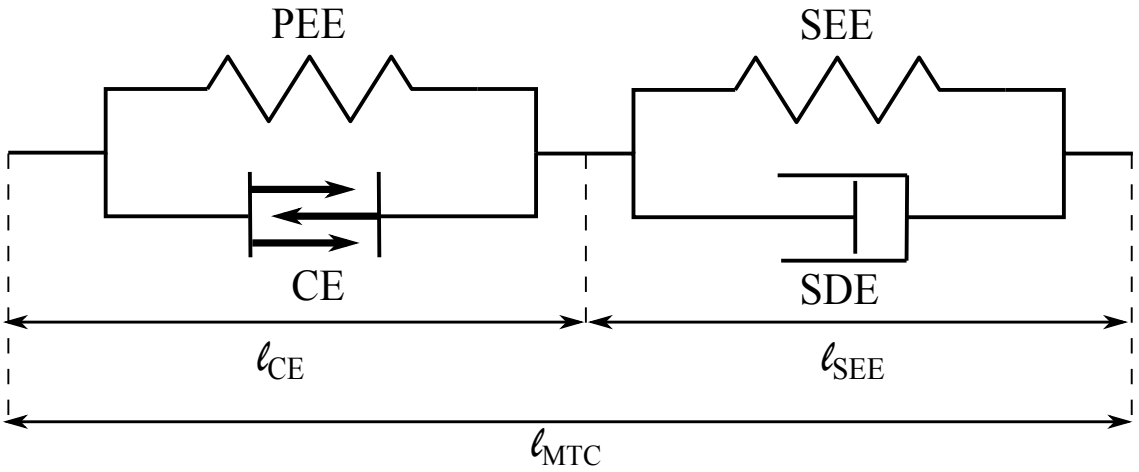

Figure 1.2.: Sketch of the four elements of the Hill–type muscle model according to [30].

And what is the aim of this thesis?

This thesis reviews known mathematical methods and works them up to a final use in the field of biomechanics or, more exactly, in muscle modeling. In other words, this thesis is bridging between applied mathematics and the actual application. Mathematicians, especially theoretical ones, often content themselves with the demonstration of proven theorems within their own community. The implications, interpretations or applications in the real world are often subsidiary (the author speaks out of personal experience, regarding his diploma thesis [65]). As one consequence, many theorems do not see the light of day or, if found somewhere, are hard to understand for someone who lacks a certain mathematical education. As another consequence, the findings from mathematical theorems are processed into user software that works like a "black box", i.e. the user has to trust the mode of operation, because he can not comprehend it. Both consequences are very unsatisfying.

After reading this thesis, a biomechanist, or whoever wants to gain an insight on muscle modeling, can rely on three pillars. First, the presentation of a state–of–the–art muscle model. Second, a condensed preparation of necessary mathematical theories, including basic notations as well as fundamental coherences (which are also applicable to other ODE–based models). Third and most important, *comprehensible* as well as *replicable* applications of the mathematical theory on the given model, including results, interpretations and discussions for a deeper understanding.

How is the thesis structured? Which mathematical methods are utilized? What are the goals being achieved?

In Part I, we will show the application of *stability theory* on ODE–based models. Stability theory investigates the numerical behavior of equilibrium states with respect to perturbations. The stability of critical solutions of muscle model equations is of great interest for their application, see for example [71]. Chapter 2 contains an introduction to stability theory and the calculation of critical solutions within activation and contraction dynamics as stated above. The stability of these critical solutions is also investigated.

In Part II, we will show the application of *sensitivity analysis* on ODE–based models. With the help of sensitivity analysis, the influence of certain parameters on the model output can be determined. More mathematically, we state how a change in the parameter value changes the model output value. Our first research paper in Chapter 3 contains a

description of the mathematical theory as well as an application on the two mentioned activation dynamics. In Chapter 5, we extend the approach to a sensitivity analysis of the whole muscle model among different contraction modes; in detail isometric contractions, isotonic contractions, quick–release contractions, and concentric contractions versus an inertial mass. In our second research paper, in Chapter 4, sensitivity analysis is used as a tool to reach two goals: First, to prove that isometric contractions are influenced by dynamic muscle parameters. Second, to specifically design an isometric contraction experiment for determining an eccentric contraction parameter.

In Part III, we will show the application of *optimal control theory* on ODE–based models. Briefly, optimal control theory is used to obtain model input, e.g. $\sigma(t)$, from a given model output, e.g. $F_{MTC}(t)$. In contrast to model evaluation, i.e. obtain model output from model input, optimal control requires optimization methods. Chapter 6 outlines the fundamentals of functional analysis and gives simple examples to re-enact the theory step by step. Our third research paper in Chapter 7 contains the application of optimal control theory on the presented muscle model. This paper focuses on isometric muscle contractions, where the MTC is held at constant length. Our fourth research paper in Chapter 8 carries the previous method forward and contains a further application of optimal control in biosciences: the modeling of dengue fever transmission. The final Chapter 9 presents an alternative optimal control approach known as *space–mapping*. This theory might be a good example for mathematical work that has not yet been discovered for a large scale application outside a confined community. The idea behind this approach is to simplify the ODE–based model as much as possible to cheapen optimization processes. The results from this optimization are then transferred back to the original model via the so–called space–mapping function. We give two examples of simplifying our model and perform the respective optimizations.

Part IV provides a final conclusion as well as an outlook for future research in Chapter 10, and the bibliography of all sections that are not research papers.

Part I.

Stability Theory

2. Stability Investigations of Dynamic Muscle Properties

This chapter gives an overview of common techniques in stability theory and their application on muscle dynamics. Regarding a model of a dynamical system, the question arises whether there exists a state at which the model reaches an equilibrium. Typical examples for systems with equilibrium points are the predator–prey model from Lotka–Volterra, the mathematical pendulum or a free fall with air resistance. It is of interest to know, if small perturbations of the equilibrium only cause small long–term deviations of the system. The system is then called *stable*. The formal definitions and theorems are given below.

Modeling a musculo–skeletal system requires a variety of muscles, each one including a differential–algebraic equation system (DAE), a parameter set and a set of initial conditions. After applying a constant neural stimulation on every muscle, the system tends to reach an isometric equilibrium, for example sitting or standing. Although the respective MTC lengths are easily determined by basic mechanics, the equilibrium lengths of the contractile elements are not. These equilibria should be attained, independent of the initial conditions' choice, and persist after small perturbations. Otherwise, even a small deviation in the initial guess or error in measurement can lead to a large deviation in the model output. To investigate, whether an attained equilibrium is stable with respect to minor perturbations, results from stability theory are applied on the muscle model from [27, 30]. The underlying ordinary differential equations (ODEs) are autonomous, which means they do not explicitly depend on the independent variable time. Note that future improvements of the model including history effects, fatigue, force enhancement or force depression might add non–autonomous parts to the model. For these parts, the presented approaches do not apply generally, because it is less likely for an equilibrium to occur, cf. [80].

2.1. Introduction to Stability Theory

Let Ω be an open subset of $\mathbb{R}^n$, $f : \Omega \to \mathbb{R}^n$ and consider the autonomous, ordinary, first order initial value problem (IVP):

$$\dot{x} = f(x(t)), \qquad x(0) = x_0 \quad , \tag{2.1}$$

where $x(t) = (x_1(t), x_2(t), \ldots, x_n(t))$ and $f = (f_1, f_2, \ldots, f_n)$ denote the vectors of state variables and right–hand sides of the ODE, respectively.

The following definitions and theorems are mainly taken from [78] but can also be found in most introductory literature about ODEs.

Definition 2.1.1. A function $f : \Omega \to \mathbb{R}^n$ is called **Lipschitz continuous** or **L–continuous** on Ω, if there exist an $L \in \mathbb{R}^0_+$ such that

$$||f(x) - f(y)|| \leq L \cdot ||x - y||$$

for all $x, y \in \Omega$, where $||\,.\,||$ denotes an arbitrary norm.

Definition 2.1.2. A point $x^* \in \Omega$ of the state space is called **equilibrium point** (or *stationary point* in the case $n = 1$) of ODE (2.1), if $f(x^*) = 0$ (zero vector).

Definition 2.1.3. Let x^* be an equilibrium point of Eqn. (2.1). Then x^* is called

- **stable**, if for all $\varepsilon > 0$ with $B_\varepsilon(x^*) \subseteq \Omega$, there exist a $\delta > 0$ with $B_\delta(x^*) \subseteq \Omega$, such that for every solution $x(t)$ with $x(0) \in B_\delta(x^*)$ it holds that $x(t) \in B_\varepsilon(x^*)$, for all $t \in \mathbb{R}_+$
- **asymptotically stable**, if x^* is stable and $\lim\limits_{t\to\infty} x(t) = x^*$
- **exponentially stable**, if x^* is asymptotically stable and there exist $\alpha, \beta > 0$ such that, if $x(0) \in B_\delta(x^*)$, then $x(t) \in B_{\alpha\delta e^{-\beta t}}(x^*)$, for all $t \in \mathbb{R}_+$
- **unstable**, if x^* is not stable.

This definition of stability was first given by Aleksandr Lyapunov in [52] and therefore is called **Lyapunov stability**. Note that all of the above definitions hold for linear as well as non–linear right hand sides and do not provide any insight on how the stability can be calculated in practise. However, if f is linear in x, the autonomous equation $\dot{x} = f(x(t))$ can be written as the homogeneous linear system $\dot{x} = A \cdot x$ with $A \in \mathbb{R}^{n\times n}$. Hence, we can determine the stability of the solution by the following theorem, see [78, Section 4.3].

Theorem 2.1.4. *Let $\dot{x} = Ax$ be a linear homogeneous ODE system and $\sigma(A)$ the spectrum of A, i.e. the set of eigenvalues. The system is then*

1. *asymptotically stable, if for all $\lambda \in \sigma(A)$ it holds: $\Re(\lambda) < 0$ (real part of λ),*
2. *stable, if for all $\lambda \in \sigma(A)$ it holds: $\Re(\lambda) \leq 0$ and the algebraic multiplicity of all $\lambda_i \in \sigma(A)$ with $\Re(\lambda_i) = 0$ is equal to their geometric multiplicity,*
3. *unstable, if it is not stable, i.e. if*
   (a) *there exist at least one $\lambda \in \sigma(A)$ with $\Re(\lambda) > 0$ or*
   (b) *there exist at least one $\lambda \in \sigma(A)$ with $\Re(\lambda) = 0$ and the algebraic multiplicity of λ is greater than its geometric multiplicity.*

If the right hand side is non–linear, we first need to linearize f by its Jacobian, which has the same local behavior as the system itself according to the theorem of Hartman–Grobman [12]. The asymptotic stability of an equilibrium point x^* can be obtained as follows:

Theorem 2.1.5. *Let f and x be defined as in (2.1). Additionally, let f be continuously differentiable w.r.t. x and let x^* be an equilibrium point. Set $M := d/dx f(x^*)$.*

1. *If $\Re(\lambda) < 0$ for every $\lambda \in \sigma(M)$ then x^* is asymptotically stable.*
2. *If there exist at least one $\lambda \in \sigma(M)$ for which holds $\Re(\lambda) > 0$ then x^* is unstable.*

Unlike the linear case, there is no possible statement about the stability of x^*, if $\max\{\Re(\lambda) \mid \lambda \in \sigma(M)\} = 0$, see [78, Remark 8.12.1].

The method using Theorem 2.1.5 is called the *indirect* method of Lyapunov, since the system has to be linearized first. A more general method, the *direct* method of Lyapunov, uses the trajectories of the ODE to determine the stability as follows:

Definition 2.1.6. Let $V : U \to \mathbb{R}$ be a continuous function, where $U \subseteq \Omega$ is an open subset containing x^*. Then V is called a *Lyapunov function* for the differential equation (2.1) at x^* if

(1) $V(x^*) = 0$,

(2) $V(x) > 0$ for all $x \in U \setminus \{x^*\}$,

(3) V is continuously differentiable on $U \setminus \{x^*\}$ and $\dot{V} := \langle \nabla V, f(x) \rangle \leq 0$ holds for all $x \in U \setminus \{x^*\}$, where $\langle\ ,\ \rangle$ denotes the canonical inner (scalar) product.

If furthermore $\dot{V} < 0$ for all $x \in U \setminus \{x^*\}$ then V is called a *strict Lyapunov function.*

Theorem 2.1.7. *Let x^* be an equilibrium point of Eqn. (2.1). Then x^* is*

1. *stable, if there is a Lyapunov function for system (2.1) at x^*,*
2. *asymptotically stable, if there is a strict Lyapunov function for system (2.1) at x^*,*
3. *unstable, if V satisfies theorem 1.56 from [11, p. 31]: Let V be a smooth function on U with $V(x^*) = 0$ and $\dot{V} > 0$ on $U \setminus \{x^*\}$. If V has a positive value somewhere in each open set containing x^*, then x^* is unstable.*

In the following, we want to determine the equilibrium points of muscle activation and contraction dynamics and investigate their stability.

2.2. Stability of Activation Dynamics

2.2.1. Zajac's Activation Dynamics

The simplest dynamical system of the muscle model from [27, 30] is the activation dynamic according to Zajac. It consists of a linear ODE that phenomenologically describes the relation of a neural stimulation σ and the resulting activity q as:

$$\dot{q}_Z = f_1(q_Z) = \frac{1}{\tau(1-q_0)} \left[\sigma(1-q_0) - \sigma(1-\beta)(q_Z - q_0) - \beta(q_Z - q_0)\right] \tag{2.2}$$

with $q_Z(0) = q_{Z,0}$. As in [66, 68] the parameter τ denotes the activation time constant, β the activation–deactivation ratio, q_0 the minimum activation, and σ the neural stimulation, which is considered to be constant. Calculating the equilibrium point q_Z^* yields:

$$f_1(q_Z) = 0 \qquad \Longleftrightarrow \qquad q_Z^* = \frac{\sigma + \beta q_0 - \beta\sigma q_0}{\beta + \sigma - \beta\sigma} \tag{2.3}$$

Since $0 \leq \sigma, \beta \leq 1$, we note that the denominator $\beta + \sigma - \beta\sigma$ is only 0, if $\sigma = \beta = 0$. In that case, the solution of equation (2.2) is already an equilibrium $q_Z(t) = q_{Z,0} = q_Z^*$. Furthermore, we can verify immediately that $q_0 \leq q_Z^* \leq 1$.

We calculate the derivative of the right hand side f_1 w.r.t. q_Z and obtain:

$$\frac{\mathrm{d}}{\mathrm{d}q_Z} f_1(q_Z) = \frac{\beta + \sigma - \beta\sigma}{\tau(q_0 - 1)} < 0 \tag{2.4}$$

Note that $\mathrm{d}/\mathrm{d}q_Z\, f_1(q_Z)$ does not depend on q_Z and is always < 0, in particular at the equilibrium point q_Z^*. That is, because $q_0 - 1 < 0$ and $\beta + \sigma - \beta\sigma > 0$. Hence, the solution of equation (2.2) is always asymptotically stable and even exponentially stable, since the system is linear. As illustrated in Fig. 2.1, applying a constant simulation σ always yields a unique and asymptotically stable equilibrium for Zajac's activation dynamics, regardless the initial value. The arrows (quivers) indicate the slope field of the IVP.

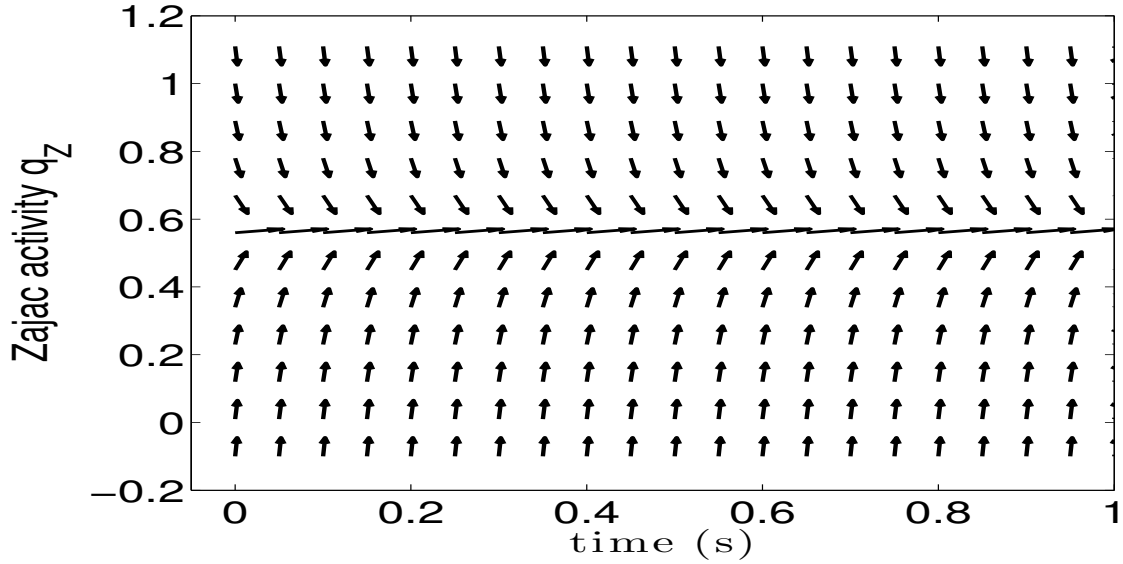

Figure 2.1.: Slope field (or direction field) for Zajac's activation dynamics (2.2). The parameters are chosen as follows: $\sigma = 0.5$, $\beta = 0.8$, $\tau = 1/40$, $q_0 = 0.01$. The equilibrium point $q_Z^* = 0.556$ is exponentially stable.

2.2.2. Hatze's Activation Dynamics

An alternative approach for describing the muscle activation dynamics was given by H. Hatze, see [35]. In contrast to the phenomenological description from Zajac, it contains physiological observations regarding the calcium ion concentration and a continuous, monotonously increasing length–dependency function $\rho(\ell_{CE}) > 0$. The non–linear Hatze formulation writes as:

$$\dot{q}_H = f_2(q_H) = \frac{\nu m}{1 - q_0} \left[\sigma\rho(\ell_{CE})(1 - q_H)^{1+\frac{1}{\nu}}(q_H - q_0)^{1-\frac{1}{\nu}} - (1 - q_H)(q_H - q_0) \right], \tag{2.5}$$

where $q(0) = q_{H,0}$, cf. [26, 68]. The parameters q_0 and σ are defined equally to Zajac's formulation. As in [68], the parameter m denotes a time constant and ν a dimensionless exponent.

Calculating the equilibrium points yields three candidates $q^*_{H,i}$ where $i \in \{1,2,3\}$:

$$f_2(q_H) = 0 \qquad \Longleftrightarrow \qquad q^*_{H,1} = q_0, \quad q^*_{H,2} = 1, \quad q^*_{H,3} = \frac{\rho(\ell_{CE})^\nu \sigma^\nu + q_0}{\rho(\ell_{CE})^\nu \sigma^\nu + 1} \tag{2.6}$$

The first two equilibrium points occur as a direct consequence of the shape of f_2 and require $\nu \neq 1$, whereas the third equilibrium point is a consequence of the build–up of f_2 in [26] from the original formulation by [35], cf. Eqns. (3.3) – (3.5). We insert these equilibrium points in the derivative of the right hand side:

$$\frac{\mathrm{d}}{\mathrm{d}q_H} f_2(q_H) = \frac{m\nu}{1-q_0}\left[2q_H - q_0 - 1 + \sigma\rho(\ell_{CE})\left(\frac{1-q_H}{q_H - q_0}\right)^{\frac{1}{\nu}}\left(-2q_H + q_0 + 1 + \frac{q_0 - 1}{\nu}\right)\right]$$

$$\begin{aligned}
\Longrightarrow \quad \frac{\mathrm{d}}{\mathrm{d}q_H} f_2(q^*_{H,1}) \quad & \text{is not defined, since } (q^*_{H,1} - q_0)^{-\frac{1}{\nu}} = 0^{-\frac{1}{\nu}} \text{ is not defined,} \\
\frac{\mathrm{d}}{\mathrm{d}q_H} f_2(q^*_{H,2}) \quad & = m\nu > 0\,, \quad \text{since } m, \nu > 0, \\
\frac{\mathrm{d}}{\mathrm{d}q_H} f_2(q^*_{H,3}) \quad & = -m < 0
\end{aligned}$$

Hence, we can conclude that $q^*_{H,2}$ is an unstable equilibrium, whereas $q^*_{H,3}$ is asymptotically stable. However, for $q^*_{H,1} = q_0$ we cannot provide any statement, but have to further investigate the right hand side f_2. We make two observations:

1) If $\sigma = 0$ then q_0 is still an equilibrium point of $f_2\,\big|_{\sigma=0}$ and

$$\frac{\mathrm{d}}{\mathrm{d}q_H} f_2(q_0)\,\Big|_{\sigma=0} = -m\nu < 0$$

that means at zero neural stimulation q_0 is an asymptotically stable equilibrium point.

2) The function $f_2(q_H)$ is not Lipschitz continuous in $q_H = q_0$, see Definition 2.1.1. The L–continuity constitutes a sufficient condition for uniqueness of a solution of the ODE (2.1) according to the theorem of Picard–Lindelöf. Before deriving consequences for this observation, we try to illustrate these consequences on a simpler example.

Example 2.2.1. Let $g:\ [0,\infty) \to \mathbb{R}$ and $\dot{u} = g(u) := \sqrt{|u|}, \quad u(0) = \eta$ with $\eta \in \mathbb{R}$ be a first order IVP. Assuming $\eta > 0$, a unique solution can be given by

$$u(t) = \left(\sqrt{\eta} + \frac{t}{2}\right)^2.$$

Obviously, the right hand side $g(u)$ is not L–continuous in $u = 0$, but L–continuous on the interval $[\varepsilon, \infty)$ for every $\varepsilon \in \mathbb{R}_+$ with $L_\varepsilon = 1/(2\sqrt{\varepsilon})$.

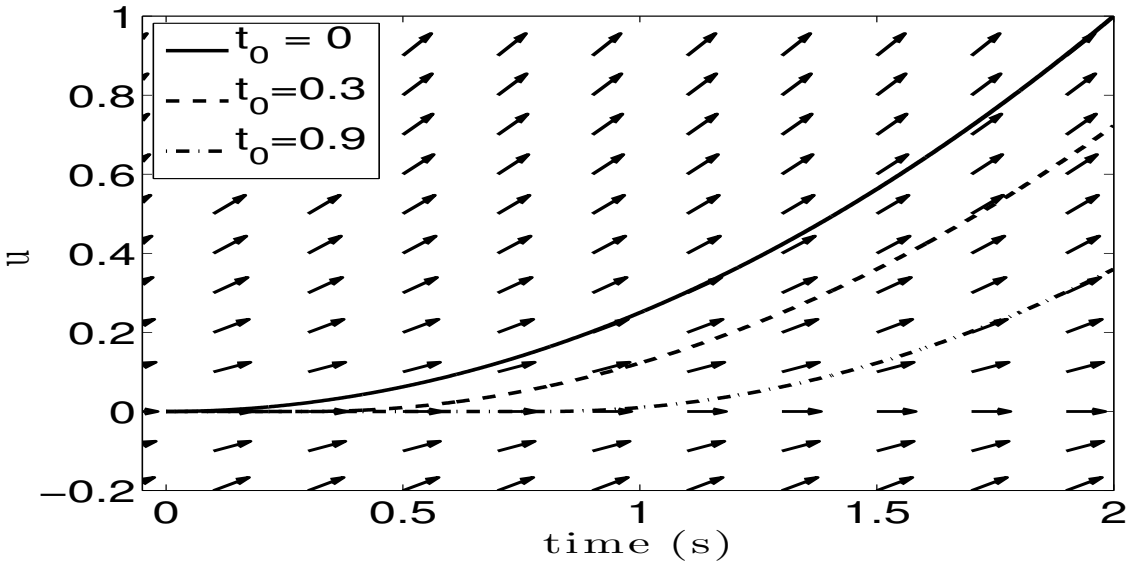

Figure 2.2.: Slope field of the ODE $\dot{u} = \sqrt{|u|}$. Solutions of the form $u(t) = (t - t_0)^2/4$ are delineated for $t_0 \in \{0, 0.3, 0.9\}$ to show the non–uniqueness..

Consequently, the uniqueness of the solution vanishes, if u passes the zero value. Provided $\eta = 0$ we get infinitely many solutions of the above IVP, for example of the form

$$u(t) = \begin{cases} 0, & t \leq t_0 \\ \frac{(t-t_0)^2}{4}, & t > t_0 \end{cases} ,$$

where $t_0 \in \mathbb{R}_+$. Figure 2.2 shows possible solutions for various t_0 values on the interval $[0, 2]$.

We see that, once the solution attains the zero value, it is either possible for u to stay in zero or to continue as a quadratic function at any time t_0. This phenomenon can be called *semi–stability* in the one–dimensional case, see [11, p. 13].

We transfer the example to Hatze's ODE (2.5), because $\mathrm{d}/\mathrm{d}q_H \, f_2(q_H)$ is not L–continuous in $q_H = q_0$. But for every suitable small $\varepsilon > 0$ it holds

$$\frac{\mathrm{d}}{\mathrm{d}q_H} f_2(q_0 + \varepsilon) > 0 \quad \text{and} \quad \Re\left(\frac{\mathrm{d}}{\mathrm{d}q_H} f_2(q_0 - \varepsilon)\right) < 0 \, .$$

Figure 2.3 shows the slope field of the right hand side of Hatze's formulation with the unstable equilibrium at 1 and the asymptotically stable equilibrium at $q^*_{H,3}$ as expected. For q_0 we have a semi–stable equilibrium, because the equilibrium point switches stability by passing through q_0 and the solution therefore loses its uniqueness.

Remark 2.2.2. In numerical experiments, we would try to avoid the semi–stable case, because it is not physiologically interpretable. In the example we stated that for every initial value $\eta > 0$ the solution would be unique. Same holds true for Hatze's equation when $q_{Z,0}$ is not equal to $q^*_{H,1}$ or $q^*_{H,2}$. Therefore we choose $q_{Z,0}$ in the open interval $(q_0, 1)$ in numeric simulations.

Besides gaining uniqueness of the solution, the suggested strategy also ensures that the equilibrium point $q^*_{H,1} = q_0$ becomes unstable. Consequently, in a numeric simulation, $q^*_{H,3}$ is attained by the system.

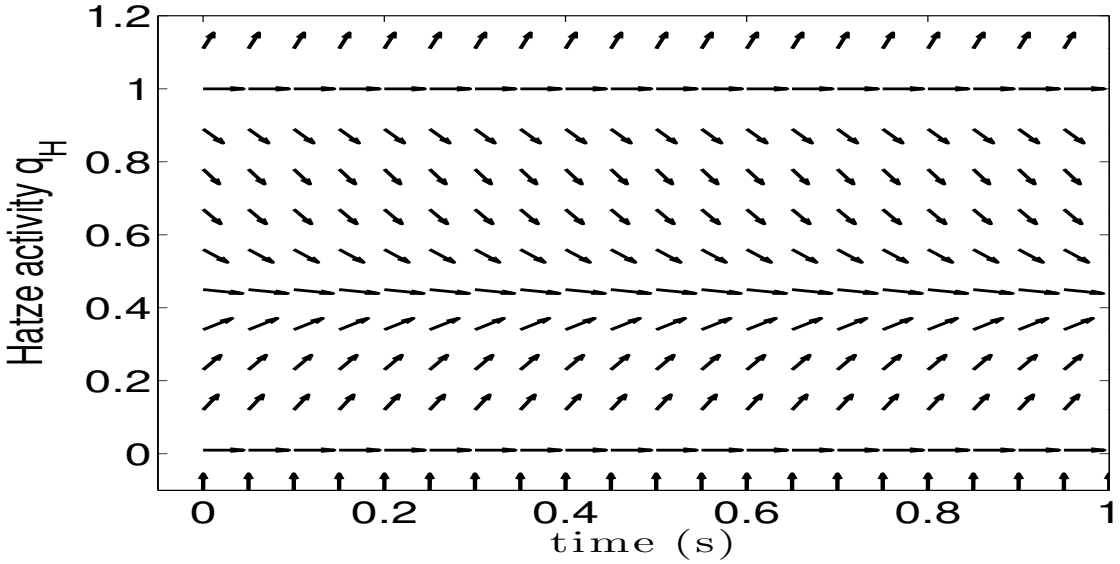

Figure 2.3.: Slope field for Hatze's activation dynamics equation (2.5). The parameters are chosen as follows: $\sigma = 0.1,\ \nu = 3,\ m = 11,\ \rho_c = 9,\ \ell_{CE} = \ell_{CE,opt},\ \ell_p = 2.9,\ q_0 = 0.001$. The equilibrium points are $q^*_{H,1} = q_0$ (semi–stable), $q^*_{H,2} = 1$ (unstable) and $q^*_{H,3} = \frac{\rho(\ell_{CE})^\nu \sigma^\nu + q_0}{\rho(\ell_{CE})^\nu \sigma^\nu + 1} \approx 0.4$ (asymptotically stable).

2.3. Contraction Dynamics

2.3.1. Simplified Contraction Dynamics

In addition to the equilibrium points of the activation dynamics, we are naturally interested in statements about possible equilibrium points of a muscle's inner dynamic. As a simplified example we start by investigating the hyperbolic equation from Hill [41], which has been modified by [79] and is also used as a basis for the model presented in [27] (and the remaining thesis). This reduced model of contraction dynamics only consists of the muscle's CE without any serial or parallel elastic element. Furthermore, to exclude couplings with other state variables, we use Zajac's activation dynamics. Thus, the simplified right hand side f_S reads as

$$\dot{\ell}_{CE} = f_S(\ell_{CE}) = b_{rel}\ell_{CE,opt}\left(1 - \frac{q^*_Z F_{isom}(\ell_{CE}) + a_{rel}}{\frac{F_{CE}}{F_{max}} + a_{rel}}\right) \tag{2.7}$$

where q^*_Z denotes the only equilibrium point of Zajac's formulation. The parameters a_{rel} and b_{rel} are fit parameters for the hyperbolic force–velocity relation and known as "Hill–parameters". The maximum isometric muscle force is denoted by F_{max} and the length at which this force is exerted is denoted by $\ell_{CE,opt}$. We assume that the parameters F_{CE}, a_{rel} and b_{rel} are constants, i.e. independent of ℓ_{CE} or q (cf. [27]).

Setting the right hand side equal to zero yields:

$$f_S(\ell_{CE}) = 0 \quad \Longleftrightarrow \quad F_{CE} = q_Z^* F_{max} F_{isom}(\ell_{CE}) \; . \tag{2.8}$$

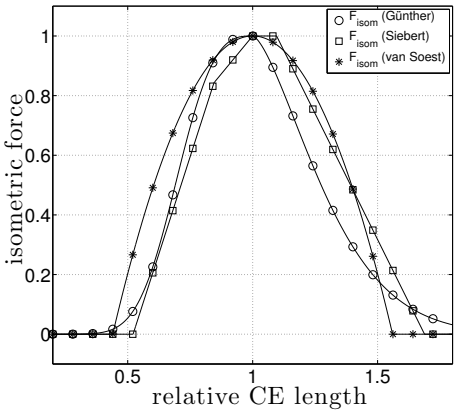

The explicit solution for ℓ_{CE} now depends on the structure of F_{isom}, whether it has the form of a parabola [79] (van Soest), is piecewise linear [75] (Siebert) or has a bell–shaped form [27] (Günther), see alongside figure. The term "relative CE length" indicates a normalization of the CE length w.r.t. $\ell_{CE,opt}$ via $\ell_{CE,rel} = \ell_{CE}/\ell_{CE,opt}$. Regardless the shape of F_{isom}, the solution for ℓ_{CE} is not unique in general. In all cases there is the possibility of two solutions $\ell_{CE,1}^* \leq \ell_{CE,opt} \leq \ell_{CE,2}^*$ (see Fig. 2.4), if $F_{CE} < q_Z^* F_{max}$. For the parabola and the bell–shaped curve there is the possibility of the unique equilibrium point $\ell_{CE}^* = \ell_{CE,opt}$, if $F_{CE} = q_Z^* F_{max}$. For the piecewise linear curve there even might exist infinitely many equilibrium points, which lie in the plateau region, denoted by $[\ell_{CE,opt}, \ell_3]$ in [75]. A last possibility is for the system to have no equilibrium point at all, if $F_{CE} > q_Z^* F_{max}$. In general, it is not possible to give a closed–form solution for ℓ_{CE}^*, hence we use the implicit Eqn. (2.8).

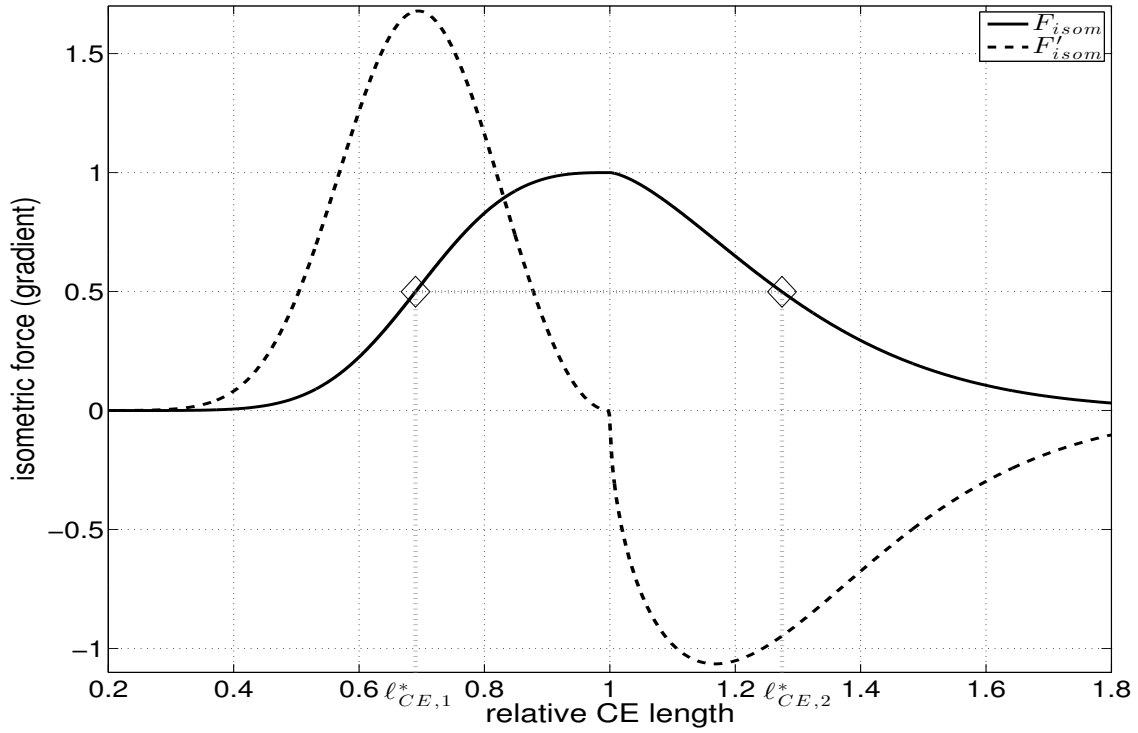

Figure 2.4.: Isometric force–length curve from [27] along with its derivative. For the choice of $F_{CE} = 1/2 q_Z^* F_{max}$ there exist two equilibrium points $\ell_{CE,1}^* < \ell_{CE,opt} < \ell_{CE,2}^*$. One verifies immediately that in general the derivative $\mathrm{d}/\mathrm{d}\ell_{CErel} F_{isom}(\ell_{CE,1}^*) > 0$ and $\mathrm{d}/\mathrm{d}\ell_{CErel} F_{isom}(\ell_{CE,2}^*) < 0$.

Remark 2.3.1. The described change in the qualitative behavior of the ODE solution with respect to a containing parameter, in the above case the CE force F_{CE}, is called a **bifurcation**. The bifurcation theory, we base our observations on, can be found in [11], [32] or [80]. In the case of the simplified contraction dynamics, we more precisely speak of a *saddle–node bifurcation* or *fold bifurcation*, whose normal form is the family of ODEs

$$\dot{u} = \mu - u^2 = (\sqrt{\mu} + u) \cdot (\sqrt{\mu} - u), \quad u, \mu \in \mathbb{R} \, . \tag{2.9}$$

In practice, a differential equation of this form can be utilized to describe a free fall with air resistance and turbulent flow or, assuming $\mu > 0$, can be transformed into a logistic ODE.

For $\mu < 0$ there is no (real) equilibrium point existing. For $\mu = 0$ there is one rest point (the saddle–node) $u^* = 0$. Finally, for $\mu > 0$ there are two equilibria $u^*_{1,2} = \pm\sqrt{\mu}$ existing, where $u^*_1 = \sqrt{\mu}$ is asymptotically stable and $u^*_2 = -\sqrt{\mu}$ is unstable. According to Theorem 2.1.7 the respective Lyapunov functions can be chosen as $V_1(u) = (u - \sqrt{\mu})^2$ on $U_1 = (-u^*_1, \infty)$ for u^*_1 as well as $V_2(u) = (u + \sqrt{\mu})^2$ on $U_2 = (-\infty, u^*_1)$ for u^*_2. For the respective bifurcation diagram see [11, p. 13] or [80, p. 199]. The change of the slope field of ODE (2.7) w.r.t. changes in F_{CE} is displayed in Fig. 2.5.

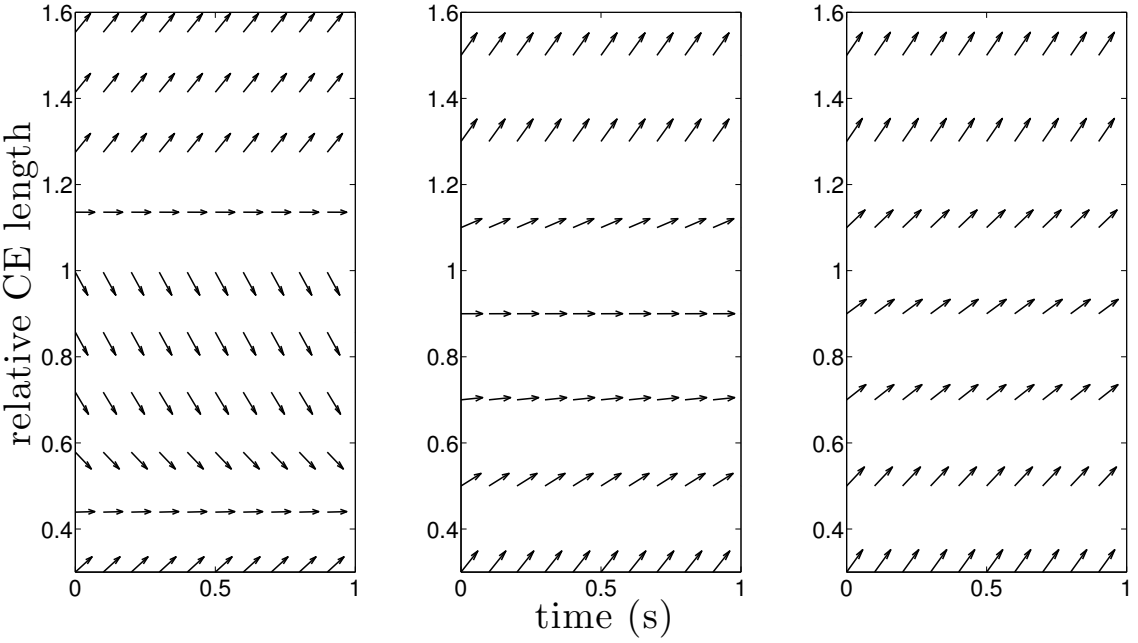

Figure 2.5.: Bifurcation, visualized by a changing slope field in dependence of one parameter. The slope field of the simplified contraction dynamics equation (2.7) in dependence of the parameter F_{CE} is shown. For $F_{CE} = 0.4 \cdot F_{max}$ (left), we have two equilibrium points, where one is asymptotically stable and the other, called the saddle, is unstable. For $F_{CE} = F_{max}$ (middle), there is a collision of the two equilibria, which results in one semi–stable equilibrium. For $F_{CE} = 2 \cdot F_{max}$ (right), the equation has no equilibrium at all. In all cases it holds $q^*_Z = 1$. The remaining parameter values were taken from [27, Table 1].

To investigate the stability of the equilibrium point(s) ℓ^*_{CE}, we take the derivative

$$\frac{\mathrm{d}}{\mathrm{d}\ell_{CE}} f_S(\ell_{CE}) = -b_{rel}\ell_{CE,opt}\left(\frac{q^*_Z \frac{\mathrm{d}}{\mathrm{d}\ell_{CE}} F_{isom}(\ell_{CE})}{\frac{F_{CE}}{F_{max}} + a_{rel}}\right) \tag{2.10}$$

and look at its sign. Since all occurring parameters are positive, the sign is opposite to the sign of $\mathrm{d}/\mathrm{d}\ell_{CE}\, F_{isom}(\ell_{CE})$. As illustrated in Figures 2.4 and 2.5, in the case of two equilibrium points $\ell^*_{CE,1} < \ell_{CE,opt} < \ell^*_{CE,2}$, it holds that $\ell^*_{CE,1}$ is asymptotically stable, whereas $\ell^*_{CE,2}$ is unstable. For the cases $\ell^*_{CE} = \ell_{CE,opt}$ (parabola, bell–shaped) and $\ell^*_{CE} \in [\ell_{CE,opt}, \ell_3]$ (piecewise linear) the derivative of the right hand side is zero, which means that no prediction can be made. However, the slope fields in Fig. 2.5 indicate that those points might be semi–stable.

Naturally the question arises, whether this mathematical observation is of any biomechanical relevance. We recall that our observed contractile component only consist of a single CE with no parallel or serial elastic element. In other words: in the stationary state, we are looking at a spring with a non–linear force–length characteristic. For a biomechanical interpretation, we want to verify the meaning of $\ell^*_{CE,1} < \ell_{CE,opt}$ being asymptotically stable and $\ell^*_{CE,2} > \ell_{CE,opt}$ being unstable. The definition of stability states that a small change of the equilibrium state should only lead to a small change of the solution over time, which even tends to zero in the case of asymptotic stability. For $\ell^*_{CE,1}$, a small diminution of ℓ_{CE} means a decrease in force production. Hence, the outer force is going to lengthen the muscle again until $\ell^*_{CE,1}$ (see Figs. 2.4 and 2.5). In contrast, increasing the length $\ell_{CE} > \ell^*_{CE,1}$ would result in a force production increase and thus in a shortening of the muscle until the equilibrium is reached. On the other hand diminishing $\ell_{CE} < \ell^*_{CE,2}$ results in an increase in force production and in a further shortening until $\ell^*_{CE,1}$. Consequently, if $\ell_{CE} > \ell^*_{CE,2}$ is increased, the muscle's force decreases and the outer force further lengthens the muscle arbitrarily.

2.3.2. Complete Contraction Dynamics

In a final step, we are considering the complete state–of–the–art muscle model from [27, 30]. Besides including a parallel elastic element (PEE), a serial elastic element (SEE) and a damping element (SDE), we also take the coupling with Hatze's activation dynamics into account. The question, whether there exist equilibrium points and whether they are stable is very important. This is, because in *in vivo* experiments one can only observe the outer (MTC) dynamics, but has to model the inner (CE) dynamics. As stated in [67], during an isometric contraction cycle, the MTC length does not change, but the CE passes through a concentric and an eccentric contraction phase with two different steady states. The respective model equations are obtained by inserting the contraction dynamics into the muscle force equilibrium and can be found in [27, 30, 66]:

$$\begin{aligned} \dot{q}_H &= f_2(q_H)\ , \\ 0 &= C_2 \cdot \dot{\ell}^2_{CE} + C_1 \cdot \dot{\ell}_{CE} + C_0\ . \end{aligned} \tag{2.11}$$

We recall the occurring coefficients for clarity:

$$
\begin{aligned}
C_0 &= D_0\,\dot{\ell}_{MTC} + \ell_{CE,opt}\,b_{rel}\,(F_{SEE} - F_{PEE} - F_{max} q F_{isom})\,,\\
C_1 &= -(C_2\,\dot{\ell}_{MTC} + D_0 + F_{SEE} - F_{PEE} + F_{max} a_{rel})\,,\\
C_2 &= d_{SE,max}\left(R_{SDE} - \left[a_{rel} - \frac{F_{PEE}}{F_{max}}\right](1 - R_{SDE})\right)\,,\\
D_0 &= \ell_{CE,opt}\,b_{rel}\,d_{SE,max}\left(R_{SDE} + (1 - R_{SDE})\left(qF_{isom} + \frac{F_{PEE}}{F_{max}}\right)\right)\,,\\
d_{SE,max} &= D_{SDE}\,\frac{F_{max} a_{rel,0}}{\ell_{CE,opt} b_{rel,0}}\,,
\end{aligned}
$$

where F_{PEE} and F_{isom} are functions of ℓ_{CE}, further F_{SEE} is a function of ℓ_{CE} and ℓ_{MTC}, and finally a_{rel} and b_{rel} are functions of ℓ_{CE} and q, see Eqns. 7.4 – 7.12.

The equilibrium points for q_H were already given in Eqn. (2.6). For the equilibrium points ℓ^*_{CE} we see that

$$
\dot{\ell}_{CE} = 0 \iff C_0 = 0 \iff F_{SEE} = F_{PEE} + F_{max} \cdot q^*_H \cdot F_{isom} - \frac{D_0 \dot{\ell}_{MTC}}{b_{rel}\ell_{CE,opt}} \tag{2.12}
$$

In this formulation, the equilibria would depend on the velocity of the MTC, because of the damping element. Since a shortening or elongating muscle would hardly allow for an inner steady state, we only consider an isometric equilibrium where $\dot{\ell}_{MTC} = 0$. Note that this does not imply on overall isometric contraction, but we assume that, after performing any contraction mode, the MTC attains a fixed length $\ell_{MTC,end}$. Hence, the equilibrium points ℓ^*_{CE} are the roots of the function:

$$
\Phi(\ell_{MTC,end}, \ell_{CE}, \sigma) := F_{SEE}(\ell_{MTC,end}, \ell_{CE}) - F_{PEE}(\ell_{CE}) - F_{max} \cdot q^*_H(\ell_{CE}, \sigma) \cdot F_{isom}(\ell_{CE}) \tag{2.13}
$$

For $\ell_{CE} \ll \ell_{CE,opt}$, the force of the serial elastic element is positive and the force of the parallel elastic element and the isometric force is approximately zero. In contrast, for $\ell_{CE} \gg \ell_{CE,opt}$, the force of the SEE is zero and the force of the PEE is positive. Hence, assuming $\sigma \in [0, 1]$ is constant, there exists a root according to the *mean value theorem*, since Φ is continuous. Furthermore, because in our case $\Phi(\,.\,, \ell_{CE}, \,.\,)$ is strictly monotonic decreasing, the equilibrium is unique.

Remark 2.3.2. The monotonicity of Φ w.r.t. ℓ_{CE} is dependent on the parameter values. A different set of parameters may strengthen the isometric properties. For example increasing $\mathcal{L}_{PEE}$ to a value greater than one would result in a local minimum–maximum pair of Φ. Consequently, there could be up to three roots of Φ resulting in one stable and two unstable equilibria.

Figure 2.6 shows the values of Φ for three different MTC lengths. For short muscle length (e.g. $\ell_{MTC,end} = 0.9 \cdot \ell_{MTC,ref} \approx 5,54\,\text{cm}$) the equilibrium points are strongly dependent on the applied stimulation, whether $\ell^*_{CE} \approx 0.67\ell_{CE,opt}$ for $\sigma = 1$ or $\ell^*_{CE} \approx 0.95\ell_{CE,opt}$ for $\sigma = 0$. The longer the MTC length, the lesser the equilibrium depends on the value of σ. For a long muscle length (e.g. $\ell_{MTC,end} = 1.1 \cdot \ell_{MTC,ref} \approx 6.77\,\text{cm}$) the stimulation has no effect on the equilibrium at all, because the passive behavior is dominating the force output.

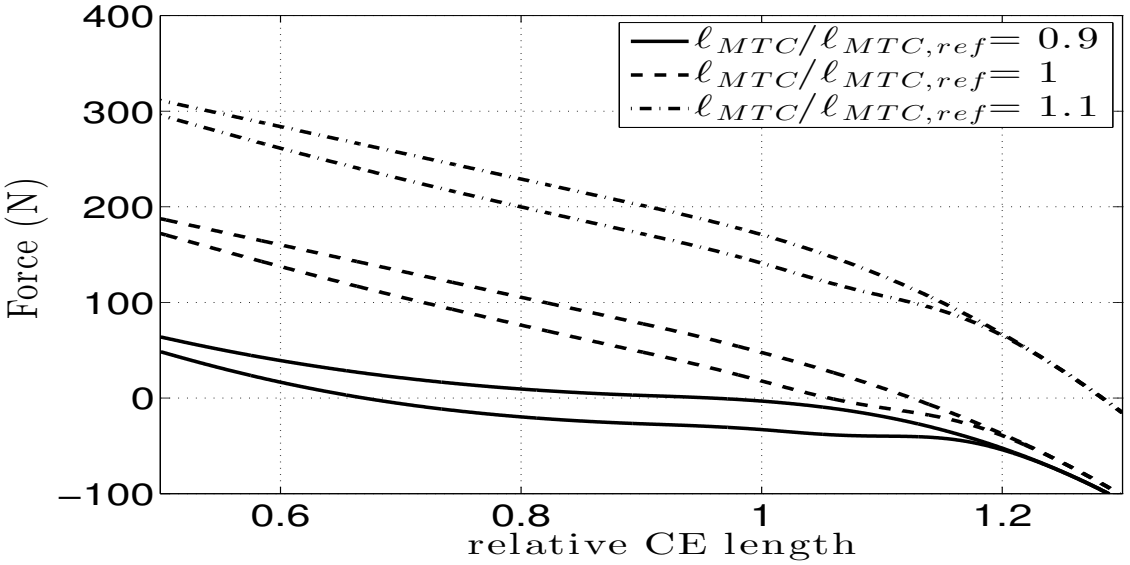

Figure 2.6.: Graphs of $\Phi(\ell_{MTC,end}, \ell_{CE}, \sigma) = F_{SEE} - F_{PEE} - F_{max} \cdot q_H^* \cdot F_{isom}$ applying different MTC lengths and $\sigma \in \{0; 1\}$. Regarding every line type, the lower function belongs to the case $\sigma = 1$ and the upper function to the case $\sigma = 0$. All graphs are strictly monotonic decreasing resulting in a unique root and therefore a unique equilibrium point ℓ_{CE}^*.

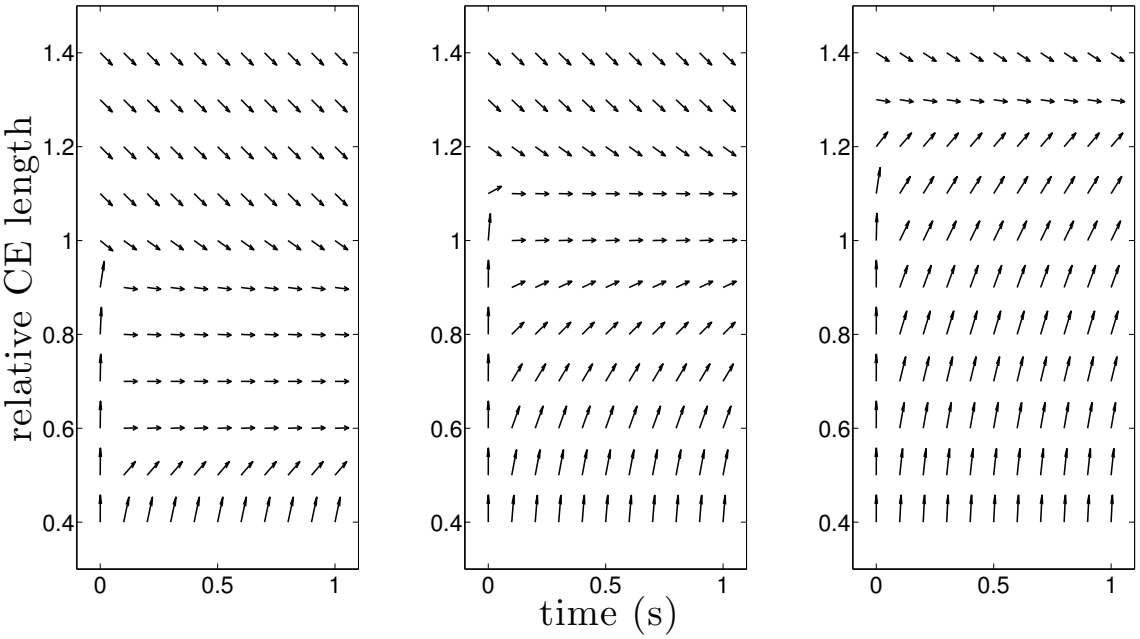

Figure 2.7.: Slope fields of the complete contraction dynamics from (2.11). From left to right, the MTC length varied over $0.9 \cdot \ell_{MTC,ref}, \ell_{MTC,ref}$ and $1.1 \cdot \ell_{MTC,ref}$. The initial conditions were $\ell_{CE,0}$ (ordinate at $t = 0$) and $1.1 q_0$ (see Remark 2.2.2). Stimulation was chosen as $\sigma(t) = 1$.

Figure 2.7 shows the respective slope fields for a fully stimulated muscle held at lengths $\ell_{MTC}/\ell_{MTC,ref} \in \{0.9, 1, 1.1\}$. For the short MTC length, the equilibrium is not as obvious or sharp as for the long MTC length, but is still unique, see Fig. 2.6.

The slope fields from Fig. 2.7 indicate that the unique equilibrium ℓ^*_{CE} is stable. However, an analytical validation requires to linearize the right hand side of model (2.11) and determine the definiteness of the resulting Jacobian. We relinquish an explicit derivation due to the complexity and nesting of the model functions. For the example cases in Figs. 2.6 and 2.7, the resulting Jacobian proofed to be negative definite in our numerical simulations. Hence, the equilibria were stable.

Regarding model (2.11), we want to state additional influences on the equilibria ℓ^*_{CE} among a broad variety of cases. Therefore we varied the MTC length, the stimulation and the activation dynamics. The MTC lengths were chosen relative to the reference length $\ell_{MTC}/\ell_{MTC,ref} \in \{0.7, 0.8, 0.9, 1, 1.1, 1.2\}$, the stimulation was chosen from $\sigma \in \{0, 0.2, 0.4, 0.6, 0.8, 1\}$ and the activation dynamics were chosen from Hatze and Zajac. In each case, the equilibria were determined. Figure 2.8 contains an overview of the attained CE lengths.

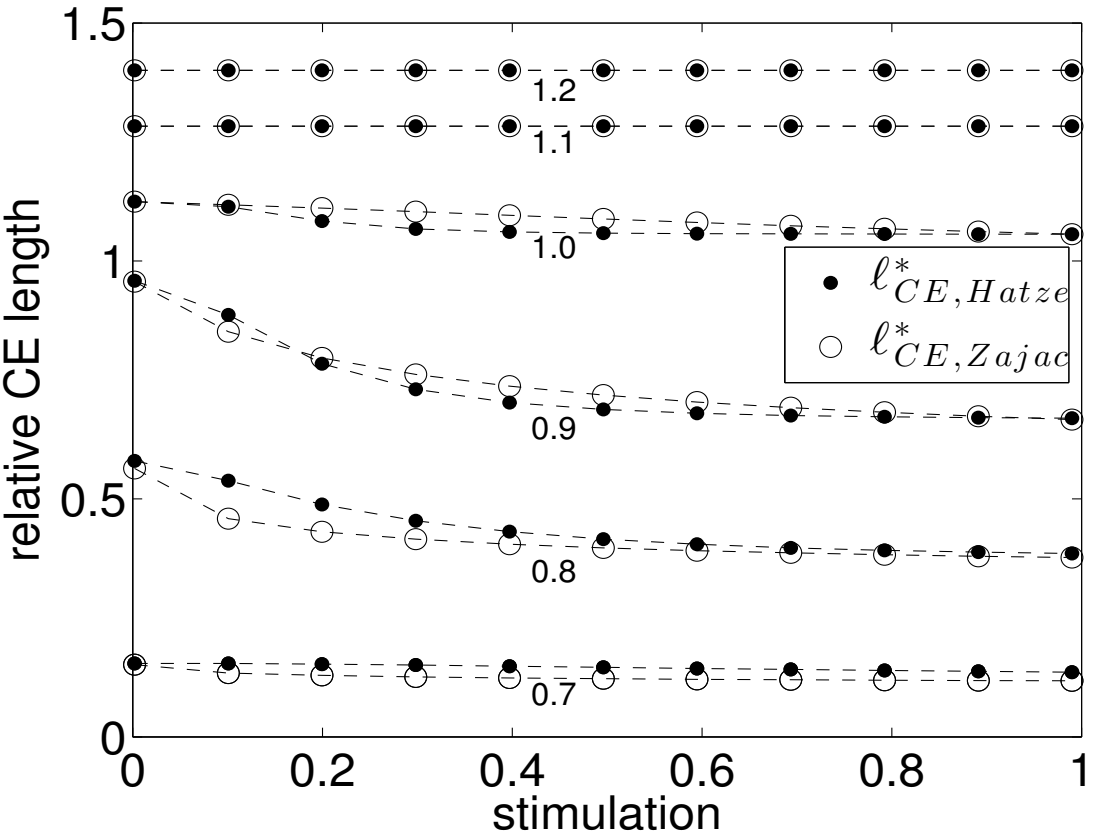

Figure 2.8.: Attained equilibrium points ℓ^*_{CE} of model (2.11), in dependence on the relative MTC length (dashed lines), the stimulation (abscissa) and the activation dynamics according to Hatze (filled circles) or Zajac (open circles). The respective relative MTC lengths are indicated with little numbers $0.7, \ldots, 1.2$.

The dependence of the equilibria on the MTC lengths was stated above and recovered in Fig. 2.8. For short (0.7) and long (> 1.1) relative muscle lengths, the equilibria do not depend on the level of stimulation, because the passive behavior of the muscle is dominating the force output. For relative MTC lengths from 0.8 to 1.0, an increasing stimulation expectably results in a shortened CE. At zero, as well as at full stimulation, the equilibria are not dependent on the activation dynamics. At short relative muscle lengths $(0.7, 0.8)$ and for sub–maximal stimulation, model (2.11) together with Zajac's activation yields lower CE equilibria than with Hatze's formulation. The opposite holds true for longer lengths $(0.9, 1.0)$. This effect may be associated with an observation from [68]: Zajac's activation dynamics seemed to fit better, regarding experimental data at short relative muscle lengths, whereas Hatze's formulation seemed to be more valid at longer muscle lengths.

Part II.

Sensitivity Analysis

3. Research Paper I: Comparative Sensitivity Analysis of Muscle Activation Dynamics

R. Rockenfeller M. Günther S. Schmitt T. Götz

The following is a reformatted and slightly modified copy of the open source article
R. Rockenfeller et al. "Comparative Sensitivity Analysis of Muscle Activation Dynamics". In: Computational and Mathematical Methods in Medicine. Article ID 585409, doi:10.1155/2015/585409 (2015), 16 pages
available at http://www.hindawi.com/journals/cmmm/2015/585409.
This article is also referred to as [50] (in Chapter 4), [24] (in Chapter 7) or [68] (in the remaining work).

The initial idea for this article originated from T. Götz. Structure, calculations and results were given by R. Rockenfeller. The sections "Introduction", "The Numerical Approach" and "Consequences, Discussion and Conclusion" originated from a direct, personal collaboration of R. Rockenfeller and M. Günther. The publication fee was sponsored by S. Schmitt.

Abstract

We mathematically compared two models of mammalian striated muscle activation dynamics proposed by Hatze and Zajac. Both models are representative for a broad variety of biomechanical models formulated by ordinary differential equations (ODEs). These models incorporate some parameters that directly represent known physiological properties. Other parameters have been introduced to reproduce empirical observations. We used sensitivity analysis as a mathematical tool to investigate the influence of model parameters on the solution of the ODEs. Thereto, we calculated first order, local sensitivities according to a former approach adopted from literature. We expanded this approach to treat initial conditions as parameters and to calculate second order sensitivities, the latter quantifying the non–linearly coupled effect of any combination of two parameters. Furthermore, we used a global sensitivity analysis approach to factor in finite ranges of parameter values. The methods we suggest have numerous uses. A theoretician striving for model reduction could use them to identify particularly low sensitivities to detect superfluous parameters. An experimentalist could use them to identify particularly high sensitivities to facilitate determining parameter values with maximized precision.

Hatze's non–linear model incorporates some parameters to which activation dynamics is more sensitive than to any parameter in Zajac's linear model. Other than Zajac's model, Hatze's model can moreover reproduce measured shifts in optimal muscle length with varied muscle activity. Accordingly, we extracted a specific parameter set for Hatze's model that led to optimal fits, in combination with a particular muscle force–length relation. We also provide an outlook on how sensitivity analysis could be used for optimizing parameter sets in future work.

Keywords: Biomechanical Model, Direct Dynamics, Ordinary Differential Equation

List of Symbols

Symbol	Meaning	Value
ℓ_{CE}	contractile element (CE) length	time–depending
$\dot{\ell}_{CE}$	contraction velocity	first time derivative of ℓ_{CE}
$\ell_{CE,opt}$	optimal CE length	muscle–specific
ℓ_{CErel}	relative CE length	$\ell_{CErel} = \frac{\ell_{CE}}{\ell_{CE,opt}}$ (dimensionless)
F_{max}	maximum isometric force of the CE	muscle–specific
σ	neural muscle stimulation	usually time–depending ; here constant
q	muscle activity (bound Ca^{2+} concentration)	time–depending
q_0	basic activity according to [11]	0.005
q_H	activity according to [10]	time–length–depending
$q_{H,0}$	initial condition for Hatze's activation ODE	mutable
$q_{Z,0}$	initial condition for Zajac's activation ODE	mutable
τ	activation time constant in [27]	here: $\frac{1}{40}\ s$
τ_{deact}	deactivation time constant in [27]	here: $\frac{1}{40}\ s$ or $\frac{3}{40}\ s$
β	corresponding deactivation boost [27]	$\beta = \tau / \tau_{deact}$
ν	exponent in Hatze's formulation	2 or 3
m	activation frequency constant in [10]	range: $3.67 \ldots 11.25\ \frac{1}{s}$; here: $10 \frac{1}{s}$
c	maximal Ca^{2+} concentration in [9]	$1.37 \cdot 10^{-4}\ \frac{mol}{l}$
γ	representation of free Ca^{2+} concentration [10, 11]	time–depending
ρ	length dependency of [9] activation dynamics	$\rho(\ell_{CErel}) = \rho_c \cdot \frac{\ell_\rho - 1}{\frac{\ell_\rho}{\ell_{CErel}} - 1}$
ℓ_ρ	pole in Hatze's length dependency function	2.9
ρ_0	factor in [10, 25]	$6.62 \cdot 10^4\ \frac{l}{mol}$ or $5.27 \cdot 10^4\ \frac{l}{mol}$
ρ_c	merging of ρ_0 and c	$\rho_c = \rho_0 \cdot c$; here: 9.10 or 7.24
Λ	model parameter set	$\Lambda = \{\lambda_1, \ldots, \lambda_n\}$

3.1. Introduction

Scientific knowledge is gained by an interplay between quantitative real world measurements of physical, chemical, or biological phenomena and the development of mathematical models for understanding the dynamical processes behind. In general, such phenomena are determined as spatio–temporal patterns of physical measures (state variables). Modeling consists of distinguishing the surrounding world from the system that yields the phenomena and formulating a mathematical description of the system, which is called a model. A model can predict values of the state variables. The calculations depend on model parameters and often on giving measured input variables. By changing parameter values and analyzing the resulting changes in the values of the state variables, the model may then be used as a predictive tool. This way, the model's validity can be verified. If the mathematical model description is moreover derived from first principles, the model has the potential to explain the phenomena in a causal sense.

Calculating the sensitivities of a model's predicted output, i.e. the system's state variables, with respect to model parameters is a way of eliminating redundancy and indeterminacy from models, and thus helps to identify valid models. Sensitivity analyses can be helpful both in model–based experimental approaches and in purely theoretical work. A modeling theoretician could be looking for parameters to which all state variables are non–sensitive. Such parameters might be superfluous. An experimentalist may inspect the model that represents his working hypothesis and analyze, which of the model's state variables are specifically sensitive to a selected parameter. Hence the experimentalist would have to measure exactly this state variable to identify the value of the selected parameter.

A biomechanical study [21] applied sensitivity analysis to examine the dynamics of a mechanical multi–body system: a runner's skeleton coupled to muscle activation–contraction dynamics. They calculated specific sensitivity coefficients in three slightly different ways. A sensitivity coefficient is the difference quotient calculated from dividing the change in a state variable by the change in a model parameter value, evaluated in a selected system state [16]. The corresponding partial derivative may be simply called "sensitivity". Therefore, a sensitivity function is the time evolution of a sensitivity [16]. Accordingly, [16] proposed a more general and unified approach than [21], which allows to systematically calculate the sensitivities of any dynamical system described in terms of ordinary differential equations. As an example for sensitivity functions, [16] applied their proposed method to a muscle–driven model of saccadic eye movement. By calculating a percentage change in a state variable value per percentage change in a parameter value, all sensitivities can be made comprehensively comparable, even across models.

Sensitivity, as defined so far, is of first order. Methodically, we aim at introducing a step beyond, namely at calculating second order sensitivities. These measures are suited to quantify, how much the sensitivity of a state variable with respect to (w.r.t.) one model parameter depends on changing another parameter. By analyzing second order sensitivities, the strength of their interdependent influence on model dynamics can be determined. In addition to this so–called local sensitivity analysis, we will take the whole parameter variability into account by calculating global sensitivities according to [3] and [19]. This approach allows to translate the impact of one parameter on a state variable into a parameter's importance, by completely comprising its interdependent influence in combination with all other parameters' sensitivities.

In this study, we will apply sensitivity analysis to models that predict how the activity of a muscle (its chemical state) changes, when the muscle is stimulated by neural signals (electrical excitation). Such models are used for simulations of muscle contractions coupled

to their activation dynamics. Models for coupled muscular dynamics are often part of neuro–musculo–skeletal models of biological movement systems. In particular, we want to try and rate two specific model variants of activation dynamics, formulated by Zajac [27] and by Hatze [10]. As a first result, we present an example of a simplified version of the Zajac model, in which sensitivity functions can in fact be calculated in closed form. Subsequently, we calculate the sensitivities numerically w.r.t. all model parameters in both models, aiming at an increased understanding of the influence of changes in model parameters on the solutions of the underlying ordinary differential equations (ODEs). Additionally, we discuss which of both models may be physiologically more accurate. The arguments come from a mixture of three different aspects: sensitivity analysis, other experimental findings, and an additional attempt to best fit different combinations of activation dynamics and force–length relations of the contractile element (CE) in a muscle to known data on shifts in optimal CE length with muscle activity [14].

3.2. Two Models for Muscle Activation Dynamics

Macroscopically, a muscle fiber or an assembly thereof, a muscle belly, is often mapped mathematically by a one–dimensional massless thread called "contractile component" or "contractile element" (CE) [4, 7, 8, 25, 26]. Its absolute length is ℓ_{CE}, which may be normalized to the optimal fiber length $\ell_{CE,opt}$ by $\ell_{CErel} = \ell_{CE}/\ell_{CE,opt}$. In macroscopic muscle models, the CE muscle force is usually modeled as a function of a (CE–)force–length relation, a (CE–)force–velocity relation, and (CE–)activity q. Commonly, the muscle activity q represents the number of attached cross–bridges within the muscle, normalized to the maximum number available ($q_0 \leq q \leq 1$). It can also be considered as the concentration of bound Ca^{2+} ions in the muscle sarcoplasma relative to its physiological maximum. The parameter q_0 represents the minimum activity that is assumed to occur without any stimulation [10].

We analyze two different formulations of muscle activation dynamics, i.e. the time (its symbol: t) evolution of muscle activity $q(t)$. One formulation of muscle activation dynamics was suggested by Zajac, which we modified slightly to take q_0 into account:

$$\dot{q}_Z = \frac{1}{\tau \cdot (1 - q_0)} \cdot [\sigma \cdot (1 - q_0) - \sigma \cdot (1 - \beta) \cdot (q_Z - q_0) - \beta \cdot (q_Z - q_0)] \quad , \tag{3.1}$$

with the initial condition $q_Z(0) = q_{Z,0}$. In this context, σ is supposed to represent the (electrical) stimulation of the muscle, being a parameter for controlling muscle dynamics. It represents the output of the nervous system applied to the muscle, which in turn interacts with the skeleton, the body mass distribution, the external environment, and therefore with the nervous system in a feedback loop. Electromyographic (EMG) signals can be seen as a compound of such neural stimulations collected in a finite volume (being the input to a number of muscle fibers) over a frequency range and coming from a number of (moto–)neurons. The parameter τ denotes the activation time constant, and $\beta = \tau/\tau_{deact}$ is the ratio of activation to deactivation time constants (deactivation boost).

An alternative formulation of muscle activation dynamics was introduced by Hatze in [10]:

$$\dot{\gamma} = m \cdot (\sigma - \gamma) \quad . \tag{3.2}$$

We divided the original equation from [10] by the parameter $c = 1.37 \cdot 10^{-4}\,\mathrm{mol/l}$, which represents the maximum concentration of free Ca^{2+} ions in the muscle sarcoplasm. Thus, the value of the corresponding normalized Ca^{2+} concentration is $0 \leq \gamma \leq 1$. The activity

is finally calculated by the function

$$q_H(\gamma, \ell_{CErel}) = \frac{q_0 + [\rho(\ell_{CErel}) \cdot \gamma]^\nu}{1 + [\rho(\ell_{CErel}) \cdot \gamma]^\nu} \quad , \tag{3.3}$$

and the parameter c is shifted to the accordingly renormalized function

$$\rho(\ell_{CErel}) = \rho_c \cdot \frac{\ell_\rho - 1}{\frac{\ell_\rho}{\ell_{CErel}} - 1} \quad , \tag{3.4}$$

with $\rho_c = c \cdot \rho_0$ and $\ell_\rho = 2.9$. Two cases have been suggested by [11]: $\rho_0 = 6.62 \cdot 10^4$ l/mol (i.e. $\rho_c = 9.10$) for $\nu = 2$ and $\rho_0 = 5.27 \cdot 10^4$ l/mol (i.e. $\rho_c = 7.24$) for $\nu = 3$, which have been applied in literature [12, 13, 14, 25]. By substituting equations (3.2) and (3.3) into $\dot{q}_H = \mathrm{d}/\mathrm{d}\gamma\, q_H(\gamma, \ell_{CErel}) \cdot \dot{\gamma}$ and re–substituting the inverse of (3.3) afterwards, Hatze's formulation of an activation dynamics can be transformed into a single non–linear differential equation:

$$\dot{q}_H = \frac{\nu m}{1 - q_0} \left[\sigma \rho(\ell_{CErel})(1 - q_H)^{1+1/\nu} (q_H - q_0)^{1-1/\nu} - (1 - q_H)(q_H - q_0) \right] \quad , \tag{3.5}$$

with the initial condition $q_H(0) = q_{H,0}$.

The solutions $q_Z(t)$ and $q_H(t)$ of both formulations of activation dynamics, (3.1) and (3.5), can now be directly compared by integrating them with the same initial condition $q_{Z,0} = q_{H,0}$ using the same stimulation σ.

3.3. Local First and Second Order Sensitivity of ODE Systems Regarding Their Parameters

Let $\Omega \subseteq \mathbb{R} \times \mathbb{R}^M \times \mathbb{R}^N$ and $f : \Omega \to \mathbb{R}^M$. We then consider a system of ordinary, first order initial value problems (IVPs)

$$\dot{Y} = f(t, Y(t, \Lambda), \Lambda) \quad , \qquad Y(0, \Lambda) = Y_0 \quad , \tag{3.6}$$

where $Y(t, \Lambda) = (y_1(t, \Lambda), y_2(t, \Lambda), \ldots, y_M(t, \Lambda))$ denotes the vector of state variables. Furthermore, let denote $f = (f_1, f_2, \ldots, f_M)$ the vector of right–hand sides of the ODE, and $\Lambda = \{\lambda_1, \lambda_2, \ldots, \lambda_N\}$ the set of parameters that the ODE depends on. The vector of initial conditions is abbreviated by

$$Y(0, \Lambda) = (y_1(0, \Lambda), y_2(0, \Lambda), \ldots, y_M(0, \Lambda)) = (y_{1,0}, y_{2,0}, \ldots, y_{M,0}) = Y_0 \quad . \tag{3.7}$$

The first order sensitivity of the solution $Y(t, \Lambda)$ with respect to the parameter set Λ is defined as the matrix

$$S(t, \Lambda) = (S_{ik}(t, \Lambda))_{i=1,\ldots,N, k=1,\ldots,M} \quad , \qquad \text{with} \qquad S_{ik}(t, \Lambda) = \frac{\mathrm{d}}{\mathrm{d}\lambda_i} y_k(t, \Lambda) \quad . \tag{3.8}$$

Simplifying, we denote $Y = Y(t, \Lambda)$, $f = f(t, Y, \Lambda)$, $S_{ik} = S_{ik}(t, \Lambda)$ but keep the dependencies in mind. Because the solution Y might only be gained numerically rather than in a closed–form expression, we have to apply the well–known theory of sensitivity analysis as stated in [5, 16, 24, 28]. Differentiating equation (3.8) w.r.t. time t and applying the chain rule yields

$$\frac{\mathrm{d}}{\mathrm{d}t} S_{ik} = \frac{\mathrm{d}^2}{\mathrm{d}t\, \mathrm{d}\lambda_i} y_k = \frac{\mathrm{d}^2}{\mathrm{d}\lambda_i\, \mathrm{d}t} y_k = \frac{\mathrm{d}}{\mathrm{d}\lambda_i} f_k = \frac{\mathrm{d}}{\mathrm{d}\lambda_i} Y \cdot \frac{\partial}{\partial Y} f_k + \frac{\partial}{\partial \lambda_i} f_k \quad ,$$

with $\partial/\partial Y$ being the gradient of state variables. Hence, we obtain the following ODE for the first order solution sensitivity:

$$\dot{S}_{ik} = \sum_{l=1}^{M} S_{il} \cdot \frac{\partial}{\partial y_l} f_k + \frac{\partial}{\partial \lambda_i} f_k \quad , \qquad S_{ik}(0) = \frac{\partial}{\partial \lambda_i} y_{k,0} = 0 \quad , \tag{3.9}$$

or in short terms

$$\dot{S} = S \cdot J + B \quad , \qquad S(0) = \mathbf{0}_{N \times M} \quad ,$$

where S is the $N \times M$ sensitivity matrix, J is the $M \times M$ Jacobian matrix containing the partial derivatives $J_{kl} = \partial/\partial y_l \, f_k$, furthermore B the $N \times M$ matrix containing the partial derivatives $B_{ik} = \partial/\partial \lambda_i \, f_k$ and $\mathbf{0}_{N \times M}$ the $N \times M$ matrix consisting of zeros only.

By analogy, the second order sensitivity of Y with respect to Λ is defined as the following $N \times N \times M$ tensor

$$R(t, \Lambda) = (R_{ijk}(t, \Lambda))_{i,j=1,\dots N, k=1,\dots M} \quad ,$$

with

$$R_{ijk}(t, \Lambda) = \frac{\mathrm{d}}{\mathrm{d}\lambda_i} S_{jk} = \frac{\mathrm{d}}{\mathrm{d}\lambda_j} S_{ik} = \frac{\mathrm{d}^2}{\mathrm{d}\lambda_i \, \mathrm{d}\lambda_j} y_k = R_{jik}(t, \Lambda) \quad , \tag{3.10}$$

assuming $R_{ijk} = R_{jik}$ for all $k = 1, \dots, M$, therefore assuming that the prerequisites of Schwarz' Theorem (symmetry of the second derivatives) are fulfilled throughout. Differentiating w.r.t. time t and applying the chain rule leads to the ODE

$$\dot{R}_{ijk} = \sum_{l=1}^{M} \left(R_{ijl} \frac{\partial}{\partial y_l} f_k + S_{il} \frac{\partial}{\partial \lambda_j} f_k + S_{jl} \frac{\partial}{\partial \lambda_i} f_k \right) + \sum_{l_1=1}^{M} \sum_{l_2=1}^{M} S_{il_1} S_{jl_2} \frac{\partial^2}{\partial y_{l_1} \partial y_{l_2}} f_k + \frac{\partial^2}{\partial \lambda_i \partial \lambda_j} f_k \tag{3.11}$$

with $R_{ijk}(0) = 0$. For purposes beyond the aim of this paper, a condensed notation introducing the concept of tensor (or Kronecker) products as in [28] may be helpful. For a practical implementation in MATLAB see [1].

Furthermore, if an initial condition $y_{k,0}$ (see (3.7)) is considered as another parameter, we can derive a separate sensitivity differential equation by rewriting equation (3.6) in its integral form

$$Y(t, \Lambda) = Y_0 + \int_0^t f(s, Y(s, \Lambda)) \, \mathrm{d}s \quad .$$

Differentiating this equation w.r.t. Y_0 yields

$$S_{Y_0}(t, \Lambda) = \frac{\partial}{\partial Y_0} Y(t, \Lambda) = 1 + \int_0^t \frac{\partial}{\partial Y} f \cdot \frac{\partial}{\partial Y_0} Y(s, \Lambda) \, \mathrm{d}s$$

and differentiating again w.r.t. time t results in a homogeneous ODE for each component $S_{y_{k,0}}(t, \Lambda)$, namely

$$\dot{S}_{y_{k,0}}(t, \Lambda) = \sum_{l=1}^{M} \frac{\partial}{\partial y_l} f_k \cdot S_{y_{l,0}} \quad , \qquad \text{with} \qquad S_{y_{k,0}}(0, \Lambda) = \frac{\partial}{\partial y_{k,0}} y_{k,0} = 1 \quad . \tag{3.12}$$

The parameters of our analyzed models are supposed to represent physiological processes, and therefore bear physical dimensions. For example, m and $1/\tau$ are frequencies measured in [Hz], whereas c is measured in [mol/l]. Accordingly, $S_\tau = \mathrm{d}/\mathrm{d}\tau \, q_Z$ would be

measured in [Hz] and S_m in [s] (note that our model only consists of *one* ODE, which makes a second index superfluous). Normalization provides a comprehensive comparison between all sensitivities, even across models. For any parameter, the value λ_i fixed for a specific simulation is a natural choice. For any state variable, we chose its current value $y_k(t)$ at each point in time of the corresponding ODE solution. Hence, we normalize each sensitivity $S_{ik} = \mathrm{d}/\mathrm{d}\lambda\, y_k$ by multiplying it with the ratio $\lambda_i/y_k(t)$ to get the relative sensitivity

$$\tilde{S}_{ik} = S_{ik} \cdot \frac{\lambda_i}{y_k} \quad . \tag{3.13}$$

A relative sensitivity $\tilde{S}_{ik}$ thus quantifies the percentage change in the k–th state variable value per percentage change in the i–th parameter value. This applies accordingly to the second order sensitivity

$$\tilde{R}_{ijk} = R_{ijk} \cdot \frac{\lambda_i \cdot \lambda_j}{y_k} \quad . \tag{3.14}$$

It can be shown that this method is valid and mathematically equivalent to another common method in which the whole model is non–dimensionalized a priori [20]. A non–normalized model formulation has the additional advantage of usually allowing a more immediate appreciation and transparent access for experimentalists. In the remainder of this manuscript, we are always going to present and discuss relative sensitivity values normalized that way.

In our model, the specific case $M = 1$ applies, so equations (3.9) and (3.11) simplify to the case $k = 1$ (no summation).

3.4. Variance–Based Global Sensitivity Analysis

The differential sensitivity analysis above is called a local method, because it does not take the physiological range of parameter values into account. Additionally factoring in such ranges characterizes so–called global methods. The main idea behind most global methods is to include a statistical component to scan the whole parameter space $\mathcal{C}$. Thus they combine the percentage change in a state variable value per percentage change in a parameter value with the variability of all parameters. The parameter space $\mathcal{C}$ can be seen as a N–dimensional cuboid $\mathcal{C} = [\lambda_1^-; \lambda_1^+] \times \ldots \times [\lambda_N^-; \lambda_N^+]$, where λ_i^- and λ_i^+ are the minimum and maximum parameter values and N is the number of parameters. We can now fix a certain point $\hat{\Lambda} = (\hat{\lambda}_1, \ldots, \hat{\lambda}_N) \in \mathcal{C}$ and calculate the local gradient of the solution w.r.t. $\hat{\Lambda}$. The volume of the star–shaped area, investigated by changing only one parameter at once and lying within a ball around $\hat{\Lambda}$, vanishes in comparison to $\mathcal{C}$ for an increasing number of parameters [18]. For an overview of the numerous methods like ANOVA, FAST, Regression, or Sobol' Indexing, the reader is referred to [6, 19].

In this section we want to sketch the main idea of the variance–based sensitivity analysis approach as presented in [3], which is based on Sobol' Indexing. We chose this method, because of its transparency and low computational cost. This method aims at calculating two measurands for the sensitivity of a state variable w.r.t. parameter λ_i: the variance–based sensitivity function denoted by $VBS_i(t)$ and the total sensitivity index function denoted by $TSI_i(t)$. The VBS functions give a normalized first order sensitivity quite similar to $\tilde{S}$ from the previous section, but include the parameter range. The TSI functions, however, additionally include higher order sensitivities and give a measurand for interdependencies of parameter influences.

A recipe for calculating VBS and TSI is as follows: first of all, set boundaries for all model parameters, either by model assumptions or by literature reference, thus fixing

$\mathcal{C}$. Secondly, generate two sets of n sample points $\hat{\Lambda}_{1,j}, \hat{\Lambda}_{2,j} \in \mathcal{C},\ j = 1, ..., n$ suited to represent the underlying probability distribution of each parameter, in our case the uniform distribution. Thirdly, with i indicating a certain parameter, generate $2nN$ sets of new sample points $\hat{\Lambda}^i_{1,j}, \hat{\Lambda}^{\sim i}_{1,j},\ j = 1, ..., n,\ i = 1, ..., N$, where $\hat{\Lambda}^i_{1,j}$ consists of all sample points in $\hat{\Lambda}_{1,j}$ except for its i–th component (parameter value) replaced by the i–th component of $\hat{\Lambda}_{2,j}$. Consequently, $\hat{\Lambda}^{\sim i}_{1,j}$ consists of the i–th component of $\hat{\Lambda}_{1,j}$ and every other component taken from $\hat{\Lambda}_{2,j}$. Fourthly, evaluate the model from equation (3.6) at all of the $2n(N+1)$ sample points $\hat{\Lambda}_{1,j}, \hat{\Lambda}_{2,j}, \hat{\Lambda}^i_{1,j}, \hat{\Lambda}^{\sim i}_{1,j}$ resulting in a family of solutions.

For this family perform the following calculations:

1. Compute the variance of the family of all $2n(N+1)$ solutions as a function of time, namely $V(t)$. This variance function indicates the general model output variety throughout the whole parameter range.

2. Compute the variances V_i of the family of $n(N+1)$ solutions resulting from an evaluation of the model at all $\hat{\Lambda}_{1,j}$ and $\hat{\Lambda}^i_{1,j}$, i.e. for every j and i. Each $V_i(t)$ is a function of time and indicates the model output variety, if solely the value λ_i of the i-th parameter is changed.

3. Compute the variances $V_{\sim i}$ of the family of $n(N+1)$ solutions resulting from an evaluation of the model at all $\hat{\Lambda}_{1,j}$ and $\hat{\Lambda}^{\sim i}_{1,j}$, i.e. for every j and i. Each $V_{\sim i}(t)$ is a function of time and indicates the model output variety, if the value of λ_i is fixed, whereas all other parameter values are changed.

Note that the computations in [3] were conducted using Monte–Carlo integrals as an approximation. The VBS and TSI can be finally calculated as

$$VBS_i(t) = \frac{V_i(t)}{V(t)}, \qquad TSI_i(t) = 1 - \frac{V_{\sim i}(t)}{V(t)} \tag{3.15}$$

The normalization entails additional properties of VBS and TSI (see [3, Fig. 1]):

$$\sum_{i=1}^{N} VBS_i(t) \leq 1, \qquad \sum_{i=1}^{N} TSI_i(t) \geq 1 \tag{3.16}$$

In other words, $VBS_i(t)$ gives the normalized global first order sensitivity function of the solution w.r.t. λ_i in relation to the model output range. Accordingly, $TSI_i(t)$ quantifies a relative impact of the variability in parameter λ_i on the model output, factoring in the interdependent influence in combination with all other parameters' sensitivities. In [3] it was suggested to characterize the $TSI_i(t)$ value as the "importance" of λ_i.

3.5. An Analytical Example for Local Sensitivity Analysis Including a Link Between Zajac's and Hatze's Formulations

By further simplifying Zajac's activation dynamics (3.1), through assuming an deactivation boost $\beta = 1$ (activation and deactivation time constants are equal) and a basic activity $q_0 = 0$, we obtain a linear ODE for this specific case q_Z^{sp}, which is similar to Hatze's equation (3.2), modeling the time evolution of the free Ca^{2+} ion concentration:

$$\dot{q}_Z^{sp} = \frac{1}{\tau}(\sigma - q_Z^{sp}) \quad , \qquad q_Z^{sp}(0) = q_{Z,0} \quad . \tag{3.17}$$

By analyzing this specific case, we aim at making the above described sensitivity analysis method more transparent for the reader. Solving equation (3.17) analytically yields

$$q_Z^{sp}(t) = \sigma \cdot (1 - e^{-t/\tau}) + q_{Z,0} \cdot e^{-t/\tau}\,, \tag{3.18}$$

depending on just two parameters σ (stimulation: control parameter) and τ (time constant of activation: internal parameter) in addition to the initial value $y_0 = q_{Z,0}$. The solution $q_Z^{sp}(t)$ equals the σ value after about τ.

We apply the more generally applicable, implicit method (3.9),(3.12) to determine the derivatives of the solution w.r.t. the parameters (the sensitivities), although we already know the solution (3.18) in a closed form. Hence, for the transparency of our method, we calculate the gradient of the right hand side $f(q_Z^{sp}, \sigma, \tau)$ of the ODE (3.17)

$$\frac{\partial}{\partial q_Z^{sp}} f = -\frac{1}{\tau} \quad , \quad \frac{\partial}{\partial \sigma} f = \frac{1}{\tau} \quad \text{, and} \quad \frac{\partial}{\partial \tau} f = -\frac{\sigma - q_Z^{sp}}{\tau^2} = \frac{q_{Z,0} - \sigma}{\tau^2} e^{-t/\tau}$$

and insert these partial derivatives into equations (3.9) and (3.12). Solving the respective three ODEs for the three parameters (σ, τ, $q_{Z,0}$) and normalizing them according to (3.13) gives the relative sensitivities of q_Z^{sp} w.r.t. σ, τ, and $q_{Z,0}$ as functions of time (see Fig. 3.1):

$$\tilde{S}_\sigma(t) = (1 - e^{-t/\tau}) \cdot \frac{\sigma}{q_Z^{sp}(t)} = \frac{\sigma \cdot (e^{t/\tau} - 1)}{\sigma \cdot (e^{t/\tau} - 1) + q_{Z,0}} \quad , \tag{3.19}$$

$$\tilde{S}_\tau(t) = \left(\frac{(q_{Z,0} - \sigma) \cdot t}{\tau^2} e^{-t/\tau} \right) \cdot \frac{\tau}{q_Z^{sp}(t)} = \frac{t \cdot (q_{Z,0} - \sigma)}{\tau \cdot [\sigma \cdot (e^{t/\tau} - 1) + q_{Z,0}]} \quad \text{, and} \tag{3.20}$$

$$\tilde{S}_{q_{Z,0}}(t) = e^{-t/\tau} \cdot \frac{q_{Z,0}}{q_Z^{sp}(t)} = \frac{q_{Z,0}}{\sigma \cdot (e^{t/\tau} - 1) + q_{Z,0}} \quad . \tag{3.21}$$

One verifies immediately that the results are equivalent to taking the derivatives of q_Z^{sp} w.r.t. the occurring parameters, cf. the definition of sensitivity in Eqn. (3.8). A straightforward result is that the time constant τ has its maximum effect on the solution (Fig. 3.1: see $\tilde{S}_\tau(t)$) at time $t = \tau$. In case of a step in stimulation, the sensitivity $\tilde{S}_\tau(t)$ vanishes in the initial situation and exponentially approaches zero again after a few further multiples of the typical period τ. Note that $\tilde{S}_\tau(t)$ is negative, which means that an increase in τ decelerates activation. Thus, for a fixed initial value $q_{Z,0}$, the solution value $q_Z^{sp}(t)$ decreases at a given point in time, if τ is increased. After a step in stimulation σ, the time in which the solution $q_Z^{sp}(t)$ bears some memory of its initial value $q_{Z,0}$ is equal to the period of being non–sensitive to any further step in σ (compare $\tilde{S}_{q_{Z,0}}(t)$ to $\tilde{S}_\sigma(t)$ and (3.19) to (3.21)). After about $\tau/2$ the sensitivity $\tilde{S}_{q_{Z,0}}(t)$ has already fallen to about 0.1 and $\tilde{S}_\sigma(t)$ to about 0.9 accordingly.

3.6. The Numerical Approach and Results

Typically, biological dynamics are represented by non–linear ODEs. Therefore the linear ODE used for describing activation dynamics in the [27] case (3.1) is more of an exception. A closed–form solution can be given in (3.18), as shown in the previous section .

In general, however, non–linear ODEs used in biomechanical modeling, as the Hatze case (3.5) for describing activation dynamics, can only be solved numerically. It is understood that any explicit formulation of a model in terms of ODEs allows to provide the partial derivatives of their right hand sides f w.r.t. the model parameters in a closed form.

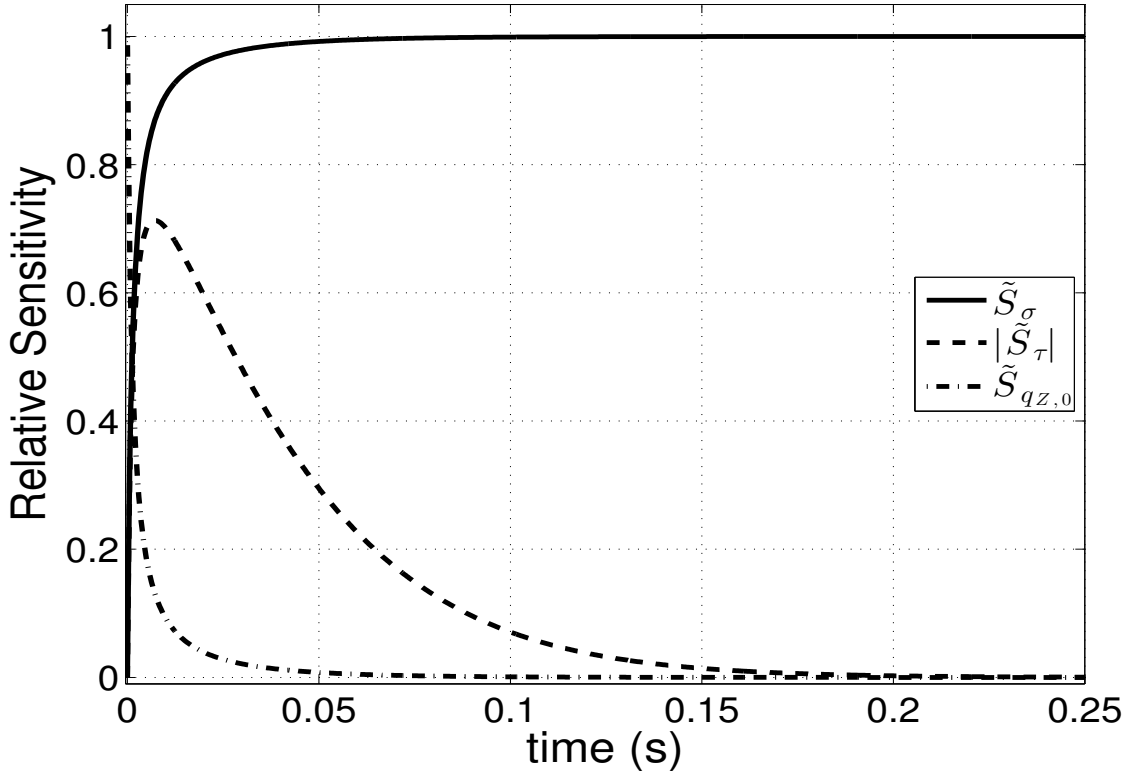

Figure 3.1.: Relative sensitivities $\tilde{S}_{\lambda_i}$ w.r.t. the three parameters in the simplified formulation (3.17) of Zajac's activation dynamics (3.1). Parameters: stimulation σ (see (3.19): solid line), activation time–constant τ (see (3.20): dashed line), and initial activation $q_{Z,0}$ (see (3.21): dash–dotted line). Note that $\tilde{S}_\tau$ is negative, but for reasons of comparability, we have plotted its absolute value. Parameter values are $\sigma = 1$, $\tau = 1/40\,\mathrm{s} = 0.025\,\mathrm{s}$, and $q_{Z,0} = 0.05$. Because the ODE (3.17) for q_Z^{sp} is equivalent to Hatze's ODE (3.2) for the free Ca^{2+}–ion concentration γ, we can identify the sensitivity of $1/\tau$ with that of m.

Fortunately, this is exactly what is required as part of the sensitivity analysis approach presented in Section 3.3, in particular in equation (3.9).

As an application for this approach, we will now present a comparison of both formulations of activation dynamics. The example indicates that the approach may be of general value because it is common practice in biomechanical modeling to formulate the ODEs in closed form and integrate the ODEs numerically. Adding further sensitivity ODEs for model parameters then becomes an inexpensive enhancement of the procedure used to solve the problem anyway.

For the two different activation dynamics from [27] and [10], the parameter sets Λ_Z and Λ_H, respectively, consist of

$$\Lambda_Z = \{\, q_{Z,0},\, \sigma,\, q_0,\, \tau,\, \beta \,\} \quad , \tag{3.22}$$

$$\Lambda_H = \{\, q_{H,0},\, \sigma,\, q_0, m,\, \rho_c,\, \nu,\, \ell_\rho,\, \ell_{CErel} \,\} \quad , \tag{3.23}$$

including the initial conditions. The numerical solutions for these ODEs were computed within the MATLAB environment (The MathWorks, Natick, USA; version R2013b), using the pre–implemented numerical solver *ode*45, which is a Runge–Kutta algorithm of order 5 (for details see [2]).

3.6.1. Results for Zajac's Activation Dynamics: Sensitivity Functions

We simulated activation dynamics for the parameter set Λ_Z (3.22) leaving two of the values constant ($q_0 = 0.005$, $\tau = \frac{1}{40}\,s$) and varying the other three (initial condition $q_{Z,0}$, stimulation σ, and deactivation boost β). The time courses of the relative sensitivities $\tilde{S}_i(t)$ w.r.t. all parameters $\lambda_i \in \Lambda_Z$ are plotted in Fig. 3.2. In the left column of Fig. 3.2 we used $\beta = 1$, in the right column $\beta = 1/3$. Pairs of the parameter values $q_0 = 0.005 \leq q_{Z,0} \leq 0.5$ and $0.01 \leq \sigma \leq 1$ are specified in the legend of Fig. 3.2, with increasing values of both parameters from top to bottom.

Relative sensitivity $\tilde{S}_{q_0}$: Solutions are non–sensitive to the q_0 choice, except the case that initial activity and stimulation (also approximating the final activity if $\beta = 1$ and $\sigma >> q_0$) are very low, i.e. nearby q_0 itself.

Relative sensitivity $\tilde{S}_{q_{Z,0}}$: The memory (influence on solution) of the initial value is lost after about 2τ, almost independently of all other parameters. This loss in memory is obviously slower than in the case from Section 3.5, see Fig. 3.1). In that extreme case, the influence (relative sensitivity) of the lowest possible initial value ($q_{Z,0} = 0$) on the most rapidly increasing solution (maximum possible final value: $\sigma = 1$) is lost earlier.

Relative sensitivity $\tilde{S}_\tau$: The influence of the time constant τ on the solution is reduced with decreasing difference between initial and final activity values (compare maximum $\tilde{S}_\tau$ values in Figs. 3.1 and 3.2) and, no matter the β value, with compound raised levels of initial activity $q_{Z,0}$ and σ, the latter determining the final activity value if $\beta = 1$. When deactivation is slower than activation ($\beta < 1$: right column in Fig. 3.2), $\tilde{S}_\tau$ is higher than in the case $\beta = 1$, both in its maximum amplitude and for longer times after the step in stimulation, especially at low activity levels (upper rows in Fig. 3.2).

Relative sensitivity $\tilde{S}_\sigma$: Across all parameters, the solution in general is most sensitive to σ. However, the influence of the deactivation boost parameter β is usually comparable. In some situations, this also applies for the activation time constant τ (see below). For $\beta = 1$ (Fig. 3.2, left), the solution becomes a little less sensitive to σ with decreasing activity level ($\tilde{S}_\sigma < 1$), which reflects that the final solution value is not determined by σ alone, but by q_0 and β as much. If deactivation is much slower than activation ($\beta = 1/3 < 1$: Fig. 3.2, right), we find the opposite to the $\beta = 1$ case : the more the activity level rises, the lesser σ determines the solution. Additionally, stimulation σ somehow competes with both deactivation boost β and time constant τ (see further below). Using the term "compete" illustrates the idea that any single parameter should have an individual interest in influencing the dynamics as much as possible in order not to be considered superfluous.

Relative sensitivity $\tilde{S}_\beta$: Sensitivity w.r.t β generally decreases with increasing activity $q_{Z,0}$ and stimulation σ levels. It vanishes at maximum stimulation $\sigma = 1$.

Relative sensitivities $\tilde{S}_\sigma$, $\tilde{S}_\beta$, $\tilde{S}_\tau$: At sub–maximal stimulation levels $\sigma < 1$, the final solution value is determined to almost the same degree by stimulation σ and deactivation boost β, yet with opposite tendencies ($\tilde{S}_\sigma > 0$, $\tilde{S}_\beta < 0$). As explained, both parameters compete for their impact on the final solution value. Only at maximum stimulation ($\sigma = 1$, lowest row in Fig. 3.2), this parameter competition is resolved in favor of σ. In this specific case, β does not influence the solution at all. For $\beta = 1$ the competition about

influencing the solution is intermittently, but only slightly biased by τ: sensitivity $\tilde{S}_\tau$ peaks at comparably low magnitude around $t = \tau$. This τ influence comes likewise intermittently at the cost of β influence: the absolute value of $\tilde{S}_\beta$ rises a little slower than $\tilde{S}_\sigma$. In the case $\beta < 1$, this competition becomes more differentiated and spread out in time. Again at sub–maximal stimulation and activity levels, the absolute value of $\tilde{S}_\tau$ is lower than that of $\tilde{S}_\sigma$ but higher than that of $\tilde{S}_\beta$, making all three parameters σ, β, and τ compete to comparable degrees for an impact on the solution until about $t = 4\tau$. Also, $\tilde{S}_\tau$ does not vanish before about $t = 10\tau$.

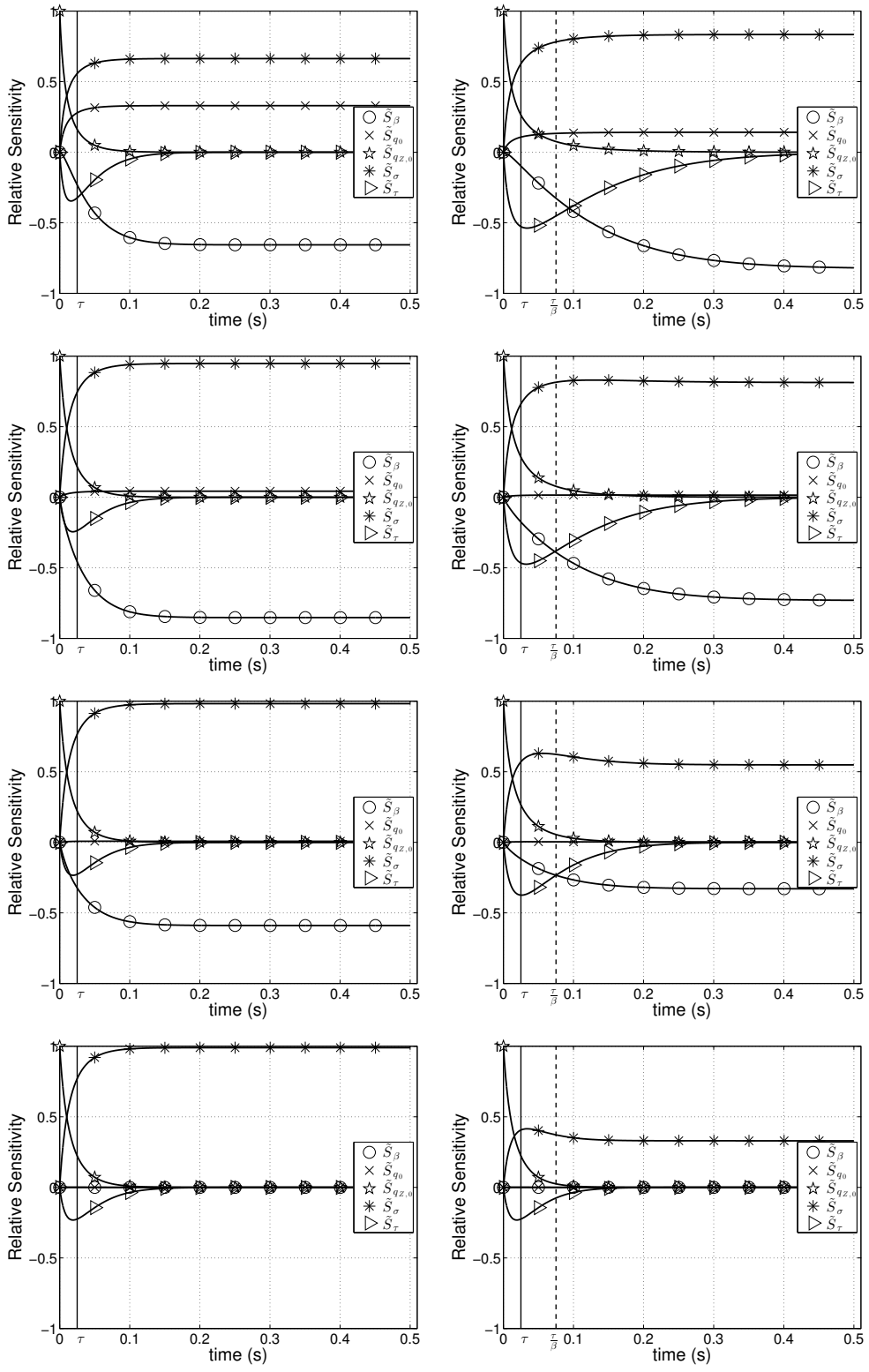

Figure 3.2.: Relative sensitivities $\tilde{S}_{\lambda_i}$ w.r.t. all parameters $\lambda_i \in \Lambda_Z$ from (3.22) in Zajac's activation dynamics (3.1). Parameter values varied from top (i) to bottom (iv) row: (i) $q_{Z,0} = q_0 = 0.005$, $\sigma = 0.01$, (ii) $q_{Z,0} = 0.05$, $\sigma = 0.1$, (iii) $q_{Z,0} = 0.2$, $\sigma = 0.4$, (iv) $q_{Z,0} = 0.5$, $\sigma = 1$; left column: $\beta = 1$, right column: $\beta = 1/3$.

3.6.2. Results for Hatze's Activation Dynamics: Sensitivity Functions

We also simulated activation dynamics for the parameter set Λ_H (3.23), leaving now four of the values constant ($q_0 = 0.005$, $m = 10\,\mathrm{s}$, $\ell_\rho = 2.9$, $\ell_{CErel} = 1$) and again varying three others (initial condition $q_{Z,0}$, stimulation σ, and non–linearity ν), keeping in mind that the eighth parameter (ρ_c) is assumed to depend on ν. Time courses of the relative sensitivities $\tilde{S}_i(t)$ w.r.t. all parameters $\lambda_i \in \Lambda_H$ are plotted (see Fig. 3.3). In the left column of Fig. 3.3, $\nu = 2$, $\rho_c = 9.10$ is used, in the right column $\nu = 3$, $\rho_c = 7.24$. Here, the same pairs of parameter values ($q_0 = 0.005 \leq q_{Z,0} \leq 0.5$ and $0.01 \leq \sigma \leq 1$, increasing from top to bottom; see legend of Fig. 3.3) are used as in the previous Section 3.6.1, see Fig. 3.2 (author's note: as seen in Chapter 2 Remark 2.2.2, choosing $q_{Z,0} = q_0$ would lead to a numeric instability. Therefore, we used $q_{Z,0} = q_0 + eps$, where $eps = 2^{-52} \approx 2 \cdot 10^{-16}$ is a pre–implemented MATLAB variable).

Hatze's activation dynamics (3.5) are non–linear unlike Zajac's activation dynamics (3.1). This non–linearity manifests particularly in a changeful influence of the parameter ν. Additionally, the parameter m is hardly comparable to the inverse of the exponential time constant τ in Zajac's linear activation dynamics.

Relative sensitivity $\tilde{S}_m$: In Zajac's linear differential equation (3.1), τ establishes a distinct time scale, which is independent of all other parameters. The parameter m in Hatze's activation dynamics (3.5) is just formally equivalent to the reciprocal of τ: the sensitivity $\tilde{S}_m$ does not peak stringently at $t = 1/m = 0.1\,\mathrm{s}$ but rather diffusely between about $0.05\,\mathrm{s}$ and $0.1\,\mathrm{s}$ in both of the cases $\nu = 2$ and $\nu = 3$. This may at first be not surprising, because the scaling factor in Hatze's dynamics is $\nu \cdot m$ rather than just m. However, $\nu \cdot m$ does neither fix an invariant time scale for Hatze's non–linear differential equation. This fact becomes particularly prominent at extremely low activity levels for $\nu = 2$ (Fig. 3.3, left, top row) and up to moderately sub–maximal activity levels for $\nu = 3$ (Fig. 3.3, right, top two rows). Here, $\tilde{S}_m$ is negative, which means that increasing the parameter m results in less steeply increasing activity. This observation is counter–intuitive to identifying m with a reciprocal of a time constant like τ. Rather than expected from the product $\nu \cdot m$, the exponent ν does not linearly scale the time behavior, because $\tilde{S}_m$ peaks do not occur systematically earlier in the $\nu = 3$ case as compared to $\nu = 2$.

Relative sensitivity $\tilde{S}_{q_{H,0}}$: Losing the memory of the initial condition confirms the analysis of time behavior based on $\tilde{S}_m$. At high activity levels (Fig. 3.3, bottom row), Hatze's activation dynamics lose memory at identical time horizons (no matter the ν value) seemingly slower for higher ν at intermediate levels (Fig. 3.3, two middle rows), and faster at very low levels (Fig. 3.3, top row). The parameter m still does roughly determine the time horizon in which the memory of the initial condition $q_{H,0}$ is lost and the influence of all other parameters is continuously switched on from zero influence at $t = 0$.

Relative sensitivity $\tilde{S}_{q_0}$: As in Zajac's dynamics the solution is generally only sensitive to q_0 at very low stimulation levels $\sigma \approx q_0$ (Fig. 3.3, top row). At such levels, the $\nu = 3$ case shows the peculiarity that the solution becomes strikingly insensitive to any other parameter than q_0 itself (and $q_{H,0}$). The time evolution of the solution is more or less determined by just this minimum (q_0) and initial ($q_{H,0}$) activities, and m determining the approximate switching time horizon between both. The ℓ_{CE} dependency, constituting a crucial property of Hatze's activation dynamics, is practically suppressed for $\nu = 3$ at very low activities and stimulations. In contrast, for $\nu = 2$, the sensitivity $\tilde{S}_{\ell_{CErel}}$ remains on

a low, but still significant level of about a fourth of the three dominating quantities $\tilde{S}_{q_0}$, $\tilde{S}_{q_{H,0}}$, and $\tilde{S}_\nu$.

Relative sensitivity $\tilde{S}_\nu$: The sensitivity w.r.t. ν is extraordinarily high at low activities and stimulations around 0.1, both for $\nu = 2$ and $\nu = 3$ (Fig. 3.3, second row from top), and at extremely low levels for $\nu = 2$ (Fig. 3.3, left, top row). At moderately sub–maximal levels (Fig. 3.3, third row from top), the solution is influenced with an already inverted tendency ($\tilde{S}_\nu$ changes sign to positive) after around an $1/m$ time horizon for $\nu = 2$. However, at these levels the solution is practically insensitive to ν for any ν. At high levels (Fig. 3.3, bottom row), we find that there is no change in the character of time evolution of the solution, despite the specific value of ν. The degree of non–linearity ν is unimportant, because the time evolution and the ranking of all other sensitivities is hardly influenced by ν. In both cases, the rise in activity is quickened by increasing ν ($\tilde{S}_\nu > 0$), as opposed to low activity and stimulation levels, where rises in activity are slowed down ($\tilde{S}_\nu < 0$; see also above).

Relative sensitivities $\tilde{S}_\sigma$, $\tilde{S}_{\rho_c}$, $\tilde{S}_{\ell_{CErel}}$, $\tilde{S}_{\ell_\rho}$: Of all the remaining parameters, i.e. stimulation σ, scaled maximum free Ca^{2+} ion concentration ρ_c, relative CE length ℓ_{CErel}, and the pole ℓ_ρ of the length dependency in Hatze's activation dynamics, the latter has the lowest influence on the solution. The influence characters of all four parameters are yet completely identical. Their sensitivities are always positive and coupled by fixed scaling ratios, because all of them occurring within just one product on the right side of (3.5). The values of $\tilde{S}_\sigma$ and $\tilde{S}_{\rho_c}$ are identical, while the sensitivity w.r.t. ℓ_{CErel} is the highest, with a ratio $\tilde{S}_{\ell_{CErel}}/\tilde{S}_{\ell_\rho} \approx 3$ and $\tilde{S}_{\ell_{CErel}}/\tilde{S}_\sigma \approx 1.2$. Except at very low activity (where q_0 plays a dominating role) and except for the generally changeful ν influence, these are the four parameters that dominate the solution after an initial phase in which the initial activity $q_{H,0}$ determines its evolution. The parameter m does not have a strong direct influence on the solution. As stated above, it defines the approximate time horizon at which the $q_{H,0}$ influence gets lost.

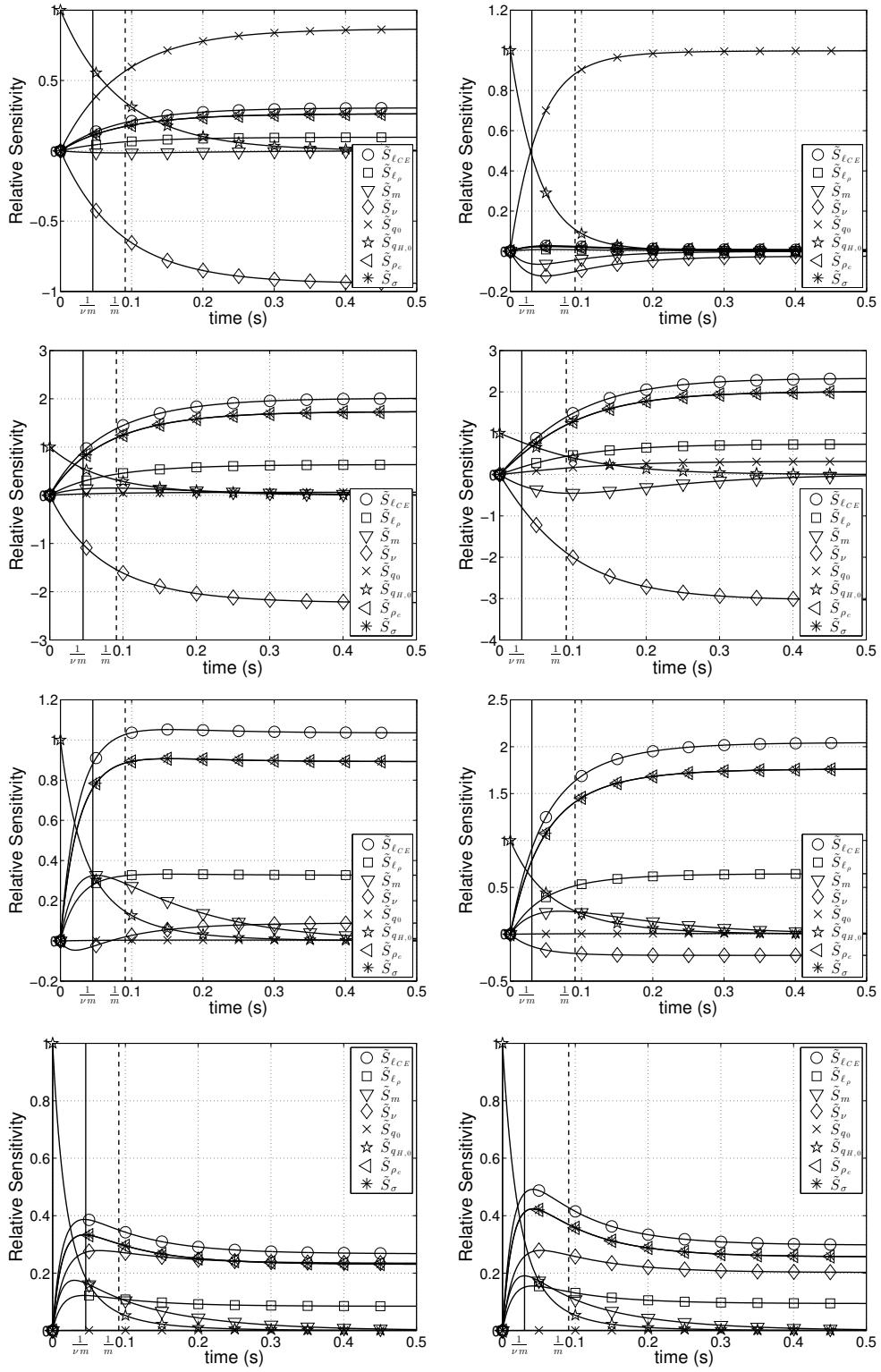

Figure 3.3.: Relative sensitivities $\tilde{S}_{\lambda_i}$ w.r.t. all parameters $\lambda_i \in \Lambda_H$ from (3.23) in Hatze's activation dynamics (3.5). Parameter values varied from top (i) to bottom (iv) row: (i) $q_{H,0} = q_0 = 0.005$, $\sigma = 0.01$, (ii) $q_{H,0} = 0.05$, $\sigma = 0.1$, (iii) $q_{H,0} = 0.2$, $\sigma = 0.4$, (iv) $q_{H,0} = 0.5$, $\sigma = 1$; left column: $\nu = 2$, $\rho_c = 9.10$, right column: $\nu = 3$, $\rho_c = 7.24$.

3.6.3. Variance–Based Sensitivity (VBS) and Total Sensitivity Indices (TSI) for Zajac's and Hatze's Activation Dynamics

Table 3.1 pools the lower and upper boundaries for every parameter in Λ_Z and Λ_H used in our calculations. We refer to [7, 9, 27] for the traceability of our choices.

Table 3.1.: Lower and upper bounds for the parameter choices in both Zajac's and Hatze's model of activation dynamics.

Parameter	β	ℓ_{CErel}	ℓ_p	m	ν	q_0	$q_{Z,0}, q_{H,0}$	ρ_c	σ	τ
Lower bound	0.1	0.4	2.2	3	1.5	0.001	0.01	4	0	0.01
Upper bound	1	1.6	3.6	11	4	0.05	1	11	1	0.05

The left hand side of Fig. 3.4 shows the VBS functions for every parameter in Λ_Z of Zajac's model. The plotted functions can be compared to our previously computed relative first order sensitivity functions from Fig. 3.2: at first sight, $\tilde{S}_{q_{Z,0}}$ and $VBS_{q_{Z,0}}$ look equal, but the VBS function indicates a slightly increased duration of influence of $q_{Z,0}$. Regarding τ, the VBS function peaks at the same time as $\tilde{S}_\tau$, but with a smaller amplitude. Likewise, the courses of VBS_σ and VBS_β are comparable to $\tilde{S}_\sigma$ and $\tilde{S}_\beta$ from the second and third row of Fig. 3.2. The calculated VBS functions in the Zajac case show what would be expected intuitively: a VBS represents a parameter's mean influence averaged over its range of values. Additionally, we plotted the sum of all first order sensitivities. This sum indicates which amount of the total variance is covered by first order sensitivities. The closer the sum comes to 1, the smaller the impact of second and higher order sensitivities gets.

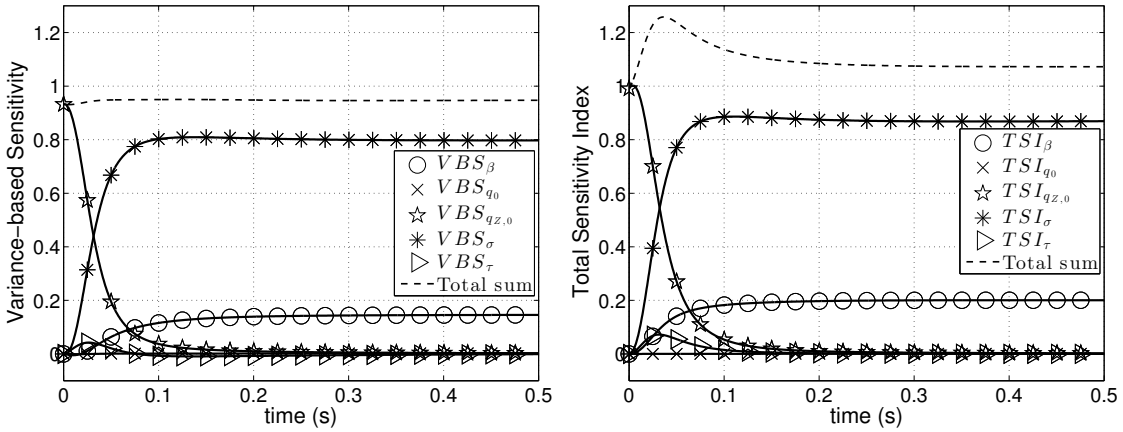

Figure 3.4.: Variance–based sensitivity (left) and total sensitivity index (right) of every parameter of Zajac's activation dynamics equation

The right hand side of Fig. 3.4 shows the TSI functions for every parameter in Λ_Z of Zajac's model. Generally, there are only minor deviations of the TSI_i functions from their counterparts VBS_i. That is, the influence of none of the parameters is significantly enhanced by an interdependent effect in combination with other parameters. According to both analyses, there are just four globally important parameters that govern the system's state throughout the whole examined solution space: the initial condition $q_{Z,0}$ within a typical time horizon τ after a step in σ, the new stimulation level σ determining activity

after about τ, the deactivation boost β with smaller impact than σ, and τ determining the time horizon itself.

The left hand side of Fig. 3.5 shows the VBS functions for every parameter in Λ_H of Hatze's model. Very similar to the Zajac case, the calculated VBS seemingly represent to a high degree a parameter's mean influence averaged over its range of values (compare Fig. 3.3). As in the Zajac case, there are four globally important parameters, according to both VBS and TSI analyses. Compared to Zajac's model, the interdependent effect in combination with other parameters (TSI: right hand side of Fig. 3.5) is more pronounced for two parameters: both the stimulation σ and the CE length ℓ_{CE} importances are distinctly higher than their first order effects as expressed by VBS functions. Furthermore, the time horizon, within the initial condition $q_{H,0}$ has an after–effect in response to a step in σ. This horizon is globally a little higher in VBS as compared to local sensitivity analysis (Fig. 3.3). In addition, the time horizon of $q_{H,0}$ is enhanced by interdependencies with other parameters (TSI: right hand side of Fig. 3.5).

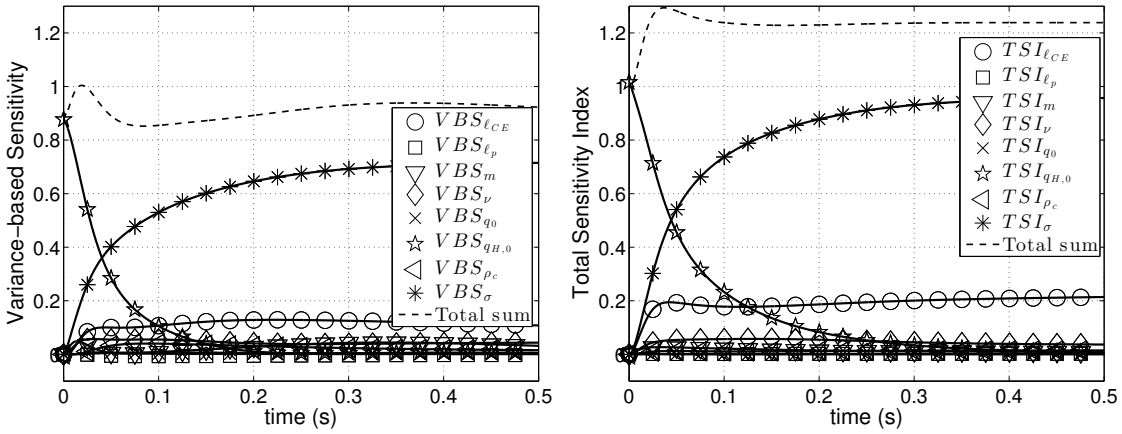

Figure 3.5.: Variance–based sensitivity (left) and total sensitivity index (right) of every parameter of Hatze's activation dynamics equation

Altogether, VBS versus TSI analysis substantiate local first and second order sensitivity analyses: for one thing, Hatze's model is more inert against steps in stimulation than Zajac's model. Furthermore, the dynamics described by Hatze's model incorporates stronger non–linear coupling effects from combinations of parameters than Zajac's model. These latter effects are better seen in detail, when looking at local sensitivities, i.e. analyzing only small and selected volumes of the parameter space $\mathcal{C}$. In turn, VBS and TSI provide a broad, but coarse overview about first and higher order sensitivities of all parameters.

3.7. Consequences, Discussion, Conclusions

3.7.1. A Bottom Line for Comparing Zajac's and Hatze's Activation Dynamics: Second Order Sensitivities

At first sight, Zajac's activation dynamics [27] is more transparent, because it is descriptive in a sense that it captures the physiological behavior of activity rise and fall in an apparently simple way. It thereto utilizes a linear differential equation with well–known properties, allowing for a closed–form solution. It needs only four parameters to describe

the Ca^{2+} ion influx to the muscle as a response to electrical stimulation: the stimulation σ itself as a control parameter, the time constant τ for an exponential response to a step increase in stimulation, a third parameter β (deactivation boost) biasing both the rise and fall times and the saturation value $q_Z|^{\infty}$ of activity, which in turn depends on σ and the basic activity q_0 being the fourth parameter. The smaller $\beta < 1$ (deactivation slower than activation), the faster the activity level $q_Z|^{\infty}_{\beta=1} = q_0 + \sigma \cdot (1 - q_0)$ is reached, at which saturation would occur for $\beta = 1$. Saturation for $\beta < 1$ occurs at a level $q_Z|^{\infty}_{\beta} = q_0 + (1 - q_0)/(1 - \beta + \beta/\sigma)$ that is higher than $q_Z|^{\infty}_{\beta=1}$. Altogether, in Zajac's activation dynamics, the outcome of setting a control parameter value σ, with regard to how fast and at which level the activity saturates, seems easier to be handled by a controller, compared to Hatze's formulation.

A worse controllability of Hatze's activation dynamics [10] may be expected from its non–linearity, a higher number of parameters, and their interdependent influence on model dynamics. Additionally, Hatze's formulation depends on the CE length ℓ_{CE}, which makes the mutual coupling of activation with contraction dynamics more interwoven. So, at first sight, Hatze's dynamics seem a less manageable construct for a controller to deal with a muscle in terms of a biological actuator. Regarding the non–linearity exponent ν, solution sensitivity further depends non–monotonously on activity level, partly even with the strongest influence, partly without any influence. We also found that the solution is more sensitive to its parameters σ, ℓ_{CErel}, ℓ_ρ than is Zajac's activation dynamics to any of its parameters.

This higher complexity of Hatze's dynamics becomes even more evident by analyzing the second order sensitivities (see (3.10), or (3.14) for their relative values). They express how a first order sensitivity changes upon variation of any other model parameter. In other words, they are a measure of model entanglement and complexity. Here, we found that the highest values among all relative second order sensitivities in Zajac's activation dynamics are about -0.8 ($\tilde{R}_{\beta\,\sigma}$) and 1.6 ($\tilde{R}_{\beta\,\beta}$). In Hatze's activation dynamics, the highest relative second order sensitivities are those with respect to ν or ℓ_{CErel} (in particular for σ, ρ_c and ν, ℓ_{CErel} themselves) with maximum absolute values between about -8.0 ($\tilde{R}_{\ell_{CErel}\,\nu}$, $\tilde{R}_{\nu\,\rho_c}$) and 13.4 ($\tilde{R}_{\ell_{CErel}\,\ell_{CErel}}$, $\tilde{R}_{\ell_{CErel}\,\rho_c}$, $\tilde{R}_{\ell_{CErel}\,\sigma}$, $\tilde{R}_{\nu\,\nu}$ at sub–maximal activity). That is, they are an order of magnitude higher than in Zajac's activation dynamics.

Despite this result, we have to acknowledge that Hatze's activation dynamics contains crucial physiological features that go beyond Zajac's description.

3.7.2. A Plus for Hatze's Approach: Length Dependency

It has been established that the length dependency of activation dynamics is both physiological [14] and functionally vital [12], because it largely contributes to low–frequency muscle stiffness. It has also been verified, that Hatze's model approach provides a good approximation to experimental data [14]. In that study, $\nu = 3$ was used without comparing to the $\nu = 2$ case. There seem to be arguments in favor of $\nu = 2$ from a mathematical point of view. Especially, the less changeful scaling of the activation dynamics' characteristics down to very low activity and stimulation levels, at which some CE length sensitivity remains, seem to be an advantage, when being compared to the $\nu = 3$ case. Up to this point, we have argued solely mathematically. However, the eventual aim is physiological reality. We therefore repeated the model fit done by [14], while now allowing a variation in ν and in force–length relations.

3.7.3. An Optimal Parameter Set for Hatze's Activation Dynamics Plus CE Force–Length Relation

Sensitivity analysis allows to rate Hatze's approach as an entangled construct. Additionally, [14] decided to choose $\nu = 3$ without giving a reason for discarding $\nu = 2$. It further seemed that they did not perform an algorithmic optimization across various sub–maximal stimulation levels to find a muscle parameter set, which works best for known shifts $\Delta\ell_{CE,opt,submax} = \ell_{CE,opt} - \ell_{CE,opt,submax}$ in optimal, sub–maximal CE length $\ell_{CE,opt,submax}$ at which isometric force $F_{isom} = F_{isom}(q, \ell_{CE})$ peaks. Accordingly, it seemed worth to perform such an optimization, because F_{isom} generally depends on length ℓ_{CE} and activity q, and the latter may be additionally biased by an ℓ_{CE}–dependent capability for building up cross–bridges at a given level γ of free Ca^{2+} ions in the sarcoplasma, as formulated in Hatze's approach: $F_{isom}(q, \ell_{CE}) = F_{max} \cdot q(\gamma, \ell_{CE}) \cdot F_\ell(\ell_{CE})$. Thus, a shift in optimal CE length $\Delta\ell_{CE,opt,submax}$ with changing γ can occur depending on the specific choices of both the length–dependency of activation $q(\gamma, \ell_{CE})$ (see (3.3),(3.4)) and the CE's force–length relation $F_\ell(\ell_{CE})$.

Consequently, we searched for optimal parameter sets of Hatze's activation dynamics in combination with two different force–length relations $F_\ell(\ell_{CE})$: either a parabola [14] or bell–shaped curves [7, 17]. For a given optimal CE length $\ell_{CE,opt} = 14.8\,\text{mm}$ [22] representing a rat gastrocnemius muscle and three fixed exponent values $\nu = 2, 3, 4$ in Hatze's activation dynamics (all other parameters as given in Section 3.2), we thus determined Hatze's constant ρ_0 and the width parameters of the two different force–length relations $F_\ell(\ell_{CE})$ ($WIDTH$ in [14, 26] and $\Delta W_{asc} = \Delta W_{des} = \Delta W$ in [17], respectively) by an optimization approach. The objective function to be minimized was the sum of squared differences between the $\Delta\ell_{CE,opt,submax}$ values as predicted by the model and as derived from experiments (see [14, Table 2]) over five stimulation levels $\sigma \in \{0.55, 0.28, 0.22, 0.17, 0.08\}$. Note that $\gamma = \sigma$ applies in the isometric situation (see (3.2) and compare (3.3)). Further note that experimental data for muscle contractions at very low stimulation levels are missing in literature so far: the lowest analyzed level available for [14] was $\sigma = 0.08$, i.e. comparable to the second rows from top in Figs. 3.2 and 3.3.

The optimization results are summarized in Table 3.2. The higher the ν value, the smaller the optimization error. The predicted width values $WIDTH$ or ΔW, respectively, decrease along with the error. We would yet tend to exclude the case $\nu = 4$, because the predicted width values seem unrealistically low when compared to published values from other sources (e.g., $WIDTH = 0.56$ [26], $\Delta W = 0.35$ [17]). Furthermore, ρ_0 decreases with ν using the parabola model for $F_\ell(\ell_{CE})$ whereas it saturates between $\nu = 3$ and $\nu = 4$ for the bell–shaped model. The bell–shaped model shows the most realistic ΔW in the case $\nu = 3$ ($\Delta W = 0.32$). Fitting the same model to other contraction modes of the muscle [17], a value of $\Delta W = 0.32$ had been found. In contrast, when using the parabola model, realistic $WIDTH$ values between 0.5 and 0.6 are predicted by our optimization for $\nu = 2$.

When comparing the optimized parameter values across all start values of the $F_\ell(\ell_{CE})$ widths, across all ν values, and across both $F_\ell(\ell_{CE})$ model functions, we find that the resulting optimal parameter sets are more consistent for bell–shaped $F_\ell(\ell_{CE})$ than for the parabola function. The bell–shaped force–length relation gives generally a better fit. For each single ν value, the corresponding optimization error is smaller, when comparing realistic, published $WIDTH$ and ΔW values that may correspond to each other ($WIDTH = 0.56$ [26] and $\Delta W = 0.35$ [17]). Additionally, the error values from our optimizations are generally smaller than the corresponding value calculated from [14, Table 2] (0.23 mm).

Summarizing, we would say that the most realistic model for the isometric force F_{isom} at sub–maximal activity levels is the combination of Hatze's approach for activation dynamics with $\nu = 3$ and a bell–shaped curve for the force–length relation $F_\ell(\ell_{CE})$ with $\nu_{asc} = 3$. As a side effect, we predict that the parameter value ρ_0, being a weighting factor of the first addend in the compact formulation of Hatze's activation dynamics (3.5), should be reduced by about 40% ($\rho_0 = 3.25 \cdot 10^4\,\mathrm{l/mol}$), compared to the value originally published in [11] ($\rho_0 = 5.27 \cdot 10^4\,\mathrm{l/mol}$).

Table 3.2.: Parameters minimizing the sum over five sub–maximal isometric stimulation levels $\gamma = \sigma \in \{0.55, 0.28, 0.22, 0.17, 0.08\}$ of squared differences between shifts in optimal CE length $\Delta\ell_{CE,opt,submax}(\gamma)$ ($\Delta l_{MA,opt}$ by Roszek et al. (1994) [14, Table 2, third column]) at these levels. The parameters were predicted by the isometric force model $F_{isom}(q, \ell_{CE}) = F_{max} \cdot q(\gamma = \sigma, \ell_{CE}) \cdot F_\ell(\ell_{CE})$ and by experiments; simulated data represent a rat gastrocnemius muscle with an optimal CE length $\ell_{CE,opt} = 14.8\,\mathrm{mm}$ [22]; start value of ρ_0 was $6.0 \cdot 10^4\,\mathrm{l/mol}$; the exponents of the bell–shaped force–length relations $F_\ell(\ell_{CE})$ were fixed according to [17] ($\nu_{asc} = 3$, $\nu_{des} = 1.5$), the corresponding width values in the ascending and descending branch were assumed to be equal: $\Delta W_{asc} = \Delta W_{des} = \Delta W$; [26] and [14] used a parabola for $F_\ell(\ell_{CE})$; for all other model parameters see Sections 3.7.3 and 3.2; optimization was done by *fminsearch* (Nelder–Mead algorithm) in MATLAB with error tolerances of 10^{-8}; *error* is the square–root of the above mentioned sum divided by five; corresponding error value given in [14, Table 2] was 0.23 mm.

ν	bell–shaped [7, 17]			parabola [14, 26]		
	$\Delta W_{start} = 0.25$			$WIDTH_{start} = 0.46$		
	ΔW []	ρ_0 [10^4 l/mol]	*error* [mm]	$WIDTH$ []	ρ_0 [10^4 l/mol]	*error* [mm]
2	0.46	3.80	0.08	0.63	8.78	0.10
3	0.32	3.25	0.05	0.41	5.45	0.07
4	0.26	3.20	0.02	0.34	4.60	0.05
	$\Delta W_{start} = 0.35$			$WIDTH_{start} = 0.56$		
	ΔW []	ρ_0 [10^4 l/mol]	*error* [mm]	$WIDTH$ []	ρ_0 [10^4 l/mol]	*error* [mm]
2	0.45	3.80	0.07	0.53	6.92	0.11
3	0.32	3.30	0.05	0.41	5.67	0.07
4	0.26	3.20	0.02	0.34	4.55	0.05
	$\Delta W_{start} = 0.45$			$WIDTH_{start} = 0.66$		
	ΔW []	ρ_0 [10^4 l/mol]	*error* [mm]	$WIDTH$ []	ρ_0 [10^4 l/mol]	*error* [mm]
2	0.45	3.78	0.07	0.55	7.35	0.11
3	0.32	3.25	0.05	0.41	5.35	0.07
4	0.26	3.20	0.02	0.34	4.56	0.05

3.7.4. A Generalized Method for Calculating Parameter Sensitivities

The findings in the last section were initiated by thoroughly comparing two different biomechanical models of muscular activation, using a systematic sensitivity analysis as introduced in [5] and [16], respectively. Starting with the latter formulation, [21] calculated specific parameter sensitivities for muscular contractions. They applied three variants of this method:

Method 1 applies to state variables that are explicitly known to the modeler as in an eye model [16], a musculo–skeletal model for running that includes a Hill–type muscle

model [21], or the activation models analyzed in our study. [21] calculated the change in the value of a state variable averaged over time per a finite change in a parameter value, both normalized to each of their unperturbed values. They thus calculated just one (mean) sensitivity value for a finite time interval (e.g. a running cycle) rather than time–continuous sensitivity functions.

Method 2: Whereas [5] and [16] had introduced the full approach for calculating such sensitivity functions, [21] distorted this approach by suggesting that the partial derivative of the right hand side of an ODE, i.e. of the *rate of change* of a state variable, w.r.t. a model parameter would be a "model sensitivity". The distortion becomes explicitly obvious from our formulation: this partial derivative is just one of two addends that contribute to the rate of change of the sensitivity function (3.9), rather than it defines the sensitivity of the state variable itself (i.e. the solution of the ODE) w.r.t. a model parameter (3.8).

Method 3: [21] also asked for calculating the influence of a parameter of the activation dynamics (like the time constant) on an arbitrary joint angle, i.e. a variable that quantifies the overall output of a coupled dynamical system. Of course, the time constant does not explicitly appear in the mechanical differential equation for the acceleration of this very joint angle, which renders applicability of Method 2 impossible. The conclusion in [21] was to apply Method 1. Here, the potential of our formulation comes particularly to the fore. It enables the user to calculate the time–continuous sensitivity of all components of the coupled solution, i.e. any state variable $y_k(t, \Lambda)$. This is because all effects of a parameter change are in principle reflected within *any* single state variable, and the time evolution of a sensitivity according to (3.9) takes this into account.

We have further worked out the sensitivity function approach by [16], presenting the differential equations for sensitivity functions in more detail to those modelers, who want to apply the method. Furthermore, we enhanced the approach by [16] to also calculating the sensitivities of the state variables w.r.t. their initial conditions (3.12). This should be helpful not only in biomechanics but also, for example, in meteorology, when predicting the behavior of storms [15]. Since initial conditions are often just known approximately but start with the relative sensitivity values of 1, their influence should be traced to verify how their uncertainty propagates during a simulation. In the case of muscle activation dynamics, the sensitivities $\tilde{S}_{q_{Z,0}}$ and $\tilde{S}_{q_{H,0}}$, respectively, decreased rapidly to zero: initial activity has no effect on the solution very early before steady state is reached.

Moreover, we included a second order sensitivity analysis which is not only helpful for an enhanced understanding of the parameter influence, but also part of mathematical optimization techniques [23]. The values of $\tilde{R}_{ijk}$ could be either interpreted as the relative sensitivity of the sensitivity $\tilde{S}_{ik}$ w.r.t. another parameter λ_j (and vice versa: $\tilde{S}_{jk}$ w.r.t. λ_i) or as the curvature of the graph of the solution $y_k(t, \Lambda)$ in the $(N + M + 2$–dimensional) solution–parameter space. The latter may help to connect the results to the field of mathematical optimization, in which the second derivative (Hessian) of a function is often included in objective functions to find optimal parameter sets.

3.7.5. Insights Through Global Methods

Some additional conclusions can be drawn from global sensitivity analysis, in particular from comparing results in Section 3.6.3 to those based on local sensitivity analysis (Sections 3.6.1, 3.6.2, and 3.7.1).

For Zajac's activation dynamics, global analysis confirms local analysis in stating that there are no significant second or higher order sensitivities, with the slight exception of the phase of rapid change in activity after a step in stimulation. An experimentalist who wants to measure the activation time constant τ, can exclude influence from potentially slower

deactivation processes ($\beta < 1$) by starting from high activity levels (Fig. 3.2, bottom). It should yet be kept in mind that the build–up of activity to a new level is not solely determined by τ, but might be biased by the other parameters than τ. This conclusion can be made, because TSI_τ peaks during the build–up phase (Fig. 3.4, right).

In Hatze's activation dynamics, the higher order sensitivities play a more significant role, even in the near–steady–state case (Fig. 3.5: stronger deviation from 1 of both VBS and TSI). When arguing in terms of controllability of the models in Section 3.7.1, we speculated that Zajac's dynamics might be easier to control than Hatze's dynamics. Notwithstanding, Fig. 3.5 shows that the stimulation is the most important control factor with even a higher importance than in Zajac's formulation.

At first sight unapparent, another result is the importance of ρ_c. From a strictly local point of view, we concluded that this parameter should have the same sensitivity as σ, since they both are formally equivalent multipliers in Hatze's ODE (see relative sensitivities in Fig. 3.3). However, the importance of ρ_c is significantly smaller than that of σ, in fact almost negligible. This may be explained by their different value variabilities. The parameter ρ_c in the product $\rho_c \cdot \sigma \in [4; 11] \cdot [0; 1]$ has a lower relative variability than σ, measured in maximum percentage deviation from the respective mean value. The parameter ρ_c thus acts as an amplifier for σ. Similarly, the parameter ν has a relatively small variability throughout literature. So, although its differential sensitivity is quite large, ν is found to have a low importance for the model output. For the latter fact there is yet another reason. In Section 3.6.2, we have emphasized that ν has a very changeful influence on solutions, depending on activity level. Additionally, its influence is highly dependent on other parameters like length ℓ_{CE} and ρ_c (see end of Section 3.7.1). Its strong influence in some situations or configurations is thus hidden by global averaging.

This demonstrates that the findings of global sensitivity analysis must be treated with caution, because the whole dynamics of a system is condensed to a single average function per whole parameter range. Without local analyses of the solution space as exemplified in Sections 3.6.1 and 3.6.2 crucial features of its topology might be lost, when solely relying on global analysis.

Acknowledgements:
Michael Günther was supported by "Berufsgenossenschaft Nahrungsmittel und Gastgewerbe, Geschäftsbereich Prävention, Mannheim" (BGN) and Deutsche Forschungsgemeinschaft (DFG: SCHM2392/5-1), both granted to Syn Schmitt.

Conflict of interest statement:
The authors declare that there is no conflict of interests regarding the publication of this article.

Bibliography

[1] B. W. Bader and T. G. Kolda. "Algorithm 862: MATLAB tensor classes for fast algorithm prototyping". In: *ACM Transactions on Mathematical Software* 32.4 (2006), pp. 635–653.

[2] H. Benker. *Differentialgleichungen mit MathCad und MatLab*. Vol. 1. Springer, 2005.

[3] K. Chan, A. Saltelli, and S. Tarantola. "Sensitivity analysis of model output: variance-based methods make the difference". In: *Proceedings of the 29th Conference on Winter Simulation*. Ed. by S. Andradóttir et al. Winter Simulation Conference. IEEE Computer Society. Washington, DC, USA, 1997, pp. 261–268.

[4] G. K. Cole et al. "Modelling of force production in skeletal muscle undergoing stretch". In: *J. Biomechanics* 29.8 (1996), pp. 1091 –1104.

[5] R. Dickinson and R. Gelinas. "Sensitivity Analysis of Ordinary Differential Equation Systems - A Direct Method". In: *Journal of Computational Physics* 21.2 (1976), pp. 123–143.

[6] H. C. Frey, A. Mokthari, and T. Danish. *Evaluation of Selected Sensitivity Analysis Methods Based Upon Application to Two Food Safety Process Risk Models*. Tech. rep. Computational Laboratory for Energy, North Carolina State University, 2003.

[7] M. Günther, S. Schmitt, and V. Wank. "High-frequency oscillations as a consequence of neglected serial damping in Hill-type muscle models". In: *Biological Cybernetics* 97.1 (2007), pp. 63–79.

[8] D. F. B. Haeufle et al. "Hill-type muscle model with serial damping and eccentric force-velocity relation". In: *Journal of Biomechanics* 47.6 (2014), pp. 1531–1536.

[9] H. Hatze. "A General Myocybernetic Control Model of Skeletal Muscle". In: *Biological Cybernetics* 28.3 (1978), pp. 143–157.

[10] H. Hatze. "A Myocybernetic Control Model of Skeletal Muscle". In: *Biological Cybernetics* 25.2 (1977), pp. 103–119.

[11] H. Hatze. *Myocybernetic control models of skeletal muscle*. University of South Africa, 1981.

[12] D. A. Kistemaker, A. J. van Soest, and M. F. Bobbert. "A model of open-loop control of equilibrium position and stiffness of the human elbow joint". In: *Biological Cybernetics* 96.3 (2007), pp. 341–350.

[13] D. A. Kistemaker, A. J. van Soest, and M. F. Bobbert. "Is equilibrium point control feasible for fast goal-directed single-joint movements?" In: *Journal of Neurophysiology* 95.5 (2006), pp. 2898–2912.

[14] D. A. Kistemaker, A. J. van Soest, and M. F. Bobbert. "Length-dependent [Ca2+] sensitivity adds stiffness to muscle". In: *Journal of Biomechanics* 38.9 (2005), pp. 1816–1821.

[15] R. Langland. "Initial condition sensitivity and error growth in forecasts of the 25 January 2000 East Coast snowstorm." In: *AMS* 130.4 (2002), pp. 957–974.

[16] S. L. Lehman and L. W. Stark. “Three algorithms for interpreting models consisting of ordinary differential equations: sensitivity coefficients, sensitivity functions, global optimization”. In: *Mathematical Biosciences* 62.1 (1982), pp. 107–122.

[17] F. Mörl et al. “Electro-mechanical delay in Hill-type muscle models”. In: *Journal of Mechanics in Medicine and Biology* 12.5 (2012), pp. 85–102.

[18] A. Saltelli and P. Annoni. “How to avoid a perfunctory sensitivity analysis”. In: *Environmental Modelling & Software* 25.12 (2010), pp. 1508–1517.

[19] A. Saltelli, K. Chan, and E. M. Scott. *Sensitivity Analysis*. 1st ed. John Wiley, 2000.

[20] O. Scherzer. *Mathematische Modellierung - Vorlesungsskript*. Universität Wien. 2009.

[21] C. Scovil and J. Ronsky. “Sensitivity of a Hill-based muscle model to pertubations in model parameters”. In: *J. Biomechanics* 39.11 (2006), pp. 2055–2063.

[22] T. Siebert, O. Till, and R. Blickhan. “Work partitioning of transversally loaded muscle: experimentation and simulation”. In: *Computer Methods in Biomechanics and Biomedical Engineering* 17.3 (2014), pp. 217–229.

[23] M. Sunar and A. Belegundu. “Trust Region Method for Structural Optimization Using Exact Second Order Sensitivity”. In: *International Journal for Numerical Methods in Engineering* 32.2 (1991), pp. 275–293.

[24] R. Tomovic and M. Vukobratovic. *General Sensitivity Theory*. American Elsevier, New York, 1972.

[25] A. J. van Soest. “Jumping from Structure to Control: A Simulation Study of Explosive Movements”. PhD thesis. Amsterdam: Vrije Universiteit, 1992.

[26] A. J. van Soest and M. F. Bobbert. “The contribution of muscle properties in the control of explosive movements”. In: *Biological Cybernetics* 69.3 (1993), pp. 195–204.

[27] F. E. Zajac. “Muscle and Tendon: Properties, Models, Scaling, and Application to Biomechanics and Motor Control”. In: *Critical Reviews in Biomedical Engineering* 17.4 (1989), pp. 359–411.

[28] H. ZivariPiran. “Efficient Simulation, Accurate Sensitivity Analysis and Reliable parameter Estimation for Delay Differential Equations”. PhD thesis. University Toronto, 2009.

4. Research Paper II: Extracting Concentric and Eccentric Dynamic Muscle Properties from Isometric Contraction Experiments

R. Rockenfeller M. Günther

The following is a reformatted and slightly modified copy of the submitted article **R. Rockenfeller and M. Günther. "Extracting Concentric and Eccentric Dynamic Muscle Properties from Isometric Contraction Experiments". Submitted to: Mathematical Biosciences.**
In the remaining work, this article is also referred to as [67].

The idea for this article was developed by R. Rockenfeller. The sections "Introduction" and "Switching Time Results and EMD" as well as a final revision originated from a direct, personal collaboration of the two authors. The remaining sections as well as the structure, computations and results originated from R. Rockenfeller.

Abstract

Determining dynamic properties of mammalian muscle, such as activation characteristics or force–velocity relation, challenges the experimentalists. Tracking system, apparatus stiffness, load oscillation and force transducer must be incorporated, synchronized and evaluated in an experimental set–up. In contrast, isometric contraction experiments (ICEs) are less challenging, but are generally not considered to reveal dynamic muscle properties. A sensitivity analysis of our muscle model discloses the influence of concentric, eccentric and activation parameters on the isometric force. Using experimental ICE data only, we validated concentric as well as eccentric muscle performance and compared two different activation dynamics in regards to their physiological relevance. To improve model–fits to ICE data, we optimized different combinations of such dynamic parameter subsets with respect to their influence on contraction solutions. As a first result, we suggest one formulation of activation dynamics to be superior. Second, the step in slope of the force–velocity relation at isometric force was found to be the least influential among all dynamic parameters. Third, we suggest a specially designed isometric experimental set–up to estimate this transition parameter. Fourth, because of an inconsistency in literature, we developed a simple method to determine exact switching times of the neural stimulation in ICEs.

Keywords: Biomechanics, Striated Muscle Model, Sensitivity Analysis, Optimization, Electro–Mechanical Delay, Experimental Design

List of abbreviations:

CC	concentric contraction
CE	contractile element
DAE	differential algebraic equation (system)
EC	eccentric contraction
EMD	electro–mechanical delay
ICE	isometric contraction experiment
MTC	muscle tendon complex
ODE	ordinary differential equation
PEE	parallel elastic element
SDE	serial damping element
SEE	serial elastic element
w.r.t.	with respect to

4.1. Introduction

Describing complex systems, models usually consist of several sub–models (or parts), delineating structurally or functionally distinct contributions to system dynamics. In biological systems, the parts interact mostly non–linearly. An essential scientific task is to validate such models by sorting out sub–models of low validity and to improve or exchange them if needed.

Muscular contraction can be examined by using macroscopic Hill–type muscle models [19]. These are often combined with model descriptions of electro–chemical processes that lead to muscle force production in response to neural stimulation, the so–called activation dynamics [13, 67]. Some properties of coupled contraction–activation dynamics are well–established, for instance the force–length relation of muscle fibers [6, 17, 18, 22, 50, 63] or the visco-elastic characteristics of tendon material [16, 26, 27, 46, 47, 48, 51, 67]. Performing isometric contractions in experiments is a well–suited method to determine muscular force–length relations. A near–static condition, such as an isometric contraction, is appropriate for determining static properties and implies minimized experimental complexity and methodical effort. It seems natural that determining dynamic properties, such as a fiber's force–velocity relation or activation dynamics, requires performing dynamic contraction modes. For this purpose, the experimentalist has to develop more elaborated and sophisticated experimental methods. Moreover, in such dynamic contraction modes, the various contributions to dynamic force, to activity development and to muscle length change superpose each other, see [21].

The concentric branch of the force–velocity relation is the most investigated dynamic muscle property. Experimental approaches are traceable to the nineteenth century and first quantitative results are dating back to the 1920s [5, 20, 35, 36], culminating in the 1930s [4, 19]. Attention has been paid to muscle activation dynamics in the late 1970s [12, 13, 14], late 1980s [67] and again during the last two decades [28, 53, 63]. Dynamic, dissipative properties of tendon and aponeurosis material [9] as well as activity–dependent, potentially visco–elastic properties of titin molecules [54] have recently been considered in muscle modeling as well.

Determining eccentric muscle properties challenges an experimentalist and requires extra–delicate set–ups. The muscle can be easily damaged [43, 61, 66], which obstructs both data quality and repeatability. Compared to the concentric case, experimental data on eccentric contractions are scarce [11, 23, 24, 25, 32, 39, 57, 58, 61]. Parameter values

describing eccentric contractions differ considerably and ought to be treated with caution.

It is assumed that there is passive visco–elastic material (serial elastic and damping elements: SEE and SDE) in series to the contractile material (contractile element: CE) in a real muscle–tendon complex (MTC). Be it in situ or in vitro, any isometric contraction experiment (ICE) on an MTC should then also be a source of information about the dynamic components, i.e. concentric and eccentric CE properties as well as activation. With the MTC held isometrically, a step in muscle stimulation from zero to maximum or vice versa will induce the CE to contract concentrically or eccentrically, respectively, against the SEE and SDE. There has not been brought attention to this fact, although ICEs are less challenging in terms of apparatus design and experimental execution, compared to eccentric contractions of the entire MTC. Furthermore, ICEs provide a physiologically tolerable eccentric loading condition for the muscle material.

The first aim of our study was to assess the validity of several parts of a Hill–type muscle model for coupled contraction–activation dynamics. For this purpose, we compared two different model descriptions of both the eccentric branch of the CE force–velocity relation and the activation dynamics. We compared model simulations containing a complete set of Hill–type model parameters to literature data of a piglet muscle experiment [9]. Subsequently, we searched for the model part combination with a minimal least–square deviation from the experimental force–time curves, measured during isometric contractions of this muscle at various MTC lengths. In these experiments, the muscle was clamped unstimulated at a particular length. After a period of rest, it was fully stimulated at a certain switch–on time. One second later, at switch–off time, the stimulation was set to zero again. During the experiment, the MTC force output was measured. The best–fitting model was then subjected to an optimization procedure that minimized the deviation from the measured data. As a consequence of checking and optimizing model validity, we determined dynamic muscle parameters of the Hill–type muscle model for concentric and eccentric contractions, together with parameters of the coupled model for contraction–activation dynamics.

Our second aim was the optimization of experimental set–ups. Therefore, we purposefully limited the information about muscle dynamics to force–time curves during isometric contractions. This self–limitation demonstrates, that dynamic contraction parameters may be determined solely from this near–static contraction mode, which is easier to perform, compared to experiments in which the MTC length changes. Based on [33, 53, 62], a sensitivity analysis of the model dynamics revealed the influence of dynamic muscle parameters on the time evolution of the isometric force. Among all dynamic parameters, the ratio between the derivatives of the concentric and eccentric branch within the force–velocity relation at the isometric point (denoted by S_e) was least sensitive. Using sensitivity analysis, we can now suggest an isometric contraction experiment, optimized for solely determining the eccentric parameter S_e.

An interesting side effect arises from the necessity of knowing when exactly the steps in stimulation occur. The activation and dynamic contraction parameters sensitively influence the electro–mechanical delay (EMD), which is the time interval between a step in stimulation input and the subsequently measurable change in force output. We realized, that the specification of the switch–off times in the experiments were unreliable. This challenge lead to a method of extracting the EMD solely from experimental data of isometric contractions.

4.2. Model and Methods

4.2.1. Model Description

The used Hill–type muscle model was initiated by [9] and further developed by [10]. We shortly outline the model structure, including activation dynamics. For a detailed description see [52]. Let $\ell_{MTC}, \ell_{SEE}, \ell_{SDE}, \ell_{CE}$ and ℓ_{PEE} denote the lengths of the constituting elements composing the whole muscle–tendon complex (MTC): the serial elastic (SEE) and damping element (SDE) in series to the contractile (CE) and parallel elastic element (PEE). For this four–element arrangement, the kinematic restrictions

$$\ell_{SEE} = \ell_{SDE}, \quad \ell_{CE} = \ell_{PEE} \quad \text{and} \quad \ell_{MTC} = \ell_{CE} + \ell_{SEE} \quad ,$$

and the one–dimensional force equilibrium

$$F_{MTC} = F_{CE} + F_{PEE} = F_{SEE} + F_{SDE} \tag{4.1}$$

apply, in which ℓ_i denotes the length of element i and F_i its generated force.

Furthermore, let σ denote the neural stimulation, which drives the MTC dynamics as an input control parameter, and q_X the muscle activity, which represents the MTC's second state variable alongside with ℓ_{CE}. The force production of the MTC within an isometric contraction can be described by the following differential–algebraic equation (DAE) system (author's note: cf. Chapter 7, Eqn. (7.18)):

$$\dot{q}_X = f_1(\ell_{CE}, q_X, \sigma) \; , \qquad q_X(0) = q_{X,0} \; , \tag{4.2a}$$

$$\dot{\ell}_{CE} = f_2(\ell_{MTC}, \dot{\ell}_{MTC}, \ell_{CE}, q_X) \; , \qquad \ell_{CE}(0) = \ell_{CE,0} \; , \tag{4.2b}$$

$$\dot{\ell}_{MTC} = 0 \; , \qquad \ell_{MTC}(0) = \ell_{MTC,0} \; , \tag{4.2c}$$

$$F_{MTC} = f_3(\ell_{MTC}, \dot{\ell}_{MTC}, \ell_{CE}, q_X) \quad . \tag{4.2d}$$

In this notation, f_1 represents the activation dynamics that is either linear according to [67] (Zajac; Models 1 – 3 and 5a, see below) or non–linear according to [12, 14] (Hatze; Models 4 and 5b). Both models are currently being used to perform state–of–the–art modeling of activation dynamics [2, 10, 28]. To reveal the validity of both formulations, we interchanged them during our study, designating $X \in \{Z, H\}$. The contraction dynamics f_2 is a modified Hill relation [13] solved for $\mathrm{d}/\mathrm{d}t \; \ell_{CE}$, which explains the model classification as "Hill–type". With the formulation by [63, 64] as a mainstay, f_2 always includes the minor reformulations and force–dependent SDE introduced by [9], the latter marginally modified by [45]. In Models 2 to 5, the right hand side f_2 is further refined by a physiologically–based eccentric branch of the force–velocity relation as described in [10], which also goes back to [63, 64]. For a given σ, initial steady–state values $q_{X,0}$ and $\ell_{CE,0}$ can be calculated by simultaneously setting f_1 and f_2 equal to zero, which corresponds to the electro–mechanical equilibrium state (author's note: cf. Chapter 2 Eqns. (2.3), (2.6) and (2.12)). As purely isometric contractions are being examined, the MTC length in a simulation is always fixed to the initial length $\ell_{MTC,0}$ that represents the corresponding whole muscle length in the experiment. Note that other contraction modes (isokinetic, isotonic, quick–release, etc.) can be modeled by formulating an adapted ODE for $\mathrm{d}/\mathrm{d}t \; \ell_{MTC}$. Those adaptations can contain an upper bound for F_{MTC} (isotonic) or an additional ODE for $\mathrm{d}/\mathrm{d}t \; \ell_{MTC}$ based on Newton's law of motion (author's note: see Chapter 5). The function f_3 calculates the MTC force output in any state. Note that Eqn. (4.2d) is no ODE but an algebraic equation and therefore does not require an initial value at $t = 0$.

Altogether, the following five model variants were investigated:

Model 1: Model from [9]. In detail: Bell–shaped force–length curve, non–linear PEE characteristics, partly non–linear partly linear SEE characteristics, force–dependent SDE adapted according to [10], single hyperbolic force–velocity relation according to Hill, no eccentric branch, Zajac's activation dynamics.

Model 2: Model from [10] with a double hyperbolic force–velocity relation (i.e. including eccentric branch) and Zajac's activation dynamics. In this set–up, we noted that the value of the activation–deactivation ratio ($\beta = 1$) was overestimated in [9] due to the missing eccentric branch, see Subsection 4.3.3. A correction is given in Model 3.

Model 3: Same as Model 2, but $\beta = 0.5$.

Model 4: Model from [10] with Hatze's activation dynamics [12, 14] and their parameters $(\ell_\rho, \rho_c, \nu, m, q_0)$ optimized, see Eqn. (4.6) and Table 4.2 (fourth column).

Model 5a: Same as Model 3, but with an optimized dynamic parameter set, including Zajac's parameters (q_0, β, τ), the Hill parameters $(a_{rel,0}, b_{rel,0})$ and the eccentric parameters (F_e, S_e), see Eqn. (4.6) and Table 4.2 (fifth column).

Model 5b: Same as Model 5a, but Zajac is exchanged by Hatze and all dynamic parameters are optimized, see Eqn. (4.6) and Table 4.2 (sixth column).

4.2.2. Determining Exact Switching Times in Experiments

Model validation is done by comparing the model's output to experimentally generated data, w.r.t. the same input. In [9, Fig. 7] the force output of Model 2 was plotted versus time during a number of isometric contractions, in which the muscle was passively ($\sigma = 0$) stretched to different MTC lengths and underwent an isometric contraction cycle. By comparison, they also plotted the corresponding experimental force–time data, denoted by $\overline{F}_{MTC}(t)$, taken from a piglet soleus muscle [9]. After having been fixed at a particular muscle length and left unstimulated (passive) for a while, the muscle was fully stimulated ($\sigma = 1$) and again left unstimulated after a finite time interval. In the experiment, the neural stimulation was induced via the intact nerve. In [9], it was stated that stimulation lasted for 'about' one second from switch–on time at $t_{start} = 0.1\,\mathrm{s}$ to switch–off time at $t_{end} = 1.1\,\mathrm{s}$. However, a close look at the plot revealed that the experimental force started to decrease partly before and partly after the stated switch–off time. Presumably, the switching times were not implemented accurately or distorted by using a filter.

A characteristic muscle property is the time difference between a step in stimulation (e.g. switch–on or switch–off) on the input side and a corresponding change in force on the output side: the electro–mechanical delay (EMD). In [45], a simulation study presented characteristic EMD values for two slightly different Hill–type muscle models [9, 56]. As a finite amount of force change, one percent of the maximum muscle force was assumed.

As we aim at finding model parameters that validly represent the physiological muscle, the quality of our results depends sensitively on reproducing the time characteristics of the real muscle in isometric contractions. Several model parameters influence the EMD: the PEE parameters, the SEE stiffness, the CE force–length relation, both concentric and eccentric parameters of the CE force–velocity relation, as well as the time constants of the activation dynamics. Therefore, knowing exact switching times of the stimulation in

the experiments is an essential prerequisite for model validity. This accuracy allows to determine parameter values that represent physiology.

Consequently, we calculated physiological EMD values based on the experimental data of isometric forces versus time. In our first order muscle model (4.2), a step in stimulation induces a step in activation $\mathrm{d}/\mathrm{d}t\ q$ as well as in CE velocity $\mathrm{d}/\mathrm{d}t\ \ell_{CE}$ and thus a step in force change rate $\mathrm{d}/\mathrm{d}t\ \overline{F}_{MTC}(t)$. Such a force change event is represented in the real muscle by a change in sign of the second derivative $\mathrm{d}^2/\mathrm{d}t^2\ \overline{F}_{MTC}(t)$, which is the curvature of the experimental force curve $\overline{F}_{MTC}(t)$. The switch–on is determined by the first time the curvature becomes strictly positive, which corresponds to an increasing force rate, and vice versa for switch–off.

The resulting switching times are shown in Figs. 4.1(a) and (b). The time derivations were calculated by the function "gradient", a centered difference method implemented in MATLAB (The MathWorks, Natick) version 8.2.0.701. The last sample, at which the value of $\mathrm{d}^2/\mathrm{d}t^2\ \overline{F}_{MTC}(t)$ was either negative (switch–on) or positive (switch–off), was taken as the respective time of the stimulation step event.

4.2.3. Sensitivity Analysis of Model Dynamics

Before assessing the validity of the whole muscle model according to Eqn. (4.2), we first checked to what extend those parts influence the model output. Since all model parts are described by parameters, this influence can be quantified using sensitivity analysis. In a recent study [53] (author's note: Chapter 3), we applied sensitivity analysis on Hatze's and Zajac's activation dynamics. The remainder of this subsection is a summary of this approach.

Let $y = (q_X, \ell_{CE}, F_{MTC})^T$ be the vector of the state variables q_X, ℓ_{CE} and the output variable F_{MTC} of our model described by Eqn. (4.2). The external state variables $\ell_{MTC},\ \mathrm{d}/\mathrm{d}t\ \ell_{MTC}$ are treated as fixed parameters in our simulations and are consequently excluded. Let further $f = (f_1, f_2, f_3)^T$ be the corresponding vector of right hand sides and $\Lambda = \{\lambda_1, \ldots, \lambda_M\}$ be the set of parameters occurring in the DAE. The sensitivity of the state y_k w.r.t. the parameter λ_i is then defined as $S_{y_k,\lambda_i}(t) := \mathrm{d}/\mathrm{d}\lambda_i\ y_k(t)$.

As described in [53], we can derive and solve a set of ordinary differential equations (ODEs) for all sensitivities S_{y_k,λ_i} corresponding to the two ODEs 4.2a,b, with right hand sides f_1 and f_2, and all parameters λ_i considered. Furthermore, the sensitivities S_{F_{MTC},λ_i} can be calculated directly. Altogether, the DAE for these sensitivity functions writes as

$$\dot{S}_{q_X,\lambda_i} = S_{q_X,\lambda_i} \cdot \frac{\partial}{\partial y_1} f_1 + S_{\ell_{CE},\lambda_i} \cdot \frac{\partial}{\partial y_2} f_1 + \frac{\partial}{\partial \lambda_i} f_1, \qquad S_{q_X,\lambda_i}(0) = 0 \tag{4.3}$$

$$\dot{S}_{\ell_{CE},\lambda_i} = S_{q_X,\lambda_i} \cdot \frac{\partial}{\partial y_1} f_2 + S_{\ell_{CE},\lambda_i} \cdot \frac{\partial}{\partial y_2} f_2 + \frac{\partial}{\partial \lambda_i} f_2, \qquad S_{\ell_{CE},\lambda_i}(0) = 0 \tag{4.4}$$

$$S_{F_{MTC},\lambda_i} = S_{q_X,\lambda_i} \cdot \frac{\partial}{\partial y_1} f_3 + S_{\ell_{CE},\lambda_i} \cdot \frac{\partial}{\partial y_2} f_3 + \frac{\partial}{\partial \lambda_i} f_3 \qquad . \tag{4.5}$$

It is necessary to normalize all sensitivities w.r.t. the parameter values as well as state variable values. Hence, the sensitivities become dimensionless and therefore comparable through different parameter units, situations, dynamics, and models. Normalized sensitivities are defined as $\tilde{S}_{y_k,\lambda_i}(t) := \lambda_i / y_k(t) \cdot S_{y_k,\lambda_i}(t)$.

The outlined method is called *differential* or *local* sensitivity analysis because the parameter space is analyzed only pointwise. In [55], a variety of additional methods are presented, including so–called *global* methods calculating the sensitivities within the possible (physiological) range of every parameter. Three reasons kept us from using these global methods. First, global methods are prone to omit local particularities, because

they average across the whole parameter space [53]. Second, an initial parameter set from [9] is available, so that we can restrict our search for optimal parameter values to a local area around this set. Third, lower and upper bounds for all examined parameters would have to be specified, which would go beyond the scope of this paper.

As stated in Subsection 4.2.2, the EMD is sensitive w.r.t. certain parameters. In [45] a coarse sensitivity analysis of the EMD was performed w.r.t. Zajac's time constant τ, the PEE rest length $\ell_{PEE,0}$, the SEE stiffness $\Delta F_{SEE,0}$ and the SEE toe zone $\Delta U_{SEE,nll}$. The corresponding values were varied by a percentage change and the model outputs were compared. However, we give a more general formulation of sensitivities as functions over time of an entire isometric contraction cycle, compare [53].

4.2.4. Estimation of Model Parameters by a Least–Square Fit

After including Hatze's activation dynamics and adding a physiologically–based eccentric branch of the contraction dynamics in (4.2), the parameter set suggested by [9] should be reconsidered. There are sources for Hatze parameters as [12, 14, 28], but they may not be adequate for the examined piglet muscle. Referring directly to [64], parameter values for the eccentric branch are given in [9]. The values, however, were not used in their model and thus not fitted to the experimental data. One can find a variety of scattering values in literature [11, 23, 24, 25, 32, 39, 43, 61, 64]. Furthermore in [9, Fig. 7], the curvatures of the simulated force curves versus time after switch–on are significantly lower than the corresponding curvatures of the experimental curves in most cases. In a first attempt to diminish this deviation, [9] varied the normalized Hill parameters $a_{rel,0}$, $b_{rel,0}$, which were suspected to have an influence on the curvature in the force–time curves, cf. [9, Fig. 10]. Taking this idea a step further, we optimized all dynamic parameters (Hatze, Hill and eccentric) simultaneously by an algorithmic procedure. All static parameters were fixed to the values given in [9], including parameters of the SDE (damping very low: cf. [9, Fig. 12]), the SEE, the PEE and the CE force–length relation $F_{isom}(\ell_{CE})$.

We optimized the model w.r.t. the set Λ_H, containing the five Hatze parameters (Model 4); the set $\Lambda_{D,Z}$, containing the dynamic CE parameters $a_{rel,0}$, $b_{rel,0}$, F_e, S_e as well as the three parameters adapted from Zajac (Model 5a); and the set $\Lambda_{D,H}$, containing all dynamic CE parameters as well as the five Hatze parameters (Model 5b).

$$\begin{aligned} \Lambda_H &= \{\ell_\rho, \rho_c, \nu, m, q_0\} \\ \Lambda_{D,Z} &= \{a_{rel,0}, b_{rel,0}, F_e, S_e, q_0, \beta, \tau\} \\ \Lambda_{D,H} &= \{a_{rel,0}, b_{rel,0}, F_e, S_e, \ell_\rho, \rho_c, \nu, m, q_0\} \end{aligned} \tag{4.6}$$

A concise presentation of Hatze's activation dynamics and the respective parameters Λ_H can be found in [8, 53]. For the adaptation of Zajac's activation dynamics see [8, 49, 67]. A description and use of the additional dynamic parameters can be found in [9]: $a_{rel,0}, b_{rel,0}$ denote the normalized (concentric) Hill parameters and F_e, S_e denote the normalized eccentric force asymptote and step in slope at the isometric point in the force–velocity relation, respectively. Typical values for all model parameters are summarized in Table 4.2.

For a mathematical formulation of the estimation process, we define the domain of the neural stimulation $\sigma = \sigma(t)$ as $\mathcal{U} := C([0,T],[0,1])$, which is the set of continuous functions $\varphi : [0,T] \to [0,1]$, mapping the time interval $[0,T]$ to values in the interval $[0,1]$. In a mathematical notation, model (4.2) then rewrites as

$$F : \mathcal{U} \times \mathbb{R}^M \longrightarrow C([0,T],\mathbb{R}), \qquad F(\sigma,\Lambda) = F_{MTC}(t), \tag{4.7}$$

where M is the number of parameters in the adaptable parameter set. Accordingly, finding an optimal parameter set, such that the model output fits best to the experimental data, can be written as the minimization problem

$$\Lambda^* = \underset{\Lambda \in \mathbb{R}^M}{\arg\min}\ \mathcal{J}(\overline{\sigma}, \Lambda) := \underset{\Lambda \in \mathbb{R}^M}{\arg\min}\ \frac{1}{2}||F(\overline{\sigma}, \Lambda) - \overline{F}_{MTC}||^2_{L^2} \quad . \tag{4.8}$$

In this context, $\overline{F}_{MTC}$ denotes the experimental force and $\overline{\sigma} = \overline{\sigma}(t) := \mathbf{1}_{[t^*_{start}, t^*_{end}]}$ the experimental stimulation, which is 1 if $t \in [t^*_{start}, t^*_{end}]$ and 0 else. The notation t^*_{start} and t^*_{end} is explained in the following (sub)section. The objective function $\mathcal{J}$ can be interpreted as the least square distance between the experimental and simulated force curves in terms of the L^2–distance: $||f - g||^2_{L^2} := \int_0^T (f(x) - g(x))^2 \, \mathrm{d}x$.

For solving non–linear problems of the form (4.8), MATLAB offers various pre–implemented algorithms. All calculations were conducted by *lsqnonlin* (for *least square non–linear*) which is a trust–region algorithm. This improvement of the well–known Gauß–Newton method is more robust than most gradient–based methods. It contains additional step–size constraints to escape poor local minima. Furthermore, it is possible to fix lower and upper boundaries for the parameter values, allowing for physiologically reasonable limits. Although *lsqnonlin* can likewise work with a Levenberg–Marquart algorithm [34, 38], we refrained from using this feature, because it does not allow boundaries. Moreover, the Levenberg–Marquart method basically becomes a damped Gauß–Newton method near local minima and is thus may converge slower, cf. MATLAB documentation based on [42]. We can assume to be near a local minimum, because the initial parameter set was taken from a previous manual optimization by [9].

4.3. Results and Discussion

4.3.1. Switching Time Results and EMD

Figures 4.1(a) and (b) show the switching times of the experimental data from [9] as determined by the curvature method described in Subsection 4.2.2. Data are plotted versus relative MTC length $\ell_{MTC,0}/\ell_{MTC,ref}$. The switch–on time was specified as $t_{start} = 0.1\,\mathrm{s}$ [9] and our calculation resulted in $t^*_{start} = 0.1\mathrm{s} \pm 0.002\,\mathrm{s}$ where 2 ms is the inverse of the sampling rate. Hence, the curvature method and data coincide perfectly within one sample. In contrast, the switch–off time was stated to be $t_{end} = 1.1\,\mathrm{s}$ whereas the curvature method yields $t^*_{end} \in [1.054\,\mathrm{s}, 1.108\,\mathrm{s}]$. There are thus deviations from -23 to $+4$ samples, i.e. about twice the time constant of the activation process (cf. Table 4.2) in the extreme case of the shortest relative MTC length $\ell_{MTC,0}/\ell_{MTC,ref} = 0.85$ ($-46\,\mathrm{ms}$ in relation to t_{end}). For the next shortest relative MTC lengths (0.88, 0.91, 0.94), the deviation accounts for $-20\,\mathrm{ms}$. In contrast, t^*_{end} overshoots t_{end} by maximal four samples at longer CE lengths ($\ell_{MTC,0}/\ell_{MTC,ref} \in \{1.03, 1.06, 1.08\}$). The curvature method may be suspected to be less reliable than the experimental specification $t_{end} = 1.1\,\mathrm{s}$. At close inspection of the extreme case $\ell_{MTC,0}/\ell_{MTC,ref} = 0.85$ in Fig. 4.4 it is evident, however, that the specification $t_{end} = 1.1\,\mathrm{s}$ has to be inaccurate, because force starts with the typical pattern of force decay before $t = 1.1\,\mathrm{s}$. Moreover, the reproducible determination of switch–on times by the curvature method at all MTC lengths, in perfect accordance with the experimental specification in [9], is a sound basis to rely on calculated t^*_{start} and t^*_{end} values. These values are delicate simulation input numbers, when determining reliable activation parameter values.

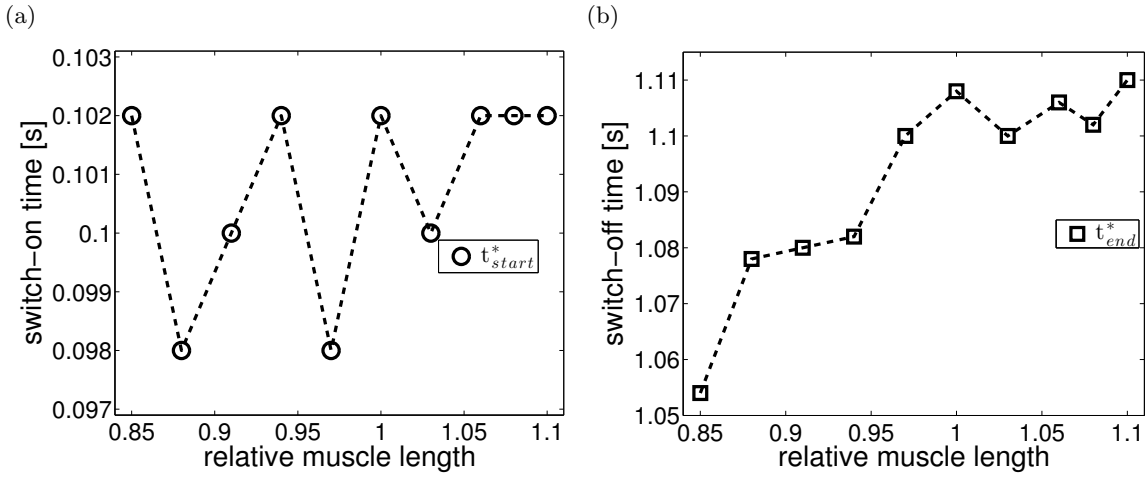

Figure 4.1.: Switch–on times t^*_{start} ((a), circles) and switch–off times t^*_{end} ((b), squares) of the isometric contraction experiments in [9] determined by the curvature method. The values according to [9] were $t_{start} = 0.1\,\mathrm{s}$ and $t_{end} = 1.1\,\mathrm{s}$. Relative muscle lengths $\ell_{MTC,0}/\ell_{MTC,ref}$ are given in relation to $\ell_{MTC,ref} = 0.0615\,\mathrm{m}$ [9].

Figure 4.2(a) shows both the switch–off times determined by the curvature method, and the times at which the force has further decayed by $F_{max}/100$, corresponding to switch–off times plus their respective EMD. By calculating the difference between both points in time, EMD values for switch–on and switch–off were determined in all isometric experiments and plotted versus relative MTC length $\ell_{MTC,0}/\ell_{MTC,ref}$ in Fig. 4.2(b). As the CE contracts eccentrically after switch–off, we use "EC" as an index to the EMD in this case, and "CC" (concentric contraction) in the switch–on case. As in Fig. 4.1, data are plotted versus relative MTC length $\ell_{MTC,0}/\ell_{MTC,ref}$.

In our model, neural stimulation σ represents the electrical stimulus at the muscle surface. The time delay between stimulation and finite force increase, inherent in the ordinary differential equation representing muscle activation dynamics (Eqn. 4.2a), is assumed to model all electrical, chemical and diffusion processes between spike arrival at the surface and myosin head conformation. It does not include the spike propagation time along the nerve from the stimulator used in the experiment to the muscle surface in [9]. Thus, EMD values occurring in our model simulations are expected to underestimate experimentally measured ones by approximately 4 milliseconds (about 0.25 ms per centimeter propagation distance on a mammalian motor nerve axon [41]). Figures 4.2(c) and (d) show EMD values for Model 3 and Model 5b, respectively.

In the following, we summarize our results. We first look at the switch–off case (EC). Adding 4 ms to any model value, Zajac's activation dynamics seems to represent real deactivation dynamics almost perfectly for $\ell_{MTC,0}/\ell_{MTC,ref} \geq 0.97$ (Fig. 4.2(c)), whereas only Hatze's activation dynamics can provide a similar degree of reproduction at all shorter MTC lengths (Fig. 4.2(d)). In the switch–on case (CC) the Zajac model is no realistic representation, aside from the small range $1.0 \leq \ell_{MTC,0}/\ell_{MTC,ref} \leq 1.03$. The range of almost realistic representations by the Hatze model is much larger, from shortest values $\ell_{MTC,0}/\ell_{MTC,ref} = 0.85$ up to $\ell_{MTC,0}/\ell_{MTC,ref} = 1.06$. However, Hatze's model predicts EMD–values that are on average 2 ms larger than measured ones.

Concentric EMD characteristics (symbol: stars) can be compared to [45, Fig. 2], who used precisely Model 1 as one model alternative (named "MOD1") for their calculations. Their model version "MOD2" differed from MOD1 in the choice of the specific functional

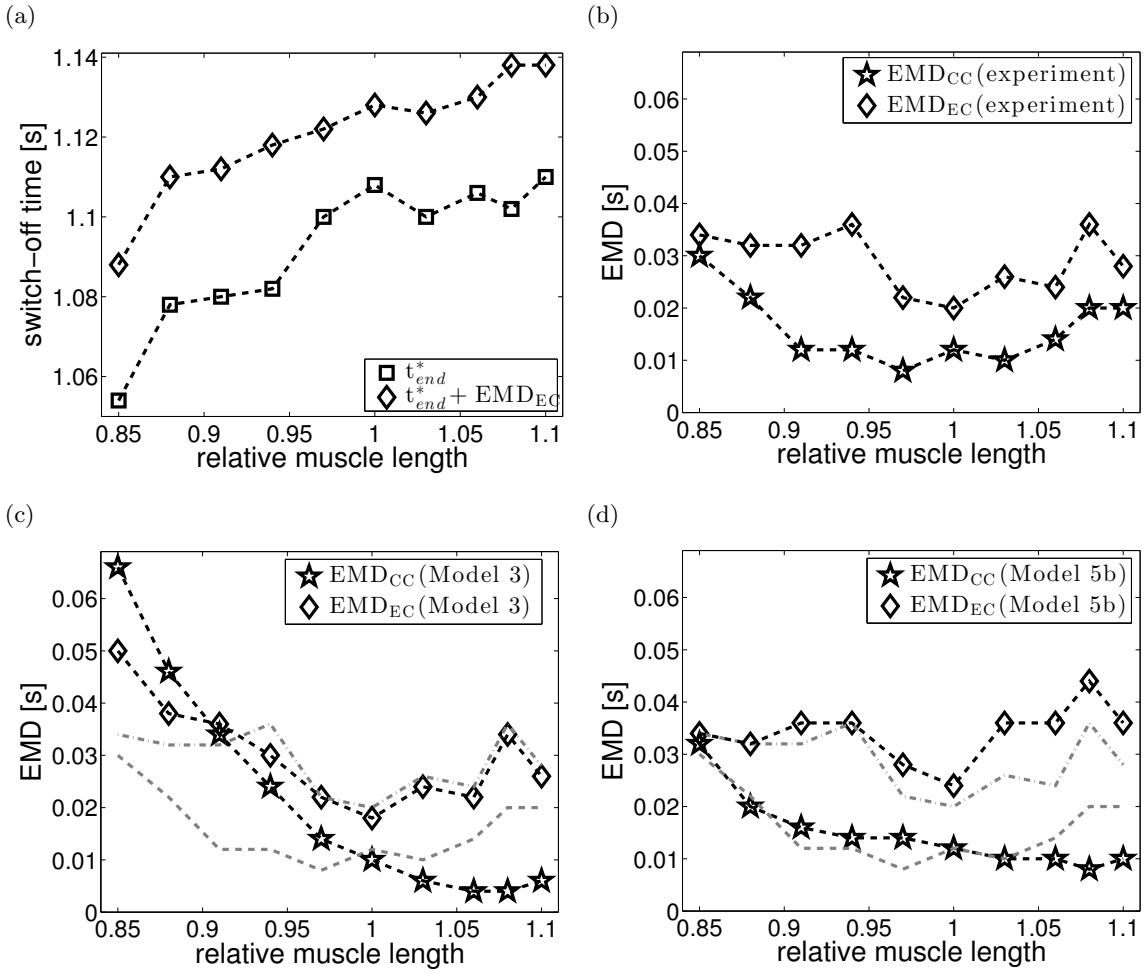

Figure 4.2.: Sub–figure (a) shows the comparison of experimental switch–off t^*_{end} (squares) determined by the curvature method, and the times at which the force has decayed by further $F_{max}/100$ after switch–off (diamonds). The resulting EMD values in the switch–off case (diamonds: t^*_{end}) and in the switch–on case (stars: t^*_{start}) are displayed in (b). The experimentally determined EMD_{CC} (dash–dotted line) and EMD_{EC} (dashed line) are juxtaposed in opposition to the EMD values from evaluating Model 3 in (c) and Model 5 in (d). Note that the CE contracts concentrically after switch–on and eccentrically after switch–off.

dependency for each element within the contraction dynamics, whereas Zajac's activation dynamics were used generally. The experimental condition was congruent to our switch–on situation. However, they examined a different muscle: a cat's soleus muscle represented by $F_{max} = 20\,\mathrm{N}$, $\ell_{CE,opt} = 5.5\,\mathrm{cm}$, $\ell_{SEE,0} = 6.0\,\mathrm{cm}$, i.e. essentially with a tendon–fiber length ratio of about 1, rather than 3 as in our piglet muscle. The relatively longer SEE length in our model explains its systematically higher EMD values, because the piglet tendon is less stiff than the cat's tendon when measured in relation to the forces exerted by the CE. In [45] it was shown that SEE stiffness has a strong influence on the EMD. Their MOD2 contained a stiffer PEE compared to their MOD1 (our Model 1). We conclude that Hatze's activation dynamics are not accountable for the increasing discrepancy between our Model 5b and the measurements. Instead, our model PEE stiffness has been underestimated. However, simply increasing PEE stiffness would lead to another dilemma, as passive forces before

stimulation would become too high.

There are strong indications [54] that implementing conservative, elastic forces via the PEE is not sufficient for representing all forces in the muscle that act parallel to the cross–bridges. It is well–established by now that forces are transmitted between titin and actin [54]. These forces act functionally in parallel to the CE and depend on activity as well as history. Hence, they can account for history effects as "force depression" and "force enhancement" and thus ought to be implemented in Hill–type muscle models as parallel, visco–elastic force elements. Based on our finding that Zajac's description can only predict realistic EMD values in a narrow range and taking further indications into account [28, 52, 53], activation dynamics ought to be based on Hatze's model. In any case, it is necessary to understand, whether existing deficits of our model are resulting from insufficient representation of activation dynamics, from absent activity–dependent, parallel forces or from other physiological processes. There is an unequivocal demand for implementing appropriate representations of history effects as part of a muscle model. The relevance of this additional sub–model has to be quantified using its interaction with the remaining model in dynamic situations.

4.3.2. Sensitivity Analysis Results

In our sensitivity study, we followed [9], applying the reference stimulation $\overline{\sigma} = \mathbf{1}_{[t_{start},t_{end}]}$ to the muscle, which was held isometrically at various MTC lengths. The muscle was represented by the model from [10] and the parameters for Hatze's activation dynamics were taken from [53], see Table 4.2, third column. Three preliminary remarks are emphasized. First, the solution has slightly different sensitivities w.r.t. some parameters at short MTC lengths and other parameters at long MTC lengths, respectively. For example, at short lengths the solution is not sensitive w.r.t. changes in ΔW_{des} because $\ell_{CE} < \ell_{CE,opt}$ during the whole contraction. For the sake of clarity, we averaged the sensitivity values at any time for all ten examined MTC lengths to obtain one meaningful, average sensitivity function for every parameter on the force production, see Fig. 4.3. Second, although we calculated the exact switching times according to Subsection 4.3.1, the presumably incorrect switch–off time $t_{end} = 1.1$ s from [9] was used for sensitivity analysis. Otherwise, the averaging of the sensitivity functions would not be meaningful. Third, the parameter set from Hatze's activation dynamics was not optimized prior to the sensitivity analysis to show the influence of the educated guess from literature (Table 4.2, third column).

Figures 4.3(a) and (b) show the averaged relative sensitivities of the force output w.r.t. the dynamic model parameters. For a better overview, we zoomed in at times t_{start} and t_{end}, because the influence of the dynamic parameters remains near–constant else. During concentric ($\sigma = 1$, $t \geq t_{start}$) and eccentric ($\sigma = 0$, $t \geq t_{end}$) contractions, the force is sensitive w.r.t. activation parameters, particularly ρ_c, m, and ν. During concentric contractions, the force is additionally sensitive w.r.t. the Hill parameters $a_{rel,0}$ and $b_{rel,0}$, whereas during eccentric contractions, the force shows sensitivity w.r.t. the activation parameter ℓ_ρ and the eccentric parameter F_e. The parameter q_0 is only influential at low activity levels [53]. Summarizing, in ICEs, the dynamic muscle parameters influence the force output shortly after switch–on and switch–off time. Consequently, it seems reasonable to perform a parameter fit of dynamic muscle parameters based on ICEs.

(a) Most sensitive dynamic parameters after t_{start}

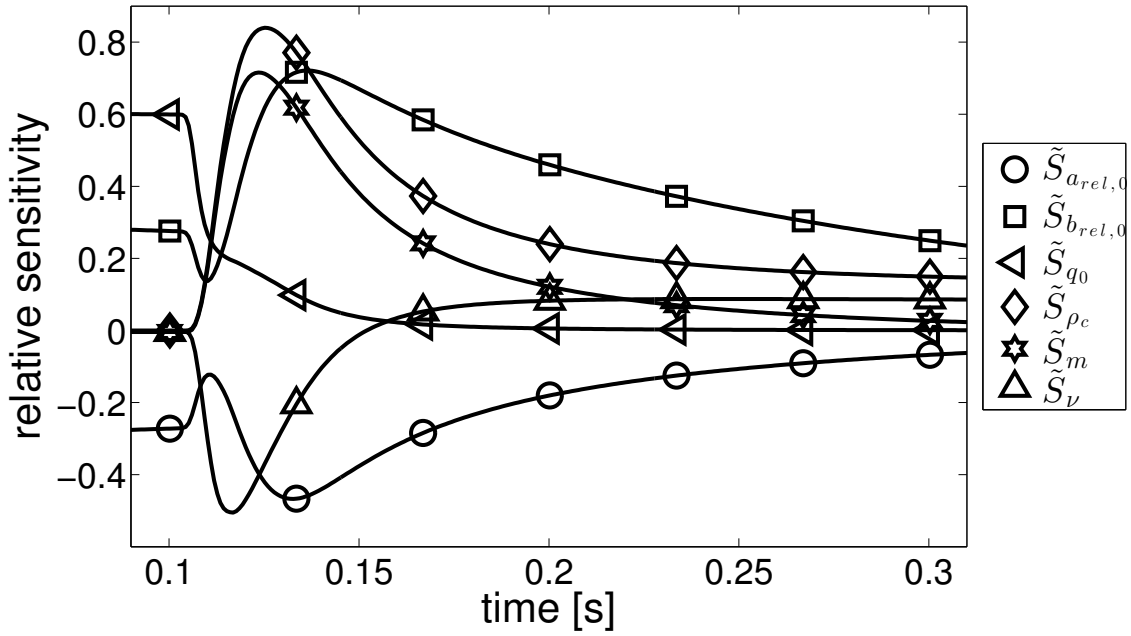

(b) Most sensitive dynamic parameters after t_{end}

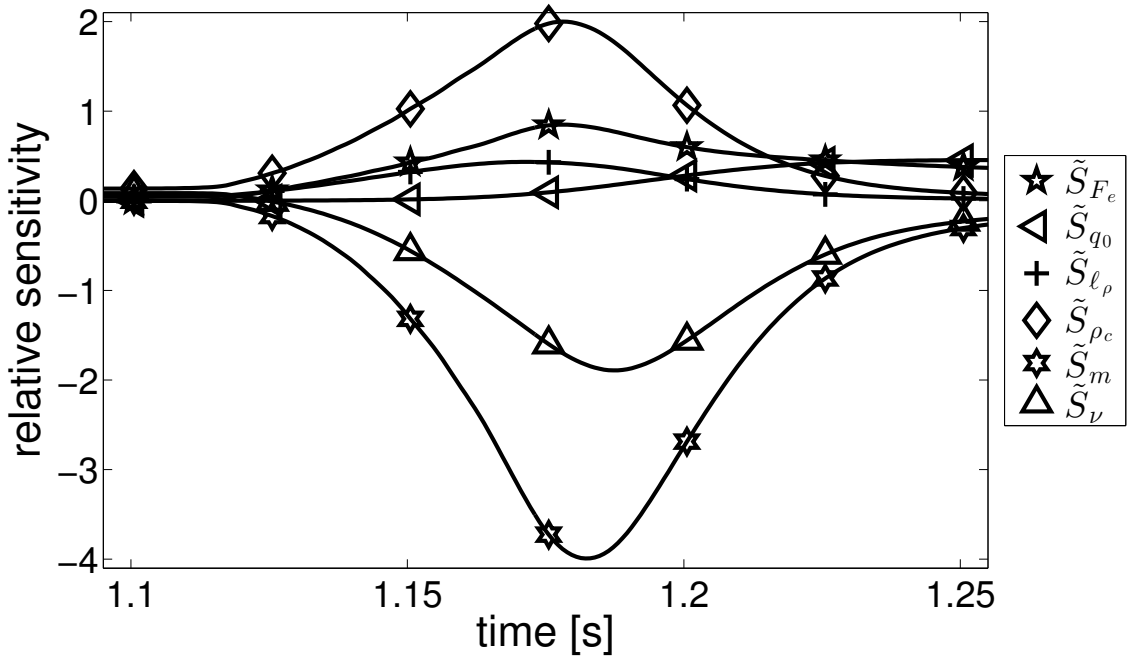

Figure 4.3.: Relative sensitivities of the isometric force output $\tilde{S}_{F_{MTC},\lambda_i}$, abbreviated as $\tilde{S}_{\lambda_i}$, w.r.t. dynamic muscle parameters. The sensitivities were averaged throughout all relative muscle lengths. The parameter values can be taken from Table 4.2 third column. Sub–figure (a) shows the largest sensitivities after $t_{start} = 0.1\,\text{s}$. Sub–figure (b) shows the largest sensitivities after $t_{end} = 1.1\,\text{s}$. The sensitivities in the concentric scenario rise instantaneously after t_{start} and have a local maximum only 30 ms after the step in stimulation. In contrast, after t_{end}, the sensitivities begin to rise mildly and reach their maximum after 85 ms. Still, the convergence to a steady state is faster than in the concentric case.

Regarding static as well as dynamic muscle parameters, the most sensitive parameters, as measured by their averaged maximum absolute sensitivities, are the SEE slack length $\ell_{SEE,0}$ ($\max|\tilde{S}_{F_{MTC},\ell_{SEE,0}}(t)| = 54.4$), the optimal fiber length $\ell_{CE,opt}$ (14.1), the PEE slack length $\mathcal{L}_{PEE,0}$ (10.6) and the SEE toe zone $\Delta U_{SEE,nll}$ (5.8). Therefore, these parameters have to be fixed before performing an optimization of the dynamic parameters. The ratio $\ell_{CE,opt}/\ell_{SEE,0}$ is a fundamental design parameter for the function fulfilled by muscle contraction [44, 67].

The least sensitive parameters, as measured by their averaged maximum absolute sensitivities, are the exponent of the descending force–length limb ν_{des} (0.02), the damping parameter R_{SE} (0.03), the step in slope parameter of the force–velocity relation S_e (0.04), the PEE curve shape parameters $\mathcal{F}_{PEE}$ (0.07), ν_{PEE} (0.08) and the damping parameter D_{SE} (0.09). These parameters are difficult to estimate in an optimization process based on ICEs, because they have little influence on the force output. Of all dynamic parameters, the step in slope parameter S_e was the least sensitive. At first glance, the parameter ought to be disregarded within the optimization process. Instead, we included S_e in Λ_D for the sake of completeness, but developed an additional isometric contraction experiment that maximizes the influence of this specific parameter, see Subsection 4.3.4.

4.3.3. Results From Evaluating Models 1–5

The aim of this section is to validate all dynamic model parts described in Eqn. (4.2) on the basis of ICEs, particularly the eccentric branch of the force–velocity relation, the activation dynamics and the Hill parameters. Therefore, we successively exchanged parts of the muscle model from [9] and calculated the objective function value (residuum) $\mathcal{J}(\sigma^*, \Lambda)$ to be minimized as the L^2–distance between the model output and the experimental force data $\overline{F}_{MTC}$, see Subsection 4.2.4. Here, $\sigma^* = \mathbf{1}_{[t^*_{start}, t^*_{end}]}$ denotes the stimulation with switching times from Subsection 4.3.1 and Λ denotes the set of parameters that corresponds to the current model in use. The optimal objective function values are summarized in Table 4.1 for each model from Subsection 4.2.1 at each relative MTC length $\ell_{MTC}/\ell_{MTC,ref} \in \{0.85, ..., 1.1\}$. In Fig. 4.4, the model outputs are graphically compared to the experimental data. For clarity, only six of the ten curves are shown.

Figure 4.4(a), showing Model 1, is almost identical to [9, Fig. 7], additionally containing the adapted switching times t^*_{start} and t^*_{end} according to Subsection 4.3.1. After switch–on time, the force rises similar to, but obviously slower than the experimental data. However, after switch–off time, the force decrease in Model 1 is almost linear, whereas the experimental force decreases exponentially. The parameter set for Model 1 was taken from [9, Table 2]. The total residuum accounts for almost 500 N, see Table 4.1. The highest contributions to the residuum were made around the MTC reference length, mainly because of the incongruous force decay.

Consequently, in Model 2, we exchanged the eccentric branch of the force–velocity relation by the double–hyperbolic formulation from [10, 64], with the eccentric parameters F_e, S_e taken from [9]. This exchange improved Model 1 in Fig. 4.4(b) and resulted in an almost halved residuum. The improvement can be seen at relative MTC lengths less than 1.06. Supplementary to [10], we showed that adding the eccentric branch results in a *physiologically more accurate* rather than only a *faster* eccentric muscle contraction.

Taking a closer look at Model 2 in Fig. 4.4(b), the force decrease is too steep, especially at long relative muscle lengths. This steep decrease is a direct consequence of the parameter fit of Model 1 in [9], because Zajac's activation–deactivation ratio β was chosen based on a model with an non–physiological eccentric branch. This ratio was maximized ($\beta = 1$) to compensate for the slow force decay. To reveal the effect of the activation–deactivation

(a) Model 1: Zajac, no eccentric branch

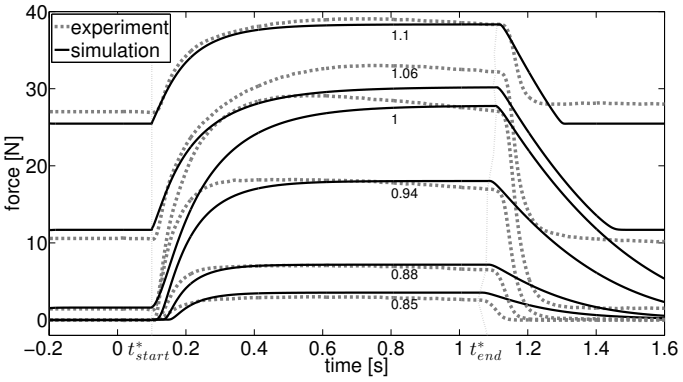

(b) Model 2: Zajac, eccentric branch, $\beta = 1$

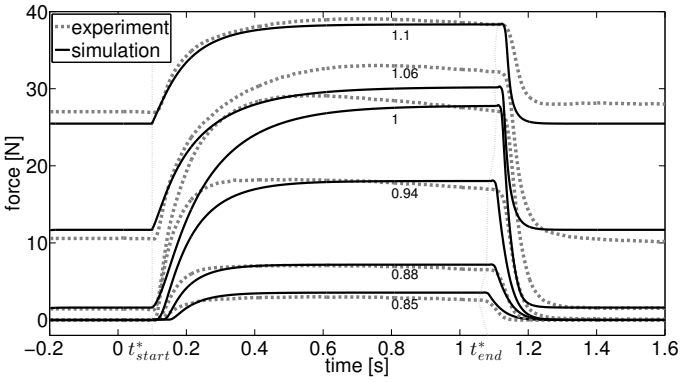

(c) Model 3: Zajac, eccentric branch, $\beta = 1/2$

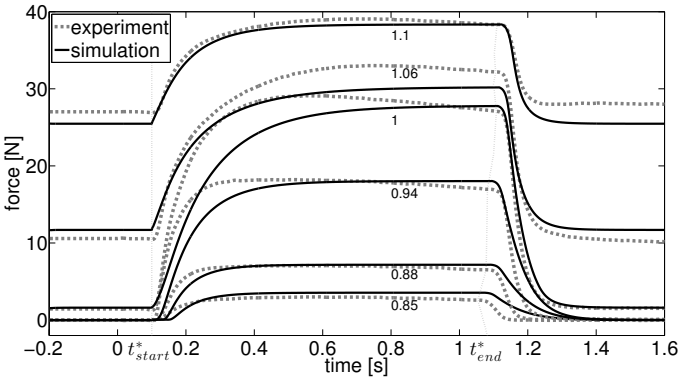

(d) Model 4: Hatze, eccentric branch

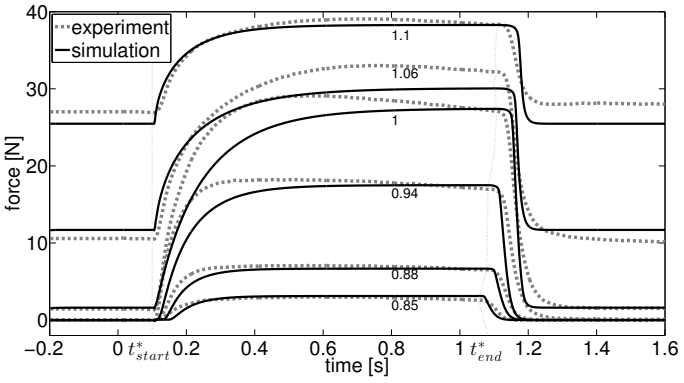

(e) Model 5a: Zajac, optimized parameters

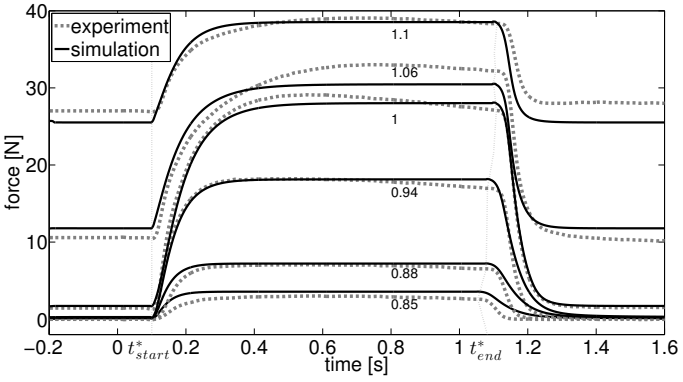

(f) Model 5b: Hatze, optimized parameters

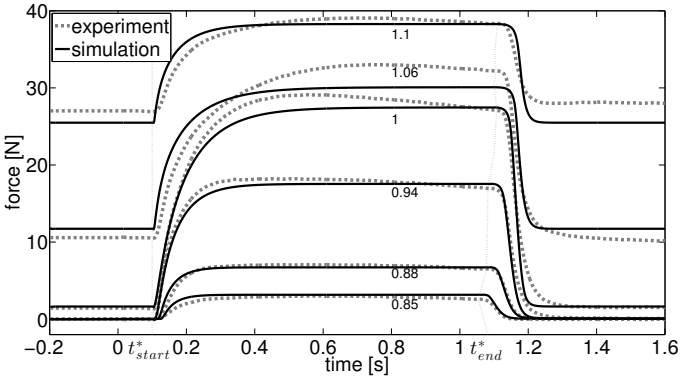

Figure 4.4.: Results from evaluating Models 1–5b from Section 4.2.1 in comparison to experimental ICEs: (a) Model 1 represents the model from [9] with Zajac's activation dynamics and non–physiological eccentric branch. (b) Model 2 includes the eccentric branch according to [10]. (c) Overestimation of force decay rate in Model 2 may be compensated by setting $\beta = 1/2$ (Model 3). (d) Model 4 replaces Zajac's with Hatze's activation dynamics with an optimized activation parameter set. (e) Model 5a contains an optimized parameter set of all dynamic parameters including Zajac's formulation. (f) Model 5b contains an optimized parameter set of all dynamic parameters including Hatze's formulation.

ratio, we halved the value of β in Model 3, which improved the residuum by approximately nine percent. The effect is particularly perceptible at long relative muscle lengths, see Fig. 4.4(c). However, at short relative MTC lengths ≤ 0.91 the residues worsened.

$\frac{\ell_{MTC,0}}{\ell_{MTC,ref}}$	Model 1	Model 2	Model 3	Model 4	Model 5a	Model 5b
0.85	12.76	7.45	9.64	3.70	10.36	**3.48**
0.88	21.67	6.88	11.76	7.12	9.81	**4.68**
0.91	40.57	15.48	20.85	13.75	14.32	**5.47**
0.94	61.04	26.88	26.37	23.56	15.42	**11.26**
0.97	85.76	33.55	35.22	28.18	19.44	**10.96**
1.00	94.26	44.51	37.76	35.28	**12.56**	14.42
1.03	80.11	48.10	38.80	38.18	**17.21**	21.69
1.06	52.36	37.30	30.23	32.45	**26.37**	29.79
1.08	26.62	28.23	19.88	24.25	**18.80**	23.49
1.10	21.79	26.62	**21.09**	24.45	23.82	22.81
Σ	496.94	275.00	251.60	230.92	168.11	**148.05**

Table 4.1.: Optimal objective function values (in Newton) for the six models in Fig. 4.4. For their respective parameter sets see Table 4.2. Each row represents an isometric contraction experiment at a given muscle length. The literature reference $\ell_{MTC,ref}$ was given as 6.15 cm in [9]. For a reliable comparison, the last row contains the sum of all objective function values. The best–fitting curve at each MTC length as well as the best overall residuum are printed in bold.

Regarding the muscle's activation dynamics, Zajac [65, Chapter 8] stated in reference to Hatze [15], that "the simplest model which fulfils the needs of the research and development project should be employed". Nevertheless, recent studies [7, 28, 52, 53] indicated that Hatze's formulation might be physiologically more relevant, because it includes a CE length dependency of the activation. Consequently, we replaced Zajac's formulation with Hatze's in Model 4 to test its validity, see Fig. 4.4(d). As no parameter set for Hatze's activation dynamics was given in [9], we performed the parameter estimation from Subsection 4.2.4 Eqns. (4.7) and (4.8) with respect to all Hatze parameters Λ_H, see (4.6). The resulting optimal parameter values Λ_H^* are shown in Table 4.2 (fourth column). The resulting parameter values are unusually large compared to literature values. For the activation time constant m this high value occurs, because the optimizer compensated the underestimated curvature of the force–time curves for times after t^*_{start} by accelerating the activation after a step in stimulation. For the parameter ℓ_ρ however, the small relative sensitivity allows the parameter to vary greatly in size with low impact on the solution. The model exchange resulted in a further eight percent decrease of the residuum, especially at short MTC lengths.

For a maximally fair comparison between Zajac's and Hatze's formulation, we chose either one or the other formulation and optimized all dynamic parameters at once.

Accordingly, in Model 5a, we optimized the parameter set $\Lambda_{D,Z}$ (cf. (4.6)) w.r.t the isometric muscle data, including Zajac parameters and the Hill constants $a_{rel,0}, b_{rel,0}$ as well as the eccentric parameters F_e, S_e. The total residuum decreased to 168.11 N, which is approximately one third of Model 1 and two thirds of Model 3 and 4. The residuum at medium MTC lengths decreased drastically, because the curvature of the force–time curves highly depends on the optimized Hill parameters, see Fig. 4.3(a). As a consequence of the optimization process, the estimated maximum CE velocity v_{max} from [9] increased by a

factor 4.5, because it depends linearly on the ratio $b_{rel,0}/a_{rel,0}$, see [9, Eqn. 7]. Additionally, the limit factor F_e increased to a value of 2.57, which seems unrealistically high compared to literature values from 1.3 to 1.8, see [11, 32, 39, 61]. Although all dynamic muscle parameters were optimized, the objective function values at short MTC lengths worsened compared to Model 4.

After having exchanged Zajac's with Hatze's formulation (Model 5b), we optimized the parameter set $\Lambda_{D,H}$ (cf. (4.6)). As shown in Table 4.1, the objective function value improved at every MTC length compared to Model 4 as well as at short lengths less than $\ell_{MTC,ref}$ compared to Model 5a. This effect is visible by comparing Figs. 4.4(e) and (f). At MTC lengths greater than $0.97 \cdot \ell_{MTC,ref}$, the residuum was approximately ten to twenty percent higher than in Model 5a, but improved altogether by twelve percent to a final value of 148.05 N. The corresponding optimal parameter values $\Lambda^*_{D,H}$ are again displayed in Table 4.2 (sixth column). Here, in contrast to Λ^*_H, every Hatze parameter stayed near to the initial guess. Similar to Model 5a, the optimized Hill parameters implied an increased v_{max}, but only by a factor of 2.2. The optimal eccentric force limit $F_e = 1.35$ is at the lower limit of the range found in literature. The most interesting optimal parameter value is found regarding S_e. Here, the ratio between eccentric and concentric slopes was determined as approximately 1, resulting in a differentiable force–velocity relation with no need for S_e. However, as stated in Subsection 4.3.2, S_e has the least sensitivity of all parameters and is therefore assumed to be unreliably estimated in these ICEs. The following Subsection 4.3.4 provides an ICE set–up in which the force output is maximally influenced by S_e.

parameter	source	Λ_{start}	Λ^*_H	$\Lambda^*_{D,Z}$	$\Lambda^*_{D,H}$
$a_{rel,0}$ [ ]	[9]	0.1		0.04	0.06
$b_{rel,0}$ [$\frac{1}{\mathrm{s}}$]	[9]	1.0		1.80	1.42
F_e [ ]	[9]	1.8		2.57	1.35
S_e [ ]	[9]	2.0		3.31	0.99
ℓ_ρ [ ]	[14, 28]	2.9	5.78		3.12
ρ_c [ ]	[14, 28, 53]	7.24	13.19		7.40
ν [ ]	[14, 28, 53]	3.0	2.44		3.14
m [$\frac{1}{\mathrm{s}}$]	adapted [14]	15.0	47.82		22.54
q_0 [ ]	[14, 28]	0.005	0.027	0.008	0.006
β [ ]	adapted [9]	0.50		0.66	
τ [s]	[9]	0.025		0.026	

Table 4.2.: Results of parameter estimation. Parameter symbols and units (first column), literature source for educated guess (second column), guessed start value for optimization (third column), results for optimizing Hatze parameters Λ_H only (Model 4: fourth column), results for optimizing all dynamic muscle parameters $\Lambda_{D,Z}$ including Zajac's formulation (Model 5a: fifth column), and results for optimizing all dynamic muscle parameters $\Lambda_{D,H}$ including Hatze's formulation (Model 5b: sixth column). The respective residues are shown in Table 4.1.

4.3.4. ICE Design for Determining S_e

Based on experiments [25] and according to models [9, 10, 64], the double hyperbolic force–velocity relation is assumed to be non–differentiable at the isometric state $\mathrm{d}/\mathrm{d}t\ \ell_{CE} = 0$. The parameter S_e describes the ratio between the slope of the eccentric and concentric branch at this point. As seen in Subsection 4.3.2, the relative sensitivity $\tilde{S}_{F_{MTC},S_e}(t)$ is the

smallest of all dynamic parameters (averaged maximum value 0.04). Thus, a parameter value increase of 10% would result in a 0.4% increase of the solution at this instant. Consequently, S_e can be chosen almost arbitrarily and is therefore hard to determine by a least square fit. The results from Table 4.2 even indicate that the parameter is superfluous in modeling isometric contractions.

Could it still be possible to determine the value of S_e using ICEs? As eccentric contraction experiments exhaust and damage the muscle [43, 61, 66], we constructed an ICE of which the output is substantially influenced by the S_e value. Our approach is based on five considerations:

1) The external conditions of ICEs are only determined by the applied stimulation σ and the fixed MTC length $\ell_{MTC,0}$.

2) Applying sensitivity analysis, we noted that changes in S_e affect the force output every time the CE switches to eccentric contraction mode, i.e. at $\mathrm{d}/\mathrm{d}t\ \ell_{CE} = 0$ transitions. Changes in S_e only influence the force output at small positive CE velocities. At larger positive velocities, the influence of the limit factor F_e takes over and at negative velocities, S_e exerts no influence at all.

3) For normalization, the sensitivities are divided by the current MTC force. Hence, the lower the force, the higher the expected relative sensitivity.

4) Forces can be systematically reduced by decreasing stimulation levels. By doing so, however, the signal to noise ratio may become too low, which is expected to be a limiting factor for the previous consideration.

5) The impacts of CE velocity and MTC force on the sensitivity may overlap or occur separately, see Fig. 4.5.

Consequently, we searched for an ICE set–up that maximized the relative sensitivity $\tilde{S}_{F_{MTC},S_e}(t) = \tilde{S}_{S_e}[\sigma, \ell_{MTC,0}/\ell_{MTC,ref}]$ w.r.t. the applied stimulation and fixed MTC length. To realize the combination of low positive CE velocities and low MTC forces, the stimulation has to be constructed as a slightly oscillating impulse at sub–maximal level. We tested four shapes of oscillating impulses, in particular rectangle, sawtooth, sine and triangle waves, but found no striking differences. Hence, for easier implementation in experiments, the oscillation was chosen as a rectangle wave of the form:

$$\sigma_R = \sigma_R(t) = a_R \cdot \mathrm{sgn}(\sin(f_R \cdot 2 \cdot \pi \cdot t)) + d_R \ ,$$

where $\mathrm{sgn}(x) := |x|/x$ denotes the sign (or signum) function. The parameters for amplitude $a_R \in [0, 1]$, frequency $f_R \in [1\,\mathrm{Hz}, 10\,\mathrm{Hz}]$, mean value $d_R \in [0, 1]$ and relative MTC length $\ell_{MTC,0}/\ell_{MTC,ref} \in \{0.85, ..., 1.1\}$ were varied systematically.

First we tried to find an ICE set–up with maximal absolute relative sensitivity, i.e. with maximum L^∞–norm $||f||_{L^\infty} = \max_{t\in[0,T]} |f(t)|$. Among all simulations, a maximum L^∞–value of $||\,\tilde{S}_{S_e}[\sigma_R, \ell_{MTC,0}/\ell_{MTC,ref}]\,||_{L^\infty} = 0.117$ occurred repeatedly at any MTC length with amplitudes below 0.4, mean value below 0.5 and frequencies between 1 Hz and 4 Hz. However, the L^∞–value of a sensitivity only refers to the influence on the output at a specific instance. Therefore as a second measurand, we investigated the overall relative sensitivity, by calculating the L^2–norm $||\,\tilde{S}_{S_e}[\sigma_R, \ell_{MTC,0}/\ell_{MTC,ref}]\,||_{L^2}$. Across all rectangle impulses, resulting in a maximum L^∞ sensitivity of 0.117, the highest L^2–value on the observed time interval $[0\,\mathrm{s}, 1.6\,\mathrm{s}]$ was 0.76 occurring for

$$\sigma_R^* = 0.2 \cdot \mathrm{sgn}(\sin(2\,\mathrm{Hz} \cdot 2 \cdot \pi \cdot t)) + 0.5, \quad \ell_{MTC,0} = 1.03 \cdot \ell_{MTC,ref} \ .$$

The resulting sensitivity $\tilde{S}_{S_e}[\sigma_R^*, 1.03]$ is displayed in Fig. 4.5. For comparison, the sensitivity $\tilde{S}_{S_e}[\overline{\sigma}, 1.03]$ is shown, exhibiting an L^∞–value of 0.03 and an L^2–value of 0.01.

Summarizing, we found an ICE set–up that is influenced by changes in S_e four times as much in terms of maximum sensitivity and around 75 times as much in terms of overall sensitivity, opposite to conventional ICEs. However, the absolute values are small compared to other parameter sensitivities, see Subsection 4.3.2. Thus, to determine the S_e value as accurately as possible, a parameter fit to the data of the suggested, additional ICE ought to be performed while fixing all remaining parameter values.

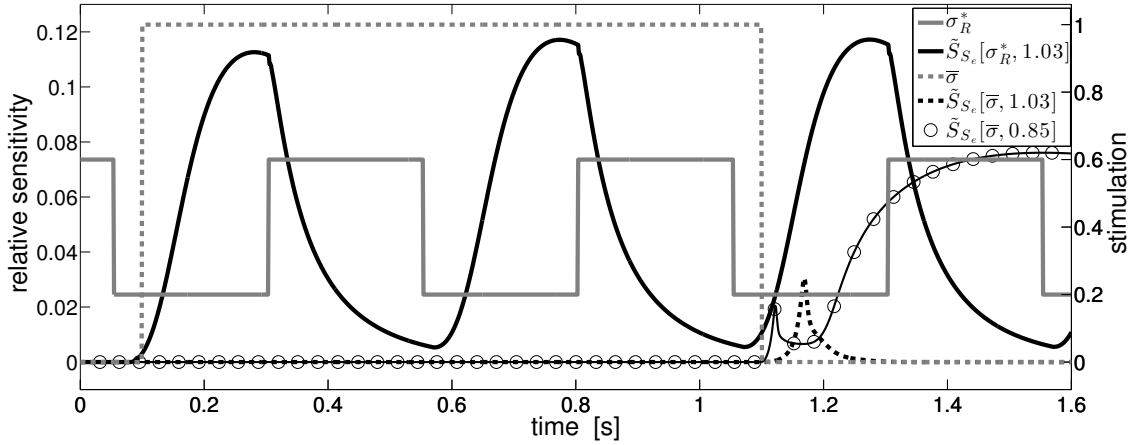

Figure 4.5.: Normalized sensitivities $\tilde{S}_{S_e}[\sigma, \ell_{MTC,0}/\ell_{MTC,ref}]$ of F_{MTC} w.r.t. S_e, dependent on the neural stimulation σ and the isometric MTC length $\ell_{MTC,0}$. The maximum sensitivity $\tilde{S}_{S_e}[\sigma_R^*, 1.03]$ (black line), subject to the L^∞–norm (0.117) as well as the L^2–norm (0.76), occurred for σ_R^* (gray line) at $\ell_{MTC,0} = 1.03 \cdot \ell_{MTC,ref} \approx 6,34\,\text{cm}$. In comparison, the sensitivity $\tilde{S}_{S_e}[\overline{\sigma}, 1.03]$ (black dashed line) is displayed, obtained from applying $\overline{\sigma}$ (gray dashed line) at the same MTC length, with an L^∞–value of 0.03 and an L^2–value of 0.01. To reveal the effects of slow positive CE velocities and low MTC forces on the sensitivity, we added the sensitivity $\tilde{S}_{S_e}[\overline{\sigma}, 0.85]$ (circles). After a step in stimulation from high to low level, the sensitivity first rises convexly due to low CE velocity until a limit velocity is exceeded. At higher velocities, the sensitivities $\tilde{S}_{S_e}[\overline{\sigma}, 1.03]$ and $\tilde{S}_{S_e}[\overline{\sigma}, 0.85]$ decrease exponentially. However, the latter begins to rise again concavely due to low MTC force, see Fig. 4.4. For sensitivity function $\tilde{S}_{S_e}[\sigma_R^*, 1.03]$, both effects superpose, resulting in a first–convex–then–concave, undulate rise of the sensitivity. After a step in stimulation from low to high level, the sensitivity decreases exponentially, tending to zero, because the concentric branch of the force–velocity relation applies.

4.4. Conclusions and Outlook

The results from Subsections 4.3.1 – 4.3.3 revealed the benefits of the interaction between physiological muscle experiments and various mathematical methods. By employing our methods on ICEs, experimentalists are in the *a–priori*–position to answer the following question: Given specific muscle model parts under test, are ICEs generally suitable for validating these parts and which set–up has to be chosen to maximize this validity? In addition, experimentalists are in the *a–posteriori*–position to answer the following questions: In terms of switching–times, do the data coincide with the experimental set–up? Furthermore, as an indicator of model validity, does a modified model improve a previous

version, in terms of a decreasing residuum?

ICEs allow extracting dynamic muscle properties. This finding was revealed by applying sensitivity analysis to an established Hill–type muscle model. The sensitivity approach enables a well–directed optimization to determine dynamic muscle parameters. As another consequence, we can give a suggestion for an experiment to estimate such an insensitive parameter as the step in slope of the force–velocity relation S_e. The eccentric branch of the force–velocity relation plays a significant role in ICEs (compare Model 1 and 2). The activation dynamics according to Hatze seems to be physiologically more valid than Zajac's formulation (Models 3–5). Furthermore, we conclude from analyzing Model 4 that the activation dynamics can not be validated in isolation, but only in combination with other model parts that have a comparable impact on contraction dynamics.

There are two conceivable continuations of this work. First, concerning theory, future model modifications should include an activity–dependent PEE, which is expected to model history effects like fatigue, force enhancement and force depression. Descriptions and attempts of modeling these known physiological effects can be found in [29, 30, 31, 37, 40, 54, 59, 60, 61], but they are phenomenological and lack a structural foundation except for [54]. Second, concerning the experimental set–up of ICEs, the theory of *optimal design* may be applied. Developed in the 1970s by [1, 3], this statistical auxiliary tool can systematically detect ICE set–ups that are optimal w.r.t. maximum absolute (or overall) parameter sensitivity. The challenge of optimal design lies in the absence of reference data. Nevertheless, it seems conceivable that every parameter of a muscle model can be accurately determined by specifically constructed ICEs.

Acknowledgements
The authors want to thank Prof. Dr.Veit Wank from the University of Tübingen for granting us access to his experimental data.

Conflict of interest
The authors declare that they have no conflicts of interest.

Bibliography

[1] H. Chernoff. *Sequential analysis and optimal design*. Society for Industrial and Applied Mathematics, 1972.

[2] S. Delp. "OpenSim: Open-Source Software to Create and Analyse Dynamic Simulations of Movement". In: *IEEE* 54.11 (2007), pp. 1940–1950.

[3] V. V. Fedorov and P. Hackl. *Theory of Optimal Experiments*. Academic Press, 1972.

[4] W. O. Fenn and B. S. Marsh. "Muscular force at different speeds of shortening". In: *The Journal of Physiology* 85.3 (1935), pp. 277–297.

[5] H. S. Gasser and A. V. Hill. "The dynamics of muscular contraction". In: *Proceedings of the Royal Society B* 96.678 (1924), pp. 398–437.

[6] A. M. Gordon, A. F. Huxley, and F. J. Julian. "The variation in isometric tension with sarcomere length in vertebrate muscle fibers". In: *The Journal of Physiology* 184.1 (1966), pp. 170–192.

[7] T. Götz, R. Rockenfeller, and K. P. Wijaya. "Optimization Problems in Epidemiology, Biomechanics & Medicine". In: *International Journal of Advances in Engineering Sciences and Applied Mathematics* 7.2 (2015), pp. 25–32.

[8] M. Günther. "Computersimulation zur Synthetisierung des muskulär erzeugten menschlichen Gehens unter Verwendung eines biomechanischen Mehrkörpermodells". PhD thesis. Universität Tübingen, 1997.

[9] M. Günther, S. Schmitt, and V. Wank. "High-frequency oscillations as a consequence of neglected serial damping in Hill-type muscle models". In: *Biological Cybernetics* 97.1 (2007), pp. 63–79.

[10] D. F. B. Haeufle et al. "Hill-type muscle model with serial damping and eccentric force-velocity relation". In: *Journal of Biomechanics* 47.6 (2014), pp. 1531–1536.

[11] J. D. Harry et al. "Cross-bridge cycling theories cannot explain high-speed lengthening behavior in frog muscle". In: *Biophysical Journal* 57.2 (1990), pp. 201–208.

[12] H. Hatze. "A General Myocybernetic Control Model of Skeletal Muscle". In: *Biological Cybernetics* 28.3 (1978), pp. 143–157.

[13] H. Hatze. "A Myocybernetic Control Model of Skeletal Muscle". In: *Biological Cybernetics* 25.2 (1977), pp. 103–119.

[14] H. Hatze. *Myocybernetic control models of skeletal muscle*. University of South Africa, 1981.

[15] H. Hatze. "Neuromusculoskeletal control systems modeling–A critical survey of recent developments". In: *IEEE Transactions on Automatic Control* 25.3 (1980), pp. 375–385.

[16] D. Hawkins and M. Bey. "Muscle and Tendon Force-Length Properties and Their Interactions In Vivo". In: *Journal of Biomechanics* 30.1 (1997), pp. 63–70.

[17] W. Herzog, S. K. Abrahamse, and H. E. D. J. ter Keurs. "Theoretical determination of force-length relations of human skeletal muscles using the cross-bridge model". In: *European Journal of Physiology* 416.1 (1990), pp. 113–119.

[18] W. Herzog et al. "Force-Length Properties and Functional Demands of Cat Gastrocnemius, Soleus and Plantaris Muscle". In: *Journal of Biomechanics* 25.11 (1992), pp. 1329–1335.

[19] A. V. Hill. "The Heat of Shortening and the Dynamic Constants of Muscle". In: *Proceedings of The Royal Society London B* 126.843 (1938), pp. 136–195.

[20] A. V. Hill. "The maximum work and mechanical efficiency of human muscles, and their most economical speed". In: *The Journal of Physiology* 56.1 (1922), pp. 19–41.

[21] P. A. Huijing. "Important experimental factors for skeletal muscle modelling: non-linear changes of muscle length force characteristics as a function of degree of activity". In: *European Journal of Morphology* 34.1 (1996), pp. 47–54.

[22] P. A. Huijing and G. J. Ettema. "Length-force characteristics of aponeurosis in passive muscle and during isometric and slow dynamic contractions of rat gastrocnemius muscle". In: *Acta morphologica Neerlando-Scandinavica* 26.1 (1988), pp. 51–62.

[23] G. C. Joyce and P. M. H. Rack. "Isotonic lengthening and shortening movements of cat soleus muscle". In: *The Journal of Physiology* 204.2 (1969), pp. 475–491.

[24] G. C. Joyce, P. M. H. Rack, and D. R. Westbury. "The mechanical properties of cat soleus muscle during controlled lengthening and shortening movements". In: *The Journal of Physiology* 204.2 (1969), pp. 461–474.

[25] B. Katz. "The Relation Between Force and Speed in Muscular Contraction". In: *The Journal of Physiology* 96.1 (1939), pp. 45–64.

[26] R. F. Ker. "Dynamic tensile properties of the plantaris tendon of sheep (*Ovis aries*)". In: *The Journal of Experimental Biology* 93 (1981), pp. 283–302.

[27] R. F. Ker, X. T. Wang, and A. V. Pike. "Fatigue quality of mammalian tendons". In: *The Journal of Experimental Biology* 203.Pt 8 (2000), pp. 1317–1327.

[28] D. A. Kistemaker, A. J. van Soest, and M. F. Bobbert. "Length-dependent [Ca2+] sensitivity adds stiffness to muscle". In: *Journal of Biomechanics* 38.9 (2005), pp. 1816–1821.

[29] N. Kosterina and A. Eriksson. "History effect and timing of force production introduced in a skeletal muscle". In: *Biomech Modell Mechanobiol* 11.7 (2012), pp. 947–957.

[30] N. Kosterina, H. Westerblad, and A. Eriksson. "Mechanical work as predictor of force enhancement and force depression". In: *Journal of Biomechanics* 42.11 (2009), pp. 1628–1634.

[31] N. Kosterina et al. "Muscular force production after concentric contraction". In: *Journal of Biomechanics* 41.11 (2008), pp. 2422–2429.

[32] A. M. Krylow and T. G. Sandercock. "Dynamic force responses of muscle involving eccentric contraction". In: *Journal of Biomechanics* 30.1 (1997), pp. 27–33.

[33] S. L. Lehman and L. W. Stark. "Three algorithms for interpreting models consisting of ordinary differential equations: sensitivity coefficients, sensitivity functions, global optimization". In: *Mathematical Biosciences* 62.1 (1982), pp. 107–122.

[34] K. Levenberg. “A Method for the Solution of Certain Problems in Least Squares”. In: *Quarterly of Applied Mathematics* 2 (1944), pp. 164–168.

[35] A. Levin and J. Wyman. “The viscous elastic properties of muscle”. In: *Proceedings of the Royal Society B* 101.709 (1927), pp. 218–243.

[36] H. Lupton. “The relation between the external work produced and the time occupied in a single muscular contraction in man”. In: *The Journal of Physiology* 57.1 (1922), pp. 68–75.

[37] B. R. Macintosh and D. E. Rassier. “What is Fatigue?” In: *Canadian Journal of Applied Physiology* 27.1 (2002), pp. 42–55.

[38] D. Marquart. “An Algorithm for Least-Squares Estimation of Nonlinear Parameters”. In: *SIAM Journal of Applied Mathematics* 11.2 (1963), pp. 431–441.

[39] H. Mashima et al. “The force-load-velocity relation and the viscous-like force in the frog skeletal muscle”. In: *Japanese Journal of Physiology* 22.1 (1972), pp. 103–120.

[40] C. P. McGowan, R. R. Neptune, and W. Herzog. “A phenomenological model and validation of shortening-induced force depression during muscle contractions”. In: *Journal of Biomechanics* 43.3 (2010), pp. 449–454.

[41] H. L. More et al. “Scaling of sensorimotor control in terrestrial mammals”. In: *Proceedings of the Royal Society B: Biological Sciences* 277.1700 (2010), pp. 3563–3568.

[42] J. J. Moré. “Numerical Analysis”. In: ed. by G. A. Watson. Dundee, 1978. Chap. The Levenberg-Marquardt Algorithm: Implementation and Theory, pp. 105–116.

[43] D. L. Morgan. “New insights into the behavior of muscle during active lengthening”. In: *Biophysical Journal* 57.2 (1990), pp. 209–221.

[44] F. Mörl, T. Siebert, and D. F. B. Haeufle. “Contraction dynamics and function of the muscle-tendon complex depend on the muscle fibre-tendon length ratio: a simulation study”. In: *Biomechanics and Modeling in Mechanobiology* (2015), published online.

[45] F. Mörl et al. “Electro-mechanical delay in Hill-type muscle models”. In: *Journal of Mechanics in Medicine and Biology* 12.5 (2012), pp. 85–102.

[46] T. J. Patel and R. L. Lieber. “Force transmission in skeletal muscle: from actomyosin to external tendons”. In: *Exercise and Sport Sciences Reviews* 25.1 (1997), pp. 321–364.

[47] C. M. Pollock and R. E. Shadwick. “Allometry of muscle, tendon, and elastic energy storage capacity in mammals”. In: *American Journal of Physiology* 266.3 Pt 2 (1994), R1022–1031.

[48] C. M. Pollock and R. E. Shadwick. “Relationship between body mass and biomechanical properties of limb tendons in adult mammals”. In: *American Journal of Physiology* 266.3 Pt 2 (1994), R1016–1021.

[49] A. Prochel. “Erstellung eines komplexen Muskel-Skelett-Modells zur Berechnung der Druckbelsastung in Gelenken bei vorwärtsdynamisch simulierten Bewegungsformen”. PhD thesis. Universität Tübingen, 2009.

[50] D. E. Rassier, B. R. Macintosh, and W. Herzog. “Length dependence of active force production in skeletal muscle”. In: *Journal of Applied Physiology* 86.5 (1999), pp. 1445–1457.

[51] J. M. Rijkelijkhuizen et al. “Extramuscular myofascial force transmission for in situ rat medial gastrocnemius and plantaris muscles in progressive stages of dissection”. In: *The Journal of Experimental Biology* 208.1 (2005), pp. 129–140.

[52] R. Rockenfeller and T. Götz. "Optimal Control of Isometric Muscle Dynamics". In: *Journal of Mathematical and Fundamental Sciences* 47.1 (2015), pp. 12–30.

[53] R. Rockenfeller et al. "Comparative Sensitivity Analysis of Muscle Activation Dynamics". In: *Computational and Mathematical Methods in Medicine* Article ID 585409, doi:10.1155/2015/585409 (2015), 16 pages.

[54] C. Rode, T. Siebert, and R. Blickhan. "Titin-induced force enhancement and force depression: A 'sticky-spring' mechanism in muscle contractions?" In: *Journal of Theoretical Biology* 259.2 (2009), pp. 350–360.

[55] A. Saltelli, K. Chan, and E. M. Scott. *Sensitivity Analysis*. 1st ed. John Wiley, 2000.

[56] T. Siebert et al. "Nonlinearities make a difference: comparison of two common Hill-type models with real muscle". In: *Biological Cybernetics* 98.2 (2008), pp. 133–143.

[57] H. Sugi and T. Tsuchiya. "Enhancement of mechanical performance in frog muscle fibres after quick increases in load". In: *The Journal of Physiology* 319.1 (1981), pp. 239–252.

[58] H. Sugi and T. Tsuchiya. "Isotonic velocity transients in frog muscle fibres following quick changes in load". In: *The Journal of Physiology* 319.1 (1981), pp. 219–238.

[59] O. Till, T. Siebert, and R. Blickhan. "A mechanism accounting for independence on starting length of tension increase in ramp stretches of active skeletal muscle at short half-sarcomere lengths". In: *Journal of Theoretical Biology* 266.1 (2010), pp. 117–123.

[60] O. Till, T. Siebert, and R. Blickhan. "Force depression decays during shortening in the medial gastrocnemius of the rat". In: *J. Biomechanics* 47.5 (2014), pp. 1099–1103.

[61] O. Till et al. "Characterization of isovelocity extension of activated muscle: A Hill-type model for eccentric contractions and a method for parameter determination". In: *Journal of Theoretical Biology* 225.2 (2008), pp. 176–187.

[62] R. Tomovic and M. Vukobratovic. *General Sensitivity Theory*. American Elsevier, New York, 1972.

[63] A. J. van Soest. "Jumping from Structure to Control: A Simulation Study of Explosive Movements". PhD thesis. Amsterdam: Vrije Universiteit, 1992.

[64] A. J. van Soest and M. F. Bobbert. "The contribution of muscle properties in the control of explosive movements". In: *Biological Cybernetics* 69.3 (1993), pp. 195–204.

[65] J. M. Winters and S. L. Y. Woo. *Multiple Muscle Systems - Biomechanics and Movement Organization*. Springer, 1990.

[66] S. A. Wood, D. L. Morgan, and U. Proske. "Effects of repeated eccentric contractions on structure and mechanical properties of toad sartorius muscle". In: *American Journal of Physiology* 265.3 Pt1 (1993), C792–800.

[67] F. E. Zajac. "Muscle and Tendon: Properties, Models, Scaling, and Application to Biomechanics and Motor Control". In: *Critical Reviews in Biomedical Engineering* 17.4 (1989), pp. 359–411.

5. Sensitivity Analysis of Different Contraction Modes

In our papers [67, 68] (Chapters 3 and 4), we investigated the influence of model parameters, which are associated to activation dynamics and other dynamic properties, on the force output of the muscle. To complete the picture of parameter–induced influences on the whole muscle model, we performed a sensitivity analysis among different contraction types. To determine a valid set of parameters, [27] used isometric, concentric and quick–release experiments to fit the model on an entire data set. During this process it was assumed that some parameters influence the output of specific experiments more than others. For example, a quick–release experiment was assumed to reveal the influence of SEE parameters [29], whereas a contraction against an inertial mass was assumed to reveal the influence of SDE parameters [27]. Since these assumptions were only based on educated guesses as well as graphical trial and error, we wanted to give a mathematical decision criterion. In the following, we outline certain muscle contraction modes, describing their set–ups, provide characteristics, and perform a sensitivity analysis including all occurring parameters. The model in use is elaborately described in Chapter 7, but we recall the DAE system for clarity.

$$\begin{aligned} \dot{q} &= f_1(\ell_{CE}, q, \sigma, \Lambda)\ , & q(0) &= q_0\ , \\ \dot{\ell}_{CE} &= f_2(\ell_{MTC}, \dot{\ell}_{MTC}, \ell_{CE}, q, \Lambda)\ , & \ell_{CE}(0) &= \ell_{CE,0}\ , \\ \ddot{\ell}_{MTC} &= f_D(\ell_{MTC}, \dot{\ell}_{MTC}, \ell_{CE}, q, \Lambda)\ , & \ell_{MTC}(0) &= \ell_{MTC,0}\ , \\ & & \dot{\ell}_{MTC}(0) &= 0 \\ F_{MTC} &= f_3(\ell_{MTC}, \dot{\ell}_{MTC}, \ell_{CE}, q, \Lambda)\ . \end{aligned} \tag{5.1}$$

Additionally, the following internal restrictions hold:

$$\begin{aligned} \ell_{CE} = \ell_{PEE}, \quad \ell_{SEE} = \ell_{SDE} \quad \text{and} \quad \ell_{MTC} = \ell_{CE} + \ell_{SEE} \\ F_{MTC} = F_{CE} + F_{PEE} = F_{SEE} + F_{SDE} \end{aligned} \tag{5.2}$$

The initial parameter set Λ was taken from [27, Table 2] and [67, Table 2, third column].

5.1. Simulated Experiments

5.1.1. Isometric Contractions

Isometric contractions experiments (ICEs) are comparatively easy to conduct by experimentalists. One end of the muscle is fixed, for example via the bone, by the use of screws or rods, to an apparatus. The other end of the muscle is also fixed, attached to a force transducer measuring the generated force, while keeping the length of the MTC constant, see Fig. 5.1 and [27, Fig. 1]. The muscle is then held passively at different lengths until the inner equilibrium is reached. In the experiments, on which this study is based on, the

muscle is fully stimulated at $t = t_{start}$ via the nerve for a certain time (in our case about one second) until $t = t_{end}$ and then left unstimulated again. Figure 5.5(a) shows the force–time curves for the simulated isometric contractions. For a comparison to experimental data see [27, Fig. 7].

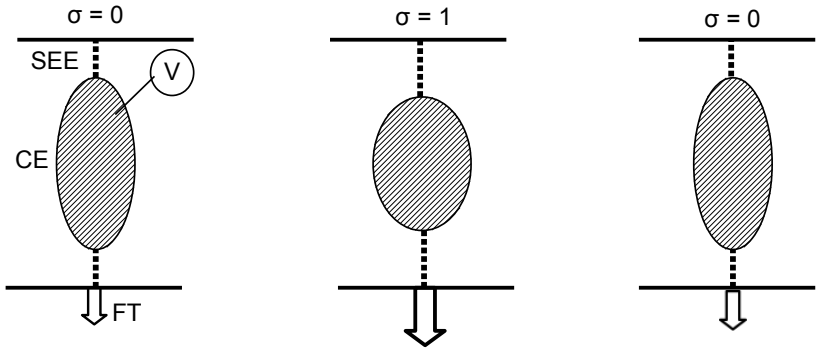

Figure 5.1.: Sketch of an isometric contraction experiment including a force transducer (FT) and a current source (V)

5.1.2. Isotonic Contractions

In contrast to isometric contractions, during an isotonic experiment, the MTC is allowed to change its length versus a controllable force. The free end of the muscle is attached to a movable lever (servo control), which is adjustable to a certain external load, see Fig. 5.2. After holding the muscle passively for a short time, the muscle is fully stimulated via the nerve at $t = t_{start}$. Consequently, the muscle first contracts isometrically and after exceeding the external load the MTC shortens at constant load (isotonically). Then, at $t = t_{ramp}$, the stimulation is switched off and the lever lengthens the muscle with a constant MTC velocity. System (5.1) has to be extended by the inequality constraint $F_{MTC} \leq F_{ext}$. Figure 5.5(b) shows the force–time curves for the simulated isotonic contractions.

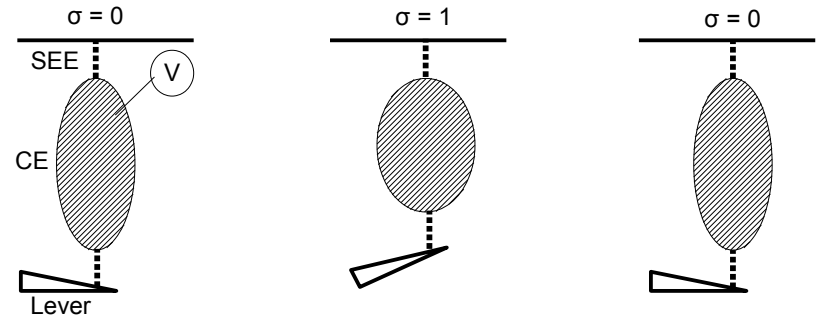

Figure 5.2.: Sketch of an isotonic contraction experiment including a lever and a current source (V)

5.1.3. Quick–Release Contractions

Quick–release experiments require a more sophisticated set–up. A mass is attached at the free end of the muscle via a (preferably stiff) rope and pulley system. At the beginning of the experiment, the free end is fixed by a controllable clamp, see Fig. 5.3 or [27, Fig. 1]. The muscle is then fully stimulated and held until the inner equilibrium is reached. At $t = t_{release}$ the clamp opens, allowing the muscle to contract against the inertial load, see below. An additional optical tracking system registers the position of the mass and the MTC length. Figure 5.5(c) shows the force–time curves for the simulated quick–release contractions.

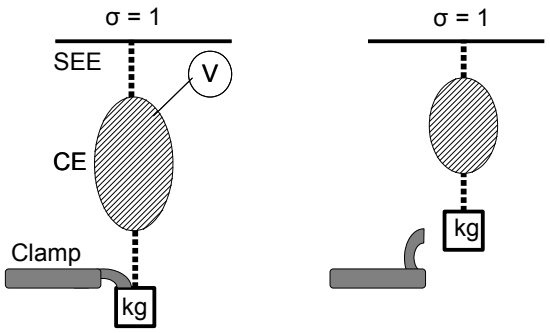

Figure 5.3.: Sketch of a quick–release contraction experiment including a mass (kg) and a current source (V)

5.1.4. Concentric Contractions Against an Inertial Mass

In contrast to quick–release, in the referred concentric contraction experiments, the mass is now placed on a solid surface and the clamp is removed, see Fig. 5.4. After reaching the inner equilibrium, the muscle is fully stimulated at $t = t_{start}$, first contracting isometrically against the mass. As soon as the muscle's force output exceeds the gravitational force on the mass, the MTC shortens and raises the attached mass. In contrast to the isotonic contraction, the acceleration of the muscle works against the gravitational acceleration g, which leads to an oscillating behavior of the MTC velocity over time, see [27, Figs. 6,11]. This effect is taken into account by writing down Newton's law of motion

$$F_{MTC} = mass \cdot (g - \ddot{\ell}_{MTC})$$

and thus a differential equation for $\dot{\ell}_{MTC}$ as

$$\ddot{\ell}_{MTC} = -\frac{1}{mass} \cdot \Big[F_{CE}(\ell_{CE}, \ell_{MTC}, \dot{\ell}_{MTC}, q) + F_{PEE}(\ell_{CE}) \Big] + g$$

Figure 5.5(d) shows the force–time curves for the simulated concentric contractions.

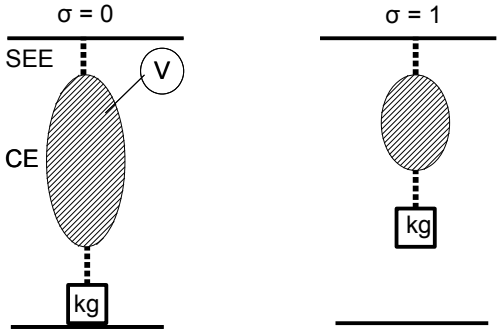

Figure 5.4.: Sketch of a concentric contraction experiment including a mass (kg) and a current source (V)

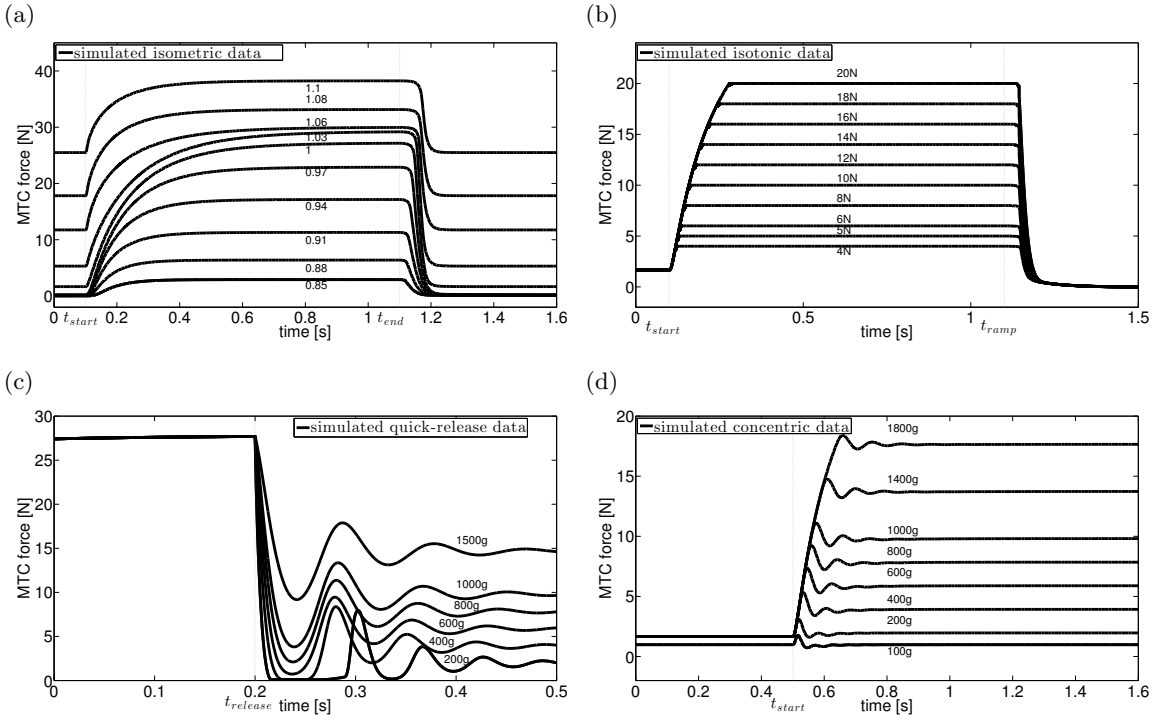

Figure 5.5.: Force–time curves of the simulated muscle experiments. (a) Isometric contraction cycle at various MTC lengths. The small numbers $0.85, ..., 1.1$ indicate the ratio $\ell_{MTC}/\ell_{MTC,ref}$, where $\ell_{MTC,ref} \approx 6.155\,\text{cm}$, see [27]. The steps in stimulation at $t_{start} = 0.1\,\text{s}$ (σ from 0 to 1) as well as at $t_{end} = 1.1\,\text{s}$ (σ from 1 to 0) are indicated with vertical dotted lines. (b) Isotonic contraction cycle with various loads, indicated by small numbers $4\,\text{N}, ..., 20\,\text{N}$. The steps in stimulation are marked at $t_{start} = 0.1\,\text{s}$ and $t_{ramp} = 1.1\,\text{s}$, where after t_{ramp} the lever lengthens the MTC with a constant velocity. (c) Quick–release contraction versus various masses, indicated by small numbers $200\,\text{g}, ..., 1500\,\text{g}$. The releasing time is marked at $t_{release} = 0.2\,\text{s}$. (d) Concentric contraction versus various masses, indicated by small number $100\,\text{g}, ..., 1800\,\text{g}$. The step in stimulation is marked at $t_{start} = 0.5\,\text{s}$.

5.2. Phase Portrait Analysis

Which contraction mode might be influenced the most by a specific parameter or whole sub–model? To answer the question, we use a phase portrait analysis. The so–called *phase space* Ψ is the space of all possible states of a (mechanical) system. The time–evolving path of the system is represented via a trajectory $\mathrm{Im}(\Gamma) \subset \Psi$ that is the image of a so–called *Jordan curve* Γ.

Definition 5.2.1. Let $I := [t_0, t_1] \subset \mathbb{R}$ and $\Psi \subseteq \mathbb{R}^n$ the phase space of the n states of a mechanical system. A curve $\Gamma : \ I \to \Psi$ is called a **Jordan curve** (or **simple curve**), if it is injective on $[t_0, t_1)$, i.e. if it does not cross itself. A Jordan curve for which holds $\Gamma(t_0) = \Gamma(t_1)$ is called **closed**.

Investigating a given Jordan curve requires an applicable depiction. In general, if $n > 3$, the image of Γ can not be fully displayed. Therefore, projections to suitable sub–spaces are performed.

Definition 5.2.2. Let Γ be a Jordan curve of a mechanical system, i.e. $\mathrm{Im}(\Gamma) \subset \Psi \subseteq \mathbb{R}^n$ represents the time evolution of the system in its phase space Ψ with $n > 3$. For $x \in \Psi$, let π_{ij} be the projection $\pi_{ij} : \ \Psi \to \mathbb{R}^2$ with $\pi_{ij}(x) = (x_i, x_j)^T$. Displaying the image of π_{ij} is called a **phase portrait**.

In the case of muscle experiments, the phase space consists of all states of system (5.1), namely $\Psi = (q, \ell_{CE}, \dot{\ell}_{MTC}, \ell_{MTC}, F_{MTC}) \subset \mathbb{R}^5$. Each muscle experiment corresponds to the image of a Jordan curve in $\mathbb{R}^5$. In order to project a curve to a two–dimensional sub–space, extrinsic restrictions such as $\ell_{CE} = \ell_{CE,opt}$ or $q = 1$ as well as intrinsic restrictions such as in Eqn. (5.2) have to be made. Figures 5.6 – 5.9 show four selected phase portraits that each reveal different muscle characteristics. In detail, the force–length, force–velocity, SEE and SDE characteristics. The figures can also be directly compared to Tables 5.2 to 5.6 in Section 5.3, containing the findings of the sensitivity analysis.

5.2.1. Force–Length Characteristics

In the first phase portrait, we project the phase space on the sub–space of two directly measurable system states: the MTC force and the MTC length. The force–length relation of muscle material is well–investigated [24, 38, 40, 45, 63, 79], because it reveals the influence of the static muscle components PEE, SEE and F_{isom} on muscle contractions. Experiments, whose trajectories best recreate the force–length relation, are thus higher influenced by the underlying parameter sets. Figure 5.6 shows the trajectories of all four contraction modes data. As a reference, the passive force–length relation $F_{SEE,pas} := F_{MTC} \mid_{q=0} = F_{PEE}$ and active force–length relation $F_{SEE,act} := F_{MTC} \mid_{q=1} = F_{PEE} + F_{isom}$ are displayed. These two characteristics ought to be extracted as good as possible from experiment data.

Isometric contractions are assumed to be static, because the MTC is held at a constant length. Hence, ICEs should provide a good characteristic of the length–dependent model

components. Figure 5.6(a) shows the phase portrait of an isometric contraction at various MTC lengths. One verifies immediately, that the passive (PEE) and active (PEE + CE) force–length curves are well recreated by taking the point of lowest and highest MTC force of each experiment.

The remaining contraction modes do neither sketch the active force–length relation above $\ell_{MTC,ref}$ nor the PEE at all, see Figs. 5.6(b) – (d). Using isotonic or concentric contractions, the ascending branch of the force–length characteristic can be extracted by taking the point of lowest MTC length of each experiment.

Summarizing, we conclude (and show in Table 5.6) that ICEs are best suited for recreating MTC force–length characteristics and thus to estimate the respective parameters.

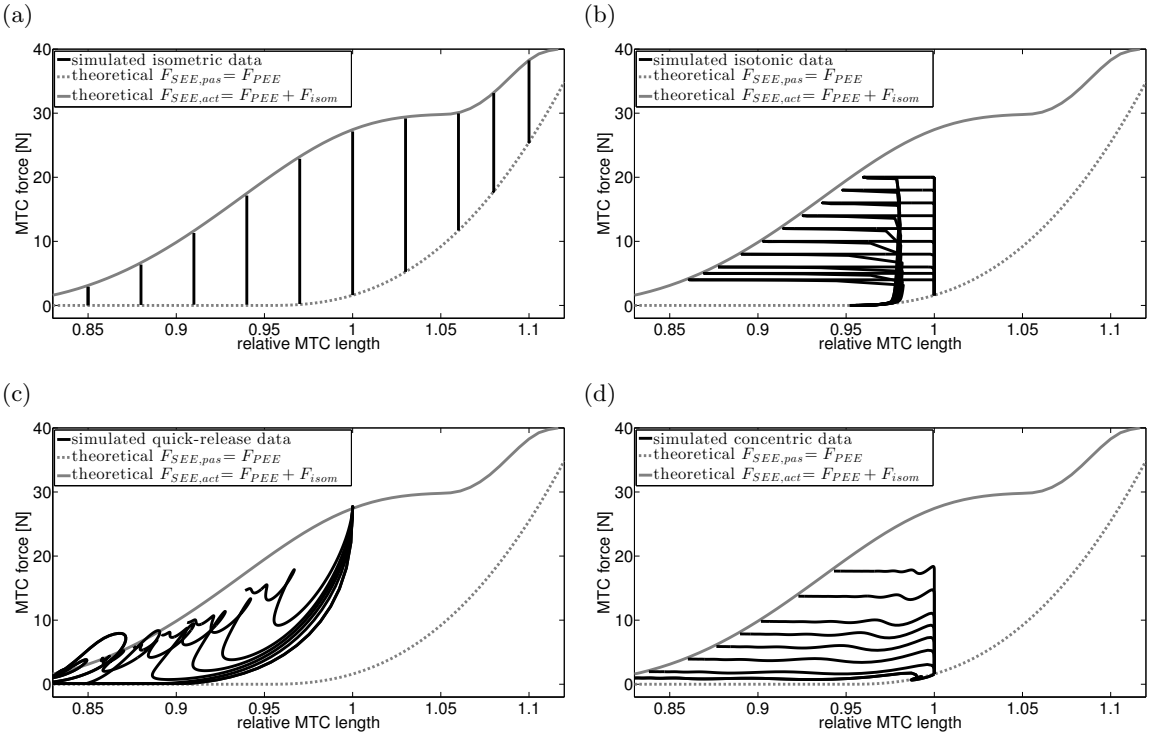

Figure 5.6.: MTC force versus relative MTC length phase portrait of the simulated muscle experiments. For comparison, the passive (no activity, i.e. $q = 0$) force $F_{SEE,pas}$ (gray dashed line) and active (full activity, i.e. $q = 1$) force $F_{SEE,act}$ (gray line) are displayed. (a) Isometric contraction: each experiment is represented by a vertical line, because the MTC length is constant. (b) Isotonic contraction: each curve starts at passive force at $\ell_{MTC} \approx \ell_{MTC,ref}$, describing an isometric contraction (vertical upward movement) up to the respective external load, a subsequent isotonic contraction (horizontal left movement), and a final eccentric contraction (relaxation, downward movement). (c) Quick–release contraction: each curve starts at active force at $\ell_{MTC} \approx \ell_{MTC,ref}$ and performs a quick contraction. For low attached masses, the curves almost reach the passive force. After this first, quick contraction, the muscle interacts with the mass, resulting in an oscillating behavior. (d) Concentric contraction: each curve starts at passive force at $\ell_{MTC} \approx \ell_{MTC,ref}$, performing an isometric contraction with a subsequent isotonic–like contraction. The slight oscillation results from the gravitational interaction with the mass.

5.2.2. Force–Velocity Characteristics

A second well–investigated characteristic is the relation between MTC force and CE velocity. As described by Hill in [41], a hyperbolic function does fit experimental data for concentric contractions ($v_{CE} < 0$). The expansion to eccentric contractions ($v_{CE} > 0$) in [30] was done by adding a hyperbolic branch with opposite curvature to bring the model closer to physiological behavior, see also [67]. Figure 5.7 shows the trajectories of all four contraction modes. As a reference, the force–velocity relation, including the restrictions $\ell_{CE} = \ell_{CE,opt}$ and $q = 1$, are displayed. Note that in our simulation, the CE lengths were obtained by solving system (5.1). When fitting experimental data, the CE lengths have to be calculated by finding the corresponding equilibria, see Section 2.3.2.

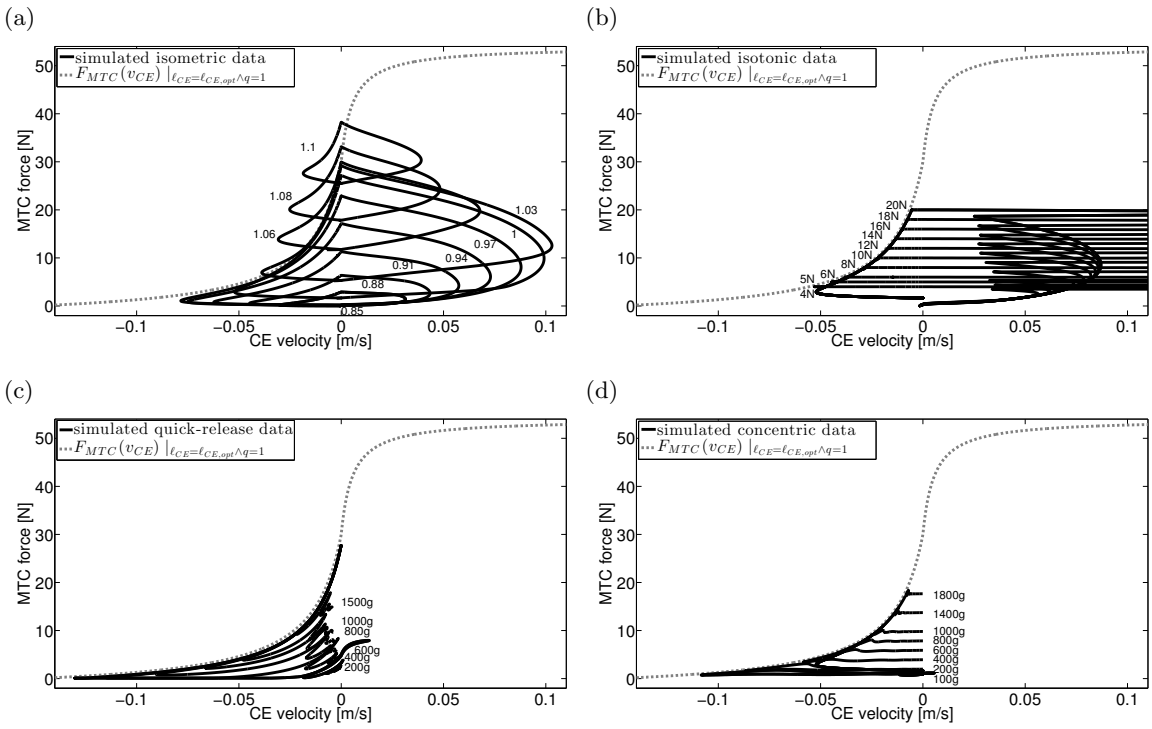

Figure 5.7.: MTC force versus CE velocity phase portrait of the simulated muscle experiments. For comparison, the force–velocity relation at optimal fiber length and full activity is displayed (gray dashed line). (a) Isometric contraction: for each experiment, the trajectory is a closed curve, because the simulation starts and ends at the passive equilibrium $v_{CE}\ |_{q=q_0} = 0$. (b) Isotonic contraction: each trajectory starts and ends at $v_{CE} = 0$. For scaling purposes, the eccentric contraction was pruned. The maximum (positive) velocity occurred at 4 N and accounted for approximately 1 m/s. During quick–release (c) and concentric contraction (d), there occurred no eccentric contraction.

Isotonic contractions against a pre–defined external load were developed to fit the theoretical force–velocity relation, cf. [47]. The idea behind this contraction mode is, that the muscle reaches its external load before its maximum CE velocity. Consequently, as displayed in Fig. 5.7(b), the force range is limited to the range of the external load. A comparison to the remaining contraction modes shows, that isotonic contraction in fact provides least information of the concentric branch of the force–velocity relation. This result can be confirmed in Table 5.6. However, isotonic contractions give indications of the eccentric behavior, because at the end of the stimulation process, the MTC as well as

the CE lengthen (relax) at sub–maximal activity level.

In the previous subsection, we stated that isometric experiments were assumed to be static. Figure 5.7(a) however, shows that they do fit the concentric force–velocity relation. Like isotonic contractions, ICEs do also provide eccentric characteristics at sub–maximal activity level. At MTC lengths greater than $\ell_{MTC,ref}$, it holds that $\ell_{CE} > \ell_{CE,opt}$ constantly, see Fig. 2.8. Hence, the simulated forces lie above the reference curve.

Quick–release and concentric experiments do provide a good fit of the concentric branch, but give no information about the eccentric behavior.

5.2.3. SEE Characteristics

Besides the MTC–force–MTC–length relation, the MTC–force–SEE–length relation can be obtained from the simulated data. Figure 5.8 displays the MTC forces w.r.t. the SEE length, which was scaled to $\ell_{MTC,ref}$. As a reference, we displayed the theoretical SEE–force–SEE–length relation that, in contrast to the MTC–force–SEE–length relation, does not include the damping force from the SDE.

The quick–release experiments were assumed to reveal SEE characteristics [27, 29], because after the release, the tendon contraction would dominate the muscle behavior. Indeed, these experiments show the widest $\ell_{SEE,rel} = \ell_{SEE}/\ell_{MTC,ref}$ range (from 0.65 to 0.83), but give the non–sharpest approximation of the corresponding SEE forces.

To measure the "sharpness" of the fits in Fig. 5.8, we provide two characteristic numbers in Table 5.1: The maximum absolute (L^∞) deviation of F_{MTC} and F_{SEE} as well as the average absolute ($\tilde{L}^1$) deviation, where

$$||f||_\infty := \max_{t\in[0,T]} |f(t)| \quad \text{and} \quad ||\tilde{f}||_1 := \frac{1}{T}\int_0^T |f(t)|\ \mathrm{d}t\ .$$

The lesser those values for $f(t) := F_{MTC}(t) - F_{SEE}(t)$, the sharper the respective fit.

Table 5.1.: Maximum absolute and average absolute deviation of experimental and theoretical MTC–force–SEE–length curves in Fig. 5.8

contraction mode	isometric	isotonic	quick–release	concentric
L^∞ deviation	3.21	2.19	8.01	0.46
average L^1 deviation	0.44	0.29	1.60	0.10

Isometric contractions provide a sharper approximation and a wider range in the "interesting" area ($\ell_{SEE} > \ell_{SEE,0}$) than the quick–release experiments. Isometric experiments have less $\ell_{SEE,rel}$ range (from 0.73 to 0.82). Concentric contractions perform the sharpest fit but do not cover $\ell_{SEE,0}$ (range from 0.75 to 0.82), see Fig. 5.7(a).

Summarizing, we conclude (and show in Table 5.6) that ICEs are best suited for recreating SEE force–length characteristics and thus to estimate the respective parameters.

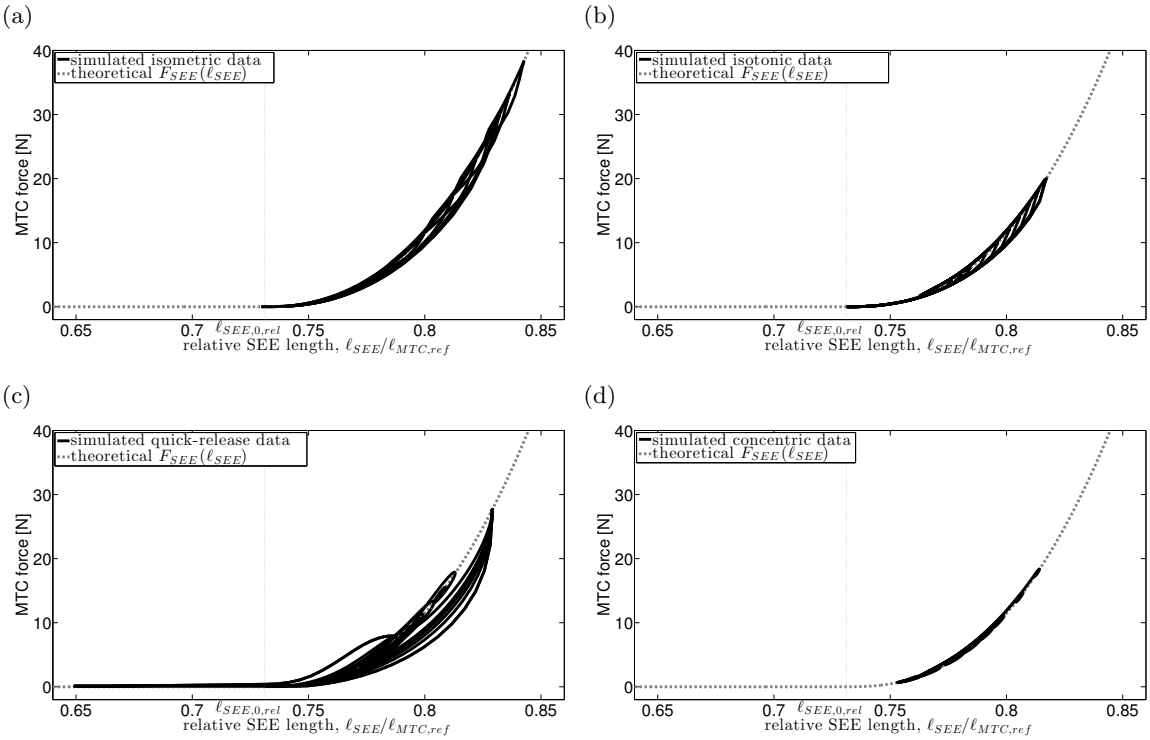

Figure 5.8.: MTC force versus relative SEE length phase portrait of the simulated muscle experiments. For comparison, the slack length $\ell_{SEE,0,rel} := \ell_{SEE,0}/\ell_{MTC,ref} = 0.73$ (gray vertical dots) as well as the theoretical F_{SEE} curve is displayed (gray dashed line). (a) Isometric contraction, (b) isotonic contraction, (c) quick–release contraction, and (d) concentric contraction. Note that (theoretically) the linear part of the SEE characteristics begins at $\ell_{SEE,rel} = (1 + \Delta U_{SEE,nll}) \cdot \ell_{SEE,0}/\ell_{MTC,ref} = 0.865$ (cf. [27, Fig. 4]) at $\Delta F_{SEE,0} = 60\,\mathrm{N}$ and lies beyond the range of any experiment.

5.2.4. SDE Characteristics

In [27, Fig. 11], the influence of a varying damping element is shown, using a concentric contraction against an inertial mass of 100 g. Figure 5.9 shows the exerted damping force of the simulated muscle at all contraction modes. As a reference, the SDE force, which depends linearly on the MTC force [66, Eqn. 12], is displayed at $\ell_{CE} = \ell_{CE,opt}$ and $v_{CE} = v_{max} := \ell_{CE,opt} q F_{isom} b_{rel}/a_{rel}$ [27, Eqn. 7]. This damping force is the maximal possible damping and serves as an lower bound. Note that the damping element acts opposite to the CE and its force is therefore negative during concentric contractions and positive during eccentric contractions.

Although [27] used concentric contractions to indicate the need for a damping element, this mode is least influenced by the underlying parameters among all contraction modes. The highest damping force is exerted in isometric experiments around $\ell_{MTC,ref}$. Hence, the assumption of ICEs only providing static characteristics of the muscle has to be revisited again. Quick–release experiments with low mass best fit the theoretical damping curve.

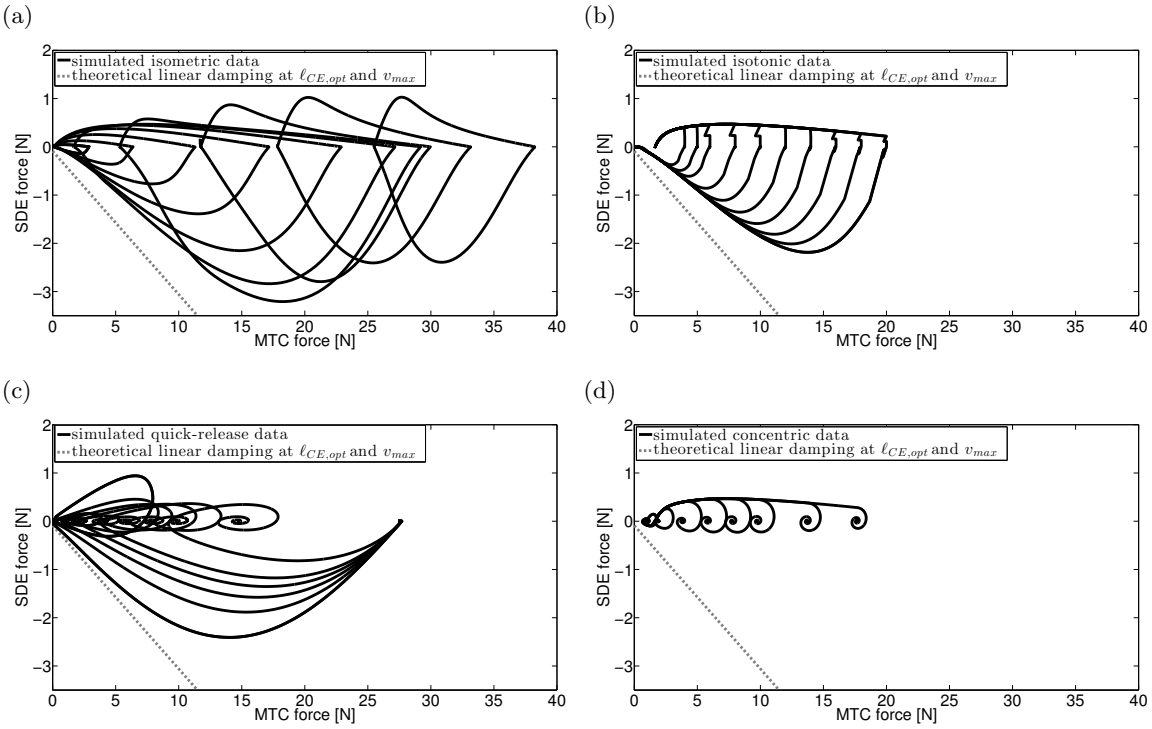

Figure 5.9.: SDE force versus MTC force phase portrait of the simulated muscle experiments. For comparison, the linear damping force at $\ell_{CE} = \ell_{CE,opt}$ and $v_{CE} = v_{max}$ is displayed (gray dashed line). (a) Isometric contraction, (b) isotonic contraction, (c) quick–release contraction, and (d) concentric contraction. Note that the *damping* is translational (unit [Ns/m]) rather than rotational (unit [Nm/s]) and depends linearly on the MTC force. The displayed *damping force* additionally depends linearly on the SEE velocity, see [30, Eqn. 13].

5.3. Sensitivity Analysis

In this section, we perform a sensitivity analysis as in [68, Eqn. (6) – (19)] of the complete activation–contraction dynamic system (5.1). We calculate the relative sensitivity of the exerted force w.r.t. the whole parameter set Λ at every contraction mode. For a better overview, we divide the set Λ into the following disjoint parameter sets:

- The SEE parameters $\Lambda_{SEE} = \{\ell_{SEE,0}, \Delta U_{SEE,nll}, \Delta F_{SEE,0}, \Delta U_{SEE,l}\}$
- The PEE parameters $\Lambda_{PEE} = \{\mathcal{F}_{PEE}, \mathcal{L}_{PEE,0}, \nu_{PEE}\}$
- The CE force–length parameters $\Lambda_{isom} = \{\Delta W_{asc}, \Delta W_{des}, \nu_{asc}, \nu_{des}, F_{max}, \ell_{CE,opt}\}$
- The Hill parameters $\Lambda_{Hill} = \{a_{rel,0}, b_{rel,0}\}$
- The SDE parameters $\Lambda_{damp} = \{D_{SE}, R_{SE}\}$
- The eccentric parameters $\Lambda_{ECC} = \{S_e, F_e\}$
- The Hatze activation parameters $\Lambda_{Hatze} = \{q_0, \ell_\rho, \rho_c, m, \nu\}$

After calculating the normalized sensitivity functions for every contraction mode w.r.t. every parameter, the maximum (L^∞) value (see [67]) of each sensitivity function served as a reference value for the corresponding parameter influence. A comparison regarding the L^2 norm is not suitable, because the contraction modes take place on different time scales.

Tables 5.2 – 5.5 show the maximal relative sensitivities, previously defined as the normalization $\max_{t\in I}|\tilde{S}_{\lambda_i,F_{MTC}}(t)| = \max_{t\in I}|S_{\lambda_i,F_{MTC}}(t)|\cdot\lambda_i/F_{MTC}$. An analysis of the entire sensitivity functions (in this section over 800) can be of interest, when tracking the influence of a specific parameter in a specific contraction mode, but is beyond the scope of this section. In the following, we give a summary of observations, tendencies and explanations for the occurring maximum sensitivity values for all simulated contraction modes. Table 5.6 contains a juxtaposition of maximum L^∞ sensitivity values among the different contraction modes.

5.3.1. Isometric Contractions

In the isometric case, the influence of $\Lambda_{SEE}, \Lambda_{Hill}, \Lambda_{damp}$ and Λ_{Hatze} parameters is tendentially decreasing with increasing MTC length. The opposite holds for parameters in Λ_{PEE}. However, we note that there is a local sensitivity maximum for most of the parameters at $\ell_{MTC}/\ell_{MTC,ref} \in \{0.97, 1\}$, especially distinct for the slack–length parameters $\ell_{SEE,0}, \ell_{CE,opt}, \mathcal{L}_{PEE,0}$.

The most sensitive parameter is the SEE slack–length $\ell_{SEE,0}$ (maximum value of 323.51), especially at short MTC lengths. The least sensitive parameters are S_e, ν_{des}, ΔW_{des}, R_{SE} and D_{SE} (maximum value of less than 0.3).

Expectably, the influence of CE force–length parameters is decreasing with increasing MTC length, if they belong to the ascending limb ($\Delta W_{asc}, \nu_{asc}$), and increasing, if they belong to the descending limb ($\Delta W_{des}, \nu_{des}$). The maximum sensitivity of F_{max} remains almost constant.

Consequently, when performing isometric contractions to estimate parameters, there should be experiments at short, medium and long MTC lengths.

5.3.2. Isotonic Contractions

Most parameter sensitivities remain constant among the various loads up to 12 N – 16 N. At higher loads, the sensitivity increases ($\Lambda_{SEE}, \Lambda_{PEE}$ and Λ_{Hill}) or remains constant ($\Lambda_{ECC}, \Lambda_{damp}$). The activation parameters m and ρ_c are the only parameters with a decreasing influence, because at higher loads, the activation process has almost come to an end before the MTC begins to shorten.

As in the isometric case, the most sensitive parameter is the SEE slack–length $\ell_{SEE,0}$ (maximum value of 19.49) at 20 N. The least sensitive parameters are $\nu_{des}, R_{SE}, S_e, D_{SE}, q_0$ and ΔW_{des} (maximum value of less than 0.3).

5.3.3. Quick–Release Contractions

With increasing mass, the influence of Λ_{SEE}, ΔW_{asc}, ν_{asc}, $\ell_{CE,opt}$ and Λ_{damp} parameters decreases. The Hill parameters as well as F_{max} have a local maximum sensitivity at $mass \in \{400\,\text{g}, 600\,\text{g}\}$.

The most sensitive parameter is the SEE slack–length $\ell_{SEE,0}$ (maximum value of 44.97) at 200 g. Parameters in $\Lambda_{PEE}, \Lambda_{Hatze}$ (maximum value less than 10^{-4}) as well as ΔW_{des}, ν_{des}, Λ_{damp} (maximum value less than 0.2) have virtually no influence on the force output, because the muscle is fully activated and shortens concentrically subject to SEE properties.

5.3.4. Concentric Contractions

Parameters from $\Lambda_{SEE}, \Lambda_{PEE}, \Lambda_{Hill}$ and Λ_{Hatze} have a decreasing influence with increasing mass and obtain a stationary value above 200 g–600 g. No parameter sensitivity value is increasing alongside the mass. Hence, these experiments are superfluous when estimating parameter values. In [27, Fig. 11], the damping is intuitively fit for the lowest mass, at which point all occurring parameters have the highest influence. But looking at Table 5.5, we see that the damping influence remains constant, whereas the influence of the other parameters decreases. Thus, it would be more advantageous to fit the damper at higher masses.

The most sensitive parameter is again the SEE slack–length $\ell_{SEE,0}$ (maximum value of 36.49) at 100 g. The least sensitive parameters are R_{SE}, D_{SE}, q_0 and ΔW_{des}. The influence of ν_{des}, S_e and F_e is almost negligible (maximum value less than $2 \cdot 10^{-4}$).

Table 5.2.: Maximum L^∞ values of the normalized sensitivity functions of the simulated isometric contraction force w.r.t. every occurring parameter (rows). The columns represent the respective relative MTC length.

		relative MTC length $\ell_{MTC}/\ell_{MTC,ref}$									
group	parameter	0.85	0.88	0.91	0.94	0.97	1.00	1.03	1.06	1.08	1.10
Λ_{SEE}	$\ell_{SEE,0}$	323.51	36.75	23.78	19.98	40.73	16.72	12.77	8.40	3.87	6.59
	$\Delta U_{SEE,nll}$	9.13	3.67	2.98	2.63	3.54	2.26	1.97	1.30	0.60	1.03
	$\Delta F_{SEE,0}$	0.84	0.60	0.57	0.57	0.60	0.66	0.61	0.40	0.19	0.35
	$\Delta U_{SEE,l}$	7.03	2.25	1.74	1.50	2.26	1.09	0.45	0.29	0.12	0.24
Λ_{PEE}	$\mathcal{F}_{PEE}$	0.00	0.00	0.00	0.00	0.10	0.16	0.14	0.13	0.16	0.27
	$\mathcal{L}_{PEE,0}$	0.00	0.00	0.00	0.00	8.20	2.81	1.16	0.30	0.30	0.47
	ν_{PEE}	0.00	0.00	0.00	0.00	0.57	0.42	0.22	0.09	0.05	0.10
Λ_{isom}	ΔW_{asc}	7.48	2.76	1.88	1.20	0.65	0.24	0.04	0.00	0.00	0.00
	ΔW_{des}	0.00	0.00	0.00	0.00	0.15	0.24	0.20	0.17	0.13	0.24
	ν_{asc}	0.69	0.45	0.34	0.24	0.24	0.16	0.05	0.00	0.00	0.00
	ν_{des}	0.00	0.00	0.00	0.00	0.00	0.00	0.00	0.04	0.11	0.21
	F_{max}	0.96	0.99	1.02	1.04	0.91	0.85	0.95	0.98	0.90	1.08
	$\ell_{CE,opt}$	5.86	3.40	2.85	2.65	10.47	4.60	3.08	2.32	1.14	2.09
Λ_{Hill}	$a_{rel,0}$	2.54	0.72	0.67	0.68	0.59	0.22	0.13	0.08	0.06	0.04
	$b_{rel,0}$	2.55	0.93	0.94	0.98	0.94	0.61	0.41	0.32	0.27	0.20
Λ_{damp}	D_{SE}	0.29	0.15	0.18	0.21	0.20	0.08	0.04	0.02	0.02	0.03
	R_{SE}	0.26	0.09	0.09	0.10	0.08	0.01	0.00	0.00	0.00	0.00
Λ_{ECC}	S_e	0.12	0.13	0.13	0.13	0.11	0.04	0.05	0.05	0.05	0.06
	F_e	0.84	0.87	0.91	0.94	0.96	0.96	0.96	0.86	0.72	0.66
Λ_{Hatze}	q_0	2.60	0.88	0.91	0.93	0.85	0.14	0.04	0.02	0.01	0.01
	ℓ_ρ	0.70	0.71	0.72	0.71	0.65	0.53	0.31	0.09	0.02	0.06
	ρ_c	2.04	1.90	2.10	2.31	2.48	2.56	2.31	1.78	1.52	1.34
	m	3.04	3.58	4.21	4.85	5.42	5.51	4.54	3.44	3.03	2.62
	ν	2.60	2.75	2.94	3.08	3.14	2.50	1.44	0.83	0.59	0.34

Table 5.3.: Maximum L^∞ values of the normalized sensitivity functions of the simulated isotonic contraction force w.r.t. every occurring parameter (rows). The columns represent the respective maximum forces.

		maximum force $[N]$									
group	parameter	4	5	6	8	10	12	14	16	18	20
Λ_{SEE}	$\ell_{SEE,0}$	14.49	14.49	14.49	14.49	14.49	14.49	14.49	15.94	17.49	19.49
	$\Delta U_{SEE,nll}$	2.03	2.03	2.03	2.03	2.03	2.03	2.03	2.11	2.24	2.39
	$\Delta F_{SEE,0}$	0.44	0.44	0.44	0.44	0.44	0.44	0.44	0.45	0.46	0.47
	$\Delta U_{SEE,l}$	0.95	0.95	0.95	0.95	0.95	0.95	0.95	1.00	1.10	1.23
Λ_{PEE}	$\mathcal{F}_{PEE}$	0.14	0.14	0.14	0.14	0.14	0.14	0.14	0.14	0.14	0.14
	$\mathcal{L}_{PEE,0}$	2.40	2.40	2.40	2.40	2.40	2.40	2.40	2.40	2.48	2.76
	ν_{PEE}	0.37	0.37	0.37	0.37	0.37	0.37	0.37	0.37	0.37	0.38
Λ_{isom}	ΔW_{asc}	0.70	0.92	1.14	1.37	1.59	1.81	2.03	2.53	2.85	3.25
	ΔW_{des}	0.21	0.21	0.21	0.21	0.21	0.21	0.21	0.21	0.21	0.21
	ν_{asc}	0.26	0.26	0.23	0.23	0.24	0.26	0.31	0.43	0.50	0.58
	ν_{des}	0.00	0.00	0.00	0.00	0.00	0.00	0.00	0.00	0.00	0.00
	F_{max}	0.72	0.74	0.77	0.79	0.81	0.82	0.84	0.85	0.86	0.95
	$\ell_{CE,opt}$	3.93	3.93	3.93	3.93	3.93	3.93	3.93	3.93	3.93	4.26
Λ_{Hill}	$a_{rel,0}$	0.22	0.22	0.22	0.22	0.22	0.24	0.26	0.32	0.39	0.50
	$b_{rel,0}$	0.60	0.60	0.60	0.60	0.61	0.67	0.78	0.92	1.02	1.16
Λ_{damp}	D_{SE}	0.08	0.08	0.08	0.08	0.08	0.08	0.08	0.08	0.08	0.10
	R_{SE}	0.01	0.01	0.01	0.01	0.01	0.01	0.01	0.01	0.01	0.01
Λ_{ECC}	S_e	0.04	0.04	0.04	0.04	0.03	0.03	0.03	0.03	0.03	0.03
	F_e	0.96	0.96	0.96	0.96	0.96	0.96	0.96	0.98	0.98	0.99
Λ_{Hatze}	q_0	0.26	0.26	0.26	0.26	0.26	0.26	0.26	0.26	0.26	0.26
	ℓ_ρ	0.67	0.71	0.75	0.78	0.80	0.83	0.85	0.88	0.89	0.90
	ρ_c	2.44	2.43	2.42	2.40	2.39	2.37	2.36	2.33	2.32	2.31
	m	4.83	4.71	4.60	4.49	4.38	4.27	4.14	3.99	3.90	3.79
	ν	3.19	3.20	3.20	3.20	3.20	3.20	3.20	3.19	3.18	3.16

Table 5.4.: Maximum L^∞ values of the normalized sensitivity functions of the simulated quick–release contraction force w.r.t. every occurring parameter (rows). The columns represent the respective attached masses.

		affixed load [g]					
group	parameter	200	400	600	800	1000	1500
Λ_{SEE}	$\ell_{SEE,0}$	44.97	29.87	15.47	11.82	9.41	6.98
	$\Delta U_{SEE,nll}$	3.05	2.60	1.64	1.21	0.98	0.90
	$\Delta F_{SEE,0}$	0.40	0.51	0.41	0.35	0.26	0.25
	$\Delta U_{SEE,l}$	2.59	2.13	1.39	1.20	1.05	0.75
Λ_{PEE}	$\mathcal{F}_{PEE}$	0.00	0.00	0.00	0.00	0.00	0.00
	$\mathcal{L}_{PEE,0}$	0.00	0.00	0.00	0.00	0.00	0.00
	ν_{PEE}	0.00	0.00	0.00	0.00	0.00	0.00
Λ_{isom}	ΔW_{asc}	9.92	5.16	2.20	1.13	0.75	0.37
	ΔW_{des}	0.00	0.00	0.00	0.00	0.00	0.00
	ν_{asc}	0.44	0.52	0.56	0.45	0.32	0.20
	ν_{des}	0.00	0.00	0.00	0.00	0.00	0.00
	F_{max}	1.36	1.43	1.44	1.33	1.15	0.90
	$\ell_{CE,opt}$	5.86	3.22	1.55	0.87	0.64	0.49
Λ_{Hill}	$a_{rel,0}$	0.90	1.51	0.81	0.43	0.19	0.12
	$b_{rel,0}$	1.00	1.72	1.26	0.95	0.61	0.29
Λ_{damp}	D_{SE}	1.44	0.42	0.26	0.22	0.18	0.12
	R_{SE}	0.19	0.05	0.02	0.01	0.01	0.00
Λ_{ECC}	S_e	0.03	0.00	0.00	0.00	0.00	0.00
	F_e	0.17	0.00	0.00	0.00	0.00	0.00
Λ_{Hatze}	q_0	0.00	0.00	0.00	0.00	0.00	0.00
	ℓ_ρ	0.00	0.00	0.00	0.00	0.00	0.00
	ρ_c	0.00	0.00	0.00	0.00	0.00	0.00
	m	0.00	0.00	0.00	0.00	0.00	0.00
	ν	0.00	0.00	0.00	0.00	0.00	0.00

Table 5.5.: Maximum L^∞ values of the normalized sensitivity functions of the simulated concentric contraction force w.r.t. every occurring parameter (rows). The columns represent the respective attached masses.

		affixed load [g]							
group	parameter	100	200	400	600	800	1000	1400	1800
Λ_{SEE}	$\ell_{SEE,0}$	36.49	24.56	17.22	13.60	13.08	13.08	13.08	13.08
	$\Delta U_{SEE,nll}$	3.28	2.59	2.13	1.90	1.90	1.90	1.90	1.90
	$\Delta F_{SEE,0}$	0.50	0.44	0.42	0.42	0.42	0.42	0.42	0.42
	$\Delta U_{SEE,l}$	2.04	1.49	1.09	0.87	0.87	0.87	0.87	0.87
Λ_{PEE}	$\mathcal{F}_{PEE}$	0.16	0.14	0.13	0.13	0.13	0.13	0.13	0.13
	$\mathcal{L}_{PEE,0}$	4.44	2.93	2.18	2.14	2.14	2.14	2.14	2.14
	ν_{PEE}	0.52	0.38	0.33	0.33	0.33	0.33	0.33	0.33
Λ_{isom}	ΔW_{asc}	7.23	4.83	3.29	2.56	2.07	1.70	1.14	0.74
	ΔW_{des}	0.23	0.20	0.19	0.19	0.19	0.19	0.19	0.19
	ν_{asc}	1.48	0.91	0.45	0.31	0.28	0.26	0.23	0.20
	ν_{des}	0.00	0.00	0.00	0.00	0.00	0.00	0.00	0.00
	F_{max}	0.93	0.91	0.90	0.88	0.85	0.83	0.79	0.75
	$\ell_{CE,opt}$	6.19	4.10	3.49	3.49	3.49	3.49	3.49	3.49
Λ_{Hill}	$a_{rel,0}$	2.30	1.14	0.53	0.33	0.26	0.22	0.22	0.22
	$b_{rel,0}$	3.04	1.87	1.22	0.96	0.80	0.70	0.60	0.60
Λ_{damp}	D_{SE}	0.07	0.07	0.08	0.08	0.08	0.08	0.08	0.08
	R_{SE}	0.01	0.01	0.01	0.01	0.01	0.01	0.01	0.01
Λ_{ECC}	S_e	0.00	0.00	0.00	0.00	0.00	0.00	0.00	0.00
	F_e	0.00	0.00	0.00	0.00	0.00	0.00	0.00	0.00
Λ_{Hatze}	q_0	0.15	0.09	0.09	0.09	0.09	0.09	0.09	0.09
	ℓ_ρ	0.31	0.22	0.14	0.10	0.08	0.06	0.04	0.03
	ρ_c	0.98	0.81	0.80	0.80	0.80	0.80	0.80	0.80
	m	0.96	0.84	0.84	0.84	0.84	0.84	0.84	0.84
	ν	0.44	0.32	0.32	0.32	0.32	0.32	0.32	0.32

5.3.5. Comparison of the Contraction Modes

Table 5.6 shows the row–wise maximum values from Tables 5.2 – 5.5 with four digits accuracy. The row–wise maximum of these values are printed in bold, i.e.

$$\max_{\text{contraction modes}} \quad \max_{\text{experiment variations}} \quad \max_{t \in I} \; |\tilde{S}_{\lambda_i, F_{MTC}}(t)| \; .$$

As seen in Fig. 5.6 – 5.9, most parameters have their highest influence on the MTC force during isometric contractions. In the case of Λ_{SEE} and Λ_{PEE}, the influence is up to seven times higher compared to the other contraction modes. Furthermore, the maximum L^∞ sensitivities of F_e, ℓ_ρ and ν in the isotonic case, and the maximum L^∞ sensitivities of ΔW_{asc} and F_{max} in the quick–release case are just slightly higher than in the isometric case. The higher values for $b_{rel,0}$ in the concentric case are explainable by the circumstance that this mode allowed the muscle to shorten quicker and thus better fit the concentric branch of the force–velocity relation.

The only parameters, whose maximum sensitivity is significantly ($\geq 50\%$) higher than in the isometric case, are D_{SE} during the quick–release experiment and ν_{asc} during the concentric experiment, both against a low mass.

Summarizing the results from Figs. 5.6 – 5.9 and Tables 5.2 – 5.6, we derive the following statements:

- Although isotonic experiments were designed to obtain meaningful force–velocity characteristics, they turned out to be least sensitive to Λ_{Hill}.
- Although quick–release experiments were designed to obtain meaningful SEE and force–velocity characteristics, they turned out to be less sensitive to Λ_{SEE} and Λ_{Hill} than ICEs.
- Although concentric contraction against an inertial mass were used to indicate a need for a SDE, they are least influenced by Λ_{damp} throughout all contraction modes.

We showed in Chapter 4 ([67]) that isometric experiments allow for determining dynamic muscle properties. In comparison with various other contraction modes, we now quantified the respective parameter influences. We saw that ICEs can provide a basis for an overall parameter estimation. Hence, instead of performing sophisticated and error–prone experiments, ICEs might solely suffice to perform a complete parameter fit with minimal effort.

Table 5.6.: Maximum of the maximum L^∞ sensitivities from Tables 5.2 – 5.5 w.r.t. every occurring parameter throughout every contraction mode. For every parameter, the highest relative sensitivity is printed in bold.

		contraction type			
group	parameter	isometric	isotonic	quick–release	concentric
Λ_{SEE}	$\ell_{SEE,0}$	**323.5132**	19.4867	44.9652	36.4870
	$\Delta U_{SEE,nll}$	**9.1263**	2.3926	3.0527	3.2789
	$\Delta F_{SEE,0}$	**0.8401**	0.4718	0.5100	0.4970
	$\Delta U_{SEE,l}$	**7.0261**	1.2333	2.5944	2.0392
Λ_{PEE}	$\mathcal{F}_{PEE}$	**0.2711**	0.1434	0.0000	0.1602
	$\mathcal{L}_{PEE,0}$	**8.1986**	2.7583	0.0000	4.4420
	ν_{PEE}	**0.5694**	0.3768	0.0000	0.5248
Λ_{isom}	ΔW_{asc}	7.4785	3.2494	**9.9165**	7.2274
	ΔW_{des}	**0.2427**	0.2091	0.0000	0.2336
	ν_{asc}	0.6852	0.5778	0.5562	**1.4842**
	ν_{des}	**0.2086**	0.0000	0.0000	0.0000
	F_{max}	1.0783	0.9489	**1.4416**	0.9256
	$\ell_{CE,opt}$	**10.4651**	4.2597	5.8570	6.1947
Λ_{Hill}	$a_{rel,0}$	**2.5406**	0.4958	1.5083	2.3035
	$b_{rel,0}$	2.5524	1.1582	1.7220	**3.0408**
Λ_{damp}	D_{SE}	0.2924	0.1040	**1.4434**	0.0751
	R_{SE}	**0.2587**	0.0084	0.1942	0.0139
Λ_{ECC}	S_e	**0.1333**	0.0365	0.0294	0.0002
	F_e	0.9649	**0.9886**	0.1698	0.0002
Λ_{Hatze}	q_0	**2.5972**	0.2591	0.0000	0.1530
	ℓ_ρ	0.7168	**0.9025**	0.0000	0.3078
	ρ_c	**2.5589**	2.4400	0.0000	0.9844
	m	**5.5087**	4.8255	0.0000	0.9630
	ν	3.1375	**3.1998**	0.0000	0.4417

Part III.

Optimal Control Theory

6. Introduction to Optimal Control Theory

This chapter contains an introduction to optimal control theory and serves as a prequel to the articles [25, 66]. The theory of optimal control was developed by the Soviet mathematician Pontryagin [61] during the cold war and was, among other fields, used to solve minimum time interception problems [60]. The main aim of an optimal control problem is to minimize an objective function with respect to boundary constraints expressed by (ordinary or partial) differential equations. A few examples of the manifold applicability are:

- the economic behavior of companies w.r.t. their assets [15],
- the vibration of civil engineering structures w.r.t. random loadings [82],
- the uniform heating of a potato on the open fire w.r.t. the position of the attached stick [56],
- the treatment of a cancer tumor w.r.t. the applied radiation [77],
- the reduction of mosquito–induced dengue infections w.r.t. different strategies [81],
- or the recreation of the force production of a human skeletal muscle w.r.t. the applied neural stimulation [25, 66].

The two mainly used approaches for solving optimal control problems are the *first discretize then optimize* (or direct) method and the *first optimize then discretize* (or indirect) method. The former method is based on discretizing the problem on a given time grid and solve the upcoming (very large) system of equations. The latter method aims on finding an optimal solution in the function space, in form of differential equations, which are then solved on a discrete time grid. In [66], we give a comparison of a direct and an indirect method by finding the optimal neural stimulation that recovers isometric muscle forces. For a detailed discussion on advantages and disadvantages of both methods see [5, 23, 36, 42]. In the following, we will address the indirect method, state some fundamentals from functional analysis and give examples of optimal control problems that can be solved using *first optimize then discretize*.

6.1. Fundamentals from Functional Analysis

We want to state some relevant notations, definitions and theorems used in [25, 66]. The presented concepts can altogether be found in literature, e.g. [21, 43, 49, 56].

Definition 6.1.1. Let X be a real vector space and $\Omega \subset \mathbb{R}^n$ open.

- If there exists a norm $||\,.\,|| : X \longrightarrow \mathbb{R}^0_+$ such that X is complete with respect to $||\,.\,||$, i.e. if any Cauchy sequence (f_n) has a limit in X under the induced metric $d(f_n, f_m) := ||f_n - f_m||$, the space $\mathcal{B} = (X, ||\,.\,||)$ is called a **Banach space**.

- If there exists an inner (scalar) product $\langle\ ,\ \rangle_X : X \times X \longrightarrow \mathbb{R}$ that induces a norm via $||\, f\,||_X^2 := \langle f, f\rangle$, the space $\tilde{\mathcal{H}} = (X, \langle\ ,\ \rangle_X)$ is called a **Pre–Hilbert space**.
- A Pre–Hilbert space $\mathcal{H} = (X, \langle\ ,\ \rangle_X)$ is called a **Hilbert space**, if X is complete w.r.t. the associated norm $||\,.\,||_X$.
- Let $C^k(\Omega)$ denote the Banach space of k–times differentiable functions from Ω to $\mathbb{R}$. Consequently, $C^0(\Omega)$ denotes the space of continuous functions and hence $C^\infty(\Omega) = \bigcap_{k=0}^{\infty} C^k(\Omega)$ the space of smooth functions. Furthermore, let $C_c^0(\Omega)$ denote the space of all continuous functions with compact support, where $\operatorname{supp}(f) := \overline{\{x \in \Omega \mid f(x) \neq 0\}}$. Then, $C_c^\infty(\Omega) = C^\infty(\Omega) \cap C_c^0(\Omega)$ is called the **space of bump functions**.
- For $1 \leq p \leq \infty$ and a function $f : \Omega \longrightarrow \mathbb{R}$ define the L^p–norm of f by

$$||f||_{L^p} = \begin{cases} \left(\int\limits_\Omega |f(x)|^p \, \mathrm{d}x \right)^{1/p}, & \text{if } p \neq \infty \\ \operatorname*{ess\,sup}_{x \in \Omega} |f(x)| := \inf\{\alpha \geq 0 \mid \mu(\{|f| > \alpha\}) = 0\}, & \text{if } p = \infty \end{cases},$$

  provided the integral exists, under the equivalence relation $f \sim g \Leftrightarrow ||f - g||_{L^p} = 0$. Here, μ denotes the Lebesgue measure. The space of Lebesgue measurable functions (up to equivalence) together with the defined norm is denoted by $L^p(\Omega) = L^p(\Omega; \mathbb{R})$.
- The space $W^{k,p}(\Omega)$ of functions $f \in L^p(\Omega)$, whose weak derivatives exist and are elements of $L^p(\Omega)$ up to order $k \in \mathbb{N}$, is called **Sobolev space**. Here, $g \in L^p(\Omega)$ is called the **weak derivative** of f, if

$$\int\limits_\Omega g(x)\varphi(x)\,\mathrm{d}x = -\int\limits_\Omega f(x)\varphi'(x)\,\mathrm{d}x, \qquad \forall \varphi \in C_c^\infty(\Omega).$$

  For $p = 2$ write $H^k(\Omega)$ instead of $W^{k,2}(\Omega)$. A prominent function space in optimal control of partial differential equations (PDEs) is $H_0^1(\Omega)$, which denotes the closure of $C_c^\infty(\Omega)$ in $H^1(\Omega)$, cf. [25, 42].

Definition 6.1.2. Using the notation from above, we call

- a (linear) map $T : X \longrightarrow \mathbb{R}$ a **(linear) functional**
- a linear functional $D : \mathcal{C}_c^\infty(\Omega) \longrightarrow \mathbb{R}$ a **distribution**
- the set of all linear functionals $T : X \longrightarrow \mathbb{R}$ the **(algebraic) dual space** of X. We denote this space with X^*.

Example 6.1.3.

a) The space $L^2(\Omega)$ of squared Lebesgue–integrable functions is complete w.r.t. the scalar product

$$\langle f, g\rangle_{L^2} = \int\limits_\Omega f(x) \cdot g(x)\,\mathrm{d}x, \qquad \text{where } f, g \in L^2(\Omega)$$

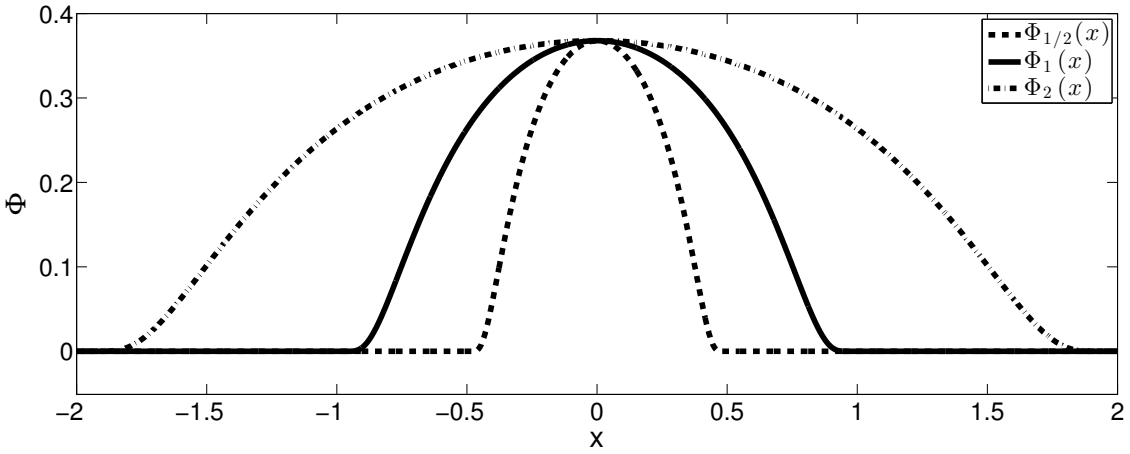

Figure 6.1.: Example bump functions $\Phi_b(x)$ for $b \in \{\frac{1}{2}, 1, 2\}$.

and the induced norm

$$||f||_{L^2}^2 = \int_\Omega f(x)^2 \, \mathrm{d}x = \langle f, f \rangle.$$

Hence, $L^2(\Omega)$ is a Hilbert space. All L^p spaces are Banach spaces.

b) Functions of the form

$$\Phi_b(x) = \begin{cases} \exp(\frac{b^2}{x^2 - b^2}) & , |x| \leq b \\ 0 & , |x| > b \end{cases}$$

are bump functions, since they are continuous, indefinitely often differentiable and with compact support, see Fig. 6.1.

c) The weak derivative of the absolute value function $f(x) = |x|$ is the sign function $\mathrm{sgn}(x) := x/|x|$, if $x \neq 0$ and $\mathrm{sgn}(0) := 0$, see Section 4.3.4 for its use.

d) Let X, Y be normed vector spaces. Let the linear mapping $A : X \longrightarrow Y$ be bounded, i.e. $||A||_{X,Y} := \sup_{||f||_X = 1} ||Af||_Y < \infty$. The set of all bounded linear mappings $L(X, Y)$ is a normed vector space and even a Banach space, if Y is a Banach space.

e) All Sobolev spaces are Banach spaces and for $p = 2$ even Hilbert spaces.

f) The *Dirac delta*, denoted by $\delta : C_c^\infty(\Omega) \longrightarrow \mathbb{R}$ with $\delta[\varphi](x) = \varphi(0)$ for every bump function φ, is a distribution. A common formulation is $\delta[f] = \lim_{n\to\infty} \langle \delta_n, f \rangle = \lim_{n\to\infty} \int_\Omega \delta_n(x) f(x) \, \mathrm{d}x$ using a sequence of functions (δ_n) such that

$$\lim_{n\to\infty} \delta_n(x) = \begin{cases} \infty, & \text{if } x = 0 \\ 0, & \text{if } x \neq 0 \end{cases} .$$

Furthermore, the Dirac delta is the weak derivative of the *Heaviside function*, denoted by

$$\Theta(x) = \begin{cases} 0, & \text{if } x < 0 \\ 1, & \text{if } x \geq 0 \end{cases} .$$

g) The dual space of L^p is $(L^p)^* \simeq L^q$ with $\frac{1}{p}+\frac{1}{q}=1$. Consequently, it holds $(L^2)^* \simeq L^2$. However, it holds that $(L^1)^* \simeq L^\infty$, but (L^1) is only a subspace of $(L^\infty)^*$, see [70].

As we aim on finding local extrema in an infinite dimensional function space, the concept of derivatives and directional derivatives has to be generalized.

Definition 6.1.4. Let X, Y be Banach spaces and $U \subseteq X$ open.

- The map $A : U \longrightarrow Y$ is called **Fréchet differentiable** in $x_0 \in U$, if there exist a continuous linear mapping $DA : X \longrightarrow L(X,Y)$ with

$$\lim_{||h||_X \to 0} \frac{||A(x_0+h) - A(x_0) - DA(x_0)(h)||_Y}{||h||_X} = 0$$

- Considering a functional $T : X \longrightarrow \mathbb{R}$,

$$T_{v_0}(x_0) = D_{v_0}T(x_0) = \lim_{h \to 0} \frac{T(x_0 + h \cdot v_0) - T(x_0)}{h}$$

denotes the **Gâteaux derivative** of T in $x_0 \in U$ in direction $v_0 \in X$.

Remark 6.1.5. (Properties of Fréchet and Gâteaux derivatives)

1) If $X = \mathbb{R}^n$ and $Y = \mathbb{R}$, the Fréchet derivative DA corresponds to the total derivative of a function $A : \mathbb{R}^n \longrightarrow \mathbb{R}$, see [21].

2) If A is Fréchet differentiable in x_0, there exist the Gâteaux derivative for every $v_0 \in X$ and it holds that $D_{v_0}A(x_0) = DA(x_0)(v_0)$, see [56]. The converse do not hold in general, inter alia because the Gâteaux derivative might not be linear.

3) If $A : X \supseteq U \longrightarrow Y$ is Gâteaux differentiable in every direction $v_0 \in X$ within an ε–ball around $x_0 \in U$, and it holds
   (a) $D_{(\cdot)}(x_0) : X \longrightarrow \mathbb{R}$ is continuous and linear,
   (b) $D_{v_0}(x) \to D_{v_0}(x_0)$ for $x \to x_0$ uniformly on $||v_0||_X = 1$,
   then A is Fréchet differentiable in x_0 and $DA(x_0) = D_{(\cdot)}(x_0)$, see [56].

6.2. Formulation and Examples for Optimal Control Problems

Let the following differential equation system

$$\dot{x} = f(t, x(t), \sigma(t)), \qquad x(0) = x_0(\sigma(0)) \in \mathbb{R}^n, \tag{6.1}$$

be influenced by an input (or better: control) function $\sigma = \sigma(t)$. The solution $x(t) = T(\sigma)$ of the system, expressed by the functional T, can be obtained analytically or numerically in dependence of the control. Furthermore, let $\Omega = [0, t_1] \subset \mathbb{R}$, $x \in L^2(\Omega; \mathbb{R}^n)$ and $\sigma \in U_{ad}(\Omega)$ where

$$U_{ad}(\Omega) := \{u \in L^2(\Omega; \mathbb{R}^m) \mid ||u||_{L^2} \leq \alpha \in \mathbb{R}\}$$

denotes the set of α–bounded L^2–functions.

The optimal control problem occurs, if a model's output $\bar{x}(t)$ is predetermined, e.g. by a desired trajectory or experimentally observed data. Hence, we want to find an optimal control function σ^*, such that $T(\sigma^*) = \bar{x}$. At first sight, the problem is solvable by computing $\sigma^* = T^{-1}(\bar{x})$, but it is not clear a priori whether T is analytic, invertible or at least covers the observation, i.e. $\bar{x} \in \mathrm{Im}(T)$. Formally, the desired output $\bar{x}$ has to be projected to the image of T, which is done by minimizing $||T(\sigma) - \bar{x}||_{L^2}$. To preserve the uniqueness of this projection and to avoid an infinite value of the control function, the minimization problem is enhanced by a *regularization term* of the control, $\omega/2 \cdot ||\sigma||^2_{L^2}$, for details see [20, 34]. The weighting factor $0 < \omega \in \mathbb{R}$ of the regularization term is assumed to be sufficiently small to not influence the output considerably while being sufficiently large to ensure convexity of the optimization problem. Thus, the optimization problem, expressed by the convex objective function $\mathcal{J} : L^2 \times U_{ad} \longrightarrow \mathbb{R}$, writes as

$$\min_{\sigma \in U_{ad}} \mathcal{J}(x(t), \sigma(t)) := \frac{1}{2}||x(t) - \bar{x}(t)||^2_{L^2} + \frac{\omega}{2}||\sigma(t)||^2_{L^2} = \int_\Omega j(t, x(t), \sigma(t)) \, \mathrm{d}t \tag{6.2}$$

$$\text{such that} \quad \dot{x} = f(t, x(t), \sigma(t)), \qquad x(0) = x_0(\sigma(0)) \tag{6.3}$$

The ODE constraint (6.3) can be included in the objective function by the introduction of a *Lagrange multiplier* $\lambda : L^2 \longrightarrow \mathbb{R}$. This so–called co–state variable serves as a penalty function, if the ODE constraint is not fulfilled. Note that $\lambda \in (L^2)^* \simeq L^2$.

Theorem 6.2.1.
Given a model of the form (6.1)*, which is dependent on a control $\sigma = \sigma(t)$, as well as a desired path $\bar{x} = \bar{x}(t)$, which should be approximated at best by the solution $x = x(t)$. The optimal control problem of minimizing the Lagrange functional $\mathcal{L} : L^2 \times U_{ad} \times L^2 \longrightarrow \mathbb{R}$, where*

$$\mathcal{L}(x, \sigma, \lambda) := \mathcal{J}(x, \sigma) + \int_\Omega \lambda(\dot{x} - f(x, \sigma)) \, \mathrm{d}t = \int_\Omega j(x, \sigma) + \lambda\dot{x} - \lambda f(x, \sigma) \, \mathrm{d}t \tag{6.4}$$

is equivalent to solving the following system:

$$\begin{aligned} \dot{x} &= f(x, \sigma) & x(0) &= x_0 \\ \dot{\lambda} &= -\lambda \partial_x f(x, \sigma) + \partial_x j(x, \sigma) & \lambda(T) &= 0 \\ \partial_\sigma j(x, \sigma) &= \lambda \partial_\sigma f(x, \sigma) & \sigma &\in U_{ad} \end{aligned} \tag{6.5}$$

Proof.

The differential–algebraic equation system (DAE) (6.5) is a direct consequence of the *Euler–Lagrange equation*, see [49, 56]. This equation originates from taking the Fréchet derivatives of $\mathcal{L}$ w.r.t. the state, the co–state and the control.

To show this connection, we rearrange $\mathcal{L}$ using partial integration (PI) on $\lambda\dot{x}$:

$$\begin{aligned}\mathcal{L}(x,\sigma,\lambda) &= \int_\Omega j(x,\sigma)\,\mathrm{d}t + \int_\Omega \lambda\dot{x}\,\mathrm{d}t - \int_\Omega \lambda f(x,\sigma)\,\mathrm{d}t \\ &\overset{\text{PI}}{=} \int_\Omega j(x,\sigma)\,\mathrm{d}t + x\lambda|_0^T - \int_\Omega \dot{\lambda}x\,\mathrm{d}t - \int_\Omega \lambda f(x,\sigma)\,\mathrm{d}t \\ &= \int_\Omega j(x,\sigma)\,\mathrm{d}t + x(T)\lambda(T) - x_0\lambda(0) - \int_\Omega \dot{\lambda}x\,\mathrm{d}t - \int_\Omega \lambda f(x,\sigma)\,\mathrm{d}t\end{aligned}$$

When taking the (Gâteaux) derivative of $\mathcal{L}$ in direction $\tilde{x}$, the initial condition $\tilde{x}(0) = x_0$ has to be fulfilled. Furthermore, the adjoint variable has to attain the boundary value $\lambda(T) = 0$, because $\tilde{x}(T)$ is free. This requirement is known as the *transversality condition*, see [21, 49, 56]. Taking the Gâteaux derivative of $\mathcal{L}$ in x in direction $\tilde{x}$ yields

$$\begin{aligned}D_{\tilde{x}}\mathcal{L}(x) &= \frac{1}{t}\left[\int_\Omega j(x+t\tilde{x},\sigma) - j(x,\sigma)\,\mathrm{d}t - \int_\Omega t\tilde{x}\dot{\lambda}\,\mathrm{d}t - \int_\Omega \lambda[f(x+t\tilde{x},\sigma) - f(x,\sigma)]\,\mathrm{d}t\right] \\ &= \int_\Omega \partial_x j(x,\sigma)\tilde{x}\,\mathrm{d}t - \int_\Omega \tilde{x}\dot{\lambda}\,\mathrm{d}t - \int_\Omega \lambda\partial_x f(x,\sigma)\tilde{x}\,\mathrm{d}t \\ &= \langle \partial_x j(x,\sigma), \tilde{x}\rangle - \langle \dot{\lambda} + \lambda\partial_x f(x,\sigma), \tilde{x}\rangle \\ &= \langle \partial_x j(x,\sigma) - \dot{\lambda} - \lambda\partial_x f(x,\sigma), \tilde{x}\rangle \overset{!}{=} 0\end{aligned}$$

To be Fréchet differentiable in x, the Gâteaux derivatives have to be zero for all $\tilde{x}$. Thus, it follows

$$\partial_x j(x,\sigma) - \dot{\lambda} - \lambda\partial_x f(x,\sigma) = 0$$

and consequently the co–state equation

$$\dot{\lambda} = -\lambda\partial_x f(x,\sigma) + \partial_x j(x,\sigma)$$

with the terminal condition $\lambda(T) = 0$. The state and control equation follow analogously by setting $D_{\tilde{\lambda}}\mathcal{L} = 0$ and $D_{\tilde{\sigma}}\mathcal{L} = 0$, respectively.

Example 6.2.2. Considering the ODE

$$\dot{x}(t) = -x(t) + \sigma(t), \qquad x(0) = 1 \quad ,$$

we want to find a control $\sigma(t) \in U_{ad}$ such that the objective function

$$\mathcal{J}(x,\sigma) = \frac{1}{2}||x - \bar{x}||^2 + \frac{\omega}{2}||\sigma||^2$$

with $\omega > 0$ is minimized. The desired output $\bar{x}$ is given by

$$\bar{x}(t) = \Theta(1-t)\,|_{[0,2]} = \begin{cases} 1 & \text{, if } t \in [0,1] \\ 0 & \text{, if } t \in (1,2] \end{cases}$$

After including the adjoint variable $\lambda = \lambda(t)$, we apply Theorem 6.2.1 and derive the Lagrange functional

$$\mathcal{L}(x,\sigma,\lambda) = \mathcal{J}(x,\sigma) + \langle \lambda, \dot{x} + x - \sigma\rangle$$

with respect to the state variable x, the co–state variable λ as well as the control σ and obtain the system:

$$\begin{aligned} -\lambda\partial_x f(x,\sigma) + \partial_x j(x,\sigma) = \quad & \dot{\lambda} = -\lambda + x - \bar{x} \qquad , \lambda(2) = 0 \\ f(x,\sigma) = \quad & \dot{x} = -x + \sigma \qquad , x(0) = 1 \\ \partial_\sigma j(x,\sigma) = \langle \lambda, \partial_\sigma f(x,\sigma)\rangle \Longrightarrow \quad & \omega\sigma = \lambda \end{aligned} \tag{6.6}$$

To solve system (6.6), we substitute $\sigma = \lambda/\omega$ in the second equation and obtain an inhomogeneous, linear first order ODE system:

$$\frac{\mathrm{d}}{\mathrm{d}t}\begin{pmatrix}\lambda\\ x\end{pmatrix} = \begin{pmatrix}-1 & 1\\ \frac{1}{\omega} & -1\end{pmatrix}\begin{pmatrix}\lambda\\ x\end{pmatrix} + \begin{pmatrix}-\bar{x}\\ 0\end{pmatrix} = A\begin{pmatrix}\lambda\\ x\end{pmatrix} + b(t) \ , \qquad \eta = \begin{pmatrix}\lambda\\ x\end{pmatrix}(0) = \begin{pmatrix}\lambda_0(\omega)\\ 1\end{pmatrix} \quad .$$

Because the initial value λ_0 is unknown, it has to be calculated a posteriori in dependence on ω. The eigenvalues of A are $\mu_{1/2} = (-\omega \pm \sqrt{\omega})/\omega$. Hence, the solution is obtained as a combination of the fundamental system $\{e^{\mu_1 t}, e^{\mu_2 t}\}$ by variation of constants via:

$$\begin{pmatrix}\lambda(t,\omega,\lambda_0)\\ x(t,w,\lambda_0)\end{pmatrix} = e^{At}\eta + \int_0^t e^{A(t-s)}b(s)\ \mathrm{d}s \quad , \tag{6.7}$$

where $e^A := \sum_{k=0}^{\infty} A^k/k!$ denotes the matrix exponential. Setting $\lambda(2,\omega,\lambda_0) = 0$, we obtain analytic expressions for x, λ and λ_0 in dependence on ω, which are, however, too longish to display here. All calculations were conducted in MATLAB.

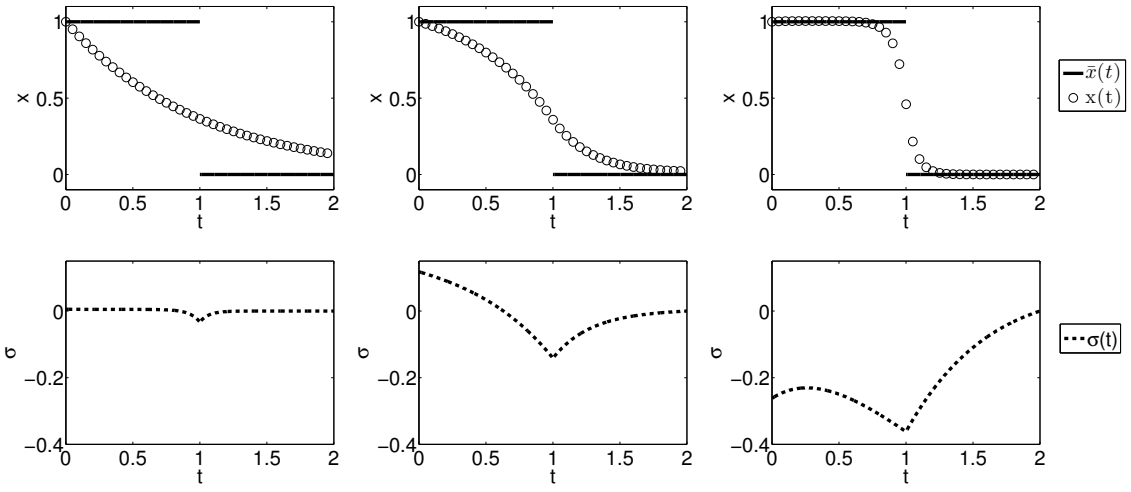

Figure 6.2.: Solution of equation system (6.6) for $\omega = 10$ (left column), $\omega = 0.1$ (mid column) and $\omega = 0.001$ (right column). The upper row shows the numerical solution $x(t)$ (circles) in comparison to the desired output $\bar{x}(t)$ (line). The corresponding control function $\sigma(t)$ (dashed line) is displayed in the lower row. The respective objective function values J_ω were $J_{10} = 28.6$, $J_{0.1} = 20.4$ and $J_{0.001} = 4.4$.

Figure 6.2 shows the analytic solution for different values of $\omega \in \{10, 0.1, 0.001\}$, revealing the effect of the regularization term. For $\omega = 10$, the minimization of the objective function is dominated by the minimization of the (absolute) control. Accordingly, the adjoint variable $\lambda(t) \approx 0$ and the solution $x(t) \approx e^{-t}$. For smaller values of ω, the term $||x - \bar{x}||^2$ becomes more important to minimize. Since this term is already convex, we

would expect an optimal fit of $x(t)$ on $\bar{x}(t)$ for $\omega = 0$. However, the analytic solution is not defined at $\omega = 0$ and we found the evaluation to be numerically susceptible for $\omega \leq 10^{-4}$, resulting in highly oscillating solutions. Hence, Fig. 6.2 only shows the solution up to $\omega = 10^{-3}$.

An attempt to better approximate this instability was a numerical approach. For iteratively solving system (6.6), we chose $\omega = 10^{-5}$ and the initial value $\sigma_0(t) = 0$. Every iteration step consisted of solving the ODE for $x(t)$ with the MATLAB pre–implemented Runge–Kutta method *ode*45, then solving the ODE for $\lambda(t)$ (backwards in time) and finally updating $\sigma(t)$. Figure 6.3 shows the solution $x(t)$ in comparison to $\bar{x}(t)$ as well as the respective control $\sigma(t)$ after 10, 100 and 1000 iteration steps.

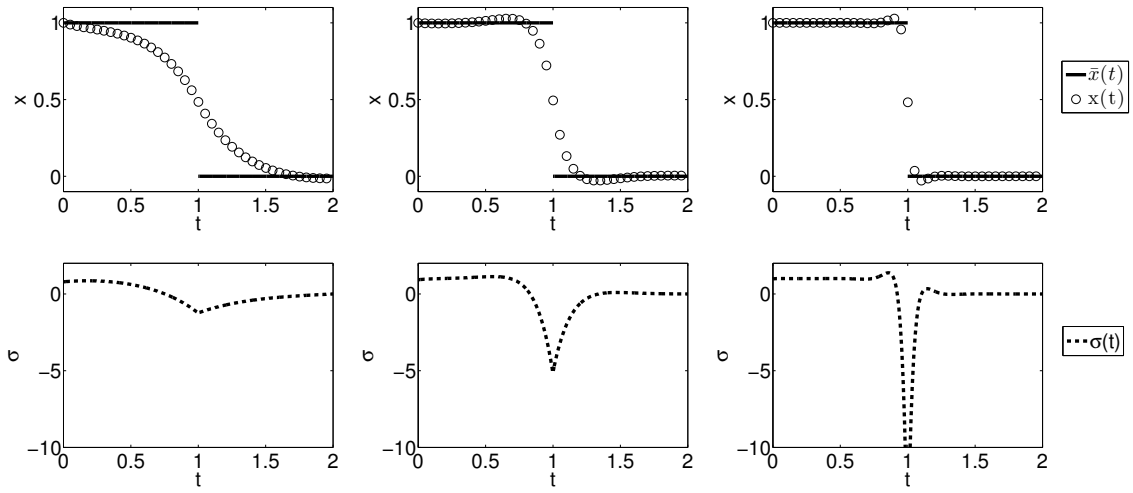

Figure 6.3.: Solution of equation system (6.6) for $\omega = 10^{-5}$ after 10 (left column), 100 (mid column) and 1000 (right column) iteration steps. The upper row shows the numerical solution $x(t)$ (circles) in comparison to the desired output $\bar{x}(t)$ (line). The corresponding control function $\sigma(t)$ (dashed line) is displayed in the lower row. The respective objective function values J_n after n iterations were $J_{10} = 17.9$, $J_{100} = 5.0$ and $J_{1000} = 1.6$.

This example leads to two observations. First, the method is not bounded to approximating continuous functions. Second, for $\omega \to 0$, the control $\sigma(t)$ converges pointwise to an optimal control $\sigma^*(t) \notin U_{ad}([0,2])$, namely

$$\sigma^*(t) = \Theta(1-t) + \delta(t-1) = \begin{cases} 1 & \text{, if } t \in [0,1) \\ -\infty & \text{, if } t = 1 \\ 0 & \text{, if } t \in (1,2] \end{cases},$$

which is not bounded and not even a function, but a distribution. To proof the optimality of σ^*, we solve the ODE

$$\dot{x} = -x + \sigma^* = -x + \Theta(1-t) - \delta(t-1)\,, \quad x(0) = 1$$

via variation of constants. The homogeneous solution is obviously $x_H(t) = e^{-t}c$. Varying the constant $c = c(t)$ to obtain the general solution $x(t) = e^{-t}c(t)$ and differentiating yields

$$\begin{aligned} & \dot{c}(t) = e^t\Theta(1-t) - e^t\delta(t-1) \\ \Longrightarrow \quad & c(t) = e^t\Theta(1-t) - e^1\Theta(t-1) + e^1\Theta(t-1) = e^t\Theta(1-t) \\ \Longrightarrow \quad & x(t) = e^{-t}e^t\Theta(1-t) = \Theta(1-t) = \bar{x}(t) \end{aligned}$$

Example 6.2.3. The described method is also applicable to ODEs of higher order. For example consider the oscillation boundary value problem:

$$\ddot{x}(t) = -x(t) + \sigma(t)\ , \qquad x(0) = 0 = x(2). \tag{6.8}$$

Let the objective function $\mathcal{J}$ be as above with a desired output $\bar{x}$ in form of an approximated triangle wave on $[0, 2]$

$$\bar{x}(t) = \begin{cases} \frac{\sin(1)}{\sin(2)} \sin(t) & , \text{if } t \in [0,1] \\ \frac{\sin(1)}{\sin(2)} \sin(t) - \sin(t-1) & , \text{if } t \in (1,2] \end{cases} = \frac{\sin(1)}{\sin(2)} \sin(t) - \Theta(t-1)\sin(t-1) \tag{6.9}$$

Differentiation of the corresponding Lagrange functional

$$\mathcal{L}(x, \sigma, \lambda) = \mathcal{J}(x, \sigma) + \langle \lambda, \ddot{x} - x + \sigma \rangle$$

w.r.t. state variable, co–state variable and control variable yields

$$\begin{aligned} \partial_x f(x,\sigma)\lambda - \partial_x j(x,\sigma) = \quad & \ddot{\lambda} = -\lambda - (x - \bar{x}) && , \lambda(0) = 0 = \lambda(2) \\ f(x,\sigma) = \quad & \ddot{x} = -x + \sigma && , x(0) = 0 = x(2) \\ \partial_\sigma j(x,\sigma) = \lambda \partial_\sigma f(x,\sigma) \Longrightarrow \quad & \omega\sigma = \lambda \end{aligned} \tag{6.10}$$

In contrast to the proof of Theorem 6.2.1, transforming the Lagrangian $\mathcal{L}$ requires two partial integrations, resulting in switched signs in the co–state equation. Moreover, the analytic solution using variation of the constant is not possible, because the matrix exponential contains expressions of the form $\exp(t^2)$, whose integral does not exist in a closed–form expression. Nevertheless, substituting $\sigma = \lambda/\omega$ as above, the pre–implemented MATLAB solver *dsolve* finds an analytic solution of the system in dependence on ω. Figure 6.4 shows the solution w.r.t. the regularization term $\omega \in \{1, 0.1, 0.001\}$, the desired output $\bar{x}$ and the respective control σ. For values of $\omega < 10^{-3}$ the solution became numerically unstable, due to occurring high–frequency oscillations. However, the analytic solutions does not give rise to the shape of the optimal control function σ^* for $\omega \to 0$.

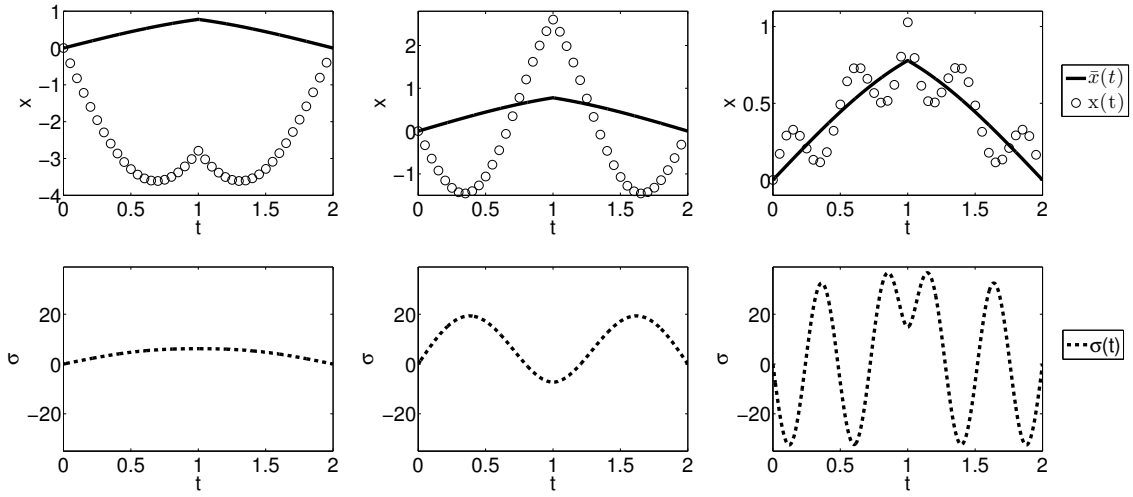

Figure 6.4.: Analytic solution of equation system (6.10) for $\omega = 1$ (left column), $\omega = 0.1$ (mid column) and $\omega = 10^{-3}$ (right column). The upper row shows the numerical solution $x(t)$ (circles) in comparison to the desired output $\bar{x}(t)$ (line). The corresponding control function $\sigma(t)$ (dashed line) is displayed in the lower row. The respective objective function values were $\mathcal{J}_1 = 53$, $\mathcal{J}_{0.1} = 15.6$ and $\mathcal{J}_{0.001} = 0.5$.

To obtain a more meaningful outline of the control function, we solved the equation system (6.10) numerically using three different approaches: a self–implemented shooting method, a self–implemented centered difference method and the state–of–the–art pre–implemented MATLAB solver *bvp4c*.

The shooting method: The main idea of the shooting method is to transform a boundary value problem (BVP), like system (6.10), into an initial value problem (IVP). In the case of a linear BVP, this transformation can be obtained by the solution of the corresponding gradient IVP, see Algorithm 1. We give a pseudocode for a simple shooting method in Algorithm 1. Details for applying this method can be found in [21, 56, 76].

Algorithm 1 Shooting Method

Solving a BVP of the form: $\ddot{x} = f(t,x),\ x(0) = a,\ x(T) = b$ by transformation into an IVP of the form $\ddot{x} = f(t,x),\ x(0) = a,\ \dot{x}(0) = s$

Require: Right hand side $f(t,x)$, boundary values $a, b \in \mathbb{R}$, initial value $s_0 = 1$

Ensure: Numerical solution $x(t)$

Set $\varepsilon = 1$ and $i = 0$

while $\varepsilon >$ error tolerance **do**

(1) Solve the IVP: $\ddot{x} = f(t,x),\ x(0) = a,\ \dot{x}(0) = s_i$

(2) Solve the corresponding (gradient) IVP: $\ddot{v} = v \cdot \dot{x} + f(t,x) \cdot \dot{v},\ v(0) = 0,\ \dot{v}(1) = 1$

(3) Update the initial value s_i by the newton step $s_{i+1} = s_i - \alpha * \frac{x(T)}{v(T)}$ with a suitable step size α

(4) $\varepsilon = |s_{i+1} - s_i|$, $i = i + 1$

end while

Return x as the solution of the IVP: $\ddot{x} = f(t,x),\ x(0) = a,\ \dot{x}(0) = s = s_i$

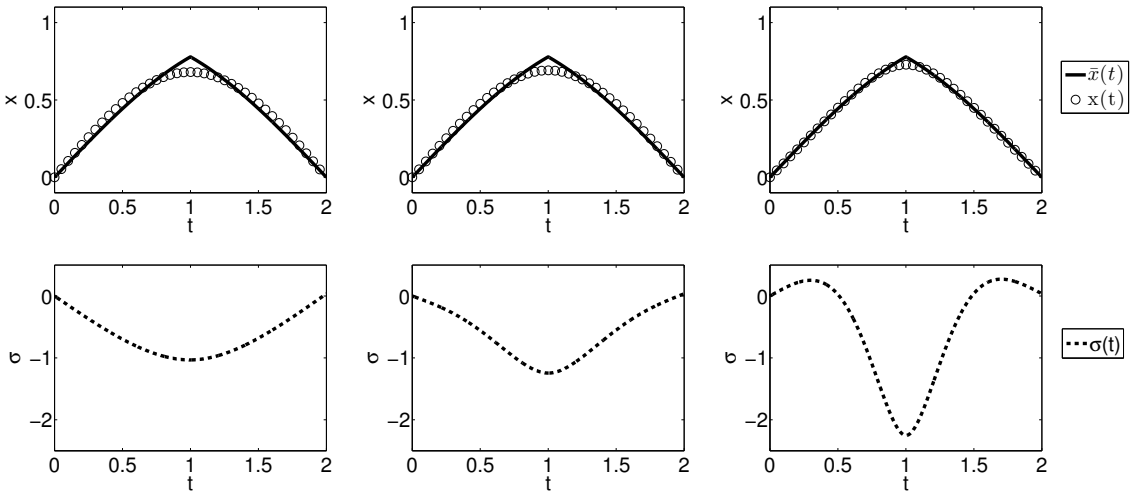

Figure 6.5.: Shooting method solution of equation system (6.10) for $\omega = 10^{-3}$ after 10 (left column), 100 (mid column) and 1000 (right column) iteration steps. The upper row shows the numerical solution $x(t)$ (circles) in comparison to the desired output $\bar{x}(t)$ (line). The corresponding control function $\sigma(t)$ (dashed line) is displayed in the lower row. The respective objective function values were $\mathcal{J}_{10} = 1.6$, $\mathcal{J}_{100} = 0.4$ and $\mathcal{J}_{1000} = 0.07$.

As in the previous example, the equation system (6.10), now transformed into a system of four ODEs of first order as well as an algebraic equation, was solved numerically. Figure 6.5 shows the solution $x(t)$ in comparison to $\bar{x}(t)$ as well as the respective control $\sigma(t)$ after 10, 100 and 1000 iteration steps. The disadvantages of the shooting method are its elaborated implementation and a slow convergence, resulting in an elapsing time of approximately 50 seconds. In the next paragraph, we present the centered difference approach as a cheaper alternative.

The centered difference method: The main idea of this second approach is to discretize the equation system (6.10) and solve the upcoming linear equation system (LES). Therefore, we recall the (forward and backward) Taylor expansion of a sufficiently often differentiable function $f : \mathbb{R} \to \mathbb{R}$ at $\hat{x}$ with step size $h > 0$:

$$f(\hat{x}+h) = f(\hat{x}) + f'(\hat{x}) \cdot h + \frac{1}{2} f''(\hat{x}) \cdot h^2 + \mathcal{O}(h^3)$$
$$f(\hat{x}-h) = f(\hat{x}) - f'(\hat{x}) \cdot h + \frac{1}{2} f''(\hat{x}) \cdot h^2 + \mathcal{O}(h^3)$$

Adding these two equations and solving for $f''(\hat{x})$ yields

$$f''(\hat{x}) \approx \frac{f(\hat{x}+h) - 2f(\hat{x}) + f(\hat{x}-h)}{h^2} \quad .$$

We discretize system (6.10) using the grid $\{0 = t_0, t_1, \ldots, t_n, t_{n+1} = 2\}$ for the time as well as $\{0 = \lambda_0, \lambda_1, \ldots, \lambda_n, \lambda_{n+1} = 0\}$ for the co–state, $\{0 = x_0, x_1, \ldots, x_n, x_{n+1} = 0\}$ for the state, and $\{0 = \bar{x}_0, \bar{x}_1, \ldots, \bar{x}_n, \bar{x}_{n+1} = 0\}$ for the desired path. This discretization leads to the following linear equation system (LES)

$$\begin{aligned} \frac{\lambda_{i+1} - 2\lambda_i + \lambda_{i-1}}{h^2} &= -\lambda_i - (x_i - \bar{x}_i) \\ \frac{x_{i+1} - 2x_i + x_{i-1}}{h^2} &= -x_i + \frac{\lambda_i}{\omega} \end{aligned} \tag{6.11}$$

for $i = 1, ..., n$. This LES can be expressed by a block–wise tridiagonal (Toeplitz) matrix

$$\left(\begin{array}{cccccc|cccccc}
h^2-2 & 1 & & & & & h^2 & & & & & \\
1 & h^2-2 & 1 & & & & & \ddots & & & & \\
 & \ddots & \ddots & \ddots & & & & & & & & \\
 & & 1 & h^2-2 & 1 & & & & & & & h^2 \\
 & & & 1 & h^2-2 & & & & & & & \\
\hline
-h^2/\omega & & & & & & h^2-2 & 1 & & & & \\
 & & & & & & 1 & h^2-2 & 1 & & & \\
 & & \ddots & & & & & \ddots & \ddots & \ddots & & \\
 & & & & & & & & 1 & h^2-2 & 1 & \\
 & & & & -h^2/\omega & & & & & 1 & h^2-2 &
\end{array}\right) \cdot \begin{pmatrix} \lambda_1 \\ \vdots \\ \lambda_n \\ x_1 \\ \vdots \\ x_n \end{pmatrix} = \begin{pmatrix} \bar{x}_1 h^2 \\ \vdots \\ \bar{x}_n h^2 \\ 0 \\ \vdots \\ 0 \end{pmatrix}$$

Due to the structure, the matrix is invertible and allows a simultaneous evaluation of the state and the co–state variable (and thus the control) in a single step via the so–called *Thomas method*, cf. [13]. For a detailed overview of methods concerning Toeplitz matrices see [55]. Our non–iterative approach is straightforward to implement and executed for $n = 1000$ in about 0.6 seconds, approximately one percent of the time of the shooting method. Figure 6.6 shows the solution w.r.t. the regularization parameter $\omega \in \{1, 10^{-3}, 10^{-6}\}$, the desired output $\bar{x}$ and the respective control σ. Unlike the analytic solution, the centered difference method is numerically stable for $\omega \ll 1$. Furthermore, the control seems to converge to $\sigma^* = \delta(t-1)$, which we will prove to be the correct solution in the following.

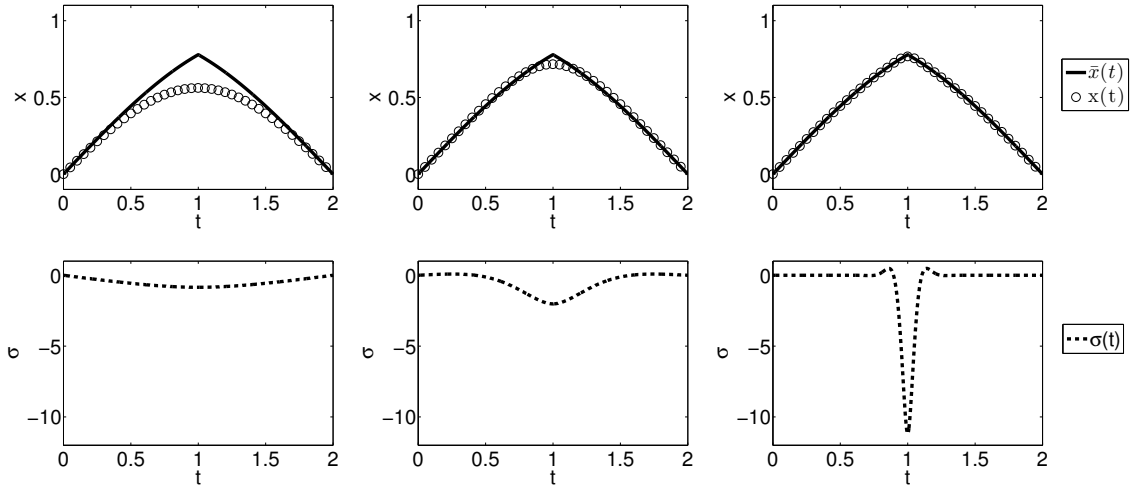

Figure 6.6.: Centered difference solution of equation system (6.10) for $\omega = 10^{-1}$ (left column), $\omega = 10^{-3}$ (mid column) and $\omega = 10^{-6}$ (right column). The upper row shows the numerical solution $x(t)$ (circles) in comparison to the desired output $\bar{x}(t)$ (line). The corresponding control function $\sigma(t)$ (dashed line) is displayed in the lower row. The respective objective function values were $\mathcal{J}_{0.1} = 10.6$, $\mathcal{J}_{10^{-3}} = 0.25$ and $\mathcal{J}_{10^{-6}} = 0.0014$.

State–of–the–art solver (*bvp4c*)**:** There exists a specific solver for BVPs in MATLAB; *bvp4c*, which is short for *boundary value problem solver of 4th order using collocation method*. According to [73], a shooting method may be too susceptible to ill–posed BVPs, leading to stiff or numerically unstable IVPs. Hence, *bvp4c* replaces the shooting method by a collocation method that approximates the solution of an IVP by a polynomial, in our case a piecewise cubic spline. The algorithm adaptively creates a grid on which the solution is evaluated. Furthermore, it is possible to include parameters (like ω) in the equation to reveal their influence. Figure 6.7 shows the solution w.r.t. the regularization parameter $\omega \in \{1, 10^{-3}, 10^{-6}\}$, the desired output $\bar{x}$ and the respective control σ. The evaluation time for *bvp4c* was 0.05 seconds, about ten percent of the centered difference method and one permil of the shooting method.

From the three numerical methods, we expect the optimal control $u^*(t)$ to be a Dirac δ of the form

$$\sigma^*(t) = \delta(t-1) = \begin{cases} \infty & \text{, if } t = 1 \\ 0 & \text{, else} \end{cases}$$

To prove this assumption, we solve the ODE $\ddot{x} = -x + \sigma^*$ with boundary values $x(0) = 0 = x(2)$ by variation of the constant, see Eqn. (6.7). Written as a system of first order equations, we obtain eigenvalues $\mu_{1/2} = \pm i$ and thus the fundamental system $\{\sin(t), \cos(t)\}$. Denoting $x_{1,0} = \dot{x}(0)$ the unknown initial value of the first derivative, we yield

$$x(t) = x_{1,0}\sin(t) - \int_0^t \sin(t-s)\delta(s-1)\,\mathrm{d}s = x_{1,0}\sin(t) + \Theta(t-1)\sin(t-1) \quad .$$

Setting $x(2) = 0$ we obtain $x_{1,0} = \sin(1)/\sin(2)$ and hence $x(t) = \bar{x}(t)$.

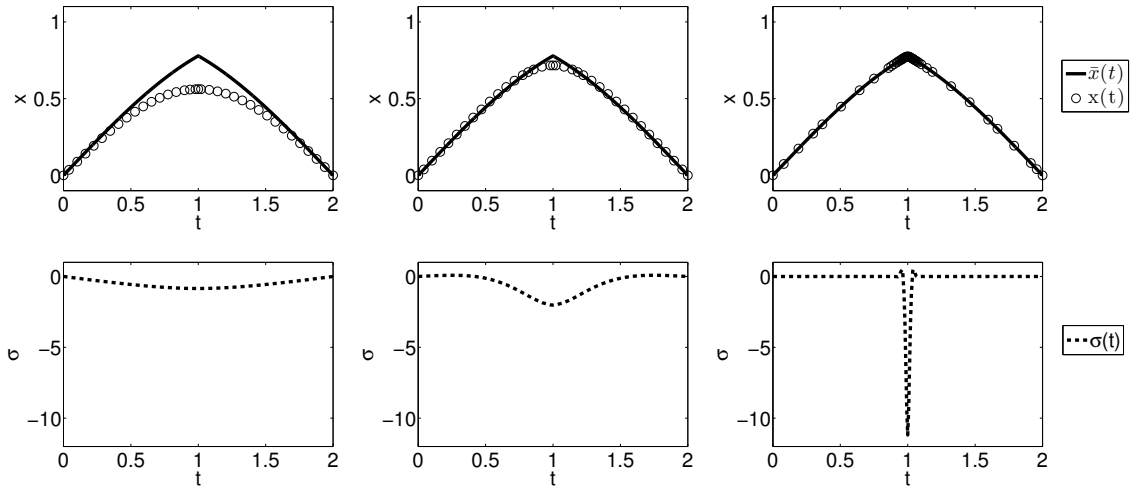

Figure 6.7.: MATLAB *bvp4c* solution of equation system (6.10) for $\omega = 10^{-1}$ (left column), $\omega = 10^{-3}$ (mid column) and $\omega = 10^{-6}$ (right column). The upper row shows the numerical solution $x(t)$ (circles) in comparison to the desired output $\bar{x}(t)$ (line). Note that the time grid is not equidistant, but is concentrated around $t = 1$s. From left to right, the number of grid points were $36, 37$ and 47. The corresponding control function $\sigma(t)$ (dashed line) is displayed in the lower row. The respective objective function values were $\mathcal{J}_{0.1} = 10.6$, $\mathcal{J}_{10^{-3}} = 0.25$ and $\mathcal{J}_{10^{-6}} = 0.0014$, i.e. exactly the same as in the centered difference method.

7. Research Paper III: Optimal Control of Isometric Muscle Dynamics

R. Rockenfeller T. Götz

The following is a reformatted and slightly modified copy of the open source article
R. Rockenfeller and T. Götz. "Optimal Control of Isometric Muscle Dynamics". In: Journal of Mathematical and Fundamental Sciences. 47.1 (2015), pp. 12–30
available at http://journals.itb.ac.id/index.php/jmfs/article/view/867.
This article is also referred to as [49] (in Chapter 4), [13] (in Chapter 8) or [66] (in the remaining work).

The idea for this article originates from T. Götz. Content, structure, calculations and presentation of the results were done by R. Rockenfeller.

Abstract

We use an indirect optimal control approach to calculate the optimal neural stimulation needed to obtain a measured muscle force. The neural stimulation of the nerve system is hereby considered to be a control function (input) of the system 'muscle' that solely determines the muscle force (output). We use a well–established muscle model and experimental data of isometric contractions. The model consists of coupled activation and contraction dynamics described by ordinary differential equations. To validate our results, we perform a comparison with a commercial optimal control software.

Keywords: Biomechanics, Muscle Model, Optimal Control, Inverse Dynamics

7.1. Introduction

Mathematical models for everyday phenomena often ask for a control or input such that a system reacts in an optimal or at least in a desired way. Whether finding the optimal rotation of a stick for cooking potatoes on the open fire such that the potato has a desired temperature, see [34], or computing the optimal neural stimulation of a muscle such that the force output is as close as possible to experimentally measured data. Typical examples for biomechanical optimal control problems occur in the calculation of goal directed movements, see [8, 15, 27] and in robotics [13]. Concerning huge musculo–skeletal systems, the load sharing problem of muscle force distribution has to be solved using optimal control [1, 19]. The most common application for solving the load sharing problem is the inverse dynamics of multi–body systems (MBS) as in [3, 28]. Its aim is to approximate observed multi–body trajectories by a forward simulation. The problem is to find a set of muscle activations such that the muscle forces resulting from the MBS simulation are similar to the measured ones.

Considering a general optimal control problem, there is a process described by a vector of state variables $\mathbf{x}$. This state vector has to be influenced by a control variable $u \in \mathcal{U}$ within a time interval $[t_0, t_1]$ such that a given objective function $\mathcal{J}(\mathbf{x}, u)$ is minimized subject to the model equations. These model equations can be either ordinary differential equations (ODE), partial differential equations (PDE) or differential–algebraic equations (DAE). Additional constraints on the control variable as well as the state variable itself can be imposed. The corresponding general optimal control problem reads as:

$$\begin{aligned} \min_{u} \quad & \mathcal{J}(\mathbf{x}, u) = \int_{t_0}^{t_1} j\left(\mathbf{x}(u,t),\, u(t),\, t\right) dt && (7.1)\\ \text{subject to} \quad & \dot{\mathbf{x}} = f(\mathbf{x}, u, t) && \text{(ODEs)}\\ & 0 = g(\mathbf{x}, u, t) && \text{(DAEs)}\\ & \mathbf{x} \in [\mathbf{x}_{min}, \mathbf{x}_{max}], \quad u \in \mathcal{U}, \quad \mathbf{x}(u(t_0), t_0) = \mathbf{x}_0, \ldots && \text{(Constraints)} \end{aligned}$$

For solving this minimization problem, we introduce an adjoint (or co–state) variable λ, which operates as a penalty function, if the ODE or DAE are not fulfilled. The optimal control variable u^* is found at the saddle point of the Lagrangian $\mathcal{L}$, where

$$\begin{aligned} \mathcal{L}(\mathbf{x}, u, \lambda) = & \int_{t_0}^{t_1} j(\mathbf{x},\, u,\, t) + \lambda_1(t)\, [\dot{\mathbf{x}} - f(\mathbf{x}, u, t)] + \lambda_2(t)\, g(\mathbf{x}, u, t)\ \ dt \\ \text{subject to} \quad & \mathbf{x} \in [\mathbf{x}_{min}, \mathbf{x}_{max}], \quad u \in \mathcal{U}, \quad \mathbf{x}(u(t_0), t_0) = \mathbf{x}_0, \ldots \end{aligned} \tag{7.2}$$

Almost exclusively in biomechanical literature, problem (7.1) is solved by the technique of *first discretize then optimize*. Therefore $\mathcal{J}$ as well as the ODE/DAE constraints are discretized on a given time grid resulting in a huge non–linear program (NLP) see [4, 10, 21, 34]. For solving such NLPs, several efficient solvers have been designed. In [28], the program DIRCOL (DIRect COLlocation) from [29] is used. But for state–of–the–art programming, MATLAB based packages exist; like GPOPS2 (General Pseudo–spectral Optimal Software) [18] or TOMLAB's developments SNOPT (Sparse Linear OPTimizer) and PROPT (Per Rutquist OPTimizer) in [14]. Those solvers commonly use a (pseudo–) gradient based method like BFGS or other quasi–Newton methods for minimizing the objective function.

However, we want to apply the approach of *first optimize then discretize*. Therefore, we derive the first order necessary conditions for problem (7.2) explicitly. We obtain the optimal control u^* by solving the upcoming coupled ODE/DAE system. A state–of–the–art solver for the so–called indirect method (BNDSCO) was developed by Oberle in [22]. The name BNDSCO indicates the use on boundary value problems with switching conditions. This solver uses a multiple shooting method to solve the resulting boundary value problem. For an enhanced discussion on both *first discretize then optimize* and *first optimize then discretize* approaches, see [10, 12, 29].

Most of the available literature on optimal control of muscle dynamics takes only place at the level of activation, see [28]. However, we choose a control on a deeper physiological level, namely the neural stimulation, to find an optimal neural stimulation such that the observed muscle forces are recovered. Furthermore, we want to think of the neural stimulation as a continuous function rather than a bang–bang impulse as in [23].

The biomechanical applications of our method are multifaceted. It is a validation for the used muscle model, because a qualitative error (objective function value) can be given. Moreover, the method's findings allow an investigation of specific parts of the model, for

example the passive and active force–length curves as well as the activation dynamics. Regaining the optimal stimulation of an isometric contraction additionally reveals information about internal concentric and eccentric contraction processes, where the latter is normally hard to investigate solely, see [32]. Finally, we obtain indications for model improvements such as the need to include the concept of fatigue, as suggested in [2].

In Section 7.2 we recapitulate the muscle model given in [7] using contraction modes from [6]. For simplicity, we only consider the situation for a single muscle. In Section 7.3 we formally derive the first order optimality conditions and present an iterative solution algorithm for the upcoming coupled state/co–state system. Our results are presented in Section 7.4. In Section 7.5 we compare our finding with the output of the above mentioned commercial software PROPT. The paper closes with an outlook on possible future work.

7.2. Model Description and Problem Formulation

We use a modified *Hill–type* model [6, 7] to describe the contraction motion of muscles. This model is based on a mechanical analogy of the muscle tendon complex (MTC) and is constituted by four basic compartments (author's note: see Chapter 1).

- The contractile element (CE) produces the force by contracting via actin–myosin cross–bridges at sarcomere level.
- The parallel elastic element (PEE) represents the connective tissues and is responsible for the muscle's passive behavior.
- The serial elastic element (SEE) represents the elastic behavior of the tendon, which connects the muscle to the skeleton.
- The serial damping element (SDE) describes the viscous damping of the tendon.

(Author's note: Figure 1.2 sketches this structure of the Hill–type muscle model consisting of those four elements)

7.2.1. Model Description

Let $\ell_{MTC}, \ell_{PEE}, \ell_{CE}, \ell_{SEE}$ and ℓ_{SDE} denote the length of the constituting elements. Due to the set–up of the model the following restrictions hold:

$$\ell_{CE} = \ell_{PEE}, \quad \ell_{SEE} = \ell_{SDE} \quad \text{and} \quad \ell_{MTC} = \ell_{CE} + \ell_{SEE} \, .$$

Using the notation F_i for the force acting on the i–th component, at equilibrium it holds that

$$F_{MTC} = F_{CE} + F_{PEE} = F_{SEE} + F_{SDE} \, . \tag{7.3}$$

In the sequel, we outline the individual force equations, details can be found in [6]. We recall that *isometric contraction* refers to the situation, where the CE exerts some force without a change of the MTC length. In contrast to that, we speak of a *concentric* or *eccentric* contraction, if the CE exerts force and shortens or elongates.

Following [6], we define the relation between the isometric force F_{isom} and the length ℓ_{CE} of the muscle

$$F_{isom}(\ell_{CE}) = \begin{cases} \exp\left(-\left|\frac{\ell_{CE}-\ell_{CE,opt}}{\ell_{CE,opt}\Delta W_{asc}}\right|^{\nu_{asc}}\right), & \text{if } \ell_{CE} < \ell_{CE,opt} \\ \exp\left(-\left|\frac{\ell_{CE}-\ell_{CE,opt}}{\ell_{CE,opt}\Delta W_{des}}\right|^{\nu_{des}}\right), & \text{if } \ell_{CE} \geq \ell_{CE,opt} \end{cases} . \tag{7.4}$$

The parameters ΔW_{asc}, ν_{asc} and ΔW_{des}, ν_{des} determine the width and slope of the ascending and descending branch of the bell–shaped F_{isom} curve. Note the normalization $F_{isom}(\ell_{CE,opt}) = 1$ at the optimal fiber length $\ell_{CE} = \ell_{CE,opt}$, where the muscle is able to produce its maximum isometric force F_{max}. Other functional dependencies appear in literature, cf. [26, 35].

Subsequently, we introduce the force–velocity relation of the contractile element

$$F_{CE}(\ell_{CE}, \dot{\ell}_{CE}, q) = \begin{cases} F_{max}\left(\frac{qF_{isom}+a_{rel}}{1-\frac{\dot{\ell}_{CE}}{b_{rel}\ell_{CE,opt}}} - a_{rel}\right), & \text{if } \dot{\ell}_{CE} < 0 \quad \text{(concentric)} \\ F_{max}\left(\frac{qF_{isom}+a_{rel,e}}{1-\frac{\dot{\ell}_{CE}}{b_{rel,e}\ell_{CE,opt}}} - a_{rel,e}\right), & \text{if } \dot{\ell}_{CE} \geq 0 \quad \text{(eccentric)} \end{cases} . \tag{7.5}$$

Note that F_{CE} is non–differentiable at $\dot{\ell}_{CE} = 0$. The variable q denotes the muscle activity. According to Zajac [37] the activity and the external neural stimulation σ are related via the ODE

$$\dot{q} = \frac{1}{\tau}\Big(\sigma - \sigma \cdot (1-\beta) \cdot (q - q_0) - \beta \cdot (q - q_0)\Big) . \tag{7.6}$$

The time constant τ and the activation–deactivation ratio β determine the velocity of activation growth or decay after a neural impulse. For a particular description of the physiological meaning of the occurring parameters see the List of Symbols in the Appendix or [6].

Another formulation of activation dynamics was given as a differential–algebraic system by Hatze [9]. A compact form of this system as a first order non–linear ODE was derived in [6, 24] (author's note: see Eqns. 3.3 – 3.5):

$$\dot{q}_H = \frac{\nu \cdot m}{1-q_0} \cdot \Big[\sigma \cdot \rho(\ell_{CErel}) \cdot (1-q_H)^{1+1/\nu} \cdot (q_H - q_0)^{1-1/\nu} - (1-q_H) \cdot (q_H - q_0)\Big] . \tag{7.7}$$

The frequency m and the parameter ν were introduced by Hatze and depend on the particular muscle. The function $\rho(\ell_{CErel})$ is monotonically increasing and introduces a length–dependency of the activation, see Fig. 7.7 in the Appendix. In [6], Hatze's activation dynamics is not used. However, [24] stated that Hatze's formulation might be physiologically more relevant than Zajac's. Hence, we want to include its impact in the discussion, cf. Fig. 7.8 in the Appendix.

Following [6, 7] the parameters $a_{rel}, a_{rel,e}, b_{rel}$ and $b_{rel,e}$ in Eqn. (7.5) depend themselves on ℓ_{CE} and q via

$$a_{rel} = \begin{cases} \frac{a_{rel,0}}{4}(1+3q), & \text{if } \ell_{CE} < \ell_{CE,opt} \\ \frac{a_{rel,0}}{4}(1+3q)F_{isom}, & \text{if } \ell_{CE} \geq \ell_{CE,opt} \end{cases} , \qquad a_{rel,e} = -F_e\, q\, F_{isom} , \tag{7.8}$$

$$b_{rel} = \frac{b_{rel,0}}{7}(3+4q) , \qquad b_{rel,e} = \frac{b_{rel}(1-F_e)}{S_e\left(1+\frac{a_{rel}}{q\,F_{isom}}\right)} . \tag{7.9}$$

The parameter S_e denotes the ratio of the slopes at $\ell_{CE} = \ell_{CE,opt}$ between the concentric and eccentric branch, see Eqn. (7.5). The parameter $F_e = \lim_{\dot{\ell}_{CE}\to\infty} F_{CE}/(F_{max}\, q\, F_{isom})$ is related to the asymptotic behavior of the eccentric force. The parameters $a_{rel,0}$ and $b_{rel,0}$ refer to the Hill parameters, see [11].

For the two elastic elements, we generally assume a non–linear behavior above a certain slack length $\ell_{PEE,0}$ respectively $\ell_{SEE,0}$

$$F_{PEE}(\ell_{CE}) = \begin{cases} 0, & \text{if } \ell_{CE} < \ell_{PEE,0} \\ F_{max}\,\mathcal{F}_{PEE}\left(\frac{\ell_{CE}-\ell_{PEE,0}}{\ell_{CE,opt}(1+\Delta W_{des})-\ell_{PEE,0}}\right)^{\nu_{PEE}}, & \text{if } \ell_{CE} \geq \ell_{PEE,0} \end{cases} . \quad (7.10)$$

The constant $\mathcal{F}_{PEE}$ is related to the force F_{PEE} of the parallel elastic element at the length $\ell_{max} = \ell_{CE,opt}(1 + \Delta W_{des})$ via $F_{PEE}(\ell_{max}) = F_{max}\mathcal{F}_{PEE}$.

Following [6], the serial elastic element is assumed to behave linear, if its length exceeds a threshold $\ell_{SEE,nll} := (1 + \Delta U_{SEE,nll})\ell_{SEE,0}$.

$$F_{SEE}(\ell_{CE}) = \begin{cases} 0, & \text{if } \ell_{SEE} < \ell_{SEE,0} \\ \Delta F_{SEE,0}\left(\frac{\ell_{SEE}-\ell_{SEE,0}}{\Delta U_{SEE,nll}\ell_{SEE,0}}\right)^{\nu_{SEE}}, & \text{if } \ell_{SEE,0} \leq \ell_{SEE} < \ell_{SEE,nll} \\ \Delta F_{SEE,0}\left(1 + \frac{\ell_{SEE}-\ell_{SEE,nll}}{\Delta U_{SEE,l}\ell_{SEE,0}}\right), & \text{if } \ell_{SEE} \geq \ell_{SEE,nll} \end{cases} . \quad (7.11)$$

The parameter $\Delta F_{SEE,0}$ refers to the force of the serial elastic element at length $\ell_{SEE,nll}$. The linear elastic regime for large length $\ell_{SEE} \geq \ell_{SEE,nll}$ is governed by the parameter $\Delta U_{SEE,l}$. The exponent of non–linearity for the serial elastic element is fixed by $\nu_{SEE} = \Delta U_{SEE,nll}/\Delta U_{SEE,l}$, whereas the exponent for the parallel elastic element is an adjustable model parameter In this work we choose $\nu_{PEE} = \nu_{SEE}$, cf. [6].

For the damping element SDE, we assume a linearly increasing damping force

$$F_{SDE}(\dot{\ell}_{MTC}, \ell_{CE}, \dot{\ell}_{CE}, q) = D_{SDE}\left((1 - R_{SDE})\frac{F_{CE} + F_{PEE}}{F_{max}} + R_{SDE}\right)(\dot{\ell}_{MTC} - \dot{\ell}_{CE}) \quad (7.12)$$

with damping parameters D_{SDE} indicating the slope and R_{SDE} indicating the rest damping at $F_{MTC} = 0$.

Solving the equilibrium equation (7.3) for the contraction velocity $\dot{\ell}_{CE}$, we obtain the following differential equation

$$\dot{\ell}_{CE} = \begin{cases} \frac{-C_1 - \sqrt{C_1^2 - 4C_2C_0}}{2C_2}, & \text{if } \dot{\ell}_{CE} < 0 \\ \frac{-C_{1,e} + \sqrt{C_{1,e}^2 - 4C_{2,e}C_{0,e}}}{2C_{2,e}}, & \text{if } \dot{\ell}_{CE} \geq 0 \end{cases} . \quad (7.13)$$

The coefficients C_0, C_1 and C_2 are given by

$$\begin{aligned} C_0 &= D_0\,\dot{\ell}_{MTC} + \ell_{CE,opt}\,b_{rel}\,(F_{SEE} - F_{PEE} - F_{max}qF_{isom})\,, \\ C_1 &= -(C_2\,\dot{\ell}_{MTC} + D_0 + F_{SEE} - F_{PEE} + F_{max}a_{rel})\,, \\ C_2 &= d_{SE,max}\left(R_{SDE} - \left(a_{rel} - \frac{F_{PEE}}{F_{max}}\right)(1 - R_{SDE})\right)\,. \end{aligned}$$

The coefficients $C_{0,e}, C_{1,e}$ and $C_{2,e}$ in the eccentric case $\dot{\ell}_{CE} \geq 0$ are obtained when replacing a_{rel}, b_{rel} with $a_{rel,e}, b_{rel,e}$. The auxiliary coefficients $d_{SE,max}$ and D_0 are given by

$$\begin{aligned} d_{SE,max} &= D_{SDE}\,\frac{F_{max}a_{rel,0}}{\ell_{CE,opt}b_{rel,0}}\,, \\ D_0 &= \ell_{CE,opt}\,b_{rel}\,d_{SE,max}\left(R_{SDE} + (1 - R_{SDE})\left(qF_{isom} + \frac{F_{PEE}}{F_{max}}\right)\right)\,. \end{aligned}$$

Summarizing the above Eqns. (7.3) – (7.13), we obtain a coupled system of equations allowing us to represent the muscle force F_{MTC} as a function of the neural stimulation σ, i.e.

$$F_{MTC} = F_{MTC}(\sigma) \, . \tag{7.14}$$

Introducing the Heaviside step function (author's note: see Example 6.1.3)

$$\Theta : \, \mathbb{R} \longrightarrow [0,1], \qquad \Theta(x) := \begin{cases} 0, & \text{if } x < 0 \\ 1, & \text{if } x \geq 0 \end{cases} \, , \tag{7.15}$$

we can rewrite the previous model equations without using piecewise defined terms, e.g. the isometric force (7.4) is given by

$$\begin{aligned} F_{isom}(\ell_{CE}) &= \exp\left(- \left| \frac{\ell_{CE} - \ell_{CE,opt}}{\ell_{CE,opt} \Delta W_{asc}} \right|^{\nu_{asc}} \right) \\ &+ \left[\exp\left(- \left| \frac{\ell_{CE} - \ell_{CE,opt}}{\ell_{CE,opt} \Delta W_{des}} \right|^{\nu_{des}} \right) - \exp\left(- \left| \frac{\ell_{CE} - \ell_{CE,opt}}{\ell_{CE,opt} \Delta W_{asc}} \right|^{\nu_{asc}} \right) \right] \, \Theta(\ell_{CE} - \ell_{CE,opt}) \, . \end{aligned} \tag{7.16}$$

7.2.2. Problem Formulation

In [6], all model parameters stated above were estimated on the basis of piglet muscle experiments within three contraction modes: isometric, quick–release and concentric contraction against an inertial mass. In the following, we will address the isometric case, i.e. we obtain a force output at different, fixed length $\ell_{MTC,0}$ of the muscle, see [6, Fig. 7] (author's note: this choice was made, because Chapter 5 showed that isometric contractions provide the widest range of information about the model). The neural stimulation σ was imposed as an electrical 0/1–impulse via a primed nerve.

$$\overline{\sigma}(t) = \begin{cases} 1 & \text{if } t \in [t_{\text{start}}, t_{\text{end}}] = [0.1\,\text{s}, 1.1\,\text{s}] \\ 0 & \text{else} \end{cases} \, . \tag{7.17}$$

In the sequel we address the following scenario: Assume, we are unable to apply or measure the stimulation σ directly, but only able to measure the force, resulting from isometric contraction. Is the stimulation $\sigma(t)$ reconstructable? In other words: We wish to find a stimulation $\sigma^*(t)$ such that the resulting force $F^*_{MTC} = F_{MTC}(\sigma^*)$ is as close as possible to the experimentally measured force denoted by $\overline{F}_{MTC} = F_{MTC}(\overline{\sigma})$.

Based on the previous muscle model, we may notate this problem as a constrained minimization problem. Let $\mathcal{U} = C([0,T],[0,1])$ denote the continuous functions from time interval $[0,T]$, which are bounded by $[0,1]$. The objective function $\mathcal{J}$ measures the distance of our simulated results and the measured experimental data. Additionally, it contains an regularization term to ensure a finite control.

$$\min_{\sigma \in \mathcal{U}} \mathcal{J}(F_{MTC}, \sigma) = \frac{1}{2} \left|\left| F_{MTC} - \overline{F}_{MTC} \right|\right|^2_{L^2} + \frac{\alpha}{2} \left|\left| \sigma \right|\right|^2_{L^2} = \frac{1}{2} \int_0^T (F_{MTC} - \overline{F}_{MTC})^2 + \alpha \sigma^2 dt \tag{7.18}$$

subject to the constraints

$$\dot{q} = f_1(q,\sigma)\,, \qquad q(0) = q_0\,, \tag{7.19a}$$
$$\dot{\ell}_{CE} = f_2(\ell_{MTC}, \dot{\ell}_{MTC}, \ell_{CE}, q)\,, \qquad \ell_{CE}(0) = \ell_{CE,0}\,, \tag{7.19b}$$
$$\ddot{\ell}_{MTC} = 0\,, \qquad \ell_{MTC}(0) = \ell_{MTC,0}\,, \quad \dot{\ell}_{MTC}(0) = 0 \tag{7.19c}$$
$$F_{MTC} = f_3(\ell_{MTC}, \dot{\ell}_{MTC}, \ell_{CE}, q)\,. \tag{7.19d}$$

The constraint $\dot{\ell}_{MTC} = 0$ in equation (7.19c) arises from the isometric contraction scenario. If other contraction types, e.g. quick–release or concentric/eccentric contractions, are considered, this condition has to be replaced by the respective equations. If furthermore Hatze's activation dynamics is considered instead of Zajac's, f_1 has to be modified, in particular an ℓ_{CE}–dependency has to be added.

7.3. Solution and Results

Minimizing a cost functional $\mathcal{J}$ with respect to a control σ and subject to constraints given by a set of differential or algebraic conditions is a well–known and well–investigated problem. We will not go into details of proving the existence or uniqueness of minimizers, but rather formally derive the first order necessary conditions for the optimum.

In the isometric case, $\ell_{MTC} = \ell_{MTC,0}$ is constant and thus $\dot{\ell}_{MTC} = 0$, therefore we skip these variables henceforth. Using this simplification, let us denote the state variable by $x = (q, \ell_{CE}, F_{MTC})$. Introducing the adjoint variable $\lambda = (\lambda_q, \lambda_{\ell_{CE}}, \lambda_{F_{MTC}})$, we formally define the Lagrangian

$$\mathcal{L}(x,\lambda,\sigma) := \mathcal{J}(x,\sigma) + \langle \lambda_q,\, \dot{q} - f_1\rangle_{L^2} + \langle \lambda_{\ell_{CE}},\, \dot{\ell}_{CE} - f_2\rangle_{L^2} + \langle \lambda_{F_{MTC}},\, F_{MTC} - f_3\rangle_{L^2}\,. \tag{7.20}$$

By $\langle u, v\rangle_{L^2} := \int_0^T u(t)\,v(t)\,\mathrm{d}t$, we denote the usual L^2–inner product. We use $D_{\tilde{u}}u$ for the (Gâteaux) derivative of u in the direction of $\tilde{u}$ and use $\partial_t u$ for the partial derivative of u w.r.t. t.

The necessary first order optimality conditions imply that at a local optimum all (Gâteaux) derivatives of $\mathcal{L}$ vanish. Computing formally the derivatives w.r.t. the adjoint variables $\lambda_q, \lambda_{\ell_{CE}}, \lambda_{F_{MTC}}$ we recover the state system

$$D_{\lambda_q}\mathcal{L} = 0 \Rightarrow \qquad \dot{q} = f_1(q,\sigma)\,, \qquad q(0) = q_0\,, \tag{7.21a}$$
$$D_{\lambda_{\ell_{CE}}}\mathcal{L} = 0 \Rightarrow \qquad \dot{\ell}_{CE} = f_2(\ell_{MTC,0}, 0, \ell_{CE}, q)\,, \quad \ell_{CE}(0) = \ell_{CE,0}\,, \tag{7.21b}$$
$$D_{\lambda_{F_{MTC}}}\mathcal{L} = 0 \Rightarrow \qquad F_{MTC} = f_3(\ell_{MTC,0}, 0, \ell_{CE}, q)\,. \tag{7.21c}$$

Taking derivatives w.r.t. the state variables q, ℓ_{CE}, F_{MTC} leads to a system of equations for the adjoint or co–state

$$D_q\mathcal{L} = 0 \Rightarrow \qquad \dot{\lambda}_q = -\lambda_{F_{MTC}}\partial_q f_3 - \lambda_{\ell_{CE}}\partial_q f_2 - \lambda_q \partial_q f_1\,, \quad \lambda_q(T) = 0\,, \tag{7.22a}$$
$$D_{\ell_{CE}}\mathcal{L} = 0 \Rightarrow \qquad \dot{\lambda}_{\ell_{CE}} = -\lambda_{F_{MTC}}\partial_{\ell_{CE}} f_3 - \lambda_{\ell_{CE}}\partial_{\ell_{CE}} f_2\,, \quad \lambda_{\ell_{CE}}(T) = 0\,, \tag{7.22b}$$
$$D_{F_{MTC}}\mathcal{L} = 0 \Rightarrow \qquad \lambda_{F_{MTC}} = F_{MTC} - \overline{F}_{MTC}\,. \tag{7.22c}$$

The derivative w.r.t. to the control σ gives rise to the gradient condition

$$D_\sigma\mathcal{L} = 0 \Rightarrow \qquad \alpha\,\sigma = \lambda_q \partial_\sigma f_1\,, \qquad 0 \le \sigma \le 1\,. \tag{7.23}$$

Note that the differential equations for the adjoint variables λ_q and $\lambda_{\ell_{CE}}$ have to be solved backwards in time, starting with the terminal conditions $\lambda_q(T) = 0$ as well as $\lambda_{\ell_{CE}}(T) = 0$. The functional expressions for the partial derivatives, appearing in Eqns. (7.22a) – (7.23), can be derived explicitly, or at least symbolically in MATLAB. Using the Heaviside function as in (7.15), these derivatives can be calculated in a closed form.

To solve the non–linear system (7.21) – (7.23), we use the iterative Algorithm 2. For the simulation results discussed in the next section, we implemented this algorithm using MATLAB (Version R2013b) including the symbolic toolbox for automatic computation of the partial derivatives and the pre–implemented ODE–solver `ode45` for the numerical solution of the differential equations.

Algorithm 2 Discretization after Optimization

Require: $f_1, f_2, f_3, \overline{F}_{MTC}, \alpha, \ell_{MTC}$, error tolerance Tol, initial guess σ_0 for the stimulation
  Calculate $\ell_{CE,0}$ using equation (7.3)
  Calculate F_{MTC} using $\sigma = \sigma_0$
  while $\mathcal{J}(F_{MTC}, \sigma) > Tol$ **do**
    Calculate $\lambda_{F_{MTC}} = F_{MTC} - \overline{F}_{MTC}$
    Solve $\dot{\lambda}_{\ell_{CE}} = -\lambda_{F_{MTC}} \partial_{\ell_{CE}} f_3 - \lambda_{\ell_{CE}} \partial_{\ell_{CE}} f_2$ with $\lambda_{\ell_{CE}}(T) = 0$
    Solve $\dot{\lambda}_q = -\lambda_{F_{MTC}} \partial_q f_3 - \lambda_{\ell_{CE}} \partial_q f_2 - \lambda_q \partial_q f_1$ with $\lambda_q(T) = 0$
    Update σ via $\sigma = (1 - \varepsilon) \cdot \sigma + \frac{\varepsilon}{\alpha} \cdot \lambda_q \partial_\sigma f_1$ with convex combination factor ε
    Solve $\dot{q} = f_1(q, \sigma_0)$ with $q(0) = q_0$
    Solve $\dot{\ell}_{CE} = f_2(\ell_{MTC,0}, 0, \ell_{CE}, q)$ with $\ell_{CE}(0) = \ell_{CE,0}$
    Calculate $F_{MTC} = f_3(\ell_{MTC,0}, 0, \ell_{CE}, q)$
  end while
  Output $F_{MTC}, \ell_{CE}, \dot{\ell}_{CE}, q, \sigma^* = \sigma$

Figures 7.1 and 7.2 show the results of the optimal control approach. Regarding Fig. 7.1, we compare the experimentally measured isometric forces $\overline{F}_{MTC}$ (thin line), see [36] with the force $F^*_{MTC} = F_{MTC}(\sigma^*)$ computed in the optimal control approach (bold line). Additionally, we plotted the direct model output $F_{MTC}(\overline{\sigma})$ of the model equation (7.14) (dashed line), using the experimentally applied 0/1–stimulation $\overline{\sigma}$, see Eqn. (7.17). In Fig. 7.2, we show the reconstructed stimulation σ^* obtained by the optimal control approach versus time. The dashed line refers to the experimental input, i.e. the 0/1–impulse $\overline{\sigma}$. The results are plotted versus time for a muscle of given length $\ell_{MTC} = \ell_{MTC,ref} = 6.15\,\text{cm}$. In the subsequent Figs. 7.3 and 7.4 this length serves as reference length.

7.4. Discussion

7.4.1. Results for Muscle Length $\ell_{MTC} = \ell_{MTC,ref}$

We start with a discussion about certain general findings for the reference muscle length $\ell_{MTC} = \ell_{MTC,ref} = 6.15\,\text{cm}$. In Figs. 7.1 and 7.2, we compare the optimal control results to the experimental and reference data.

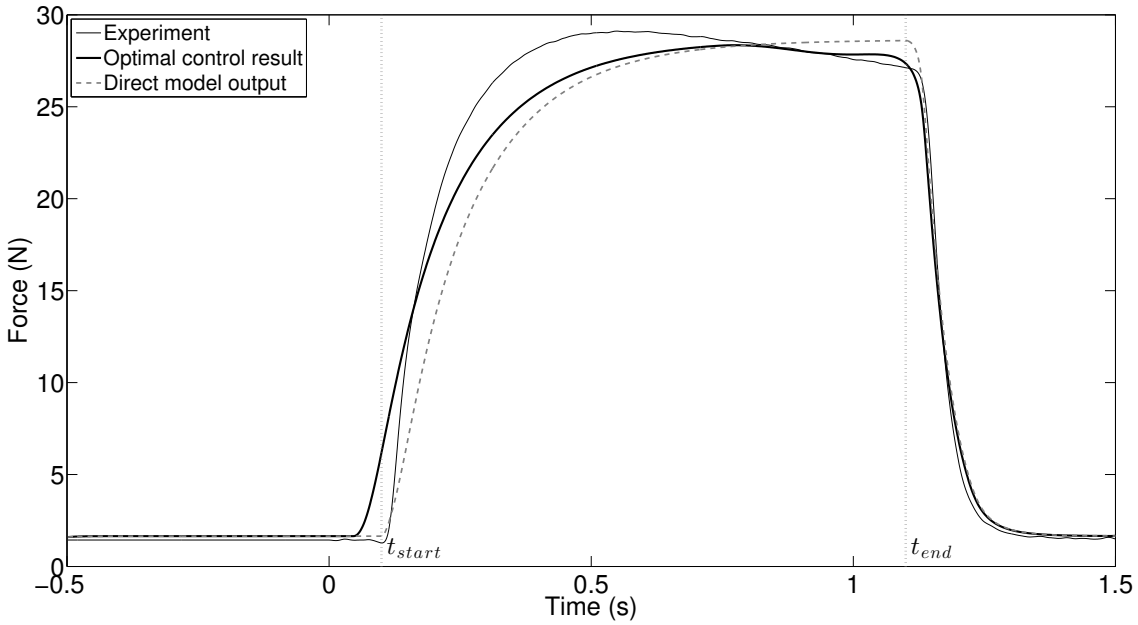

Figure 7.1.: Isometric contraction forces vs. time: Experimental data [36] (thin), optimal control results F^*_{MTC} from Algorithm 2 (bold) and direct model output $F_{MTC}(\overline{\sigma})$ using (7.14) (dashed). The relative muscle length $\ell_{MTC}/\ell_{MTC,ref} = 1$. In addition, we have marked the starting time $t_{\text{start}} = 0.1\,\text{s}$ and ending time $t_{\text{end}} = 1.1\,\text{s}$ of the experimental reference stimulation $\overline{\sigma}$.

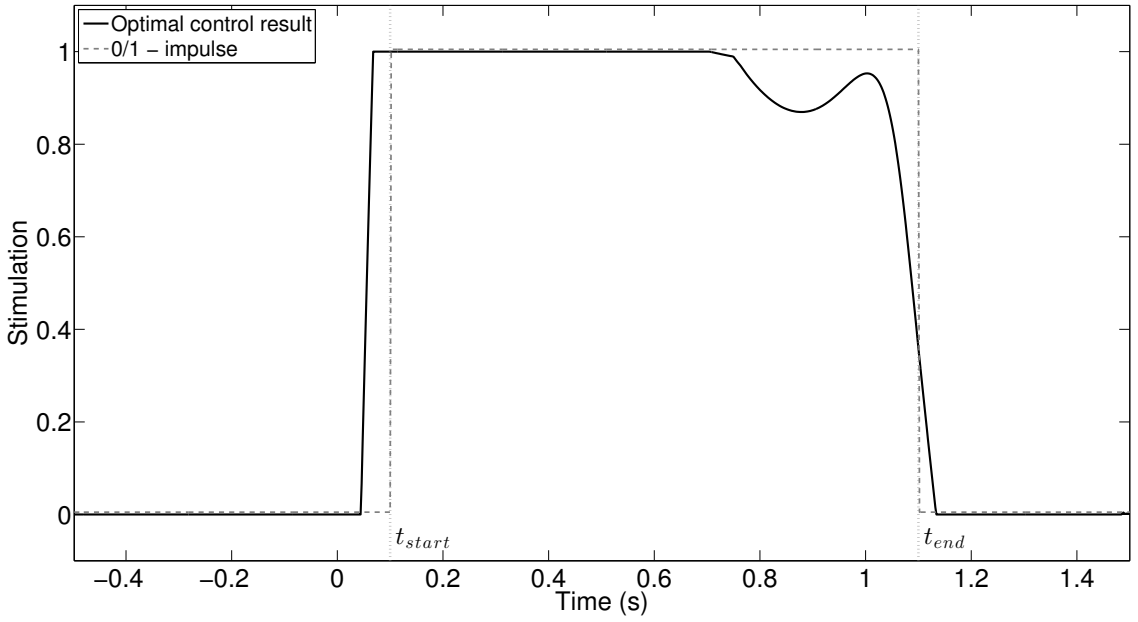

Figure 7.2.: Stimulation vs. time: Comparison of the reconstruction of the optimal stimulation via optimal control (σ^*, thick line) and the reference stimulation ($\overline{\sigma}$, dashed line), see Eqn. (7.17) applied in the experiments. As an initial guess, we used $\sigma_0(t) = 0.5$. The respective force outputs are given in Fig. 7.1.

First of all, we notice that the shape of the reconstructed stimulation σ^* is similar to the reference stimulation $\overline{\sigma}$. The same holds true for the recomputed force F^*_{MTC} (bold line) compared to the experimental data $\overline{F}_{MTC}$ (thin line) and the model output $F_{MTC}(\overline{\sigma})$ (dashed line).

However, the reconstructed stimulation starts to rise before the onset of the reference stimulation. This can be explained by looking at the force curves in Fig. 7.1. The curve for the experimental data shows a much steeper increase than both computed curves, the bold one for the optimal control results and the dashed one for the model output. To compensate for the slower rate of increase, the optimal control curve has to start at earlier times $t < t_{start}$. This is only possible, if the stimulation σ^* also switches to 1 at earlier times (author's note: cf. Chapter 4).

Secondly, one may observe that the experimental results for the force show a slow decrease right after the peak of the force at $t \approx 0.5\,\mathrm{s}$, although the muscle is still fully stimulated, see Fig. 7.2. A mathematical explanation cannot be given, but this might indicate fatigue. However, this slight decrease of the experimental force data is responsible for the rather unexpected local peak of the optimal control stimulation at times $t \approx 1\,\mathrm{s}$. Since the experimental forces decay already for $t > 0.5\,\mathrm{s}$ and the optimal control tries to determine the stimulation such that the computed force fits the experimental data, the stimulation starts to decrease at around $t = 0.8\,\mathrm{s}$. Adjusting the decay rate of the computed force to the experimental data, combined with the prior decay in the stimulation, seems to require the local peak of σ^* at $t \approx 1\,\mathrm{s}$. Once the stimulation is switched off at times $t > 1.1\,\mathrm{s}$, all three force curves show almost identical decay rates. This indicates the model's good correspondence with its parameters and the real–world situation.

The optimal control results are largely independent of the initial guess $\sigma_0(t)$; the presented results were obtained using $\sigma_0(t) = 0.5$.

7.4.2. Results for Muscle Lengths $0.85 \leq \ell_{MTC}/\ell_{MTC,ref} \leq 1.1$

Using Figs. 7.3 and 7.4, we compare the optimal control results with experimental and reference data for various muscle lengths given in [6].

The previously stated results for the shape of the calculated curves, i.e. the stimulation peak at $t = 1\,\mathrm{s}$ and the fatigue still hold true. However, the variation of the muscle length reveals some additional observations.

At short muscle lengths, the stimulation σ in Fig. 7.4 appears to be significantly lower than the expected full stimulation, e.g. $\sigma^* < 0.6$ at the shortest length $\ell_{MTC}/\ell_{MTC,ref} = 0.85$. An explanation cannot be given within the framework of the used models. However, one may suggest to replace Zajac's activation dynamics (7.6) by Hatze's formula (7.7), see [5, 9]. In this modified activation dynamics, the muscle activation q depends not only on the neural stimulation σ, but also on the current muscle length ℓ_{CE} (author's note: in Chapter 8, we realized this replacement).

For short muscles, e.g. $\ell_{MTC}/\ell_{MTC,ref} = 0.85$ and 0.88, the data show a faster decay of the experimental force compared to the simulated results. This may also indicate that the activation depends on the muscle length as explained above.

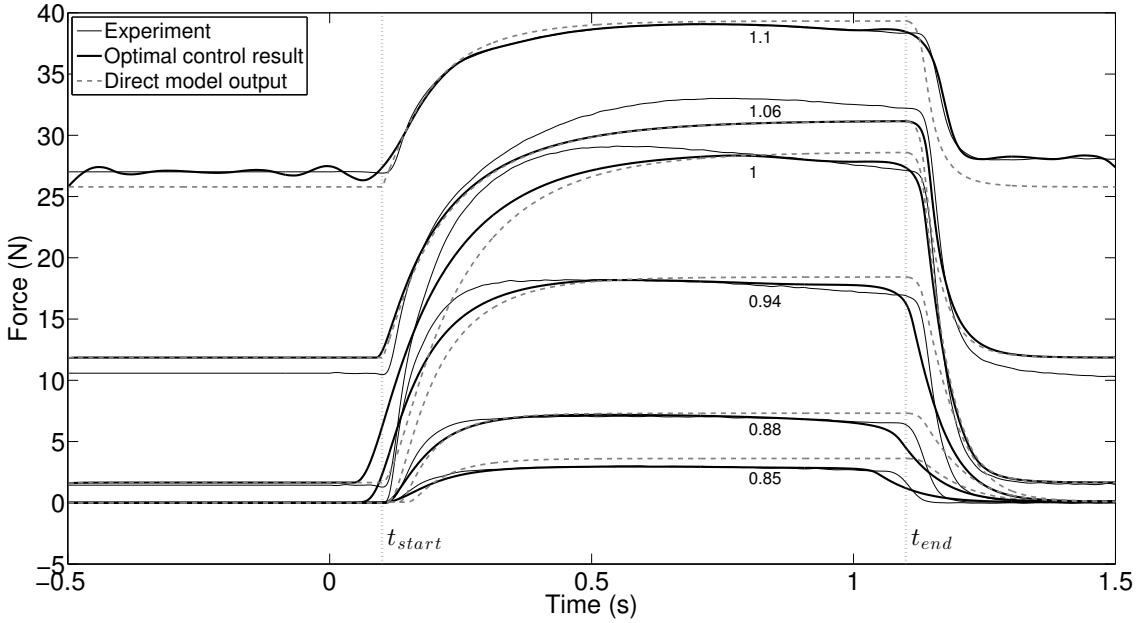

Figure 7.3.: Isometric contraction forces vs. time: Experimental data from [36] (thin black line), optimal control results (bold black line) and direct model output using (7.14) (dashed line). The different graphs refer to different relative muscle lengths $\ell_{MTC}/\ell_{MTC,ref}$, marked with little numbers $0.85, \ldots, 1.1$.

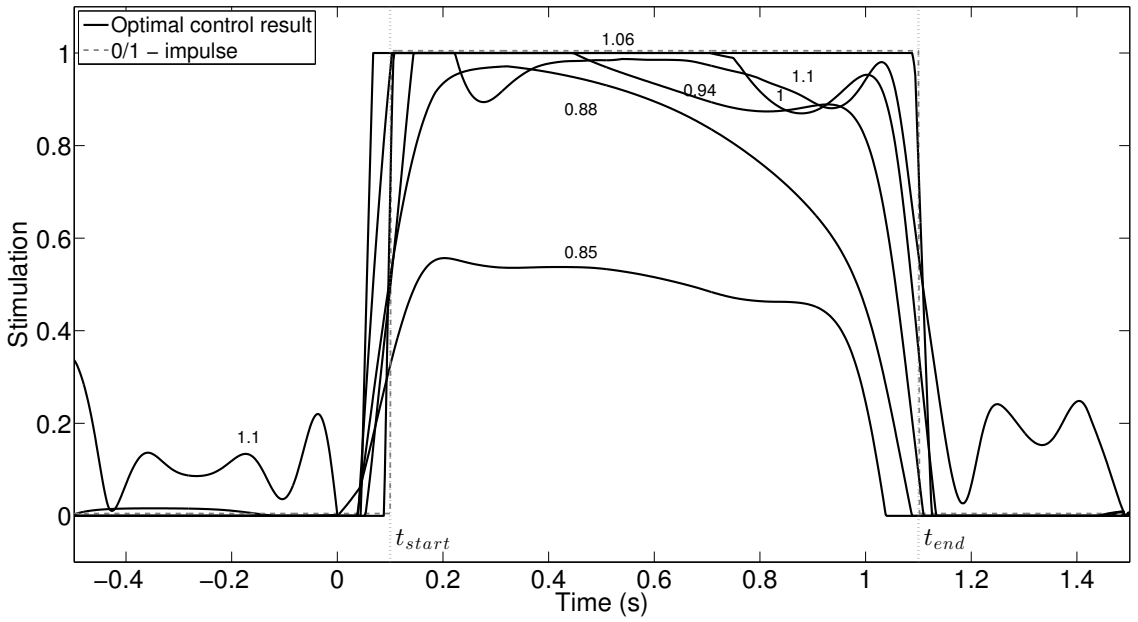

Figure 7.4.: Stimulation vs. time for different muscle lengths: Result from the reconstruction using optimal control (thick line) and literature reference $\overline{\sigma}$, see [6] (dashed line). The muscle length is indicated by the $\ell_{MTC}/\ell_{MTC,ref}$–ratio and printed besides the respective optimal control curves.

For long muscles, e.g. $\ell_{MTC}/\ell_{MTC,ref} = 1.1$, Fig. 7.4 shows, that the reconstructed stimulation is non–zero even for times $t < t_{start}$, which can be explained regarding the initial forces in Fig. 7.3. For $t < t_{start}$ the experimentally observed forces are larger than the direct model output without neural stimulation. This indicates the need for further adjustment of the model parameters in the passive regime, i.e. for zero stimulation. The optimal control algorithm tries to diminish this force difference in order to reduce the objective function value. The only option is applying some non–zero stimulation to the model, which responds in generating the missing force for $t < t_{start}$.

The results for the muscle length $\ell_{MTC}/\ell_{MTC,ref} = 1.06$ show a special behavior. Before the onset of the stimulation, i.e. for times $t < t_{start}$, the experimentally measured forces are less than the simulated forces, even with zero stimulation as seen in the direct model output (see dashed line in Fig. 7.3). In contrast to that, during the stimulation phase, i.e. for $t \in [t_{start}, t_{end}]$, the experimentally forces are larger than the simulated ones, even with maximal stimulation $\sigma = 1$. Hence, the optimal control forces F^*_{MTC} agree with the direct model output $F_{MTC}(\overline{\sigma})$ for the experimentally applied 0/1–impulse $\overline{\sigma}$ in Eqn. (7.17).

7.5. Comparison with Commercial Software

To further validate our findings, we present a comparison of the results obtained by our optimal control Algorithm 2 with a commercial software package called PROPT (see [33]). This software is based on MATLAB and available with a demo license. PROPT currently uses Gauss or Chebyshev–point collocation for solving optimal control problems. As initial input, PROPT requires the model functions (7.3) – (7.13) as well as the objective $\mathcal{J}$ and boundaries for state and control variables. The optimal control problem is discretized and the upcoming non–linear program (NLP) is solved. We are going to state some relevant factors using PROPT. For further information including some illustration problems see [25]. A similar commercial software package based on Gaussian pseudo–spectral collocation is called GPOPS2, see [18].

Since non–continuous functions cannot be handled by the above mentioned packages, we have to approximate e.g. the Heaviside function Θ by a smooth logistic function $\Theta_k(x) = 1/(1 + e^{-2kx})$, with $k \gg 1$. In our computations $k = 3000$ turned out to be a good choice. Since the commercial packages solve the optimal control problem by a *first discretize then optimize* approach, attention has to be paid to the number of discretization or grid points used in the computations. For more than 200 grid points PROPT issued a warning that the upcoming NLP matrix was close to singularity and for less than 100 grid points the results may be incorrect. With a choice of 120 grid points the algorithm was able to run all calculations, while the evaluation time was similar to our self–implemented optimal control algorithm.

In Fig. 7.5, we compare the computed muscle forces obtained by our optimal control Algorithm 2 (bold line) and the PROPT software (dashed line). As a reference, we included the experimental data (thin line). Figure 7.6 shows the stimulation σ^*_P computed by PROPT in comparison to the reference 0/1–impulse $\overline{\sigma}$ used in the experiments.

Both optimal control methods, our *first optimize then discretize* approach in Algorithm 2 and the *first discretize then optimize* method implemented in the PROPT software yield very similar results for the muscle forces, see Fig. 7.5. The initial oscillations in the PROPT–force at $\ell_{MTC}/\ell_{MTC,ref} = 1.06$ can be explained by similar reasons as the optimal control results in the previous section.

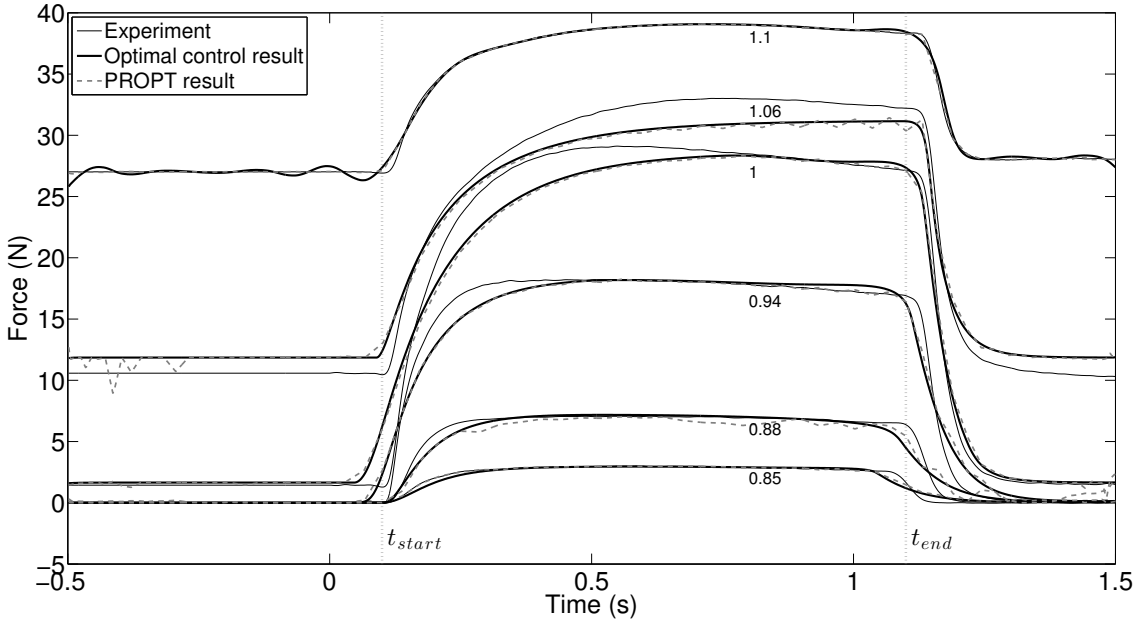

Figure 7.5.: Isometric contraction forces vs. time: Experimental data ($\overline{F}_{MTC}$, thin line), our Algorithm 2 (F^*_{MTC}, bold line) and software package PROPT ($F^*_{MTC,P}$, dashed line). The different graphs refer to different relative muscle lengths $\ell_{MTC}/\ell_{MTC,ref}$, cf. Fig. 7.3.

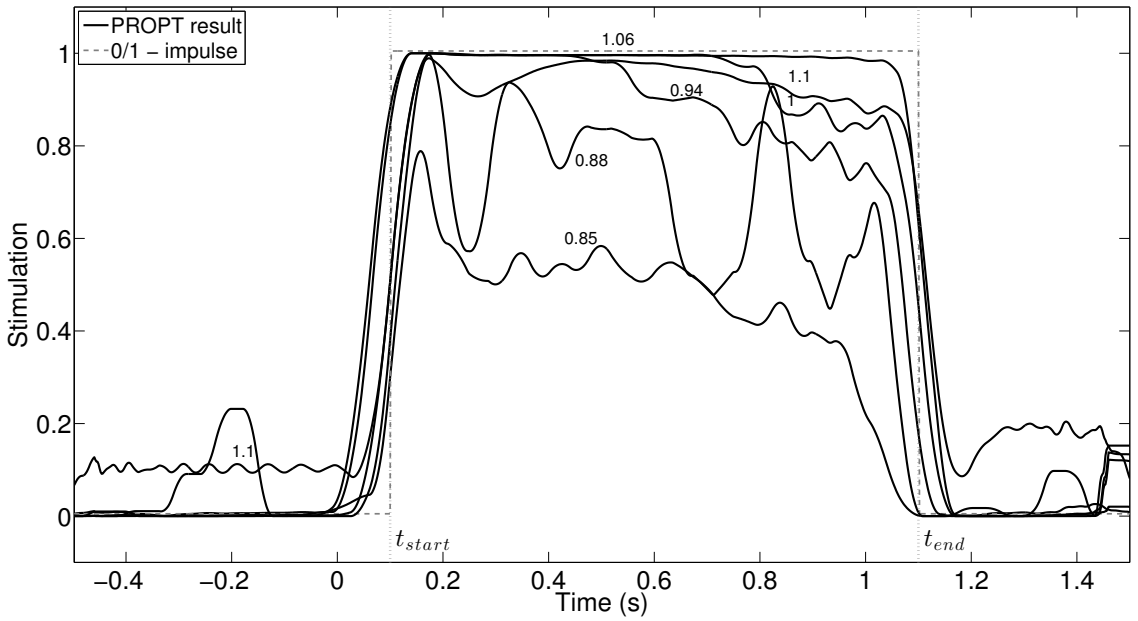

Figure 7.6.: Stimulation vs. time for different muscle lengths: Result from the reconstruction using PROPT (σ^*_P, thick line) and literature reference ($\overline{\sigma}$, dashed line). The PROPT result is smoothed by a moving average (over a time period $\mathrm{d}t = 0.08\,\mathrm{s}$) to remove highly oscillatory behavior.

Note that the stimulation σ_P^* computed by PROPT needed to be smoothed by a moving average filter. Due to the *first discretize then optimize* approach, the underlying NLP computes an individual optimal search direction for the stimulation at each discretization point. Thus, the results can exhibit artificial oscillations and peaks. In contrast to that, our Algorithm 2, which is based on the *first optimize the discretize* approach, computes globally valid search directions; hence, the results do not show discretization–dependent artefacts or oscillations.

Table 7.1 lists the values of the objective function $\mathcal{J}$, see Eqn. (7.18), for our optimal control Algorithm 2, the commercial software PROPT and the direct model output using the 0/1–impulse stimulation. Additionally to the MTC lengths from Figs. 7.3 and 7.5, we added the objective function values for lengths $\ell_{MTC}/\ell_{MTC,ref} \in \{0.91, 0.97, 1.03, 1.08\}$ (cf. [6]), which we did not display due to clarity. As expected, both optimized results yield significantly lower objective function values compared to the direct output given in the last column. Comparing the two optimization approaches to each other, the optimal control results are in most cases slightly better than the PROPT results; the total value of the objective function is about 3% lower for the optimal control methods.

Length $\frac{\ell_{MTC}}{\ell_{MTC,ref}}$	Optimal Control $\mathcal{J}(F_{MTC}^*, \sigma^*)$	PROPT $\mathcal{J}(F_{MTC,P}, \sigma_P^*)$	Comparison $\frac{1}{2}\|\|F_{MTC}^* - F_{MTC,P}\|\| + \frac{\alpha}{2}\|\|\sigma^* - \sigma_P^*\|\|$	Direct Output $\mathcal{J}(F_{MTC}(\overline{\sigma}), \overline{\sigma})$
0.85	3.3	2.9	1.9	13.4
0.88	7.6	8.7	6.0	15.0
0.91	9.7	8.9	4.8	24.0
0.94	15.3	15.0	6.0	28.1
0.97	16.5	17.2	5.4	35.3
1	22.9	24.2	4.2	33.8
1.03	24.7	26.3	4.4	32.7
1.06	24.8	25.9	6.1	26.4
1.08	8.9	9.4	3.6	21.0
1.1	4.9	3.3	3.2	21.8
$\sum$	138.6	141.9	45.6	251.5

Table 7.1.: Objective function values at different muscle lengths: Optimal control Algorithm 2 (F_{MTC}^*, second column), Commercial software PROPT ($F_{MTC,P}$, third column) and direct model output ($F_{MTC}(\overline{\sigma})$, fifth column). The regularization parameter was chosen as $\alpha = 0.1$. The fourth column shows the L^2–difference between our results and the PROPT results.

7.6. Conclusion and Outlook

We presented an optimal control algorithm to recover the stimulation of a muscle, based on its isometric force output. Simulations performed in comparison to experimental data showed the applicability of our approach. High congruence between the experimentally applied stimulation and the mathematically recovered one was found. A further comparison with commercial software validated our results. The computational results showed, that the choice of the activation dynamics could be of importance. To further investigate

the choice of activation dynamics, we derived a comparative sensitivity analysis of Hatze's and Zajac's activation dynamics by taking the effects of parameter changes into account, see [24] (author's note: see Chapter 3 and 8).

Furthermore interesting would be the parameter estimation of the whole muscle model described in Section 7.2, compared to another muscle model from [26]. In today's biomechanics, parameter estimation is still done by educated try and error, therefore we want to find an algorithmic optimization approach. Additionally, the available models might be improved by including physiologically observed effects, such as eccentric force–velocity relation, force depression, force enhancement and fatigue, see [7, 16, 31].

Eventually, regarding modern biomechanical simulations, we have to face huge multi–body systems with a multitude of muscles and boundary conditions performing a variety of movements as in human walking, jumping or scoring a soccer goal, see [8, 20, 27, 30]. Solving an optimal control problem for each muscle would be too expensive to perform within reasonable time. As an alternative optimal control strategy, the technique of *space–mapping* could be used (authors note: cf. Chapter 9). Developed for the use of microwave filter designs, see [17], the optimal control algorithm uses the idea of surrogate–based modeling: an accurate but complex model is simplified to obtain a less complex (but inexact) model. The optimization is done exclusively on the level of the simpler model, whereas the crucial part is to find a mapping of the complex model to the simpler model, the so–called *space–mapping*. This idea can be applied to control a complex multi–body system with several hundreds of components.

Acknowledgement:
The authors want to thank Dr. Michael Günther, University of Stuttgart for numerous discussions and providing us contact to experimental data. Special thanks also go directly to Prof. Dr. Veit Wank, University of Tübingen, for granting us access to his experimental results.

Appendix

Length–Dependency of Activation Dynamics

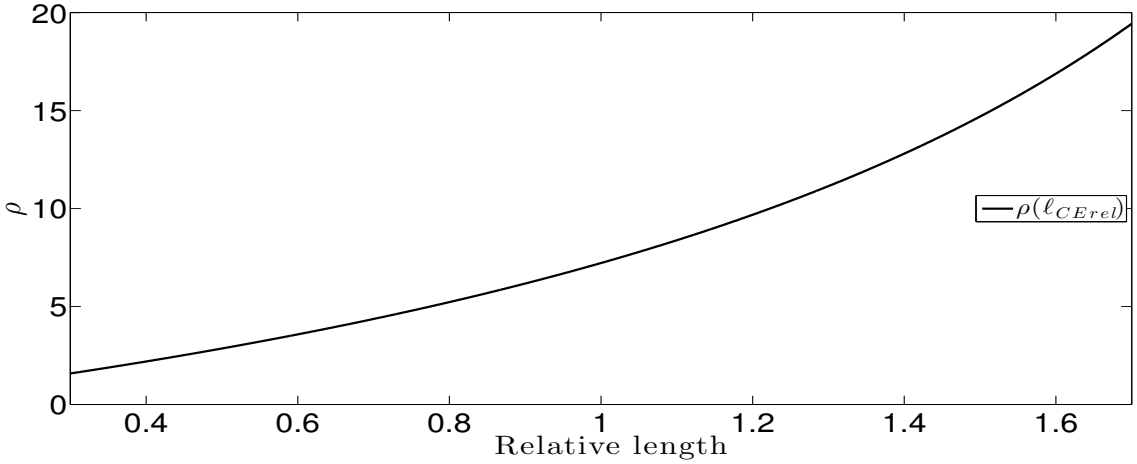

Figure 7.7.: Outline of the hyperbolic function $\rho(\ell_{CErel}) = \rho_0 \cdot c \cdot \ell_{CErel}(\ell_\rho - 1)/(\ell_\rho - \ell_{CErel})$ on the interval $0.3 \leq \ell_{CErel} \leq 1.7$. The parameters are taken from the List of Symbols below.

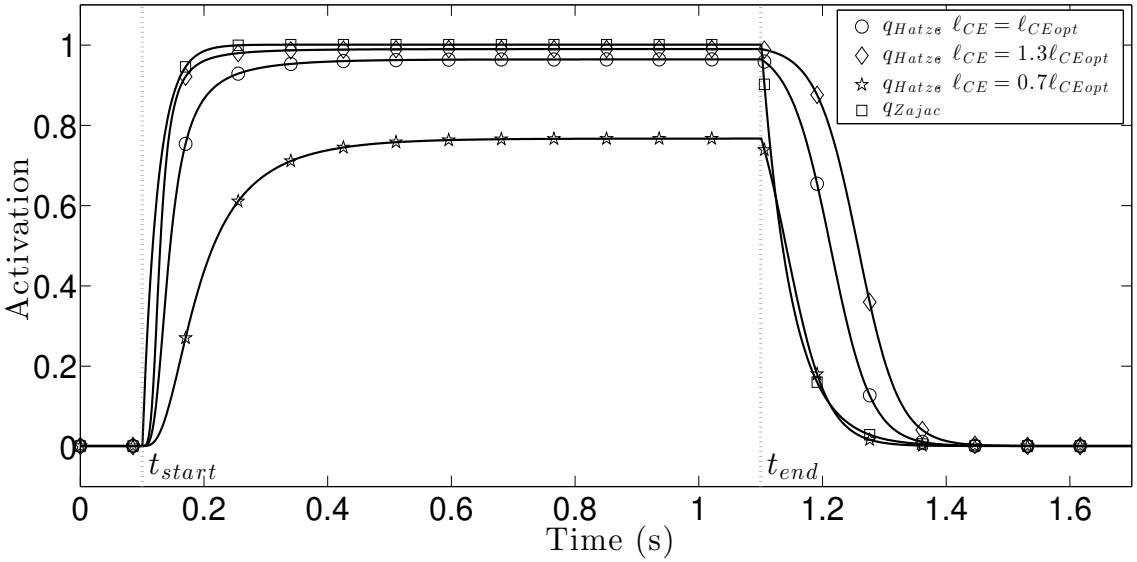

Figure 7.8.: Comparison of Zajac's and Hatze's activation dynamics. As stimulation we used the experimental input $\overline{\sigma}$. If the relative muscle lengths ℓ_{CErel} is decreasing, so is the maximum value for q_H, whereas Zajac's activation maximum is not.

List of Symbols

Symbol	Meaning	Value / Remark
$a_{rel,0}$ /$b_{rel,0}$	Hill–parameters of contraction dynamics	0.1 resp. 1 Hz (muscle–specific)
β	activation–deactivation ratio [37]	0.8 (muscle–specific)
c	maximum Ca^{2+} concentration in [9]	$1.37 \cdot 10^{-4}$ mol/l
D_{SE}	damping parameter	0.3 (muscle–specific)
ΔW_{asc}	width of ascending limb of F_{isom}–curve	0.57 (muscle–specific)
ΔW_{des}	width of descending limb of F_{isom}–curve	0.14 (muscle–specific)
$\Delta F_{SEE,0}$	reference force of SEE	60 N (muscle–specific)
$\Delta U_{SEE,nll}$	relative width of non–linear branch in SEE	0.1825 (muscle–specific)
$\Delta U_{SEE,l}$	relative width of linear branch in SEE	0.073 (muscle–specific)
F_e	limit factor for high eccentric velocities	1.8 (muscle–specific)
F_{isom}	isometric muscle force	length–depending
F_{max}	maximum isometric force of the CE	30 N (muscle–specific)
$\mathcal{F}_{PEE}$	normalization factor of F_{PEE} w.r.t. F_{max}	1 (muscle–specific)
γ	representation of free Ca^{2+} concentration [9]	time–depending
ℓ_{CE}	contractile element (CE) length	time–depending
$\dot{\ell}_{CE}$	contraction velocity	first time derivative of ℓ_{CE}
$\ell_{CE,opt}$	optimal CE length	0.015 m (muscle–specific)
$\mathcal{L}_{PEE}$	root of F_{PEE} at $\mathcal{L}_{PEE}\ell_{CE,opt}$	0.9 (muscle–specific)
ℓ_ρ	pole in Hatze's length–dependency function	2.9
$\ell_{SEE,0}$	slack length of SEE	0.045 m (muscle–specific)
m	activation frequency constant in [9]	10 Hz (muscle–specific)
ν	exponent in Hatze's formulation	3 (muscle–specific)
ν_{asc}	exponent of ascending limb of F_{isom}–curve	4 (muscle–specific)
ν_{des}	exponent of descending limb of F_{isom}–curve	3 (muscle–specific)
ν_{PEE}	exponent of F_{PEE}–curve	2.5 (muscle–specific)
q	muscle activity (bound Ca^{2+} concentration)	time–depending
q_0	basic activity according to [9]	0.005
q_H	activation dynamics from Hatze	time–depending
R_{SE}	damping parameter	0.01 (muscle–specific)
ρ	length dependency of Hatze's activation	length–depending
ρ_0	factor in [9, 35]	$5.27 \cdot 10^4$ l/mol (muscle–specific)
S_e	ratio of derivatives of F_{CE} at $\dot{\ell}_{CE} = 0$	2 (muscle–specific)
σ	neural muscle stimulation	time–depending
τ	activation time constant in [37]	here: 1/40 s

Bibliography

[1] F. Anderson and M. Pandy. “Static and dynamic optimization solutions for gait are practically equivalent”. In: *J. Biomechanics* 34.2 (2001), pp. 153–161.

[2] M. Böl. “A Finite Element Approach for the Modelling of Skeletal Muscle Fatigue”. In: *GAMM-Mitt.* 32.2 (2009), pp. 205–220.

[3] T. S. Buchanan et al. “Estimation of Muscle Forces and Joint Moments Using a Forward-Inverse Dynamics Model”. In: *J. American College of Sports Medicine (ACSM)* 37.11 (2005), pp. 1911–1916.

[4] K. Ghobadi. “On the Discretize then Optimize Approach”. Preprint for Industrial and Systems Engineering. 2009.

[5] M. Günther. “Computersimulation zur Synthetisierung des muskulär erzeugten menschlichen Gehens unter Verwendung eines biomechanischen Mehrkörpermodells”. PhD thesis. Universität Tübingen, 1997.

[6] M. Günther, S. Schmitt, and V. Wank. “High-frequency oscillations as a consequence of neglected serial damping in Hill-type muscle models”. In: *Biological Cybernetics* 97.1 (2007), pp. 63–79.

[7] D. F. B. Haeufle et al. “Hill-type muscle model with serial damping and eccentric force-velocity relation”. In: *Journal of Biomechanics* 47.6 (2014), pp. 1531–1536.

[8] R. Happee. “Inverse Dynamic Optimization Including Muscular Dynamics, a New Simulation Method Applied to Goal Directed Movements”. In: *J. Biomechanics* 27.7 (1994), pp. 953–960.

[9] H. Hatze. “A Myocybernetic Control Model of Skeletal Muscle”. In: *Biological Cybernetics* 25.2 (1977), pp. 103–119.

[10] M. Heinkenschloss. “PDE Constrained Optimization”. SIAM Conference on Optimization. May 2008.

[11] A. V. Hill. “The Heat of Shortening and the Dynamic Constants of Muscle”. In: *Proceedings of The Royal Society London B* 126.843 (1938), pp. 136–195.

[12] M. Hinze. *Mathematics of PDE constrained optimization - Discrete concepts*. Presentation in Oberwolfach. Nov. 2010.

[13] R. Höpler, M. Stelzer, and O. von Stryk. “Object-oriented dynamics modeling for legged robot trajectory optimization and control”. In: *Proc. IEEE Conf. on Mechatronics and Robotics* (2004), pp. 972–977.

[14] Toblab Optimization Inc. *http://www.tomopt.com/*.

[15] D. A. Kistemaker, A. J. van Soest, and M. F. Bobbert. “Is equilibrium point control feasible for fast goal-directed single-joint movements?” In: *Journal of Neurophysiology* 95.5 (2006), pp. 2898–2912.

[16] N. Kosterina and A. Eriksson. “History effect and timing of force production introduced in a skeletal muscle”. In: *Biomech Modell Mechanobiol* 11.7 (2012), pp. 947–957.

[17] S. Koziel and J. Bandler. “Accelerated Microwave Design Optimization With Tuning Space Mapping”. In: *IEEE Transactions on Microwave Theory and Techniques* 57.2 (2009), pp. 383–394.

[18] RP Optimization Research LLC. *http://www.gpops2.com*.

[19] R. Maas, T. Siebert, and S. Leyendecker. “On the relevance of structure preservation to simulations of muscle actuated movements”. In: *Biomech Model Mechanobiol* 11.3-4 (2012), pp. 543–556.

[20] L. Menegaldo. “A ’cheap’ optimal control approach to estimate muscle forces in musculoskeletal systems”. In: *J. Biomechanics* 39.10 (2006), pp. 1787–1795.

[21] H. J. Oberle. *Variationsrechnung und Optimale Steuerung*. Skript zur Vorlesung. 2008.

[22] H. J. Oberle and W. Grimm. *BNDSCO - A Program for the Numerical Solution of Optimal Control Problems*. Institute for Flight Systems Dynamics, DLR, Oberpfaffenhofen. 1989.

[23] M. Pandy, F. E. Zajac, and W. Levine E. Sim. “An optimal control model for maximum-height human jumping”. In: *J. Biomechanics* 23.12 (1990), pp. 1185–1198.

[24] R. Rockenfeller et al. “Comparative Sensitivity Analysis of Muscle Activation Dynamics”. In: *Computational and Mathematical Methods in Medicine* Article ID 585409, doi:10.1155/2015/585409 (2015), 16 pages.

[25] P. Rutquist and M. Edvall. *PROPT - Matlab Optimal Control Software*. TOMLAB Optimization. 2010.

[26] T. Siebert et al. “Nonlinearities make a difference: comparison of two common Hill-type models with real muscle”. In: *Biological Cybernetics* 98.2 (2008), pp. 133–143.

[27] T. Spägele, A. Kistner, and A. Gollhofer. “A multi-phase optimal control technique for the simulation of a human vertical jump”. In: *J. Biomechanics* 32.1 (1999), pp. 87–91.

[28] M. Stelzer and O. von Stryk. “Efficient Forward Dynamics Simulation and Optimization of Human Body Dynamics”. In: *ZAMM* 86.10 (2006), pp. 828–840.

[29] O. von Stryk. *Numerische Lösung optimaler Steuerungsprobleme: Diskretisierung, Parameteroptimierung und Berechnung der adjungierten Variablen*. Vol. 8. 441. VDI-Verlag, 1995.

[30] D. Thelen and F. Anderson. “Using computed muscle control to generate forward dynamic simulation of human walking from experimental data”. In: *J. Biomechanics* 39.3 (2006), pp. 1107–1115.

[31] O. Till, T. Siebert, and R. Blickhan. “Force depression decays during shortening in the medial gastrocnemius of the rat”. In: *J. Biomechanics* 47.5 (2014), pp. 1099–1103.

[32] O. Till et al. “Characterization of isovelocity extension of activated muscle: A Hill-type model for eccentric contractions and a method for parameter determination”. In: *Journal of Theoretical Biology* 225.2 (2008), pp. 176–187.

[33] TOMLAB. *http://www.tomdyn.com/*.

[34] F. Tröltzsch. *Optimale Steuerung partieller Differentialgleichungen*. Vol. 2. Vieweg + Teubner, 2009.

[35] A. J. van Soest. "Jumping from Structure to Control: A Simulation Study of Explosive Movements". PhD thesis. Amsterdam: Vrije Universiteit, 1992.

[36] V. Wank. "Muscle growth and fiber type composition in hind limb muscles during postnatal development in pigs". In: *Cells Tissues Organs* 182.3 (2006), pp. 171–181.

[37] F. E. Zajac. "Muscle and Tendon: Properties, Models, Scaling, and Application to Biomechanics and Motor Control". In: *Critical Reviews in Biomedical Engineering* 17.4 (1989), pp. 359–411.

8. Research Paper IV: Optimization Problems in Epidemiology, Biomechanics & Medicine

T. Götz R. Rockenfeller K. P. Wijaya

The following is a reformatted and slightly modified copy of the article
T. Götz, R. Rockenfeller and K. P. Wijaya. "Optimization Problems in Epidemiology, Biomechanics & Medicine". In: International Journal of Advances in Engineering Sciences and Applied Mathematics. 7.2 (2015), pp. 25–32
available at http://link.springer.com/article/10.1007/s12572-015-0130-5 .
This article is also referred to as [7] (in Chapter 4) or [25] (in the remaining work).

The introductory sections as well as the conclusion were written by T. Götz. The section "Application in Epidemiology" was written by K. P. Wijaya. The section "Application in Biomechanics" was written by R. Rockenfeller.

Abstract

Mathematical simulations are of increasing relevance for applications in engineering and the life sciences. Disciplines like epidemiology, biomechanics, medical image processing, just to name a few, are subject of academic research since decades. Modern numerical methods profit from increasing computational power, therefore simulations of complex biological systems are within reach. Furthermore, optimization of these systems, in term of goal directed behaviour, can be addressed. We will discuss some examples from epidemiology as well as biomechanical models for muscles. These models are based on a set of differential equations. Defining a suitable cost functional to measure the distance to the goal of our optimization, mathematical tools from constrained optimization can be applied to solve optimization problems and to derive suitable numerical algorithms.

Keywords: Optimal Control, Epidemiology, Biomechanics

8.1. Introduction

Mathematical models for everyday phenomena often ask for a control or input such that a system reacts in an optimal or at least in a desired way. Examples for such problems are manyfold, e.g. finding the optimal rotation of a stick for cooking potatoes on the open fire such that the potato has a desired temperature, see [15], constructing an optimal strategy against the spread of dengue disease such that maximal reduction of the number of infected cases is achieved with minimal cost [1, 18] or computing the optimal neural stimulation of a muscle such that the force output is as close as possible to experimentally measured data [13].

In the next section we will give some general outline of optimal control problems. Section 8.3 presents its application to a model for Dengue epidemics. A second application related to the neural stimulation of muscles is the content of Section 8.4. Finally, we give some conclusions and an outlook on possible topics for future research.

8.2. General Outline of Optimal Control Problems

We consider a system characterized by a state variable $x \in \mathcal{X}$ that satisfies the state equation $\dot{x} = f(x, u, t)$ on the time interval $[0, T]$ supplemented by an initial condition $x(0) = x_0$. Here, $\mathcal{X}$ denotes the state space. In case of $\mathcal{X} \subseteq C^1([0,T]; \mathbb{R}^n)$, the state equation is given by an ordinary differential equation. In case of $\mathcal{X}$ being a suitable function space, e.g. $\mathcal{X} = L^2([0,T]; H_0^1(\Omega))$ for a domain $\Omega \subseteq \mathbb{R}^m$, the state equation can be interpreted as a partial differential equation. In the sequel we consider, also for the sake of shortness, just the case $\mathcal{X} = C^1([0,T]; \mathbb{R}^n)$, and hence systems described by a set of ordinary differential equations.

The control variable $u \in \mathcal{U}$ belongs to the set $\mathcal{U}$ of admissible control functions, e.g. $\mathcal{U} \subseteq L^2([0,T]; \mathbb{R}^p)$. The goal of our optimization problems is to find an admissible control $u \in \mathcal{U}$, such that a cost functional of integral type

$$J(x,u) := \int_0^T j\left(x(t),\, u(t), t\right) \,\mathrm{d}t \;\longrightarrow \min$$

attains a minimum, provided the state x solves the state equation $\dot{x} = f(x,u,t)$, $x(0) = x_0$.

Typical control problems are so–called tracking–type problems: Find the control u such that the state x of the system is as close as possible to a desired state $x_d \in \mathcal{X}$. In that case, the cost functional is often modeled as

$$J_{track}(x,u) := \frac{1}{2}\,\|x - x_d\|_{L^2}^2 + \frac{\omega}{2}\,\|u\|_{L^2}^2 = \frac{1}{2}\int_0^T |x(t) - x_d(t)|^2 + \omega\,|u(t)|^2 \,\mathrm{d}t\,.$$

Here, the parameter $\omega > 0$ acts as a regularization parameter.

To solve the constrained minimization problem

$$\min_{u \in \mathcal{U}} J(x,u) \qquad \text{subject to} \qquad \dot{x} = f(x,u,t),\ x(0) = x_0\,, \tag{8.1}$$

we formally introduce the adjoint (or co–state) variable $z \in \mathcal{Z}$. The resulting Lagrangian $\mathcal{L} : \mathcal{X} \times \mathcal{U} \times \mathcal{Z} \to \mathbb{R}$ reads as

$$\mathcal{L}(x,u,z) := J(x,u) + \langle \dot{x} - f(x,u,t)\,,\, z\rangle\,.$$

By $\langle x, z\rangle = \int_0^T x(t)\,z(t)\,\mathrm{d}t$ we denote the usual L^2–inner product. The necessary first order optimality conditions imply that at a local optimum all (Gâteaux) derivatives of $\mathcal{L}$ vanish.

Computing the derivatives w.r.t. the adjoint variable z formally, we recover the state system

$$\dot{x} = f(x,u,t), \quad x(0) = x_0\,. \tag{8.2}$$

Taking the (vector–valued) derivative with respect to the state variable x leads to a system of equations for the adjoint

$$\dot{z} = -z \cdot \partial_x f(x,u,t) + \partial_x j(x,u), \quad z(T) = 0\,. \tag{8.3}$$

Note that the differential equation for the adjoint variable has to be solved backwards in time, starting with the terminal condition $z(T) = 0$. The derivative w.r.t. the control u gives rise to the gradient condition

$$0 = \nabla_u \mathcal{L}(x, u, z) := \partial_u j(x, u) - z \cdot \partial_u f(x, u, t) \; . \tag{8.4}$$

To solve the non–linear system (8.2) – (8.4), we use an iterative gradient method.

(Step 1) Given an initial guess $u^{(0)} \in \mathcal{U}$ for the control. Set $k := 0$.

(Step 2) Solve the state system

$$\dot{x}^{(k+1)} = f\left(x^{(k+1)}, u^{(k)}, t\right), \quad x^{(k+1)}(0) = x_0$$

for $x^{(k+1)} \in \mathcal{X}$.

(Step 3) Solve the adjoint system

$$\dot{z}^{(k+1)} = -z^{(k+1)} \cdot \partial_x f\left(x^{(k+1)}, u^{(k)}, t\right) + \partial_x j\left(x^{(k+1)}, u^{(k)}\right)$$

with $z^{(k+1)}(T) = 0$ for $z^{(k+1)} \in \mathcal{Z}$.

(Step 4) Update the control

$$u^{(k+1)} = \Pi_{\mathcal{U}}\left[u^{(k)} - \delta \cdot \nabla_u \mathcal{L}\left(x^{(k+1)}, u^{(k)}, z^{(k+1)}\right)\right]$$

with a step size $\delta > 0$. By $\Pi_U : L^2([0, T]; \mathbb{R}) \mapsto \mathcal{U}$ we denote the projection onto $\mathcal{U}$, if needed.

(Step 5) Set $k \mapsto k + 1$ and go to (Step 2) until convergence.

To determine an appropriate step size δ in the update Step 4, there exist several alternative approaches, e.g. small but fixed step sizes, the heuristic Armijo rule or an approximate line search. A detailed description can be found in [11, 15].

8.3. Application in Epidemiology

We consider a dengue transmission model as the underlying state equation. Typical samples of similar model can be found in the monographs [2, 4]. Irrespective to the possible complexity of modeling the transmission, interacting four dengue serotypes with sophisticated immune responses and possible development of clinical syndromes, we stick to the one–serotype model with assumption of no symptomatic fragmentation. The key question addressed in this research is concerned with a quest toward optimal vaccination strategy and deployment of thermal fogging based on the established model.

8.3.1. A Dengue Transmission Model

The model centers on the most endemic–situated area, representing interaction between host (human) and vector (mosquito) in this area. Let $x = (S_h, I_h, R_h, S_v, I_v)^\top \in \mathbb{R}^5$ be the state variable, summarizing the human sub–populations susceptible S_h, passively infective I_h and recovered R_h from the disease as well as the susceptible S_v and actively infective I_v vector sub–populations. By N_h, N_v we denote the total host and vector population. The

growth rate of susceptible host is assumed to be proportional with the total population size, the corresponding proportion is given by the constant μ, meanwhile the growth rate of susceptible vector is attributed to constant recruitment, given by Λ. The usual observable determinants arising in dengue dynamics are also considered, i.e. infection exposure occurring in susceptible host $\beta p S_h I_v$ (modeled by mass–action law enclosing susceptible host and infective vector with p being the infective vector's biting rate and β being the driving force), infection exposure occurring in susceptible vector $\gamma q S_v I_h$ with q being the susceptible vector's biting rate, recovering rate σ and uniform mortality rates μ (for all host sub–populations) and κ (for all vector sub–populations). The reason behind the same proportion of the growth and the mortality rates is to support our assumption that

$$N_h = S_h + I_h + R_h = \text{constant} \tag{8.5}$$

when the control is not present. The control variable $u = (u_1, u_2)^\top \in L^2([0,T];\mathbb{R}^2)$ takes two different measures against a dengue outbreak into account. The variable u_1 describes the vaccination rate and the corresponding treatment is applied to susceptible hosts, u_2 describes the thermal fogging rate affecting the vector.

Taking into account all the above mentioned effects, the state equation (8.2) is given by the following set of equations

$$\dot{S}_h = \mu N_h - \beta p S_h I_v - \mu S_h - u_1 S_h, \qquad S_h(0) > 0, \tag{8.6a}$$
$$\dot{I}_h = \beta p S_h I_v - (\sigma + \mu) I_h, \qquad I_h(0) > 0, \tag{8.6b}$$
$$\dot{R}_h = \sigma I_h - \mu R_h + u_1 S_h, \qquad R_h(0) > 0, \tag{8.6c}$$
$$\dot{S}_v = \Lambda - \gamma q S_v I_h - \kappa S_v - u_2 S_v, \qquad S_v(0) > 0, \tag{8.6d}$$
$$\dot{I}_v = \gamma q S_v I_h - \kappa I_v - u_2 I_v, \qquad I_v(0) > 0. \tag{8.6e}$$

The main aim, is optimizing the distribution of vaccination and thermal fogging such that it yields significant reduction of the dengue incidences. However, once the control is operational, an increasing trend of the corresponding accumulative usage should lead to an increasing expense. On the contrary, lesser usage of the control infers insignificant reduction of infective population. Thus, finding a minimum of the following functional is thought to reflex a compromise for the aforementioned conflicting objectives:

$$J(x,u) = J^x(I_h, I_v) + J^u(u) := \frac{1}{2}\left[\|I_h\|^2_{L^2} + \|I_v\|^2_{L^2}\right] + \frac{\omega}{2}\|u\|^2_{L^2}\ , \tag{8.7}$$

where the weighting parameter $\omega > 0$ balances the influence of reducing the infected cases (first two summands) and the cost for the control (last summand).

The control variable u is naturally bounded in $[0,1]^2$, where e.g. $u_1 = 1$ represents the maximal possible imposing vaccination rate of one hundred percent.

Following the general outline, presented in the previous section, weave at the following system for the adjoint variable $z \in \mathbb{R}^5$:

$$\dot{z}_1 = (\beta p I_v + u_1) z_1 - \beta p I_v z_2 \tag{8.8a}$$
$$\dot{z}_2 = I_h - \mu z_1 + (\sigma + \mu) z_2 - \sigma z_3 + \gamma q S_v (z_4 - z_5) \tag{8.8b}$$
$$\dot{z}_3 = \mu(z_3 - z_1) \tag{8.8c}$$
$$\dot{z}_4 = (\gamma q I_h + \kappa + u_2) z_4 - \gamma q I_h z_5 \tag{8.8d}$$
$$\dot{z}_5 = I_v + (\kappa + u_2) z_5 + \beta p S_h (z_1 - z_2) \tag{8.8e}$$

supplemented by the terminal conditions $z_i(T) = 0$ for $i = 1, \ldots, 5$. Alongside with the adjoint equation, we also obtain the gradient equation

$$0 = \omega u_1 + S_h z_1, \tag{8.9a}$$
$$0 = \omega u_2 + S_v z_4 + I_v z_5 \ . \tag{8.9b}$$

8.3.2. Numerical Results

It is generally agreed, that the main strength of a model lies in its congruousness with the data for a specific test scenario, thus the result of optimal control is expected to become a reasonable strategy. However, the model without any validation will suffer from a number of caveats in terms of practical use. The validation through matching processes, e.g. least square or maximum likelihood [17], is primarily a technique to estimate parameters in the model. That is, the set of parameters alters among different data.

μ	β	p	σ	Λ	γ	q	κ
$\frac{1}{\text{mth}}$	$\frac{1}{\text{mth}\times\text{ind}}$	-	$\frac{1}{\text{mth}}$	$\frac{\text{ind}}{\text{mth}}$	$\frac{1}{\text{mth}\times\text{ind}}$	-	$\frac{1}{\text{mth}}$
$\frac{1}{12\times 60}$	0.0025	$\frac{1}{10}$	$\frac{1}{2}$	300	0.0033	$\frac{2}{10}$	$\frac{1}{1.5}$

Table 8.1.: List, unit and estimate of all parameters; ind = individual, mth = month.

Irrespective to the afore–remarked issue, this paper hinges on putting forward an emphasis to optimal control strategy in the context of theoretical tests. Therefore, all the parameters involved in the model are sensibly estimated in order to match the preferences for pedagogical purpose. To derive the corresponding estimate, we consider a simple way based on nomenclatural derivation of each parameter. For example, μ^{-1} denotes the average host lifespan period in the area of interest. We assume it is equal to 12×60 months. The average recovering period σ^{-1} of the infective hosts, whether or not they earn clinical treatment, is assumed equal to 2 months. Additionally among p^{-1} susceptible hosts there exists, on average, 1 successful bite done by infective vector.

In Table 8.1, we summarize our estimate for the corresponding parameters, based on the preceding description. Meanwhile, Table 8.2 gives estimates for other usual components used in numerical test. Note that the time unit is month.

$S_h(0)$	$I_h(0)$	$R_h(0)$	$S_v(0)$	$I_v(0)$	T
1000	70	180	20000	100	10

Table 8.2.: Initial conditions and terminal observation time (in year).

Let I_h, I_v respectively denote the infective host and vector levels as responses of the system with zero control, and $I_h^*(\omega), I_v^*(\omega)$ be the optimal responses w.r.t. the weighting constant ω. Moreover, let $u^*(\omega)$ denote the optimal control, whose change is subject to variation of ω. Figures 8.1 and 8.2 illustrate the difference among the response with zero control and that with optimal control. The set of values for the weighting constant ω is $\Omega = \left\{10^5, 10^6, 3 \times 10^6, 10^7, 10^8, 10^9\right\}$.

As shown in Figures 8.1 and 8.2, typical trajectories generated by the optimal control show improvement in terms of size reduction compared to the trajectory with zero control.

Figures 8.3 and 8.4 present our optimal control, arising from variation of ω in the set of values Ω. The results show, that the optimal control changes w.r.t. different ω, similarly meaning that a specific imposition of weighting constant in the objective functional leads

to a unique optimal control. In the discrete set of choices Ω, the results show that the optimal control, w.r.t. its area, increases as ω increases.

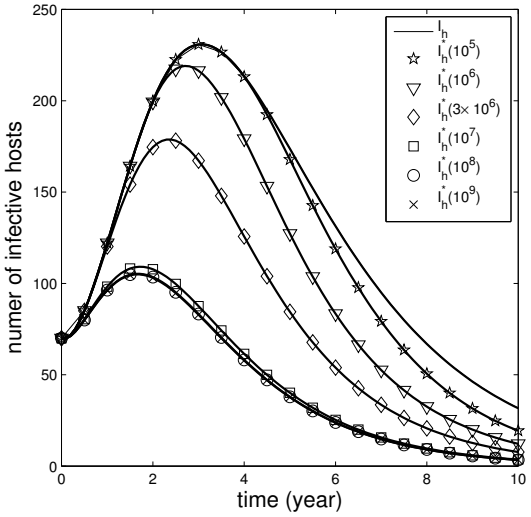

Figure 8.1.: The (optimal) trajectories of infective host.

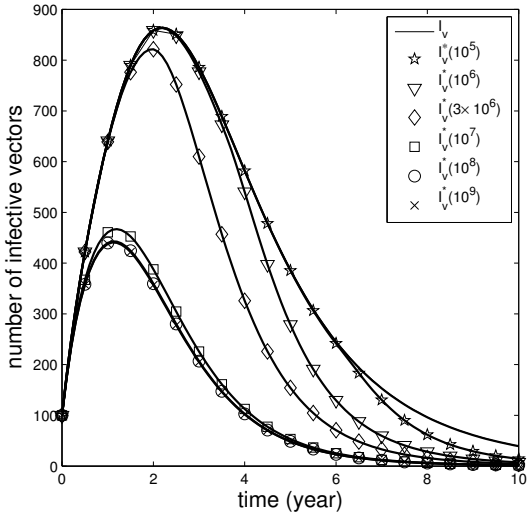

Figure 8.2.: The (optimal) trajectories of infective vector.

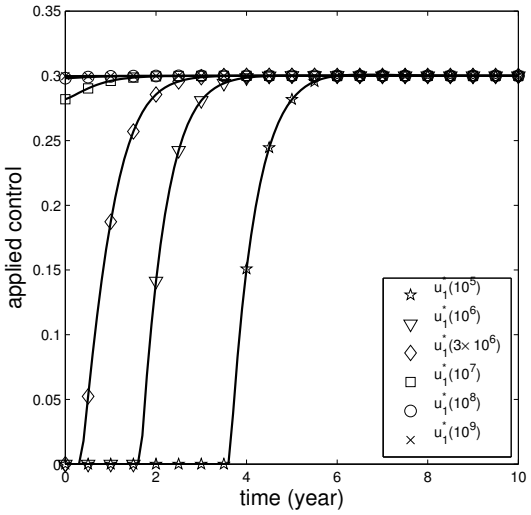

Figure 8.3.: Trajectories of optimal vaccination rate in dependence on ω.

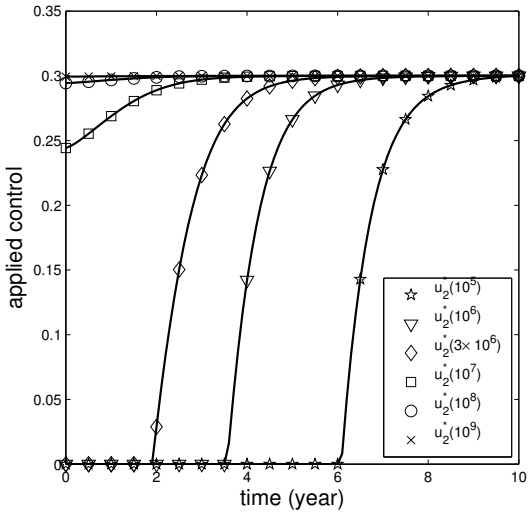

Figure 8.4.: Trajectories of optimal thermal fogging rate in dependence on ω.

Figures 8.5 and 8.6 show our result on how J^x and J^u change w.r.t. $\omega \in \Omega$. The dominance of J^x, as well as the increasing trend of J^u, admit collection of two–dimensional points (J^u, J^x) which further preserves convexity in discrete space. However, we do not exhibit the corresponding result in this paper. This result likely supports our presumption that there are conflicting objectives remaining in the application of optimal control, i.e. either the reduction–based or cost–based objective is preferable to expose. Variation of the weighting constant ω can now give more alternative strategies (i.e. variation of the population dynamics and the control) needed by the decision maker.

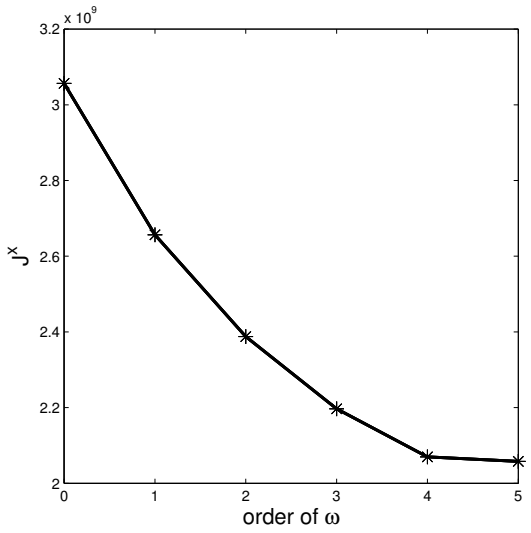

Figure 8.5.: Infection reduction (J^x) with respect to ω.

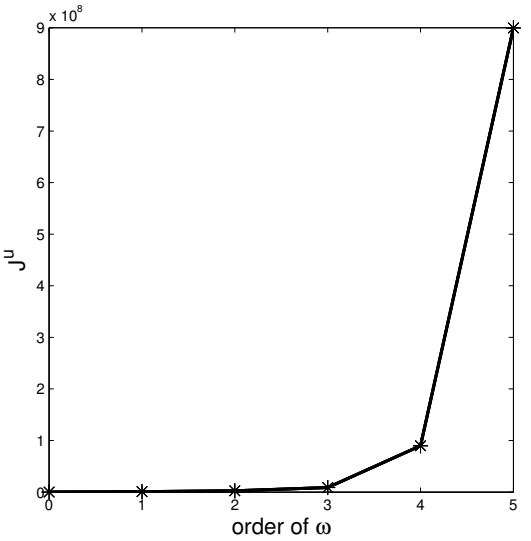

Figure 8.6.: The cost for control (J^u) with respect to ω.

8.4. Application in Biomechanics

8.4.1. Motivation, Model and Method

Within the wide field of biomechanics, the modeling of musculo–skeletal systems received increasing attention over the last decades. The applications of a realistic and individually adaptable human musculo–skeletal model are manyfold: From surgery planning [3] to safer car seats [5] through to the development of humanoid robots [14]. The passive mechanical parts of the model, the bones and ligaments, are well–understood [12]. In contrast, the dynamical parts of the model, the muscles, have not been implemented satisfactory yet. One underlying model was developed by Hill [10] and later on extended, see [6, 7]. We shortly outline the model structure based on [13].

It is assumed, that the muscle–tendon–complex MTC consists of four elements:

- the contractile element CE that is responsible for the force production,
- the parallel elastic element PEE that represents the connective tissue around the CE,
- the serial elastic element SEE that represents the tendon,
- and the serial damping element SDE that acts parallel to the SEE.

Let $\ell_{MTC}, \ell_{PEE}, \ell_{CE}, \ell_{SEE}$ and ℓ_{SDE} denote the lengths of the constituting elements. Due to the set–up of the model the following restrictions hold (author's note: cf. Fig. 1.2):

$$\ell_{CE} = \ell_{PEE}, \quad \ell_{SEE} = \ell_{SDE} \quad \text{and} \quad \ell_{MTC} = \ell_{CE} + \ell_{SEE} \, .$$

Using the notation F_i for the force acting on the i–th component, at equilibrium it holds that

$$F_{MTC} = F_{CE} + F_{PEE} = F_{SEE} + F_{SDE} \, . \tag{8.10}$$

Let the control u describe the neural stimulation, causing a chemical reaction within the muscle. In a next step, the muscle passes through an activation process, where q

denotes the activity. As a consequence, the CE produces a force, dependent on its current length and the activity. For simplicity, we consider the so–called *isometric contraction*, which means that the length of the whole MTC does not change over time. The force production of the MTC within an isometric contraction can be described by the following differential–algebraic equation system (DAE):

$$\dot{q} = f_1(\ell_{CE}, q, u) \,, \qquad q(0) = q_0 \,, \tag{8.11a}$$

$$\dot{\ell}_{CE} = f_2(\ell_{MTC}, \dot{\ell}_{MTC}, \ell_{CE}, q) \,, \qquad \ell_{CE}(0) = \ell_{CE,0} \,, \tag{8.11b}$$

$$\ddot{\ell}_{MTC} = 0 \,, \qquad \dot{\ell}_{MTC}(0) = 0, \ \ell_{MTC}(0) = \ell_{MTC,0} \,, \tag{8.11c}$$

$$F_{MTC} = f_3(\ell_{MTC}, \dot{\ell}_{MTC}, \ell_{CE}, q) \,. \tag{8.11d}$$

In this model, f_1 denotes the activation dynamics according to Hatze in [8], where the activation depends on the current CE length as well as the current activity. Additionally, f_2 denotes the contraction dynamics according to [10], extended by the eccentric branch from [7] (author's note: cf. Eqns. 7.3 – 7.13). The ODE for $\dot{\ell}_{MTC}$ ensures an isometric behavior of the muscle. Note that other contraction modes, e.g. a quick–release experiment or an interaction with an inertial mass, result in a different equation (author's note: see Chapter 5). At last, f_3 represents a double hyperbolic force–velocity characteristics, see [7].

During *in vivo* experiments, it is often possible to measure the force production $F_{MTC,exp}$ of a muscle, but not the stimulation that was needed to produce this force. Therefore, a controller has to determine the optimal stimulation such that the force output of model (8.11) is as close as possible to the measured force. In [6], the model was optimized w.r.t. parameter values, regarding isometric contraction experiments from [16]. We use this model, including the obtained parameter set, to perform an optimal control scenario. Thereto, we set $x = (q, \ell_{CE}, \ell_{MTC}, F_{MTC})^\top \in \mathbb{R}^4$ as the vector of state variables and $f = (f_1, f_2, 0, f_3)^\top$ as the vector of right hand sides. The stimulation as a control function has to be restricted to a subset of $\mathcal{U}$, namely $\mathcal{U}_b := C([0,T];[0,1])$. A zero–stimulation refers to no electrical impulse, whereas a stimulation $u = 1$ refers to the maximal possible electric potential. In the experiment, the applied stimulation was given by $u_d = \mathbf{1}_{[t_{start}, t_{end}]}$, which has the value 1 between the switch–on and switch–off times $t \in [t_{start}, t_{end}] = [0.1\,\mathrm{s}, 1.1\,\mathrm{s}]$ and is 0 else. Since the experimental data only cover the force state, set $x_d = F_{MTC,exp}$. Consequently, the cost functional writes as

$$J(x,u) := \frac{1}{2} \left\| x^{(4)} - x_d \right\|_{L^2}^2 + \frac{\omega}{2} \|u\|_{L^2}^2 \,,$$

where $x^{(4)}$ denotes the fourth component of x. The corresponding optimal control problem can finally be formulated as:

$$\min_{u \in \mathcal{U}_b} J(x,u) \quad \text{subject to} \quad \dot{x} = f(x,u,t) \,. \tag{8.12}$$

The upcoming equation system (8.2) – (8.4) was solved with Algorithm 1 from [13]. As a starting stimulation we chose $u_0(t) = 0.5$.

8.4.2. Results and Discussion

Applying the numerical iteration, we obtained a set of ten optimal control stimulations u^*. Each stimulation corresponds to an isometric contraction performed at different relative

MTC lengths from 0.85 to 1.08. The reference length was given in [6] as $\ell_{MTC,ref} = 6.15$ cm. For simplicity, we chose only five of the ten cases to display explicitly in Figs. 8.7 and 8.8. A detailed analysis of a similar scenario, including objective function values, can be found in [13].

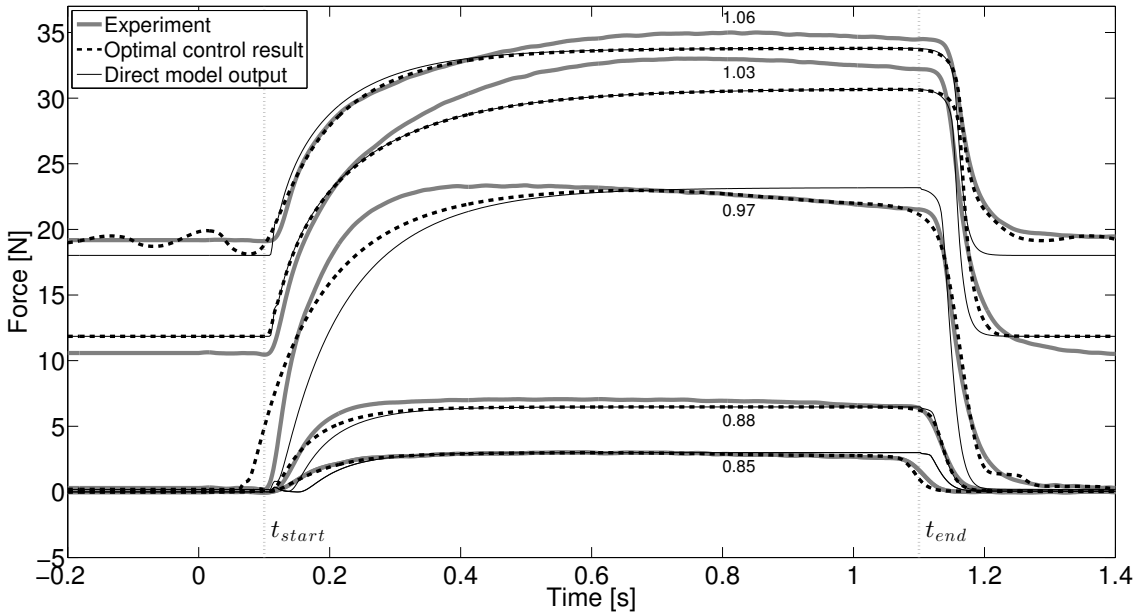

Figure 8.7.: Optimal control results for fitting experimental isometric force data (thick gray lines). The optimal curves (dashed lines) are plotted against the direct model output from the adapted model of [6] (thin black lines). The respective relative muscle lengths $\ell_{MTC}/\ell_{MTC,ref}$ are given by small numbers $0.85, \ldots, 1.06$. Switch–on and switch–off times of the experimental stimulation are indicated with $t_{start} = 0.1\,\mathrm{s}$ and $t_{end} = 1.1\,\mathrm{s}$.

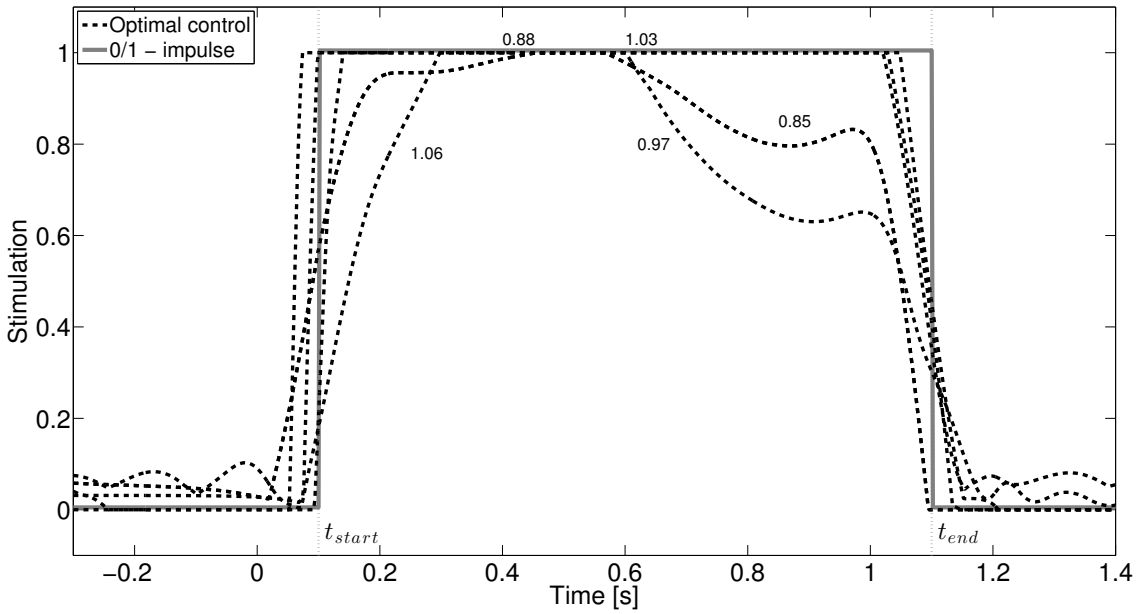

Figure 8.8.: Optimal control functions u^* (dashed lines) in comparison to the experimental 0/1–impulse (gray line). As in Fig. 8.7, the small numbers state the relative MTC lengths.

Regarding both figures, there is a high congruence of the experimental force curves, the optimal control result and the direct model output using [6]. Likewise, the obtained optimal control functions are of similar shape as the experimental stimulation. This congruence indicates the model's ability to represent physiological observations within physiologically reasonable boundaries. However, there are several observations (1) – (5) that indicate model weaknesses or incompletenesses. Therefore, the force curves in Fig. 8.7 are examined forward in time.

(1) In the passive state ($t < t_{start}$) there are force displacements of about 2 N at relative MTC lengths 1.03 and 1.06. In the former case, the passive force is overestimated, whereas in the latter case the force is underestimated. These displacements are consequences of the parameter estimation process from [6]. We want to use these cases to demonstrate the mechanisms of our algorithm. Having an overestimated passive force can not be compensated by the iterative method, because we prohibited a negative stimulation. For an underestimated passive force, the algorithm tries to diminish the displacement by applying a stimulation of about 8%, see Fig. 8.8.

(2) We notice the steep increase of the experimental force curves right after t_{start}, especially for the relative MTC length 0.97. Both the optimized results and the direct model output are unable to perform this increase. The algorithm consequently starts the stimulation earlier in time to compensate for the slower reaction, see Fig. 8.8. At this point the parameter set of the contraction dynamics could be reinvestigated, which is however beyond the aim of this paper.

(3) After reaching the maximum value, the experimental force curves perform a slight linear decrease. This effect can not be explained using model (8.11). A possible explanation could be the muscle fatigue, see [9], which is yet to be implemented in the model. However, the optimal control algorithm is able to catch this decrease, resulting in a decreasing stimulation, see relative muscle lengths 0.85 and 0.97 in Fig. 8.8.

(4) It occurs that for a relative MTC length of 0.85 the experimental force begins to rapidly decrease before the stated $t_{end} = 1.1$ s, thus resulting in an earlier decrease of the optimal stimulation. The only possible explanation is an error in the experimental set–up (author's not: see Chapter 4).

(5) The force decrease of the experimental curves after the switch–off time t_{end} is again steeper than the optimal control or direct output curves. Consequently, the algorithm begins to down–regulate the stimulation earlier in time. Since the eccentric branch was not optimized in [6], an extensive interpretation of the results is unprofitable.

In [13], an optimal control of model (8.11) was performed, using activation dynamics from Zajac in [19]. We exchanged the activation dynamics to improve the performance of the model (author's note: Comparing the above results to Figs. 7.1 – 7.4 from Chapter 5) ([13]) confirms this hypothesis). In detail, the recovered stimulation using Zajac's formulation was only about 60% of the experimental stimulation at short relative muscle lengths. In contrast, the length–depending Hatze formulation recovered 100% of the experimental stimulation at all lengths. In addition, the objective function values were also approximately 40% lower using the Hatze activation.

Summarizing, the results validate two major improvements of the muscle model from [6]; the eccentric branch of the force–velocity characteristic introduced by [7], and the activation dynamics from [8]. Furthermore, the need for further model improvements is revealed, e.g. including muscle fatigue. Finally, an algorithmic parameter optimization would be essential to validate model parts that are added or exchanged.

8.5. Conclusion and Outlook

Questions regarding the optimization and control of dynamical systems are of increasing interest, both inside the mathematical community and beyond. We have given two typical examples: optimizing strategies against diseases and identifying neural signal from measurements of muscle movements. These two case studies highlight the applicability and potential of optimization techniques in biomathematical applications.

Nevertheless, there are numerous open problems for future research. In the presented work we considered single criteria optimization problems. However, in real–world applications one typically faces questions regarding multi–criteria optimization, e.g. minimize the number of infected persons and minimize the cost at the same time. Another open topic touches the field of random or stochastic differential equations. Parameters modeling the behavior of living systems are often subject to more–or–less fluctuations and hence, the resulting models have a random or statistic component within. Extending the presented approach to cover those cases will be subject of further research.

Acknowledgements:
Karunia Putra Wijaya has been financially supported by Indonesia Endowment Fund for Education (LPDP)

Bibliography

[1] D. Aldila, T. Götz, and E. Soewono. "An optimal control problem arising from An optimal control problem arising from a dengue disease transmission model". In: *Mathematical biosciences* 242.1 (2012), pp. 9–16.

[2] N. Bailey. "The mathematical theory of infectious diseases and its application". In: *Immunology* 34.5 (1978), pp. 955–956.

[3] Sabine Bauer, Karin Gruber, and Francis Kilian. "3D-Computermodell der menschlichen Lendenwirbelsäule - Entwicklung und Anwendungsmöglichkeiten in der Medizin". In: *Biomedizinische Technik*. Gemeinsame Jahrestagung der Deutschen, Österreichi. Rostock: de Gruyter, 2010.

[4] K. Dietz. "Transmission and control of arbovirus diseases". In: *Epidemiology, D. Epidemiology, D. Ludwig and K. L. Cooke editors* (1975), pp. 104–121.

[5] M. Grujicic et al. "Musculoskeletal computational analysis of the influence of car-seat design/adjustments on long-distance driving fatigue". In: *International Journal of Industrial Ergonomics* 40.3 (2010), pp. 345 –355.

[6] M. Günther, S. Schmitt, and V. Wank. "High-frequency oscillations as a consequence of neglected serial damping in Hill-type muscle models". In: *Biological Cybernetics* 97.1 (2007), pp. 63–79.

[7] D. F. B. Haeufle et al. "Hill-type muscle model with serial damping and eccentric force-velocity relation". In: *Journal of Biomechanics* 47.6 (2014), pp. 1531–1536.

[8] H. Hatze. "A Myocybernetic Control Model of Skeletal Muscle". In: *Biological Cybernetics* 25.2 (1977), pp. 103–119.

[9] D. Hawkins and M. L. Hull. "Muscle Forces as Affected by Fatigue: Mathematical Model and Experimental Verification". In: *J. Biomechanics* 26.9 (1993), pp. 1117–1128.

[10] A. V. Hill. "The Heat of Shortening and the Dynamic Constants of Muscle". In: *Proceedings of The Royal Society London B* 126.843 (1938), pp. 136–195.

[11] M. Hinze et al. *Optimization with PDE Constraints*. Vol. 23. Springer, 2009.

[12] V. Keppler. "Biomechanische Modellbildung zur Simulation zweier Mensch-Maschinen-Schnittstellen". PhD thesis. Eberhard-Karls-Universität zu Tübingen, Fakultät für Mathematik und Physik, 2003.

[13] R. Rockenfeller and T. Götz. "Optimal Control of Isometric Muscle Dynamics". In: *Journal of Mathematical and Fundamental Sciences* 47.1 (2015), pp. 12–30.

[14] André Seyfarth et al. "Can Robots Help to Understand Human Locomotion?" In: *Automatisierungstechnik* 60.11 (2012), pp. 653–661.

[15] F. Tröltzsch. *Optimale Steuerung partieller Differentialgleichungen*. Vol. 2. Vieweg + Teubner, 2009.

[16] V. Wank. "Muscle growth and fiber type composition in hind limb muscles during postnatal development in pigs". In: *Cells Tissues Organs* 182.3 (2006), pp. 171–181.

[17] K. P. Wijaya, T. Götz, and E. Soewono. *Advances in mosquito dynamics modeling.* arXiv:1503.02573.

[18] K. P. Wijaya, T. Götz, and E. Soewono. "An optimal control model of mosquito reduction management in a dengue endemic region". In: *International Journal of Biomathematics* 7.5 (2014), [22 pages].

[19] F. E. Zajac. "Muscle and Tendon: Properties, Models, Scaling, and Application to Biomechanics and Motor Control". In: *Critical Reviews in Biomedical Engineering* 17.4 (1989), pp. 359–411.

9. Space–Mapping: An Alternative Optimal Control Approach

What is the optimal neural stimulation for a group of leg muscles such that the resulting jump is as high as possible [58]? Which electrical impulse is needed to direct a robot arm along a desired trajectory [6]? To answer these and other biomechanical questions, we investigated direct and indirect optimal control approaches in Chapter 7 and 8 ([25, 66]). Both methods were validated but we stated, they were not applicable in a multi–body system due to their huge time consumption.

An alternative optimal control approach was developed by [1] in 1994 for the purpose of *microwave filter design*. The idea behind the so–called *space–mapping* is to replace an accurate but computationally expensive (fine) model by an inaccurate but cheaper (coarse) model. The optimal solutions obtained in the coarse model are then used to update the control of the fine model via the space–mapping function. The applications of this technique are manifold, e.g. to enhance the thermal behavior of physical devices [48], to improve the bahavior of car components during crashes [64], to optimize a marine ecosystem [62], or to detect the underlying distribution of electrical brain activity [14]. However, to our knowledge, the space–mapping has not yet been applied in the field of muscle modeling.

In the following section, we give the basic definitions and ideas of the so–called *aggressive space–mapping* (ASM) according to [18]. Depending on the problem formulation, there exist alternative approaches as the *trust region ASM*, which operates in a pre–defined trust region, or the *hybrid ASM*, containing classical optimization methods. A state–of–the–art overview on space–mapping is given in [2], including numerous examples and stating advantages and disadvantages of the different methods.

9.1. Mathematical Description

Definition 9.1.1. Let X, Y be Banach spaces. A preferably accurate mathematical description of a given problem (P) is called a **fine model** and denoted by $\mathcal{F} : X \longrightarrow Y$. An elements $x \in X$ is called **control variable**. The **cost function** of the fine model $\mathcal{F}$ is defined as $F : X \longrightarrow \mathbb{R}$, where $F(x) = ||\mathcal{F}(x) - y||_Y$ and $||\ .\ ||_Y$ denotes an arbitrary norm in Y. Thus, the cost is the distance of the model output $\mathcal{F}(x)$ to a desired or observed behavior $y \in Y$, w.r.t. an arbitrary norm. Minimizing the cost function yields the optimization problem

$$x^* = \arg\min_{x \in X} F(x) = \arg\min_{x \in X} ||\mathcal{F}(x) - y||_Y \tag{9.1}$$

Remark 9.1.2. In general, optimization problem (9.1) is *not* solvable by simply evaluating $\mathcal{F}^{-1}(y) = x^*$, since the inverse does not exist or cannot be calculated in reasonable time.

Definition 9.1.3. Let $\hat{X} \subseteq X, \hat{Y} \subseteq Y$. A computationally cheap but less accurate mathematical description of problem P is called a **coarse model** and denoted by $\mathcal{C} : \hat{X} \longrightarrow \hat{Y}$. The cost function of the coarse model $\mathcal{C}$ is defined as $C(\hat{x}) = ||\mathcal{C}(\hat{x}) - y||_Y$. Consequently, the corresponding optimization problem writes as

$$\hat{x}^* = \underset{\hat{x}\in\hat{X}}{\arg\min}\, C(\hat{x}) = \underset{\hat{x}\in\hat{X}}{\arg\min}\, ||\mathcal{C}(\hat{x}) - y||_Y \tag{9.2}$$

Remark 9.1.4. There are no general instructions existing on how to choose the coarse model to an existing fine model. However, the simplest model that contains fine model characteristics should be considered. In Example 9.1.7, we give a coarse model for a linear equation system and in the next section, we give coarse models for two muscular contraction modes.

Since the aim of the space–mapping approach is to solve an optimization problem in the coarse model, these results have to be transferred into the fine model. Therefore, we define the space–mapping function.

Definition 9.1.5. The **misalignment** of the coarse and the fine model is given by $r(x, \hat{x}) = ||\mathcal{F}(x) - \mathcal{C}(\hat{x})||_Y$. A projection from X to $\hat{X}$ of the form

$$\mathcal{P}(x) := \underset{\hat{x}\in\hat{X}}{\arg\min}\, r(x, \hat{x}) = \underset{\hat{x}\in\hat{X}}{\arg\min}\, ||\mathcal{F}(x) - \mathcal{C}(\hat{x})||_Y \tag{9.3}$$

is called a **space–mapping** function. Furthermore, a space–mapping is called **perfect** mapping, if additionally $\hat{x}^* = \mathcal{P}(x^*)$ and hence $\mathcal{F}(x) = \mathcal{C}(\mathcal{P}(x))$.

Remark 9.1.6. Assuming a perfect mapping $\mathcal{P}$ is invertible, the optimal control x^* can be determined by $x^* = \mathcal{P}^{-1}(\hat{x}^*)$.

Example 9.1.7. (Linear equation system – first part)
Let $A \in \mathbb{R}^{n\times n}$ be a matrix, $y \in \mathbb{R}^n$ a vector and $||\,.\,||$ the euclidean norm. Thus, $\hat{X} = X = \hat{Y} = Y = \mathbb{R}^n$. A fine model for a linear equation system (LES) writes as $\mathcal{F}(x) = Ax$, including the cost function $F(x) = ||Ax - y||$. The optimal solution $x^* = A^{-1}y$ is easy to calculate for small n and regular matrices A, using various methods (Gauß–Jordan, BFGS, CG,... etc). But as n gets bigger or if A is singular, the algorithm becomes more time consuming with an order of $\mathcal{O}(n^3)$ or fails completely. Therefore, we derive the space–mapping function on basis of a coarse model.

One possible choice for the coarse model is $\mathcal{C}(\hat{x}) = D\hat{x}$ where $D = \mathrm{diag}(A)$ denotes the diagonal matrix, containing the main diagonal entries from A, assuming they are non–zero. Thus, the optimal solution $\hat{x}^* = D^{-1}y$ is unique and computable in $\mathcal{O}(n)$. Finally, the space–mapping function writes as

$$\mathcal{P}(x) = \underset{\hat{x}\in\mathbb{R}^n}{\arg\min}\, ||Ax - D\hat{x}|| = D^{-1}Ax$$

Obviously, it holds that $\mathcal{F}(x) = Ax = DD^{-1}Ax = D\mathcal{P}(x) = \mathcal{C}(\mathcal{P}(x))$. Consequently, $\mathcal{P}$ is a perfect mapping, according to Definition 9.1.5. Hence, the optimal fine model control

x^* can be obtained by using Remark 9.1.6:

$$x^* = \mathcal{P}^{-1}(\hat{x}^*) = A^{-1}D\hat{x}^* = A^{-1}DD^{-1}y = A^{-1}y$$

Remark 9.1.8. The example provides useful observations for the general modeling case:

1. At first, y might not be in the range of $\mathcal{F}$, write $y \notin \mathrm{Im}(\mathcal{F})$ (no solution of the LES). In that case there exist no x^* with $\mathcal{F}(x^*) = y$, but rather $x^* = \min_{x \in X} ||\mathcal{F}(x) - y||_Y$, we write $\mathcal{F}(x^*) \approx y$. If A from the example is not invertible, the minimization problem w.r.t. the euclidean norm yields to a best least–squared fit where A^{-1} is replaced by the Moore–Penrose pseudo–inverse of A, see [53, 59].

2. The optimal solution of the coarse model $\hat{x}^*$ should be cheap to calculate. This fact can be used to obtain an optimal fine model control x^*. Therefore, use $x_0 := \hat{x}^*$ as an initial guess and construct a sequence $(x_k)_{k \in \mathbb{N}} \subset X$ via the fixed–point iteration $x_k = \mathcal{P}_k^{-1}(\hat{x}^*)$. It then holds that $\lim\limits_{k \to \infty} x_k = x^*$, see [18].

3. However, in general it is not possible to give $\mathcal{P}_k$ in a closed form. To evaluate $\mathcal{P}_k$ for a given $x \in X$, an optimization in the coarse model has to be performed as well as an evaluation of the fine model, see Eqns. (9.2) and (9.3).

4. Additional to the evaluation of $\mathcal{P}_k$, inverting $\mathcal{P}_k$ could become as costly as inverting $\mathcal{F}$, as seen in the end of Example 9.1.7.

Summarizing Remark 9.1.8, it is desired to construct a sequence $(x_k)_{k \in \mathbb{N}}$ with $x_0 = \hat{x}^*$, which converges to x^*. The question remains, how the respective $\mathcal{P}_k$ can be constructed. Space–mapping evaluations should be easy to perform. Hence, $\mathcal{P}_k$ is updated via linearization. Let B_k denote the numerical approximation to the Jacobian of $\mathcal{P}_k$ at x_k. Then due to Taylor series expansion

$$\mathcal{P}_k(x) = \mathcal{P}(x_k) + B_k \cdot (x - x_k) \; . \tag{9.4}$$

Consequently, solving for $x = x_{k+1}$, the sequence recursion writes as

$$x_{k+1} = x_k - B_k^{-1} \cdot (\mathcal{P}(x_k) - \mathcal{P}_k(x_{k+1})) = x_k - B_k^{-1} \cdot (\mathcal{P}(x_k) - \hat{x}^*) \; .$$

To determine the Jacobian approximation B_k, a Broyden rank–one–update with step size $h = x_{k+1} - x_k$ is performed, see [7, 50]. Let id denote the identity mapping.

$$B_0 = id, \qquad B_k = B_{k-1} + \frac{\mathcal{P}(x_{k+1}) - \mathcal{P}(x_k) - B_{k-1} \cdot h}{h^T h} \cdot h^T \; . \tag{9.5}$$

In [18, Fig. 5] the pseudo–inverse of B_k is used instead of the inverse, because it is cheaper to calculate. In a finite dimensional Banach space however, the inverse of a rank–one–updated map can be directly calculated by the Sherman–Morrison formula from [4, 74]:

$$(B_k + uv^T)^{-1} = B_k^{-1} - \frac{B_k^{-1} u v^T B_k^{-1}}{1 + v^T B_k^{-1} u} \tag{9.6}$$

where $u = (\mathcal{P}(x_{k+1}) - \hat{x}^*)/(h^T h)$ and $v = h$. The addition of their dyadic product corresponds with a rank–one–update of B_k. This method is known as Broyden's first or "good" method. For an overview of further possible methods, see [28].

In Algorithm 3, we summarize all above considerations, which is necessary to perform an aggressive space–mapping optimization.

Algorithm 3 ASM

Require: Fine and coarse model $\mathcal{F}$ and $\mathcal{C}$, observation y, $B_0 = id$, $k = 0$, $x_0 = \hat{x}^* = \arg\min_{\hat{x}\in\hat{X}} ||\mathcal{C}(\hat{x}) - y||_Y$, upper bound of steps N, tolerance ε.

Ensure: Control variable x^* with $\mathcal{F}(x^*) \approx \mathcal{C}(\mathcal{P}(\hat{x}^*)) \approx y$

Calculate $\mathcal{P}(x_0) = \arg\min_{\hat{x}\in\hat{X}} ||\mathcal{F}(x_0) - \mathcal{C}(\hat{x})||_Y$
while $||\mathcal{P}(x_k) - \hat{x}^*||_Y > \varepsilon$ and $k < N$ **do**
  $h = B_k^{-1} \cdot (\mathcal{P}(x_k) - \hat{x}^*)$
  $x_{k+1} = x_k + \frac{h}{||h||_Y}$
  Calculate $\mathcal{P}(x_{k+1}) = \arg\min_{\hat{x}\in\hat{X}} ||\mathcal{F}(x_{k+1}) - \mathcal{C}(\hat{x})||_Y$
  $u = \frac{\mathcal{P}(x_{k+1}) - \hat{x}^*}{(h^T h)}$
  $v = h$
  $B_{k+1}^{-1} = B_k^{-1} - \frac{B_k^{-1} u v^T B_k^{-1}}{1 + v^T B_k^{-1} u}$
  $k = k + 1$
end while
Output $x^* = x_k$

Example 9.1.9. (Linear equation system – second part)
Given the notation from Example 9.1.7, choose $B_0 = I_n$ as the identity matrix of size $n \times n$. According to Algorithm 3, the update of the control is given by

$$h = B_k^{-1} \cdot D^{-1}(Ax_k - y)$$

$$x_{k+1} = x_k + \frac{h}{||h||}$$

$$B_{k+1}^{-1} = B_k^{-1} - \frac{B_k^{-1} \cdot \left[D^{-1}(Ax_{k+1} - y)h^T\right] \cdot B_k^{-1}}{\left(1 + h^T B_k^{-1} D^{-1}(Ax_{k+1} - y)\right) h^T h}$$

To validate the method, we performed the ASM algorithm in MATLAB for various n. The matrix A consists of random numbers from the interval $[-50, 50]$, the vector y of random numbers in $[-5, 5]$. Figure 9.1 compares the results of Algorithm 3 with the exact solution of the LES and the initial solution $\hat{x}^*$. The results show a high congruence of the exact solution and the ASM results.

To compare our algorithm with the exact solution, Table 9.1 contrasts the computational effort of the space–mapping method with a self–implemented Gauß algorithm as well as the pre–implemented MATLAB solver, which uses a single value decomposition (SVD). The results show, that the ASM algorithm is approximately twice as fast as a straight forward implemented Gauß method, but approximately 10 to 20 times slower compared to the SVD method.

Table 9.1.: Computational effort for solving an LES of the form $Ax = b$ with three different methods: The pre–implemented MATLAB solver (SVD), the ASM algorithm and a self–implemented Gauß method.

	times for		
n	SVD	ASM	Gauß
5	$7.1 \cdot 10^{-4}$ s	0.0014 s	0.0038 s
10	$7.6 \cdot 10^{-4}$ s	0.0015 s	0.0039 s
100	0.0013 s	0.0203 s	0.0302 s
500	0.0390 s	1.4 s	2.2 s
1000	0.1393 s	13.1 s	24.3 s

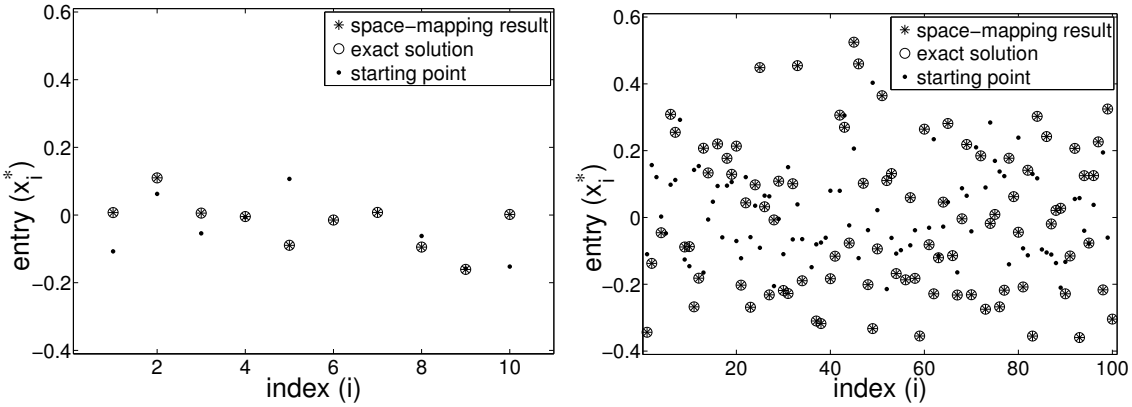

Figure 9.1.: Optimal solution x^* of the LES $Ax = y$ for $n = 10$ (left) and $n = 100$ (right). As a reference the optimal solution of the coarse problem (black dots) is given. The required accuracy of $\varepsilon = 10^{-2}$, between the exact solution (circles) and the ASM results (stars) was reached after 16 respectively 102 iteration steps.

9.2. Recovering Optimal Neural Stimulation Using ASM

As in [66, 68], we use the Hill–type muscle model from [27, 30] to apply the space–mapping method. The neural stimulation $\sigma = \sigma(t)$ acts as the control function (input), which induces an activation $q = q(t) = q[\sigma](t)$, followed by a length change of the contractile element (CE) as well as the muscle–tendon complex (MTC), and finally a force production $F_{MTC} = F_{MTC}(t)$ (output), cf. Eqn. (5.1).

$$\begin{aligned} \dot{q} &= f_1(\ell_{CE}, q, \sigma) \,, & q(0) &= q_{,0} \,, \\ \dot{\ell}_{CE} &= f_2(\ell_{MTC}, \dot{\ell}_{MTC}, \ell_{CE}, q) \,, & \ell_{CE}(0) &= \ell_{CE,0} \,, \\ \ddot{\ell}_{MTC} &= f_D(\ell_{MTC}, \dot{\ell}_{MTC}, \ell_{CE}, q) \,, & \ell_{MTC}(0) &= \ell_{MTC,0} \,, \\ & & \dot{\ell}_{MTC}(0) &= 0 \\ F_{MTC} &= f_3(\ell_{MTC}, \dot{\ell}_{MTC}, \ell_{CE}, q) \,. \end{aligned} \tag{9.7}$$

In addition to the isometric scenario from [66, 68], we want to consider a concentric contraction against an initial mass. Therefore, the right hand side of the MTC equation in (9.7) depends on the respective *dynamic* (contraction mode), which we indicate by the

notation f_D. In the following, we give a fine and a coarse model for both contraction types and calculate the respective optimal controls.

9.2.1. Isometric Contractions

We consider isometric contraction experiments from [27], which were conducted on a piglet soleus. The observed time horizon covers $T = [-0.2\,\mathrm{s}, 1.4\,\mathrm{s}]$, where the first 0.2 s were used to adapt the muscle model to the outer conditions in order to reach an internal equilibrium, see Chapter 2. In particular, the muscle was passively stretched at various MTC lengths for $t \in [-0.2, 0.1]$, fully stimulated for a one second duration $t \in [0.1\,\mathrm{s}, 1.1\,\mathrm{s}]$, and restored its passive state again for $t \in [1.1, 1.4]$.

Notation 9.2.1.

- Let $\overline{\sigma}, \overline{F}_{MTC}$ denote the experimental stimulation and force, $F_{max}(\ell_{MTC,0})$ the maximum isometric force at full activity ($q = 1$), and $F_{pas}(\ell_{MTC,0})$ the passive ($q = 0$) force exerted at $\ell_{MTC} = \ell_{MTC,0}$.
- Let $C^{pw}(I, J)$ denote the vector space of *piecewise continuous functions* from the interval I to the interval J. We assume that $\sigma \in C^{pw}(T, [0, 1])$, with $t \mapsto \sigma(t)$.
- Let $\delta \in \mathbb{R}$ and $\varphi \in C^{pw}(I_1, J_1)$ with $t \mapsto \varphi(t)$. Denote by $\mathcal{S} : \mathbb{R} \times C^{pw}(I_1, J_1) \longrightarrow C^{pw}(I_2, J_1)$ with $\mathcal{S}[\delta, \varphi](t) = S_\delta[\varphi] := \varphi(t - \delta)$ the *shift function* that shifts the time interval $I_1 = [t_1, t_2]$ backwards in time (or forward, if $\delta < 0$) to $I_2 = [t_1 - \delta, t_2 - \delta]$.

During the contraction, the MTC length was held constant. Consequently, in Eqn. (9.7), the right hand side $f_D \equiv 0$. Thus, the fine model is described by

$$\mathcal{F} : \; C^{pw}(T, [0, 1]) \longrightarrow C(T, \mathbb{R}) \; , \quad \text{with}$$

$$\mathcal{F}[\sigma](t) = \mathcal{F}(\sigma) = F_{MTC} = f_3(\ell_{MTC,0}, 0, \ell_{CE}, q) \; .$$

The force output is solely determined by the control σ, for a given $\ell_{MTC,0}$. The fine model cost function then becomes $F(\sigma) = ||\mathcal{F}(\sigma) - \overline{F}_{MTC}||_{L^2}$.

Since there exist no general instructions on how to choose a coarse model, we recall the desired properties. At first, the model should be simpler than the fine model and possibly invertible to make the optimization cheap. Secondly, it should contain similar properties as the fine model w.r.t. the control. Hence, we take the following considerations into account:

- The force $F_{pas}(\ell_{MTC,0})$ of a passively stretched muscle is exerted by applying no stimulation ($\sigma = 0$).
- The force $F_{max}(\ell_{MTC,0})$ is exerted by applying full stimulation ($\sigma = 1$).
- Assume, that the force $F_{MTC}(\sigma) \in [F_{pas}(\ell_{MTC,0}), F_{max}(\ell_{MTC,0})]$ scales linearly w.r.t. the applied stimulation ($\sigma \in [0, 1]$), compare Chapter 7, Figs. 7.1 – 7.4.
- Observe that, after a step in stimulation, the muscle reacts with a step in force after a certain period of time. This effect is known as electro–mechanical delay (EMD) and investigated in [10, 54, 68]. Usually, the EMD is length–dependent, but for simplicity, we chose it as $\delta = 20\,\mathrm{ms}$ by trial and error.

Summarizing, the coarse model at given length $\ell_{MTC,0}$ writes as

$$\mathcal{C}: \ \mathbb{R} \times C^{pw}(T,[0,1]) \to C^{pw}(T,\mathbb{R}) \ , \qquad \text{with}$$

$$\mathcal{C}[\delta,\hat{\sigma}](t) = \mathcal{C}(\delta,\hat{\sigma}) = \mathcal{S}_\delta\Big[\hat{\sigma}\cdot[F_{max}(\ell_{MTC,0}) - F_{pas}(\ell_{MTC,0})] + F_{pas}(\ell_{MTC,0})\Big]$$

The corresponding cost function becomes $C(\delta,\hat{\sigma}) = ||\mathcal{C}(\delta,\hat{\sigma}) - \overline{F}_{MTC}||$, which is minimized by the directly calculable optimal auxiliary control

$$\hat{\sigma}^* = \frac{\mathcal{S}_{-\delta}[\overline{F}_{MTC}] - F_{pas}(\ell_{MTC,0})}{F_{max}(\ell_{MTC,0}) - F_{pas}(\ell_{MTC,0})} \ .$$

Applying Algorithm 3, set $\sigma_0 = \hat{\sigma}^*$ and calculate the sequence σ_k that converges to σ^*. The space–mapping function has to be evaluated once per iteration step, resulting in one evaluation of the fine model $\mathcal{F}(\sigma_k)$ and one optimization in $\mathcal{C}$.

Results

Figure 9.2 shows the resulting optimal control σ^* (upper sub–figure) as well as the corresponding force $F^*_{MTC} = \mathcal{F}(\sigma^*)$ (lower sub–figure). The given experimental force $\overline{F}_{MTC}$ was obtained in [27] at $\ell_{MTC,0} = \ell_{MTC,ref} = 6.15\,\text{cm}$, which served as a reference length. Additionally, the figure shows the optimal control results $(\sigma^*_{OC}, F^*_{MTC,OC})$ from [66] (Chapter 7) and the model evaluation $(\overline{\sigma}, \mathcal{F}(\overline{\sigma}))$ from [27] for the corresponding MTC length.

The space–mapping results show almost identical behavior as the optimal control results from [66]. At first, σ^* as well as σ^*_{OC} begin to rise about 0.08 s resp. 0.06 s before the onset of $\overline{\sigma}$. That effect was explained in [66, 68] by an improvable fit of the curvature variables in [27]. Secondly, both optimal control functions show a characteristic peak at $t \approx 1\,\text{s}$. Using Zajac's activation dynamics, this peak seemed to be a necessary consequence to better approximate the force descent. Thirdly, the minor differences were a steeper ascend and a pronounced peak for σ^*_{OC}.

The maximal difference of the optimal forces F^*_{MTC} and $F^*_{MTC,OC}$ lies at 1.26 N, which is approximately 4.5% of the maximum isometric force. The L^2–difference of F^*_{MTC} to the experimental data accounts for 24.1, which is approximately the value from the optimal control approach (22.9) and less than the value for the direct model output (33.8), compare [66, Table 1, Row 6].

Finally, we give the computational effort of this method and the ASM algorithm, comparing both to the optimal control approach from [66]. Recall that both methods provided almost the same objective function value and therefore are directly comparable in terms of validity. In our implementation, the ASM algorithm took approximately 22 s ($\triangleq$ 10 iteration steps) and the direct optimal control approach approximately 45 s ($\triangleq$ 15 iteration steps).

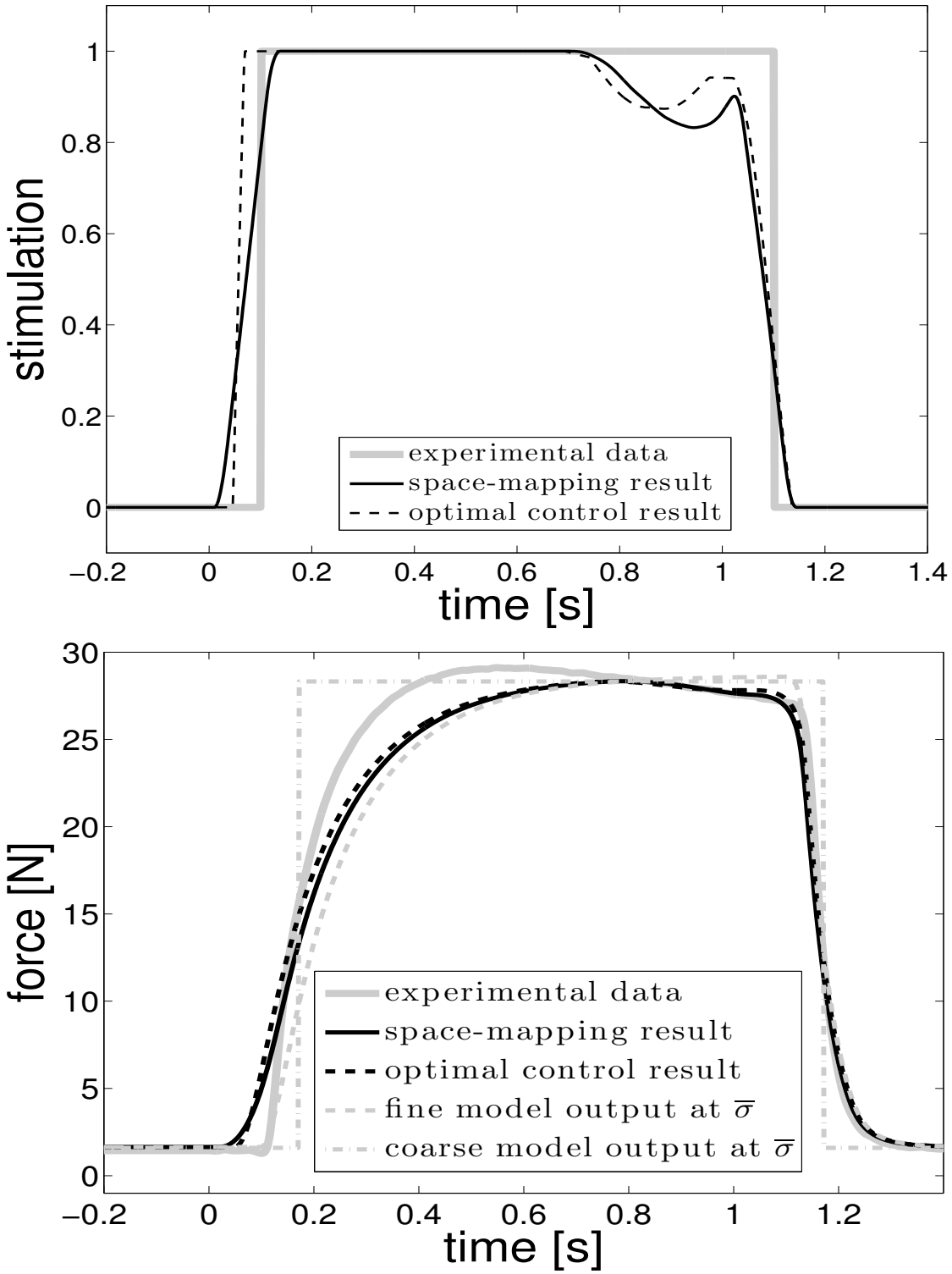

Figure 9.2.: Upper: Optimal stimulation obtained by ASM (σ^*, black line) and optimal control from [66] (σ^*_{OC}, black dashed line) in comparison to the experimentally applied stimulation ($\overline{\sigma}$, gray thick line).
Lower: Experimental force ($\overline{F}_{MTC}$, thick gray line) in comparison to the fine model output ($F^*_{MTC} = \mathcal{F}(\sigma^*)$, black line), the optimal control result from [66] ($F^*_{MTC,OC} = \mathcal{F}(\sigma^*_{OC})$, black dashed line), and the direct model output from [27] ($\mathcal{F}(\overline{\sigma})$, thin gray dashed line). Additionally, the coarse model output ($\mathcal{C}(\hat{\sigma}^*)$, gray dash–dotted line)
The MTC length was fixed at $\ell_{MTC,0} = 6.15\,\mathrm{cm}$, see [27].

9.2.2. Concentric Contractions Against an Inertial Mass

In the previous sub–section, we gave a very simplified coarse model for an isometric contraction experiment and validated the results on experimental data. In this sub–section, we want to consider an alternative muscle contraction mode: concentric contraction against an inertial mass, denoted *mass*. The detailed experimental set–up is explained in [27, Fig. 1]. In short, a mass of 100 g was placed on a table and linked to a passively fixed muscle. The muscle then was fully stimulated at $t_0 \approx 0.034\,\mathrm{s}$, performed an isometric contraction, and, after exceeding a certain force threshold, eventually lifted the mass, see Fig. 5.4. Thereto, the MTC had to shorten as well, which was measured over time. The resulting MTC velocities for various masses are displayed in [27, Fig. 6].

As before, we want to give a fine model, representing the described contraction mode. In contrast to the isometric case, the only measured quantity is the MTC length, denoted by $\overline{\ell}_{MTC}$. Thus, its acceleration can be calculated by Newton's law of motion. Let g denote the gravitational force:

$$\ddot{\ell}_{MTC} = g - \frac{F_{MTC}(\ell_{MTC}, \dot{\ell}_{MTC}, \ell_{CE}, q)}{mass} =: f_D(\ell_{MTC}, \dot{\ell}_{MTC}, \ell_{CE}, q)\ .$$

Hence, the fine model output is the MTC length according to Eqn. (9.7), again solely determined by the neural stimulation input:

$$\mathcal{F}:\ C^{pw}(T,[0,1]) \to C^2(T,\mathbb{R})\ , \quad \text{with}$$

$$\mathcal{F}[\sigma](t) = \mathcal{F}(\sigma) = \ell_{MTC}\ .$$

The cost function consequently writes as $F(\sigma) = ||\mathcal{F}(\sigma) - \overline{\ell}_{MTC}||_{L^2}$

The choice of the coarse model proves more difficult, since there is no obvious relation between σ and ℓ_{MTC}. To formulate a simpler model with the properties of Eqns. (9.7), we made the following considerations.

- Assume, the activity equals the stimulation.
- Assume, there is no CE length dependency for a_{rel}, b_{rel} and F_{isom},. Thus, replace $a_{rel} = a_{rel,0}$ and $b_{rel} = b_{rel,0}$ as well as $F_{isom}(\ell_{CE}) = 1$. Consequently, there is no CE length dependency for $\mathrm{d}/\mathrm{d}t\ \ell_{CE}$ in f_2.
- Assume, the eccentric branch of f_2 to be superfluous.
- Assume, that the velocity of the MTC equals the velocity of the CE. That is, the serial elastic element is assumed to be rigid.
- Assume, the MTC velocity to be piecewise constant, thus calculating the MTC length by $\ell_{MTC}(t) = \ell_{MTC}(0) + t \cdot \dot{\ell}_{MTC}(t)$.
- Assume, that the exerted force equals the weight of the mass, $F_{MTC} = mass \cdot g$, i.e. there is no acceleration of the MTC.

After these simplifications, the linear coarse model of the MTC length writes as

$$\mathcal{C}:\ C^{pw}(T,[0,1]) \to C^{pw}(T,\mathbb{R})\ , \quad \text{with}$$

$$\mathcal{C}[\hat{\sigma}](t) = \mathcal{C}(\hat{\sigma}) = \ell_{MTC,0} + t \cdot b_{rel} \cdot \ell_{CE,opt} \cdot \left(1 - \frac{\hat{\sigma} + a_{rel}}{\frac{mass \cdot g}{F_{max}} + a_{rel}}\right)\ ,$$

where the MTC velocity is calculated by a simplified Hill equation. The cost function $C(\hat{\sigma}) = ||\mathcal{C}(\hat{\sigma}) - \overline{\ell}_{MTC}||_{L^2}$ is minimized by

$$\hat{\sigma}^* = \frac{(F_{max} \cdot a_{rel,0} + g \cdot mass) \cdot (\ell_{MTC,0} - \overline{\ell}_{MTC})}{t \cdot F_{max} \cdot b_{rel,0} \cdot \ell_{CE,opt}}$$

As above, we apply Algorithm 3 with initial stimulation $\hat{\sigma}^*$.

Results

Figure 9.3 shows the resulting optimal control σ^* (upper sub–figure), the corresponding length $\ell^*_{MTC} = \mathcal{F}(\sigma^*)$ (mid sub–figure) as well as the resulting velocity $\mathrm{d}/\mathrm{d}t\ \ell^*_{MTC}$ (lower sub–figure). Although our fine model response was compared to experimental MTC length, in [27, Fig. 6] only the MTC velocity is displayed. We calculated the experimental length out of the experimental velocity with an initial length of $\ell_{MTC,0} = 5.97\,\mathrm{cm}$, approximately 0.97 times the reference length. To recall, the applied mass was $mass = 100\,\mathrm{g}$. Additionally, the figure shows the model evaluation $(\overline{\sigma}, \mathcal{F}(\overline{\sigma}))$ from [27] for the corresponding MTC length and mass. Note that our time $t = 0$ differs from [27]. There, the time was shifted to the first instant where $\mathrm{d}/\mathrm{d}t\ \ell_{MTC} < 0$. The displayed results were reached after 10 iteration steps.

Like in the isometric contraction case, the optimal control stimulation begins to rise slightly before the experimental stimulation. In the concentric contraction scenario, a step in stimulation does not immediately produce a measurable effect on the output. That is, because the inner (CE) dynamic has to exceed a force threshold, depending on the weight, before the muscle begins to shorten. In the further evolution, the optimal control oscillates unsteadily between 0.6 and 1, in order to approximate the interactions of the mass and the elastic muscle components. In the model of [27], these oscillations were modeled by a linear, force–dependent serial damping element (SDE).

The MTC length and velocity, from the ASM algorithm as well as from the direct model output, show almost exact congruence to the experimental data. For comparison, the L^2-distances of the experimental data to the optimal solutions from the ASM and [27] were:

$$||\mathcal{F}(\sigma^*) - \overline{\ell}_{MTC}||_{L^2} = 4.2 \cdot 10^{-4}, \qquad ||\mathcal{F}(\overline{\sigma}) - \overline{\ell}_{MTC}||_{L^2} = 3.8 \cdot 10^{-3}.$$

Thus, although the direct model output gives a good approximation of the data, the space–mapping error is one magnitude lower. The computational time for the ASM was approximately 6 s ($\triangleq$ 8 iteration steps).

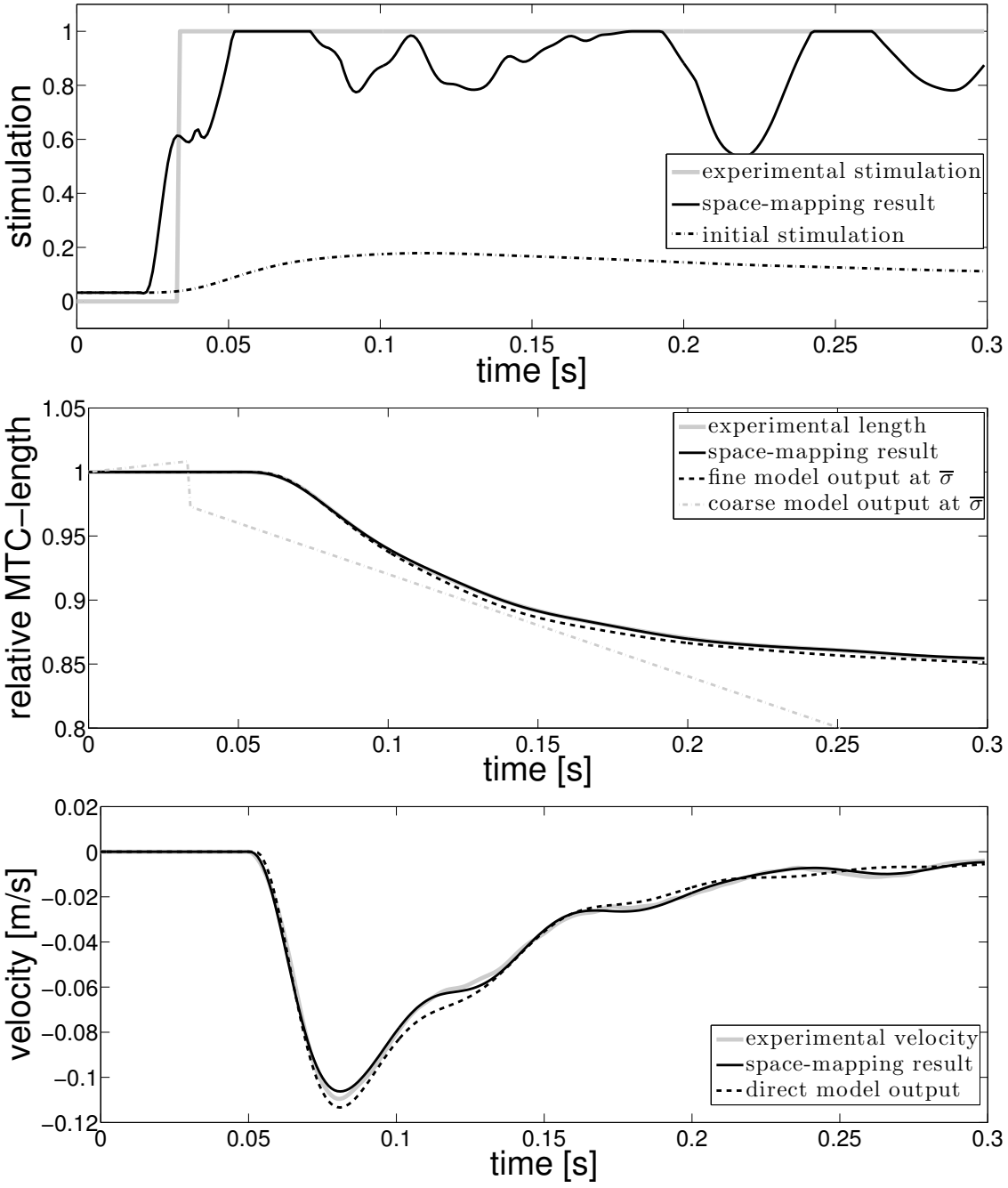

Figure 9.3.: Concentric contraction against an inertial mass of $mass = 100\,\mathrm{g}$ at an initial length of $\ell_{MTC,0} = 5.97\,\mathrm{cm} \approx 0.97\ell_{MTC,ref}$.
Upper: Experimentally applied stimulation ($\overline{\sigma}$, thick gray line) compared to the optimal stimulation (σ^*, black line). Additionally the optimal stimulation of the coarse model ($\hat{\sigma}^*$, black dashed line), which served as an initial guess, is displayed.
Mid: Experimental MTC length ($\overline{\ell}_{MTC}$, thick gray line), calculated from measured velocities, compared to the fine model output ($\mathcal{F}(\sigma^*)$, black line), the direct model output from [27] ($\mathcal{F}(\overline{\sigma})$, black dashed line), and the coarse model output ($\mathcal{C}(\hat{\sigma}^*$, gray dash–dotted line).
Lower: Experimental MTC velocity ($\mathrm{d}/\mathrm{d}t\ \overline{\ell}_{MTC}$, thick gray line) compared to the gradient of the fine model output (black line) and the direct model output (black dashed line), displayed in [27, Fig. 6].

Part IV.

Closing

10. Conclusion

10.1. Summary

We investigated an ODE–based state–of–the–art Hill–type muscle model with well–known mathematical methods.

In the first part, stationary solutions and their stability were calculated, regarding the activation dynamics according to Hatze and Zajac as well as the complete coupled contraction–activation dynamics.

In the second part, we investigated the influence of model parameters on the solution using sensitivity analysis. Two different activation dynamics were compared in our first research paper, regarding the sensitivity of their underlying parameter set. Therefore, we gave a detailed approach for a local sensitivity method and sketched the idea of a global method. The latter was found to coincide with the previous, but to cover some local peculiarities. As a consequence of calculating the respective sensitivities, we found that Hatze's formulation might be physiologically more appropriate than Zajac's. Consequently, within our second research paper, we used sensitivity analysis and optimization methods to extract dynamic muscle properties using solely ICEs. We provided an optimized dynamic parameter set and designed an ICE for a particular unsensitive parameter. Furthermore, we developed a curvature method to gain physiological electro–mechanical delay (EMD) values from isometric force data. In an additional chapter, the sensitivity analysis was extended to the complete muscle model, passing through different contraction modes. We found that isometric contraction experiments (ICEs) expose the most information about system parameter values, among different contraction modes.

In the third part, we presented the recovery of the neural stimulation from force data only, using optimal control. We stated the basics of optimal control theory and gave small examples using the indirect method. Our third research paper applied the indirect optimal control approach to regain the neural stimulation from experimental isometric force data. We validated our approach by comparing the results to the experimentally applied stimulation. Subsequently, the approach was tested against a commercial direct optimal control program and was shown to be equal in accuracy. Our fourth research paper demonstrated the application of indirect optimal control approaches in epidemiology (dengue fever transmission) and biomechanics. In the final chapter, we presented the space–mapping technique as an alternative optimal control approach. With two surrogate models for isometric and concentric contractions, we recovered experimental stimulation from force and length data, respectively.

10.2. Outlook and Future Work

A consequent continuation of this thesis results in an algorithmic parameter estimation (PE) for (Hill–type) muscle models. In the first decade of the 2000s, the demand for estimating parameters from experimental data increased. However, there is only few literature on PE, which is mostly conducted by brute–force least–square fits [8, 17, 22, 83] or by trial and error respectively educated guesses [27, 54, 75]. Obviously the main

problem is the large number of parameters (> 20), cf. [8, "Too many parameters is not good"]. An approach containing sensitivity analysis [9] only dealt with a reduced set of parameters.

In Chapter 5, we linked phase portrait analysis and sensitivity analysis, which might be a powerful tool to estimate sub–model parameters in a feedback–loop with a global PE. Furthermore, we saw that isometric contraction experiments contain information about every model parameter. We aim at extracting a complete parameter set by using ICEs only. How many force curves are sufficient to perform a decent PE? Can such a parameter set predict a muscle's behavior throughout different contraction modes and boundary conditions?

Bibliography for Chapters 1, 2, 6, 9, 5 & 10

[1] J. W. Bandler. "Space Mapping Technique for Electromagnetic Optimization". In: *IEEE Transactions on Microwave Theory and Techniques* 42.12 (1994), pp. 2536–2544.

[2] J. W. Bandler. "Space Mapping: The State of the Art". In: *IEEE Transactions on Microwave Theory and Techniques* 52.1 (2004), pp. 337–361.

[3] Y. Bar-Cohen. *Electroactive Polymer (Eap) Actuators as Artificial Muscles: Reality, Potential, and Challenges*. Vol. 2. SPIE Press, 2004.

[4] M. S. Bartlett. "An Inverse Matrix Adjustment Arising in Discriminant Analysis". In: *Annals of Mathematical Statistics* 22.1 (1951), pp. 107–111.

[5] J. T. Betts and S. L. Campbell. "Discretize then Optimize". In: *Mathematics for Industry: Challenges and Frontiers*. Ed. by D. R. Ferguson and T. J. Peters. SIAM, 2005.

[6] J. E. Bobrow, S. Dubowsky, and J. S. Gibson. "Time-Optimal Control of Robotic Manipulators Along Specified Paths". In: *The International Journal of Robotics Research* 4.3 (1985), pp. 3–17.

[7] C. G. Broyden. "A Class of Methods for Solving Nonlinear Simultaneous Equations". In: *Mathematics of Computation (American Mathematical Society)* 19.92 (1965), pp. 577–593.

[8] T. S. Buchanan et al. "Neuromusculoskeletal Modeling: Estimation of Muscle Forces and Joint Moments and Movements From Measurements of Neural Command". In: *Journal of Applied Biomechanics* 20.4 (2004), pp. 367–395.

[9] A. van Campen. "Identification of subject-specific parameters of a Hill-type muscle-tendon model for simulations of human motion". PhD thesis. Aalborg University, 2014.

[10] P. R. Cavanagh and P. V. Komi. "Electromechanical Delay in Human Skeletal Muscle Under Concentric and Eccentric Contractions". In: *European Journal of Applied Physiology* 42.3 (1979), pp. 159–163.

[11] C. Chicone. *Ordinary Differential Equations with Applications*. Vol. 2. Springer, 2000.

[12] E. A. Coayla-Teran, S. E. A. Mohammed, and P. R. C. Ruffino. "Hartman-Grobman Theorems Along Hyperbolic Stationary Trajectories". In: *Discrete and Continuous Dynamical Systems* 17.2 (2007), pp. 281–292.

[13] S. D. Conte and C. deBoor. *Elementary Numerical Analysis*. McGraw-Hill, New York, 1972.

[14] G. Crevecoeur et al. "EEG source analysis using space mapping techniques". In: *Journal of Computational and Applied Mathematics* 215.2 (2008), pp. 339–347.

[15] R. Dorfman. "An Economic Interpretation of Optimal Control Theory". In: *The American Economic Review* 59.5 (1969), pp. 817–831.

[16] N. E. Dowling. *Mechanical Behaviour of Materials*. Vol. 4. Prentice Hall, 2012.

[17] W. K. Durfee and K. I. Palmer. "Estimation of Force-Activation, Force-Length, and Force-Velocity Properties in Isolated, Electrically Stimulated Muscle". In: *IEEE Transactions on Biomedical Engineering* 41.3 (1994).

[18] D. Echeverria and P. W. Hemker. "Space Mapping and Defect Correction". In: *Computational Methods in Applied Mathematics* 5.2 (2005), pp. 107–136.

[19] M. Egermann and M. Thomsen. "Myoelektrische Prothesen bei Kindern im Kindergartenalter". In: *Der Orthopäde* 32.2 (2003), pp. 164–169.

[20] L. Franek. "Anwendung optimaler Steuerungsprobleme mit L^∞-Steuerbeschränkung auf ein Modellproblem der Bildverarbeitung". MA thesis. Westfälische Wilhelms-Universität Münster, 2007.

[21] M. Gerdts. *Optimale Steuerung*. Lecture Notes. 2009.

[22] P. Gerus, G. Rao, and E. Berton. "Ultrasound-based subject-specific parameters improve fascicle behaviour estimation in Hill-type muscle models". In: *Computer Methods in Biomechanics and Biomedical Engineering* 18.2 (2015).

[23] K. Ghobadi. "On the Discretize then Optimize Approach". Preprint for Industrial and Systems Engineering. 2009.

[24] A. M. Gordon, A. F. Huxley, and F. J. Julian. "The variation in isometric tension with sarcomere length in vertebrate muscle fibers". In: *The Journal of Physiology* 184.1 (1966), pp. 170–192.

[25] T. Götz, R. Rockenfeller, and K. P. Wijaya. "Optimization Problems in Epidemiology, Biomechanics & Medicine". In: *International Journal of Advances in Engineering Sciences and Applied Mathematics* 7.2 (2015), pp. 25–32.

[26] M. Günther. "Computersimulation zur Synthetisierung des muskulär erzeugten menschlichen Gehens unter Verwendung eines biomechanischen Mehrkörpermodells". PhD thesis. Universität Tübingen, 1997.

[27] M. Günther, S. Schmitt, and V. Wank. "High-frequency oscillations as a consequence of neglected serial damping in Hill-type muscle models". In: *Biological Cybernetics* 97.1 (2007), pp. 63–79.

[28] R. Haelterman. "Analytic study of the Least Squares Quasi-Newton method for interaction problems". PhD thesis. Universiteit Gent - Faculteit Ingenieurswetenschappen, 2009.

[29] D. F. B. Haeufle et al. "Can Quick Release Experiments Reveal the Muscle Structure? A Bionic Approach". In: *Journal of Bionic Engineering* 9.2 (2012), pp. 211–223.

[30] D. F. B. Haeufle et al. "Hill-type muscle model with serial damping and eccentric force-velocity relation". In: *Journal of Biomechanics* 47.6 (2014), pp. 1531–1536.

[31] C. Hai and R. Murphy. "Cross-bridge phosphorylation and regulation of latch state in smooth muscle". In: *American Physiological Society* 254.1 Pt 1 (1988), pp. C99–106.

[32] J. K. Hale and H. Kocak. *Dynamics and Bifurcations*. Vol. 3. Springer-Verlag, 1991.

[33] J. D. Harry et al. "Cross-bridge cycling theories cannot explain high-speed lengthening behavior in frog muscle". In: *Biophysical Journal* 57.2 (1990), pp. 201–208.

[34] R. F. Hartl, S. P. Sethi, and R. G. Vickson. "A Survey of the Maximum Principles for Optimal Control Problems with State Constraints". In: *SIAM Review* 37.2 (1995), pp. 181–218.

[35] H. Hatze. "A Myocybernetic Control Model of Skeletal Muscle". In: *Biological Cybernetics* 25.2 (1977), pp. 103–119.

[36] M. Heinkenschloss. "PDE Constrained Optimization". SIAM Conference on Optimization. May 2008.

[37] F. Heinrich. "Vorhersage der Fahrerbelastung während der Fahrt". MA thesis. Universität Stuttgart, 2012.

[38] W. Herzog, S. K. Abrahamse, and H. E. D. J. ter Keurs. "Theoretical determination of force-length relations of human skeletal muscles using the cross-bridge model". In: *European Journal of Physiology* 416.1 (1990), pp. 113–119.

[39] W. Herzog and B. Nigg. *Biomechanics of the Musculo-skeletal System*. John Wiley, 2007.

[40] W. Herzog et al. "Force-Length Properties and Functional Demands of Cat Gastrocnemius, Soleus and Plantaris Muscle". In: *Journal of Biomechanics* 25.11 (1992), pp. 1329–1335.

[41] A. V. Hill. "The Heat of Shortening and the Dynamic Constants of Muscle". In: *Proceedings of The Royal Society London B* 126.843 (1938), pp. 136–195.

[42] M. Hinze. *Mathematics of PDE constrained optimization - Discrete concepts*. Presentation in Oberwolfach. Nov. 2010.

[43] M. Hinze et al. *Optimization with PDE Constraints*. Vol. 23. Springer, 2009.

[44] H. Hu and D. Gu. "Reactive behaviours and agent architecture for Sony legged robots to play football". In: *Industrial Robot: An International Journal* 28.1 (2001), pp. 45–54.

[45] P. A. Huijing and G. J. Ettema. "Length-force characteristics of aponeurosis in passive muscle and during isometric and slow dynamic contractions of rat gastrocnemius muscle". In: *Acta morphologica Neerlando-Scandinavica* 26.1 (1988), pp. 51–62.

[46] H. Huppelsberg and K. Walter. *Kurzlehrbuch Physiologie*. Vol. 2. Thieme, 2005.

[47] B. R. Jewell and D. R. Wilkie. "The mechanical properties of relaxing muscle". In: *The Journal of Physiology* 152.1 (19660), pp. 30–47.

[48] R. Khlissa et al. "Application of Output Space Mapping Method for Fast Optimization Using Multi-Physical Modeling". In: *Energy Conversion Congress and Exposition (ECCE), 2012 IEEE* (2012).

[49] B. Kummer. *Skript und Ergänzung für "Variationsrechnung und Optimale Steuerung"*. 2010.

[50] E. Kvaalen. "A faster Broyden method". In: *BIT Numerical Mathematics (SIAM)* 31.2 (1991), pp. 369–372.

[51] R. L. Lieber. *Skeletal Muscle Structure, Function, and Plasticity*. Vol. 3. Wolters Kluwer - Lippincott Wiliams and Wilkins, 2009.

[52] A. M. Lyapunov. "The General Problem of the Stability of Motion (In Russian)". PhD thesis. Univ. Kharkov, 1892.

[53] E. H. Moore. "On the reciprocal of the general algebraic matrix". In: *Bulletin of the American Mathematical Society* 26.9 (1920), pp. 394–395.

[54] F. Mörl et al. "Electro-mechanical delay in Hill-type muscle models". In: *Journal of Mechanics in Medicine and Biology* 12.5 (2012), pp. 85–102.

[55] S. Noschese, L. Pasquini, and L. Reichel. "Tridiagonal Toeplitz matrices: properties and novel applications". In: *Numerical Linear Algebra with Applications (Special Issue: Inverse Problems Dedicated to Biswa Datta)* 20.2 (2013), pp. 302–326.

[56] H. J. Oberle. *Variationsrechnung und Optimale Steuerung.* Skript zur Vorlesung. 2008.

[57] J. Östh, J. M. Ólafsdóttir, and K. Brolin. "Modeling Active Human Muscle Responses during Modelling Acitve Human Muscle Responses during Driver and Autonomous Avoidance Maneuvers". In: *3rd Workshop on Computational Engineering.* 2014, pp. 46–51.

[58] M. Pandy, F. E. Zajac, and W. Levine E. Sim. "An optimal control model for maximum-height human jumping". In: *J. Biomechanics* 23.12 (1990), pp. 1185–1198.

[59] R. Penrose. "A generalized inverse for matrices". In: *Proceedings of the Cambridge Philosophical Society* 51 (1955), pp. 406–413.

[60] H. J. Pesch and M. Plail. "The Maximum Principle of optimal control: A history of ingenious ideas and missed opportunities". In: *Control and Cybernetics* 38.4A (2009), pp. 973–995.

[61] L. S. Pontryagin. *The Mathematical Theory of Optimal Processes.* Interscience Publishers, 1962.

[62] M. Prieß and T. Slawig. "Aggressive space mapping for optimisation of a marine ecosystem model". In: *International Journal of Mathematical Modelling and Numerical Optimisation* 3.1-2 (Jan. 2012), pp. 98–116.

[63] D. E. Rassier, B. R. Macintosh, and W. Herzog. "Length dependence of active force production in skeletal muscle". In: *Journal of Applied Physiology* 86.5 (1999), pp. 1445–1457.

[64] M. Redhe and L. Nilsson. "Optimization of the new Saab 9-3 exposed to impact load using a space mapping technique". In: *Structural and Multidisciplinary Optimization* 27.5 (2004), pp. 411–420.

[65] R. Rockenfeller. "Translationsebenen der Ordnung 32". MA thesis. Technische Universität Kaiserslautern, 2011.

[66] R. Rockenfeller and T. Götz. "Optimal Control of Isometric Muscle Dynamics". In: *Journal of Mathematical and Fundamental Sciences* 47.1 (2015), pp. 12–30.

[67] R. Rockenfeller and M. Günther. "Determining Concentric and Eccentric Dynamic Muscle Properties from Isometric Contraction Experiments". In: *Submitted to: Mathematical Biosciences* ((November 2015)).

[68] R. Rockenfeller et al. "Comparative Sensitivity Analysis of Muscle Activation Dynamics". In: *Computational and Mathematical Methods in Medicine* Article ID 585409, doi:10.1155/2015/585409 (2015), 16 pages.

[69] C. Rode, T. Siebert, and R. Blickhan. "Titin-induced force enhancement and force depression: A 'sticky-spring' mechanism in muscle contractions?" In: *Journal of Theoretical Biology* 259.2 (2009), pp. 350–360.

[70] E. Schechter. *Handbook of Analysis and its Foundations,* London: Academic Press Inc., 1997.

[71] S. Schmitt et al. "Theoretical Hill-Type Muscle and Stability: Numerical Model and Application". In: *Computational and Mathematical Methods in Medicine* (Volume 2013 (2013), Article ID 570878), 7 pages.

[72] André Seyfarth et al. "Can Robots Help to Understand Human Locomotion?" In: *Automatisierungstechnik* 60.11 (2012), pp. 653–661.

[73] L. F. Shampine, J. Kierzenka, and M. W. Reichelt. *Solving Boundary Value Problems for Ordinary Differential Equations in MATLAB with bvp4c*. The MathWorks, Natick, MA. 2000.

[74] J. Sherman and W. J. Morrison. "Adjustment of an Inverse Matrix Corresponding to a Change in One Element of a Given Matrix". In: *Annals of Mathematical Statistics* 21.1 (1950), pp. 124–127.

[75] T. Siebert et al. "Nonlinearities make a difference: comparison of two common Hill-type models with real muscle". In: *Biological Cybernetics* 98.2 (2008), pp. 133–143.

[76] J. Stoer and R. Bulirsch. *Introduction to Numerical Analysis*. Springer-Verlag, 1980.

[77] G. W. Swan. "Role of optimal control theory in cancer chemotherapy". In: *Mathematical Biosciences* 101.2 (1990), pp. 237–284.

[78] G. Sweers. *Gewöhnliche Differentialgleichungen - Vorlesungsskript*. Universität Köln. 2008.

[79] A. J. van Soest. "Jumping from Structure to Control: A Simulation Study of Explosive Movements". PhD thesis. Amsterdam: Vrije Universiteit, 1992.

[80] F. Verhulst. *Nonlinear Differential Equations and Dynamical Systems*. Springer-Verlag, 1990.

[81] K. P. Wijaya, T. Götz, and E. Soewono. "An optimal control model of mosquito reduction management in a dengue endemic region". In: *International Journal of Biomathematics* 7.5 (2014), [22 pages].

[82] J. N. Yang. "Application of Optimal Control Theory to Civil Engineering Structures". In: *Journal of the Engineering Mechanics Division* 101.6 (1975), pp. 819–838.

[83] T. F. Yu and A. J. Wilson. "A passive movement method for parameter estimation of a musculo-skeletal arm model incorporating a modified hill muscle model". In: *Computer Methods and Programs in Biomedicine* 114.3 (2014).

[84] F. E. Zajac. "Muscle and Tendon: Properties, Models, Scaling, and Application to Biomechanics and Motor Control". In: *Critical Reviews in Biomedical Engineering* 17.4 (1989), pp. 359–411.